CONCURRENT AERODYNAMIC SHAPE / COST DESIGN OF MAGNETIC LEVITATION VEHICLES USING MULTIDISCIPLINARY DESIGN OPTIMIZATION TECHNIQUES

By

Jason Scott Tyll

a dissertation submitted to the faculty of

virginia polytechnic institute and state university

in partial fulfillment of the requirements for the degree of

doctor of philosophy

in

Aerospace Engineering

Joseph A. Schetz, Chairman

Dean T. Mook

William H. Mason

James F. Marchman III

Michael P. Deisenroth

July 1997

Blacksburg, Virginia

Concurrent Aerodynamic Shape / Cost Design of Magnetic Levitation Vehicles Using Multidisciplinary Design Optimization Techniques

by

Jason Scott Tyll

Committee Chairman: Joseph A. Schetz
Aerospace Engineering

(ABSTRACT)

A multidisciplinary design optimization (MDO) methodology is developed to link the aerodynamic shape design to the system costs for magnetically levitated (MAGLEV) vehicles. These railed vehicles can cruise at speeds approaching that of short haul aircraft and travel just inches from a guideway. They are slated for high speed intercity service of up to 500 miles in length and would compete with air shuttle services. The realization of this technology hinges upon economic viability which is the impetus for the design methodology presented here. This methodology involves models for the aerodynamics, structural weight, direct operating cost, acquisition cost, and life cycle cost and utilizes the DOT optimization software. Optimizations are performed using sequential quadratic programming for a 5 design variable problem. This problem is reformulated using 7 design variables to overcome problems due to non-smooth design space. The reformulation of the problem provides a smoother design space which is navigable by calculus based optimizers. The MDO methodology proves to be a useful tool for the design of MAGLEV vehicles. The optimizations show significant and sensible differences between designing for minimum life cycle cost and other figures of merit. The optimizations also show a need for a more sensitive acquisition cost model which is not based simply on weight engineering. As a part of the design methodology, a low-order aerodynamics model is developed for the prediction of 2-D, ground effect flow over bluff bodies. The model employs a continuous vortex sheet

to model the solid surface, discrete vortices to model the shed wake, the Stratford Criterion to determine the location of the turbulent separation, and the vorticity conservation condition to determine the strength of the shed vorticity. The continuous vortex sheet better matches the mechanics of the flow than discrete singularities and therefore better predicts the ground effect flow. The predictions compare well with higher-order computational methods and experimental data. A 3-D extension to this model is investigated, although no 3-D design optimizations are performed.

Acknowledgments

The author would like to acknowledge the following people for their involvement in this work and in his life.

I would first like to express my appreciation and admiration for my committee chairman, Dr. Joseph A. Schetz. I could not imagine a better choice for a research advisor and mentor. His guidance, and the opportunities he afforded me were invaluable elements of my education.

I would like to thank Dr. Dean T. Mook, Dr. William H. Mason, Dr. James F. Marchman III, and Dr. Michael P. Deisenroth for serving as members of my committee. Thank you for your insightful input during my research proposal and for reading this dissertation. Special thanks goes to Dr. Mook for all of the help he has given in the development of the aerodynamics model. Thanks also goes to Dr. Roger Simpson and Dr. Eugene Cliff for their insight into technical problems we encountered along the way, and to Dr. Deisenroth and Mark A. Eaglesham for developing the cost models. I would also like to acknowledge the Multidisciplinary Analysis and Design Center for Advanced Vehicles for supporting this work.

On a more personal note, I would like to acknowledge my friends for being just that. Thanks for all of the support, advice, loyalty, love, companionship and good times.

All that I have I owe to my family; my parents, Howard and Harriet Tyll, my sister, Erika, and my aunt, Rochelle Zaltzman. Thanks for all of the love and support you have given me over the years. Your ceaseless encouragement gives me the strength and self confidence I need to reach my potential.

Lastly, I would like to acknowledge two people who had a tremendous impact

on my life; my grandparents, Joseph and Nesi Zaltzman. They came to the United States in 1949 as refugees; World War II Holocaust survivors . They came here with nothing ,and like so many others, faced adversity. Their tremendous personal strength enabled them to build a life and learn a new language after all that they had and knew were destroyed. Within ten years they owned a business and within fifteen, a house. I was fortunate enough to be raised partially in their household where I learned, by example, the power of determination and hard work. They instilled in me their values, strength, and a sense of tradition. And so, it is to their memory that I dedicate this work.

To bobi & zady

Contents

List of Figures

List of Tables

Nomenclature

c chord

$\mathbf{c}$ constraints

C_p pressure coefficient

C_D drag coefficient

C_L lift coefficient

C_m pitching moment coefficient

d characteristic diameter

D drag, and
structural depth

e internal energy

$\mathbf{g}$ gradient of the objective function

h height

H Hessian matrix

k thermal conductivity

l direction along line integral

L lift, and
structural length

m pitching moment

$\mathbf{n}$ unit normal

N_Z ultimate load factor

OBJ objective function

p pressure

$\mathbf{p}$ search direction

q dynamic pressure

R region

$\mathbf{r}$ position vector

Re Reynolds number

S region boundary

S_f surface area

t time

u tangential surface velocity

u_* friction velocity

$\mathbf{V}$ velocity vector

W weight

x dimension parallel to solid surface

$\mathbf{x}$ design variables

y dimension perpendicular to solid surface

α angle of attack

γ vortex sheet strength

Γ circulation

δ boundary layer height

η Lagrange multiplier

μ distributed doublet strength, and
viscosity

ν kinematic viscosity

ρ density

σ vortex blob diameter, and
source strength

Φ velocity potential, and
dissipation function (energy equation)

ϕ disturbance potential

$\mathbf{\Omega}$ vorticity vector

Subscript

B	Boundary Layer
dg	design gross
f	fluid
h	gap height
L	lower
TE	trailing edge
S	solid
T	turbulent
U	upper
w	wake
∞	infinity

Chapter 1

Introduction

1.1 Overview

The design of advanced aerospace vehicles is inherently multidisciplinary and should therefore be reflected in a suitable design methodology. Approximately 80% of the cost associated with the product is committed during the conceptual and preliminary design phases [1]. Since very little money has actually been spent at this stage in the design process, the gravity of the design decisions and the pivotal nature of these early phases becomes evident. In the design of most aerospace vehicles, aerodynamics plays a major role in determining propulsion, structural, and control requirements. Aerodynamics also has strong ties to the overall cost. Designing for good aerodynamics while ignoring cost as a design objective will surely result in a flawed design which will incur many off-design penalties over the life of the vehicle. It is, therefore, important to develop a design methodology which will incorporate all essential disciplines. This research involves the development of such a methodology which includes cost as a figure of merit for the shape design of high speed, magnetically levitated vehicles (trains).

The technological advantage of MAGnetically LEVitated (MAGLEV) vehicles over trains is that they lack wheels which cap the maximum speed at approximately 200 mph. This technology is capable of speeds approaching that of aircraft, so the

target speed for this first generation of MAGLEV vehicles is 300 mph. Market analyses have, therefore, slated MAGLEV vehicles for high speed intercity service of up to 500 miles in length. This would put MAGLEV vehicles in competition with short haul air transportation and shuttle service. It could complete this mission, with approximately two stops, in under two hours and embark and terminate in city centers. This would relieve highway and air traffic congestion and offset the need to add highway lanes and build new airports near cities to accommodate for growth. In addition to this, the MAGLEV system has low energy consumption per seat mile estimated at one quarter of that of a commercial aircraft for a similar mission [2].

The design challenges for the aerodynamic shape of MAGLEV vehicles are greatly different from that of airplanes. With magnetic suspension, aerodynamic forces are not the only source of lift and drag, so the performance parameters are not as strong a function of the aerodynamic lift to drag ratio. The inclusion of cost as a design goal is, therefore, essential in making design decisions involving magnetic vs. aerodynamic forces and moments. The absence of onboard fuel removes range from the problem. Performance is based on cruise Mach number, energy used, and payload weight. The close proximity of the track changes the aerodynamics, necessitating specific ground effect analyses for design. Cross wind sensitivity is important due to the small track clearances involved and the need for lateral directional control. The design for some service corridors will be based heavily on the issues of vehicle aerodynamics in tunnels and vehicle passing. The potential proximity to areas of human population makes noise abatement a prominent design goal. The aerodynamic shape must also be chosen with respect to manufacturing complexities and concerns. The issue of manufacturability strongly connects the aerodynamic design to the life cycle cost of the vehicle.

The study of life cycle costs is important for measuring the economic viability of the project. Use of only the acquisition cost, or only the operating cost as the primary measure, neglects the real operating environment of the system. Life cycle cost captures all relevant costs for the project, from the conceptual design phase, through the detailed design phases, production of the system, deployment of the system, operation and maintenance of the system, and the planned retirement and

disposal of the system. This analysis takes account of the economic factors relevant to the life cycle, such as the cost of capital, the time value of money, tax effects on cash flows, and the costs of disposal of the system. For this work, the life cycle cost model uses capital cost elements from the work breakdown structure prepared for the Northrop Grumman MAGLEV vehicle [3]. Using projected passenger traffic loading, the profitability of the project can be calculated using discounted cash flow analysis. The realization of this technology hinges upon economic viability which is the impetus for the design approach presented here.

The concurrent handling of aerodynamic and economic performance is accomplished using multidisciplinary design optimization techniques (MDO). Multidisciplinary design optimization is the instrument by which one can consider several disciplines at once and mathematically link them to consider the interactions. This is advantageous over dealing with each discipline sequentially. Using such tools, one can deal with numerous individual disciplines and satisfy mission requirements while achieving optimum performance with respect to some predetermined figure of merit. Such an approach is very useful for conceptual and preliminary design phases where analyses are, by definition, simple and inexpensive to perform. The work here employs the sequential quadratic programming method. It is a gradient based optimization method and is considered to be the current state of the art in this "mature" area of optimization theory.

The work presented here involves the development of a design methodology for the concurrent aerodynamic and cost design of MAGLEV vehicles. The design methodology has been created to operate in an automated fashion, and it is modular to allow for the continual improvement of the individual models. This attribute is particularly important for the cost models which are low fidelity at this early stage in the development process. The design loop is set up around the sequential quadratic programming optimizer which can perform constrained optimizations. The objective functions for the optimization are provided by several modules which are shown in Fig. 1.1. The module input, output, and contents are discussed in the following chapters. A great deal of effort was put into developing the aerodynamics model which is a low-order model for the flow over bluff bodies in ground effect. "Low-order" refers to methods

based upon Laplace's equation (to be discussed in Chapter 2) while "high-order" refers to models based upon the Navier-Stokes equation. One of the largest problems involved in performing multidisciplinary design optimizations of vehicles is in acquiring the aerodynamic coefficient sensitivities. The method developed here is a low-order (simple and quick) method which can predict flow phenomena normally attributed to high-order methods. This model overcomes this obstacle which stems from the prohibitive cost of high-order aerodynamic calculations for these complicated flow fields. The cost models were assembled by Eaglesham and Deisenroth from the Industrial and Systems Engineering Department at Virginia Tech [4]. A five design variable test problem (2-D, side view) is performed to evaluate the methodology and determine design optima for several figures of merit. These are drag coefficient, lift to drag ratio, empty weight, acquisition cost, operating cost, and life cycle cost. The extension to full 3-D designs is discussed in the section on the 3-D aerodynamics model (Section 2.3). Optimizations have not yet been performed using full 3-D aerodynamics.

1.2 Ground Effect

The aerodynamics problem being dealt with in this work is the incompressible, exterior flow over a bluff body in close ground proximity. The ground effect flow is different than that of an automobile or conventional train. The MAGLEV vehicle is in close proximity to a guideway, which is raised above the ground. The modeling of such flows is a difficult problem and is one which involves non-linear aerodynamics and consequently expensive solution methods. A new development associated with this work is the use of low-order aerodynamic computations to solve for these flows. The method proposed is capable of generating solutions which are comparable to higher-order methods and experiments. The "lift reversal" phenomena is captured, and quantitative aerodynamic characteristics are obtained. It is also shown that the choice of panel method singularities is crucial to the calculation of flow over bodies in strong ground effect.

1.3 System Requirements

The MAGLEV transportation system technical requirements can be found in a report put together by ENSCO, Inc. [5]. This document discusses the different operation concepts and specific factors outlined by the Intermodal Surface Transportation Efficiency Act of 1991. Requirements are outlined in the general categories of basic performance, system operations, operating environment, safety and security, environmental impacts, ride quality and passenger environment, and cost. Most of these requirements involve detailed design parameters which are not dealt with here. This report describes a balance between technical performance and capital and operating costs. This design methodology is developed to address such requirements in the conceptual design phase.

1.4 A Brief History of MAGLEV Vehicles

Magnetic levitation (MAGLEV) is finding its way into many applications ranging from space launch systems to bearings. It had initially been proposed as a means of high speed ground transportation at the beginning of the twentieth century. Interest has been intermittent throughout this century, and financial backing materialized when technological obstacles broke down and the political climate allowed. A brief history of MAGLEV Vehicles can be seen in the following subsections each pertaining to a specific country which is participating in the development of such vehicles [6].

1.4.1 United States of America

The use of magnetic levitation as a means of high speed ground transportation was first proposed by Robert Goddard in 1909. His idea involved a vehicle traveling through a tube in partial vacuum [7]. In 1912, a french engineer named Emile Bachelet built and patented a small scale prototype vehicle which achieved levitation using AC current repulsive magnets. Due to the level of technology at the time, Bachelet's ideas could not be extrapolated to a full-scale vehicle.

Superconductivity paved the way for a full-scale magnetically suspended vehicle. Powell and Danby worked in the area throughout the 1960s at Brookhaven National Laboratory. Their work which involved superconducting levitation magnets and vehicle propulsion via linear synchronous motors became well known, and they received a patent in 1969. Work continued in the US under Federal Railroad Administration funding through the High Speed Ground Transportation Act of 1965. A 1/25th scale model riding on a guideway was completed at the Stanford Research Institute in 1973. Research ended abruptly in 1975 when all funding was cut by the federal government.

After fifteen years of technological progress abroad, interest was renewed in the US. The National Maglev Initiative was founded in 1990 as a consortium consisting of the Federal Railroad Administration, the Department of Transportation, the US Army Corp of Engineers, and the Department of Energy. The Intermodal Surface Transportation Efficiency Act of 1991 stipulated the adaptation of the national intermodal transportation system to new technologies, including magnetic levitation vehicles. It also established a US MAGLEV prototype development program for the design and building of a prototype system. Senator Daniel Patrick Moynihan (D-NY) was instrumental in the inclusion of MAGLEV technology in the highway bill, which appropriated $725 million for the prototype development program. Under this program, the National MAGLEV Initiative chose four companies to propose system concept definitions; Bechtel, Magneplane, Foster Miller, and Northrop Grumman. Their respective designs can be seen in Fig. 1.2.

As part of this program Virginia Polytechnic Institute was contracted to perform wind tunnel testing on the Northrop Grumman vehicles (1993) [8]. In an effort separate from that of the NMI, American Maglev Technologies of Florida received a contract from the federal government to develop and build a prototype of their own system along with a test track. Ground was broken in 1995. Virginia Polytechnic Institute was also involved in the aerodynamic testing of the American MAGLEV Technology [9] vehicle whose shape was design by Lockheed Martin Georgia Company. Interest by the federal government has since waned.

1.4.2 Germany

German involvement in MAGLEV vehicle technology began with Kemper who performed research in the 1930's and received a patent in 1934. A consortium of German companies began a program to develop and test vehicles in 1969. Their seventh vehicle, the Transrapid 07 (TR07) was certified for operation in 1991 (Fig. 1.3). Their system is of the ElectroMagnetic Suspension (EMS) type which is characterized by their attractive magnets and their configuration which has the vehicle wrapped around a "T" shaped track. EMS systems are unstable since a perturbation upwards brings the attractive magnets closer together, increasing the attractive force. A perturbation downwards moves the attractive magnets further apart, decreasing their attractive force, and therefore their ability to return to the neutral position. Active control is required to maintain stability. A schematic diagram of an EMS system can be seen in Fig. 1.4. It shows the vehicle, "T" shaped track, and attractive magnets. The TR07 was the first MAGLEV vehicle system ready to enter commercial service. Plans to build the TR07 system for a 13 mile stretch from Orlando airport to Walt Disney World in Florida by 1996 ($98 million) was later cancelled by the US government. The author is unaware of any current plans to implement this transportation system.

1.4.3 Japan

The Japanese program is run by the Japanese National Railways. Their first vehicle was built in 1970, and the first successful levitation was achieved in 1972. The Japanese system employs ElectroDynamic Suspension (EDS) which is characterized by repulsive magnets and a "U" shaped track similar to a bobsled. A schematic diagram of an EDS system can be seen in Fig. 1.5. EDS systems are stable since perturbations are naturally corrected by the change in magnet proximity. A perturbation upwards moves the repulsive magnets apart, decreasing their repulsive force, and returning the vehicle to the neutral point. A perturbation downward also returns to the neutral point since the reduced proximity of the magnets increases its repulsive force. The Miyazaki test track, a 4.4 mile long facility was opened in 1977 for

the testing of Japanese vehicle prototypes. Testing began on the MLU002 system in 1987. In 1990 the project gained the status of a nationally funded project [10], and building began on a new test facility called the Yamanashi Test line. The MLU002 was destroyed in a fire, and the MLU002N began testing in 1993. In the spring of 1997, full-scale tests began using the Yamanashi test line which could become part of the Tokyo/Osaka line after tests are completed in 1999 [11].

1.5 Literature Review

1.5.1 MAGLEV Design

The work presented here deals with the design of MAGLEV vehicles with respect to aerodynamic shape and its effect on system cost. Numerical optimization is employed to formally link the individual disciplines. Such an optimization design requires choosing a specific MAGLEV system, since each differs in the method for propulsion and levitation. A review of the existing system concepts and some past design efforts is presented here.

The Japanese design teams have been developing MAGLEV vehicle concepts for almost thirty years. A great deal of information concerning their current activities and a brief history of their designs can be seen on the Japanese Railroad homepage [10]. The aerodynamic design for their current MLU002N can be seen in reports by Mitsubishi Heavy Industries, Central Japan Railway Company, and Railway Technical Research Institute. The evaluation of their aerodynamic model is reported by Kaiden, Hosaka, and Mazda [12]. Experimental validation for these computations is described in a report by Shimbo and Hosaka [13]. The aerodynamic design of the current Japanese vehicle (MLU002N) is discussed in a report by Miyakawa and Hosaka [14]. This work involves the design of frontal shapes using both experimental and computational tools. Consideration is given towards structural and manufacturing issues although no specifics are mentioned. The resulting design is a double cusp shape which has complex curvatures. The cause for such a complicated shape is the flow of air over the vehicle in the EDS ("U" shaped) track and for the aerodynamic

behavior during vehicle passing.

Aerodynamic work undertaken in Germany for the flow over MAGLEV vehicles and high speed trains is reviewed in a journal article by Peters of Krauss-Maffei [15]. In this paper, he discusses the aerodynamic issues involved with these vehicles, analysis methods (computational, track tests, wind tunnel tests, towing tank tests), drag breakdowns, and transient phenomena (cross-wind sensitivity, tunnels, and noise). Test track results for the German Transrapid system are discussed in a paper by Merklinghaus and Mnich [16].

Although the concept of MAGLEV vehicles has been known in the United States for most of the twentieth century, full-scale vehicle designs only began with the National MAGLEV Initiative in 1991. Details of the four system concept definitions can be seen in the final report of the government MAGLEV system assessment team [6]. This document compares the system concepts of Bechtel, Foster Miller, Grumman, and Magneplane. It also weighs the attributes of these designs against that of the German TRO7. The work presented here uses design specifics from the Northrop Grumman design, since this design concept went the furthest out of all the American concepts and the most information is available for it. The Grumman MAGLEV design is outlined in a summary report by the Grumman Team. This report consists of ten individual papers dealing with the system concept definition [17], the benefits of MAGLEV technology [18] [19], magnet design [20], power generation [21], the MAGLEV suspension system [22], structures and materials [23], aerodynamic design and analysis [24], cost [3], guideway cost [25], guideway design [26], and vehicle control [27].

Details of the aerodynamic design are covered in a paper by Siclari, et.al. [28]. This paper discusses the aerodynamic analysis method using the Reynolds Averaged Navier-Stokes equation (RANS), the design selection process, and the details of the final designs. The high cost of performing such computations precludes the incorporation of this type of analysis in an MDO framework. This aerodynamic analysis forms the baseline for the formal optimization work described here. The only evidence of another formal optimization design performed for the aerodynamic design of such vehicles is presented in a National MAGLEV Initiative report [29]. A minimization

of the front end drag of an EDS type vehicle is performed. Such a minimization is accomplished by minimizing the strength of the vortex that comes off the channel guideway as the vehicle passes ("bow vortex"). The channel is simulated using point vortices, and the passing vehicle is modeled using a point source of varying strength. This is used to control the rate at which the cross sectional area of the passing vehicle changes (circular cross section). An analytic function is obtained for the drag coefficient and it is minimized by plotting the function over a range of the single design variable and visually determining the minimum point.

1.5.2 MDO in Vehicle Design

Multidisciplinary design optimization enables the designer to consider several disciplines at once and design a vehicle concurrently for multiple objectives. This work deals specifically with linking the aerodynamic design to the system economics. This type of formal optimization hasn't been done before for MAGLEV vehicles, although there has been work performed for subsonic aircraft. Johnson [30] looked at minimizing life cycle cost for these aircraft. She considered fuel burned, take off gross weight, direct operating cost, acquisition cost, and life cycle cost as figures of merit. The results of this study showed different designs for the different figures of merit. Jensen [31] also looked at designing subsonic aircraft for various figures of merit. This work focused on determining which figures of merit to design for. He considered gross weight, life cycle cost, acquisition cost, fly-away cost, direct operating cost and fuel as figures of merit. Optimizations were performed based upon the different figures of merit, and off-design penalties were calculated. The inclusion of cost in multidisciplinary design of aircraft is discussed in an article by Rais-Rohani [32]. He discusses the different types of cost estimation models and addresses the issues involved in implementing them in such a design methodology.

1.5.3 Lower-Order Aerodynamic Analysis

Low-order aerodynamics analyses generally deal with the solution to Laplace's

equation which results from simplifying the Navier-Stokes equations for an incompressible, inviscid, irrotational flow. As part of this work, a low-order method is developed for the analysis of flow over a bluff body in ground effect. This method is a vortex panel method with continuous surface vorticity, a discrete vortex wake, separation location model, base pressure model, and ground effect model.

Vortex methods with discrete vortex shedding were first used by Rosenhead in the early 1930's. Since then, many methods have been developed which employ free vortices (vortex cloud). Leonard [33] discusses several methods along with the intricacies of vorticity transport and some insight into the theory and its capabilities. With the proper simulation of the flow mechanics, vortex methods are capable of simulating real flows including viscous layer velocity profiles, and boundary layer separation. These capabilities are usually attributed to high-order aerodynamics methods.

Katz [34] uses a discrete vortex method and sheets of free vortices to model the post-stall aerodynamics of wings. Vorticity is shed from the trailing edge and a predetermined separation location on the top surface of the airfoil at high angle of attack. Katz suggests the need to model thickness effects and to employ a separation criteria to allow for the calculation of flows at varied Reynolds numbers over bodies of arbitrary geometry. This idea forms the basis for the model used here to predict the ground effect flow, over bluff bodies.

A similar vortex method with separation criterion can be seen in work by Mendenhall [35]. This work deals with the flow around tactical missiles at angle of attack. Mendenhall uses the cross-flow analogy to determine the formation of the cross-flow separation. The cross flow planes are mapped into circles, and the bluff body flow around a circle is solved using a vortex method with sheets of shed vorticity. The location of the separation points is determined using the Stratford criteria, much the same way as it is done here.

The model used here is centered around a continuous vortex sheet method discussed in a paper by Mook and Dong [36]. That work is concerned with blade-vortex interaction and uses a continuous sheet vortex panel method for the flow over sharp trailing edge bodies. The trailing edge is treated using a flow model discussed by Giesing [37] and Basu and Hancock [38]. This model allows for an analogy to bluff

body separation if one does not consider flow entrainment into the separation bubble.

The problem of an airfoil in ground effect is discussed in a paper by Coulliette and Plotkin [39]. They perform calculations on a zero thickness parabolic arc airfoil and a Joukowski airfoil in ground effect conditions. The calculations are performed using both numerical and analytic solutions. This work is mentioned here because Coulliette employs a piecewise linear vortex panel method similar to the one used in this work. They were unable to calculate lift reversal, since flow separation was not modeled. A 3-D extension to the continuous vortex sheet method was developed by Mracek and Mook [40].

1.6 Design Problem Statement

The problem is to design the aerodynamic shape of a railed MAGLEV vehicle based on several figures of merit; drag coefficient, lift to drag ratio, empty weight, acquisition cost, direct operating cost, and life cycle cost. The vehicles use the Northrop Grumman geometry definition and the Grumman propulsion and levitation system. The system mission is for a corridor with an $800km$ trip distance, passenger load of 2000 per hour, and top speed of $134m/s$. The vehicle structure is composed of aluminum and they each carry 50 passengers. The economic factors used and the design specifics are discussed in the proper chapters to follow.

1.7 Outline

This dissertation is organized in the following manner. Chapters 2 through 6 discuss the different analyses employed in this design optimization. The multidisciplinary design optimization problem statement is described in Chapter 7. The basic 5 design variable problem is posed and a replacement 7 design variable problem is proposed. Chapter 8 shows the results from the optimizations. The 7 design variable problem is used to overcome the obstacle of non-smooth design space. Optimizations are performed for the following figures of merit; drag coefficient, lift to drag ratio,

empty weight, direct operating cost, acquisition cost, and life cycle cost. The resulting designs are compared. Conclusions and recommendations for future work in this area are shown in Chapter 9.

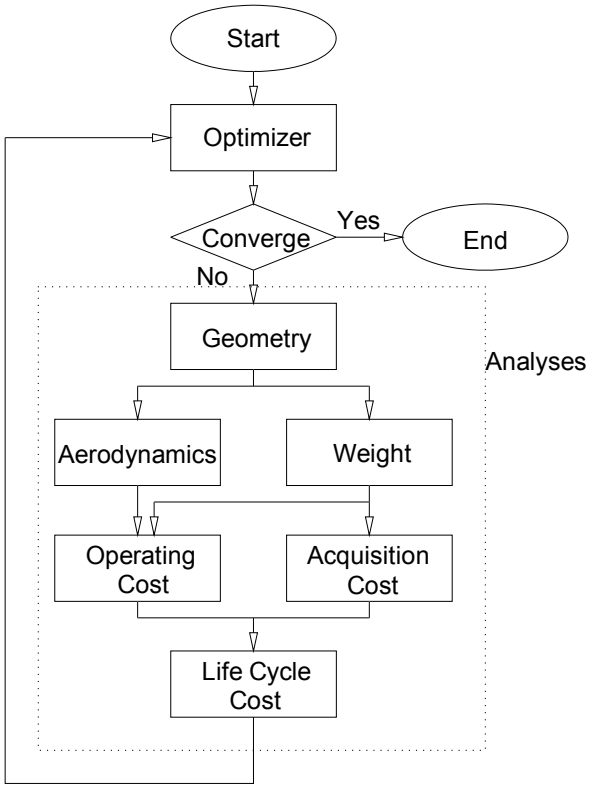

Figure 1.1: Design Methodology Flow Diagram

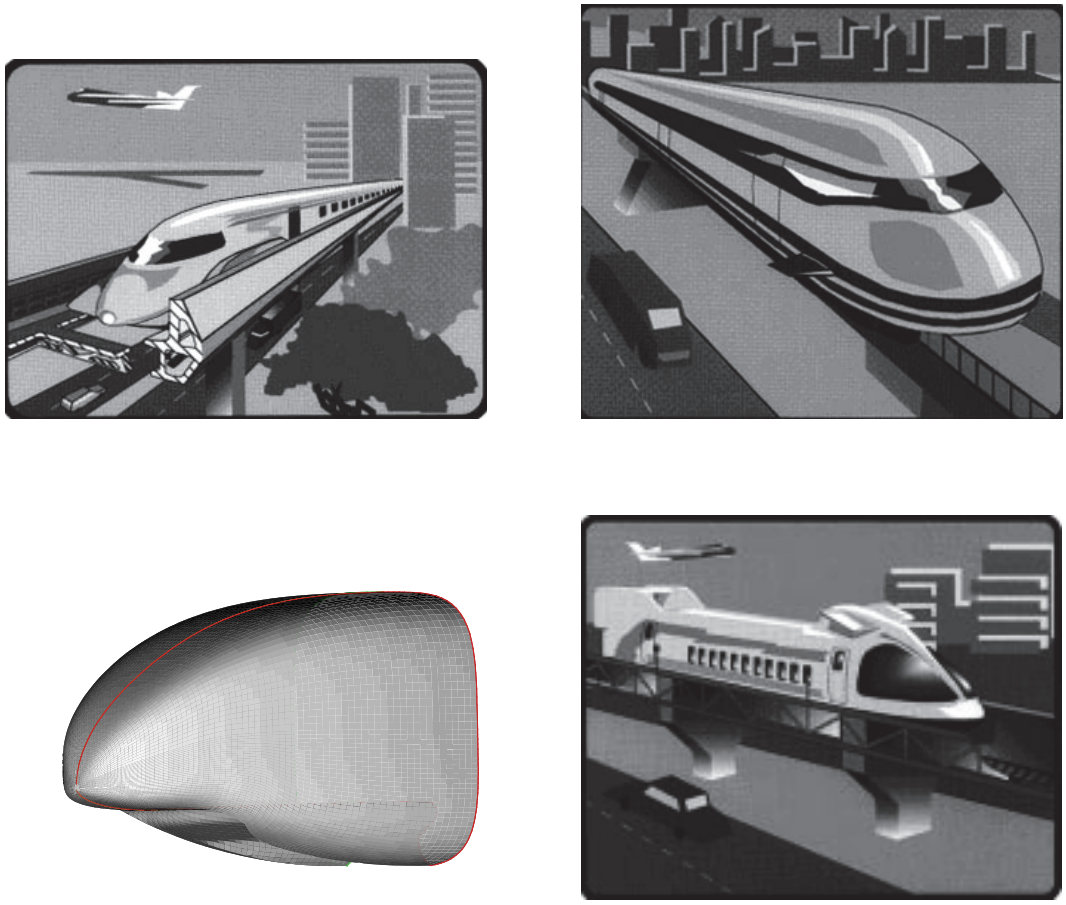

Figure 1.2: National MAGLEV Initiative System Concept Definitions [41]

Figure 1.3: Germany's Transrapid 07 [42]

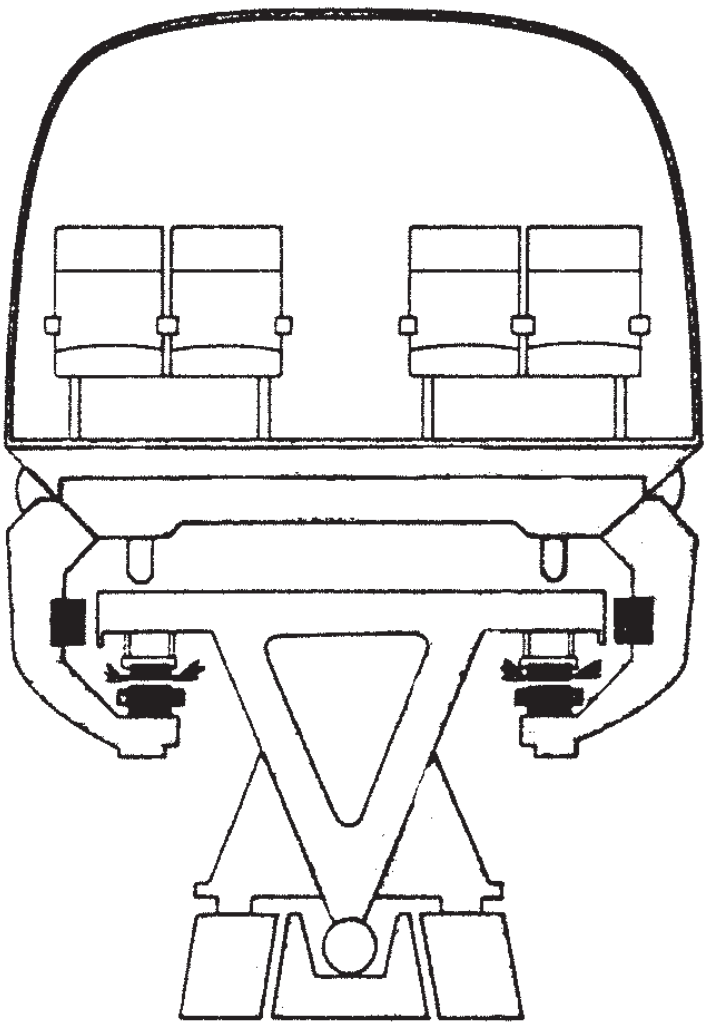

Figure 1.4: A Schematic Diagram of an ElectroMagnetic Suspension System [7]

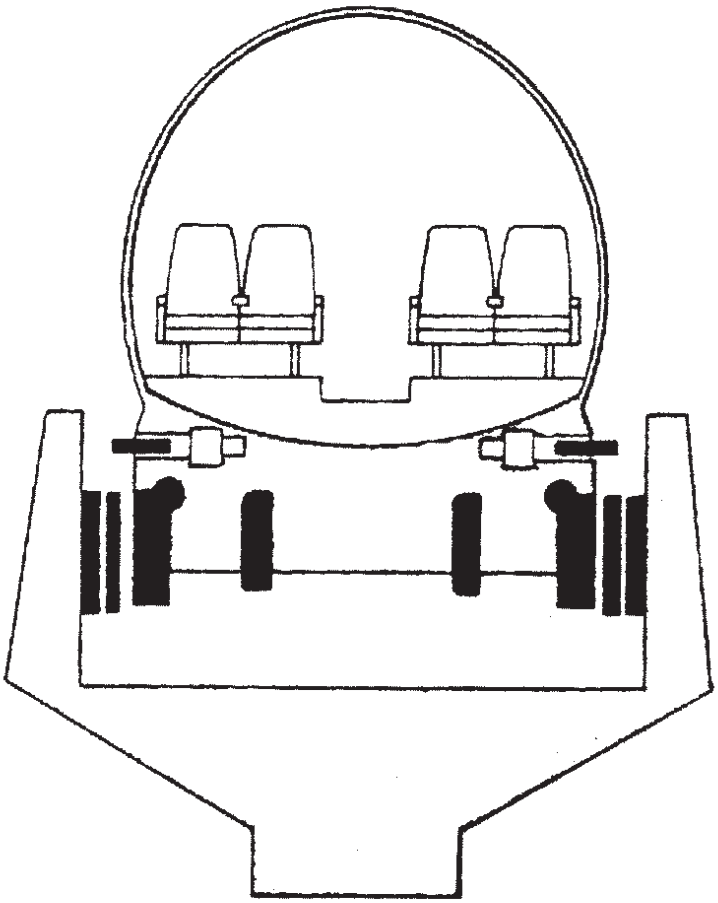

Figure 1.5: A Schematic Diagram of an ElectroDynamic Suspension System [7]

Chapter 2

Aerodynamics Model

2.1 Background Information

The aerodynamics problem being dealt with as part of the design of MAGLEV vehicles is an exterior flow over a bluff body in close ground proximity. The target speed is 300 MPH which corresponds to a cruise Mach number of 0.4. In general, these vehicles experience flow separation on the last car as well as strong ground effect augmentation of the aerodynamic force and moment coefficients (lift reversal). As a body is brought closer to a ground plane the lift coefficient will initially decrease (and may even become negative) due to the Venturi effect. According to this largely inviscid phenomena, the flow must accelerate to travel through the thin gap between the vehicle and the ground plane, thereby lowering the pressure on the underside and reducing the lift. If the body is situated below a critical ground clearance, the lift will reverse and increase for any further reduction in the height above the ground plane. This is due to viscous effects which include a repositioning of the stagnation point and the separation lines whereby the lower portion of the separation line moves forward and the upper portion of the separation line moves aft. For flow over a body with a sharp trailing edge, lift reversal can involve flow separation on the lower surface. The problem of lift reversal is a difficult one to solve since it usually involves flow separation which has to be predicted by any flow solution method tackling the problem. Bearman [43] discusses some of these difficulties.

The prediction of reasonable force and moment coefficients is pivotal to the success of this shape optimization design, therefore much thought and work has gone into the development of this model. Aerodynamic analyses are developed for 2-D and 3-D flows. This chapter discusses the theoretical background for the aerodynamic models used for the design optimizations and also points out important implications these models make about the simulation of ground effect aerodynamics.

Aerodynamic analysis involves the solution of mass, momentum, and energy conservation equations.

$$\begin{aligned} \frac{\partial \rho}{\partial t} + \nabla \cdot \rho \mathbf{V} &= 0 \\ \rho \left(\frac{\partial V_i}{\partial t} + \mathbf{V} \cdot \nabla V_i \right) &= \rho f_i - \frac{\partial}{\partial x_i} \left(p + \frac{2}{3} \mu \nabla \cdot \mathbf{V} \right) + \frac{\partial}{\partial x_j} \mu \left(\frac{\partial V_i}{\partial x_j} + \frac{\partial V_j}{\partial x_i} \right) \\ \rho \frac{De}{Dt} + p \nabla \cdot \mathbf{V} &= \sum_{i=1}^{3} \frac{\partial}{\partial x_i} \left(k \frac{\partial T}{\partial x_i} \right) + \Phi(\text{Dissipation Function}) \end{aligned} \tag{2.1}$$

Although it only strictly refers to the conservation of momentum equations, this collection of equations is often referred to as the Navier-Stokes equations by the Computational Fluid Dynamics (CFD) community. In this discussion, we will be loose with this term and will specifically refer to momentum conservation when appropriate. Navier-Stokes calculations, especially subsonic ones, are computationally intensive and expensive in terms of CPU time. These calculations require both surface and volume grids with enough resolution to capture important flow phenomena. For the case of the MAGLEV vehicle, this would include the viscous flow in the gap between the vehicle and the track and that in the separation region. For turbulent flows, the Reynolds averaged form of these equations is used.

The difficulty presented by the problem size for Navier-Stokes calculations of MAGLEV vehicles is evident in the design work performed by Northrop Grumman Corporation [28]. The analysis of the full three dimensional vehicle with an elevated guideway required an 18 block grid with 1.1 million points for the half plane model. Twelve hundred multigrid cycles were needed to reduce the residual by three to four orders of magnitude. They were able to perform one such analysis and instead performed smaller three dimensional and two dimensional Navier-Stokes calculations for most of the design process. Similar calculations performed at NASA Ames Research

Center [44] were also costly, requiring a 12 block grid with $876,912$ cells. It is abundantly clear that using Navier-Stokes analyses to analyze the flow over such vehicles within an optimization loop is too expensive and quite possibly implausible to automate at this time. Changes made to the surface geometry during an optimization loop might cause problems when mapping the grid, requiring manual repair.

Alternatively , the use of linear methods would require solely a surface grid and would require much less CPU time, making it more conducive for use in an MDO framework. The disadvantages of using such methods are that they cannot predict the effects of diffusion (skin friction and separation) and therefore rely on empirical relationships for this information. The advantages of using such methods are that boundary layer strip theory can provide reliable skin friction values, consistent separation criteria exist for two dimensional and axially symmetric turbulent flow, there is no need for the empiricism involved with turbulence models, they are easy to discretize, and fast to solve. It is for these reasons that the work presented here employs such methods.

Linear methods deal with the solution to Laplace's equation which results from several simplifying assumptions to the Navier-Stokes equations. Since the cruise Mach number is not high, the flow can be assumed incompressible. Since the density is then known throughout the flowfield there is no coupling of the energy conservation equation with those of mass and momentum conservation so the energy equation is not needed to uniquely determine the flowfield. Mass conservation is accomplished by maintaining that the velocity vector field is solenoidal.

$$\nabla \cdot \mathbf{V} = 0 \tag{2.2}$$

Assuming the flow is inviscid and irrotational, the continuity equation can be solved independently. The irrotational assumption allows the velocity vector to be derived from a scalar potential function, Φ, such that the gradient of Φ is the velocity vector. This is a result of the requirement that the circulation be zero for any arbitrary closed, reducible path in the fluid region. In order for this to be true, the integrand in the definition of circulation must be an exact differential. This can be seen in Eq.

2.3.

$$\begin{aligned}
\Gamma &= \oint_C \mathbf{V} \cdot dl = 0 \\
\Gamma &= \oint_C [udx + vdy + wdz] \\
&= \oint_C d\Phi \\
\Gamma &= \oint_C \left[\frac{\partial \Phi}{\partial x} dx + \frac{\partial \Phi}{\partial y} dy + \frac{\partial \Phi}{\partial z} dz \right] \\
\mathbf{V} &= \nabla \Phi
\end{aligned} \tag{2.3}$$

If the velocity vector is replaced in the continuity equation the resulting equation is Laplace's Eq. (2.4).

$$\nabla^2 \Phi = 0 \tag{2.4}$$

The flow can be completely determined based on mass conservation which involves one equation and one scalar unknown. The pressure field can then be found using the momentum equation (Bernoulli equation). Laplace's equation is a linear, homogeneous, partial differential equation. The analytic solutions to this equation are referred to as harmonic functions and can be linearly superimposed to satisfy the two boundary conditions.

Laplace's equation is solved by setting up a collection of these mathematically singular solutions on the solid boundaries of the flow. This separates the flow into two regions of potential flow (incompressible, irrotational, inviscid), one exterior to and one interior to a closed body. For our application, we will be concerned with the flow exterior to the boundary. This region is bounded by an interior boundary (the solid surface) and an exterior boundary at an infinite distance from the solid surface. The strengths of these functions are determined by imposing the aforementioned boundary conditions. This boundary condition is that of no-penetration of the fluid through the body surface and can be generally handled in one of two ways. The Neumann boundary condition is a direct implementation of no-penetration stating that the flow cannot have a velocity component normal to the boundary at the boundary surface. This condition is explicitly imposed at control points on the interior boundary and is

mathematically shown in Eq. 2.5.

$$\nabla\Phi \cdot \mathbf{n} = 0 \tag{2.5}$$

The harmonic functions automatically satisfy the no-penetration boundary condition at the infinity boundary. The Dirichlet boundary condition states that the no-penetration condition is equivalent to setting the potential inside the body described by the boundary to a constant. This boundary condition will be described in greater detail in the discussion of the doublet panel method for 2-D (Section 2.2.1) and 3-D flow (Section 2.3.1).

Another possible boundary condition is the no-slip condition which states that there is no relative tangential velocity between the solid and fluid at the boundary. It is generally not imposed for inviscid flows since the no-penetration condition on the two boundaries makes up the two necessary boundary conditions for the second order partial differential equation. The no-slip condition is mentioned here because it will be employed for the vortex panel method used in this work. It will be further discussed in Section 2.2.2 for the 2-D case and Section 2.3.3 for the 3-D case.

The formulation of the solution to Laplace's equation via the superposition of harmonic functions is different for lifting and non-lifting bodies. For non-lifting bodies, one can proceed with the solution without any additional information. On the other hand, the flow around lifting bodies cannot be calculated due to the implications of the irrotational assumption. Using Stokes Theorem with the irrotational flow assumption for a 3-D flow around a closed body in an infinite fluid region, one finds that the flow is acyclic ($\Gamma = 0$) and therefore cannot produce lift according to the Kutta-Joukowski theorem. For 2-D flow around an infinite cylinder of arbitrary cross section in an infinite fluid, the flow may or may not be cyclic, although the circulation is indeterminate. In order to calculate the flow around lifting bodies, auxiliary conditions are needed to uniquely determine the circulation around the body. These conditions are imposed in various ways but invariably stem from a condition on vorticity conservation.

Vorticity conservation conditions for incompressible flow with uniform density and

kinematic viscosity are shown in Eq. 2.6 for several different flow situations [45].

$$\begin{array}{ll} 3-D & \begin{cases} Viscous: \iiint_{R_\infty} \mathbf{\Omega} dR = 0 \\ Inviscid: \iiint_{R_f} \mathbf{\Omega} dR = 0 \end{cases} \\ 2-D & \begin{cases} Viscous: \frac{d}{dt} \iint_{R_\infty} \mathbf{\Omega} dR = 0 \\ Inviscid: \frac{d}{dt} \iint_{R_f} \mathbf{\Omega} dR = 0 \end{cases} \end{array} \tag{2.6}$$

These conditions stem from conservation of angular momentum. Their derivation along with a brief discussion can be found in Appendix A. All of the conditions shown here are in terms of the integral of vorticity over a region. R_f refers to the fluid region and R_∞ refers to the combined fluid and solid regions. For viscous flow cases, the integral of vorticity over the combined solid/fluid region is always a constant. For three dimensional flow, this constant is always zero, while for two dimensional flow this constant is zero if the flow begins from rest. Since this condition is imposed over the entire region, R_∞, it provides a relationship between the vorticity in the fluid and the vorticity of the solid regions which is two times the angular velocity of the solid body rotation. This vorticity is transported across the solid boundary via the no-slip condition. The vorticity diffuses and convects into the fluid region in such a way as to obey the equations of motion and the boundary conditions.

The vorticity conservation conditions for the inviscid flow cases closely resemble the vorticity conservation conditions for viscous flow except the integral excludes the solid regions. This is a result of the absence of a no-slip condition, so vorticity associated with the angular velocity of the solid regions cannot be transported across the solid boundaries. The difference between this condition and that for the viscous case is a crucial one which has a large impact on the solution to many flowfields, especially unsteady ones. For an obvious example, one can look at the 2-D flow around an airfoil oscillating in pitch. If Eq. A.24 is used as the vorticity conservation condition and the problem is impulsively started, then the integral of the vorticity throughout the fluid region will be zero for all time. If Eq. A.22 is used as the vorticity conservation condition and the problem is impulsively started, then the integral of the vorticity over the fluid region is equal to the negative of two times the angular velocity of the pitching airfoil. The latter case for this example is closer to reality

and can be implemented as a conservation condition even if the inviscid assumption is made (diffusion of vorticity is ignored). In doing so ,the mechanics of the creation of vorticity at a solid boundary is properly modeled.

The correct implementation of these vorticity conservation conditions is essential for properly modeling flows as will be shown in the following sections of this chapter. These conditions are both imposed explicitly and used to determine a shedding rate for the convection of vorticity away from the solid bodies.

A brief description of the nature of real flows over solid bodies is useful here. Flow will attach itself to a solid body at an upstream attachment point and remain attached to the solid surface until it reaches a line of separation. Vorticity is created at the solid boundary between the attachment point and separation line and is carried away from the solid surface by diffusion. Vorticity is also carried into the fluid region by convection from the separation lines. This process is discussed in greater detail in Ref. [46].

The locations of attachment and separation points along with the shedding rates at the separation locations determine the circulation around the solid body and, therefore, the forces and moments on that body. For 2-D flows over bodies with sharp trailing edges, there is an attachment point near the leading edge, a separation point at the trailing edge and possibly other separation and attachment points depending upon the angle of attack. For 2-D bluff body flows there is an attachment point near the leading edge and two separation points which form the boundary for a separation "bubble" at the aft portion of the body. For bluff body flow, there is also the possibility for additional localized separations and reattachments. The corresponding 3-D flows involve separation lines which can form closed curves for the bluff body case. The 2-D cases can be seen in Fig. 2.1 which is a replication of a figure from Ref. [46].

For the case of linear aerodynamics, the shedding rates can be determined by using the vorticity conservation condition and an auxiliary condition which describes the nature of the flow at the separation locations. For attached flow over sharp trailing edge bodies, this additional condition which is applied at the trailing edge is the well-known Kutta condition. The Kutta condition states that the circulation is set to make the flow leave an airfoil smoothly at the sharp trailing edge (Ref. [47]). The proper

implementation of the Kutta condition is different for steady and unsteady flow. A comparable condition exists for bluff body separation and can only be implemented in an unsteady fashion.

Some implications of the vorticity theory on the flow problem at hand are worth mentioning here, prior to their discussion in the appropriate sections. The first is that vorticity conservation conditions will dictate the type of solution process needed for the analysis of the flow. For example, a 2-D flow over a body with a single separation point will shed vorticity during unsteady motion only. On the other hand, a 2-D, separated flow over a bluff body always sheds vorticity, so the solution for the flow around such bodies using linear methods must always be solved in an unsteady fashion to allow for the proper wake development. Similarly, for 3-D flows over bodies with sharp trailing edges and 3-D, separated flows over bluff bodies, vorticity is always shed. These flows must also be solved in an unsteady fashion. An unsteady solution means that the flow is solved over successive time steps during which the wake is developed. At each individual time step, the flow is solved in the same steady fashion since the governing equation is elliptic.

The second implication is that linear aerodynamic predictions can detect phenomena normally attributed to high-order aerodynamics if the flow mechanics are properly modeled. This has been demonstrated already in the use of the Kutta condition and vorticity conservation. Laplace's equation is purely kinematic, so in order to predict lifting flows the necessary kinetics are embodied in the auxiliary conditions. Other examples of this are given in a review article by Leonard ([33]). One impressive example uses discrete vortices to model a viscous boundary layer. The vortices are formed at the solid surface and are free to convect and required to diffuse (using a time varying vortex blob diameter) in order to satisfy the viscous vorticity transport equation. An image method is used to assure no-penetration and the discrete vortex strengths are determined to satisfy the no-slip condition. Such a method can be converged to the Navier-Stokes solution to the flow and can even accurately predict flow separation. In Section 2.2, we show the importance of properly modeling the mechanics of a flow for the case of ground effect aerodynamics.

2.2 2-D Model

This section considers two different models which are referred to as the "Doublet Panel Method" (DPM) and the "Vortex Panel Method" (VPM). They are described in detail in their respective subsections and then compared to illustrate the importance of properly modeling the mechanics for ground effect aerodynamics.

The doublet panel method is formulated from the solution to Laplace's equation based on Green's Identity. The vortex panel method is based on a model described by Mook and Dong in Ref. [36]. Both of the methods are extended here for flow around a bluff body and for ground effect aerodynamics. It is shown that the vortex panel method is kinematically closer to a real flow and is able to predict some aspects of viscous flow which are normally attributed only to higher-order models.

The vortex panel method is used for all of the 2-D optimizations. Extensions are made to include some aspects of viscous flow. These extensions include a turbulent flow separation criterion and a model for the base pressure in the separation bubble for bluff body calculations. Skin friction is calculated along the solid surface from the stagnation point (attachment) to the separation points using boundary layer integral methods and a transition criterion. A separate viscous flow model was developed for the lower surface of bluff bodies in ground effect. This model is a turbulent Couette/Poiseuille flow calculation which can calculate the fully developed, 2-D, parallel flow between flat plates with one moving wall, one stationary wall, and a pressure gradient. Each model is described in its own subsection below.

2.2.1 Doublet Panel Method

As was previously mentioned, linear methods deal with the solution of Laplace's equation. The doublet panel method involves the solution based on Green's Identity [48]. Green's Identity is the divergence theorem written for a vector composed of two scalar functions of position, $\Phi_1 \nabla \Phi_2 - \Phi_2 \nabla \Phi_1$. If we set $\Phi_1 = \ln \mathbf{r}$ and $\Phi_2 = \Phi$ the components of the Green's Identity resemble distributed sources and doublets with the strengths σ and μ respectively. An overview of this formulation can be found in Appendix D. The no-penetration boundary condition is imposed implicitly using

the Dirichlet boundary condition. This states that imposing no-penetration explicitly is equivalent to setting the potential inside the solid surface equal to a constant or to the free stream potential, ϕ_∞. The simulation of ground effect is accomplished using the method of images which is described in greater detail in Section 2.2.5. The aforementioned distributed doublet is mathematically equivalent to discrete vortices at the panel nodes. This discrete vorticity is not kinematically identical to a real flow which has continuous vorticity being created at the solid surface.

This model is capable of handling sharp trailing edge flow and bluff body flow. It accomplishes this by incorporating both steady and unsteady auxiliary conditions for the separation lines. For flows over bodies with sharp trailing edges, there is no vortex shedding for steady state flow. The trailing edge condition specifies that the circulation at the trailing edge be zero (stagnation point). This is accomplished using Eq. 2.7 which sets the panels adjacent to the trailing edge to equal strength.

$$\begin{aligned} \Gamma_{TE} &= 0 \\ \mu_U - \mu_L &= 0 \end{aligned} \tag{2.7}$$

The subscripts refer to "upper" and "lower" respectively. For bluff body separation or unsteady sharp trailing edge vortex shedding, an unsteady auxiliary condition is necessary. This condition stems from the vorticity conservation condition for 2-D, inviscid flow (Eq. 2.6). This condition requires that $\frac{d\Gamma}{dt} = 0$ so the time rate of change of circulation around the solid body is the negative of that in the wake. Therefore, the circulation at the separation line is that which is entering the wake. Equation 2.8 shows how this condition is used to set the strength of the wake doublet panel shed at time, t.

$$\begin{aligned} \frac{d\Gamma}{dt} &= \frac{d\Gamma_B}{dt} + \frac{d\Gamma_w}{dt} = 0 \\ \frac{\Delta\Gamma_{TE}}{\Delta t} &= \frac{(\mu_U - \mu_L)_t - (\mu_U - \mu_L)_{t-\Delta t}}{\Delta t} \\ \mu_w &= (\mu_U - \mu_L)_{t-\Delta t} \end{aligned} \tag{2.8}$$

The wake of doublet panels convect with the local velocity so as to remain force free. The baseline code for the one used here was one from Katz and Plotkin (Ref. [48]).

2.2.2 Vortex Panel Method

The vortex panel method is described in Ref. [36] and will be outlined here for the reader's convenience. This method has strong parallels to boundary layer theory so it is enlightening to begin the description by juxtaposing the two approaches. The boundary layer assumptions state that the Reynolds number is very large so that the viscous effects are confined to a small region bordering the solid surface. Along with an assumption of modest surface curvature, the boundary layer equations describe the viscous flow as being forced by the pressure at the boundary layer edge which can be determined using linear methods. The vortex panel method makes similar assumptions and takes an opposite approach, that the vorticity in the viscous regions determines the flow in the inviscid region through a kinematic relationship.

A kinematic relationship between vorticity and velocity can be determined simply using the continuity equation for an incompressible flow and the definition of vorticity. This relation is shown in Eq. 2.9 and is derived in Section 18.6 of Ref. [47].

$$\mathbf{V}(\mathbf{r},t) = \frac{1}{2\pi}\iint_{S_\infty} \frac{\mathbf{\Omega}(\mathbf{r_o},t)\times(\mathbf{r}-\mathbf{r_o})}{|\mathbf{r}-\mathbf{r_o}|^2} dS(\mathbf{r_o}) + \mathbf{V}_\infty \tag{2.9}$$

Figure 2.2 shows the arrangement of vectors in Eq. 2.9. Equation 2.9 states that the velocity at a point in the flow is composed of the uniform free stream flow and the sum of the perturbations from the vortical fluid elements. This perturbation term is the Biot Savart law. Since this kinematic relation was derived solely using continuity and the definition of vorticity, it holds for both viscous and inviscid flows. The flow induced by the viscous boundary layer can therefore be described using the perturbation term of Eq. 2.9. This can be seen in Eq. 2.10.

$$\mathbf{V}_B(\mathbf{r},t) = \frac{1}{2\pi}\iint_{S_B} \frac{\mathbf{\Omega}(\mathbf{r_o},t)\times(\mathbf{r}-\mathbf{r_o})}{|\mathbf{r}-\mathbf{r_o}|^2} dS(\mathbf{r_o}) \tag{2.10}$$

If we integrate Eq. 2.10 with respect to the boundary layer thickness and take the limit of the Reynolds number approaching infinity while the boundary layer thickness approaches zero we obtain Eq. 2.11.

$$\mathbf{V}_B(\mathbf{r},t) \;=\; -\frac{1}{2\pi}\mathbf{e}_z \times \oint_c \frac{\gamma[l(\mathbf{r_o}),t](\mathbf{r}-\mathbf{r_o})}{|\mathbf{r}-\mathbf{r_o}|^2} dl(\mathbf{r_o})$$

where

$$\gamma(l,t)\mathbf{e}_z = \lim_{\substack{Re\to\infty \\ \delta\to 0}} \left[-\int_0^{\delta(l)} \mathbf{\Omega}(l,n,t)dn \right] \tag{2.11}$$

So, for very high Reynolds number ($Re \to \infty$) the boundary layer can be approximated by a continuous vortex sheet. This assumption infers that convection of vorticity is infinitely faster than diffusion of vorticity (inviscid flow). This vortex sheet is a solution to Laplace's equation, so the solution will proceed accordingly. Since the vorticity is the curl of the velocity vector and there is no normal velocity at the surface, the vortex sheet strength, γ, described in Eq. 2.11 is the difference in tangential velocity across the sheet.

$$\begin{aligned} \gamma(l,t) &= \lim_{\substack{Re\to\infty \\ \delta\to 0}} \left[\int_0^{\delta(l)} \frac{\partial u}{\partial n} dn \right] \\ &= u(l,0^+,t) - u(l,0,t) \\ &= \Delta u(l,t) \end{aligned} \tag{2.12}$$

If we now apply the no-slip condition ($u(l,0,t) = 0$) the strength of the vortex sheet is equal to the tangential velocity at the edge of the infinitely thin boundary layer.

$$\gamma(l,t) = u(l,0^+,t) \tag{2.13}$$

The flow outside the infinitely thin boundary layer "slips" over the solid surface where the velocity is discontinuous. The inviscid assumption ($Re \to \infty$) is kinematically identical to the impulsively started viscous flow over the solid body in the limit as time approaches zero. At that instant, all of the vorticity generated during the impulsive start resides in an infinitely thin sheet at the solid surface. For the viscous case, as time proceeds this vorticity diffuses into the flow creating the boundary layer. It is this kinematic similarity to viscous flow which allows this model to predict ground effect flow more accurately than the doublet panel method, as will be demonstrated later.

Since we are neglecting diffusion, convection is the only mechanism for the transport of vorticity. As was previously discussed in this chapter, convection occurs from separation points only and can therefore be determined by vorticity conservation conditions. The derivation of this vortex panel method is concerned with flow

over bodies with sharp trailing edges. Flows over bluff bodies will be discussed in a separate section on the extension of this model to that case.

For flow over bodies with sharp trailing edges, we have already stated that the circulation is set such that flow leaves the trailing edge smoothly (Kutta condition). This is implemented here by requiring that the pressures match at the upper and lower surfaces of the trailing edge. Since the flow is inviscid, Euler's equation (momentum conservation) can be used to relate the velocity to the pressure. Euler's equation is shown (Eq. 2.14) here where l is the tangential direction around the surface of the airfoil.

$$\frac{\partial \gamma}{\partial t} + \gamma \frac{\partial \gamma}{\partial l} = -\frac{1}{\rho}\frac{\partial P}{\partial l} \tag{2.14}$$

Multiplying across by dl and integrating around the airfoil from the lower surface of the trailing edge, L, to the upper surface of the trailing edge, U, gives Eq. 2.15.

$$\begin{aligned} \frac{\partial \gamma}{\partial t} dl + \gamma d\gamma &= -\frac{1}{\rho} dP \\ \frac{d}{dt}\left[\oint_c \gamma(l,t) dl\right] + \frac{\gamma^2}{2}\Big|_L^U &= -\frac{1}{\rho} P\Big|_L^U \end{aligned} \tag{2.15}$$

Figure 2.3 shows the path of integration. The integral on the left hand side is the definition of the circulation around the solid body, so Eq. 2.15 can be rewritten as shown in Eq. 2.16.

$$\frac{d\Gamma(t)}{dt} + \frac{\gamma_U^2 - \gamma_L^2}{2} = -\frac{1}{\rho}(P_U - P_L) \tag{2.16}$$

Imposing the Kutta condition such that the pressure is equal across the trailing edge ($P_U = P_L$) one concludes that the rate of change of circulation in the flow is a function of the tangential velocity at the upper and lower surfaces of the trailing edge (Eq. 2.17).

$$\frac{d\Gamma(t)}{dt} = \frac{\gamma_L^2 - \gamma_U^2}{2} \tag{2.17}$$

The vorticity conservation condition for 2-D flow (Eq. 2.6) is rewritten in Eq. 2.18 in terms of the circulation ($\Gamma(t)$).

$$\frac{d\Gamma}{dt} - 2\dot{\theta} S_S + \frac{d\Gamma_w}{dt} = 0 \tag{2.18}$$

This is the conservation condition for viscous flow, so the circulation includes a term for the solid body rotation of the solid region at an angular velocity, $\dot{\theta}$. We are not dealing with these flows specifically here so this term will be dropped from the present derivation. It can always be added in later. Substituting Eq. 2.17 into Eq. 2.18, one arrives at the vortex shedding rate for the convection of vorticity from the separation point at the trailing edge into the fluid region (Eq. 2.19).

$$\begin{aligned} \frac{d\Gamma_w}{dt} &= -\frac{d\Gamma}{dt} \\ &= \frac{\gamma_U^2 - \gamma_L^2}{2} \end{aligned} \tag{2.19}$$

Observations of the flow at the trailing edge provide additional necessary information to include along with the vortex shedding rate equation. For this information, we use the Giesing/Maskell model for the trailing edge flow [37] [38]. The statement of this model (Eq. 2.20) discusses the possible values of the trailing edge velocities (sheet strength) depending upon the value of the derivative of the circulation.

$$\begin{aligned} \frac{d\Gamma}{dt} > 0 \quad & \begin{cases} \gamma_L \neq 0 \\ \gamma_U = 0 \end{cases} \\ \frac{d\Gamma}{dt} = 0 \quad & \begin{cases} \gamma_L = 0 \\ \gamma_U = 0 \end{cases} \\ \frac{d\Gamma}{dt} < 0 \quad & \begin{cases} \gamma_L = 0 \\ \gamma_U \neq 0 \end{cases} \end{aligned} \tag{2.20}$$

If the flow is unsteady and $\frac{d\Gamma}{dt}$ is positive, the flow over the bottom of the airfoil leaves the trailing edge at γ_L, while the flow over the top of the airfoil meets a stagnation point at the trailing edge. If the flow is unsteady and $\frac{d\Gamma}{dt}$ is negative, the flow over the top of the airfoil leaves the trailing edge at γ_U, while the flow over the bottom of the airfoil meets a stagnation point at the trailing edge. If the flow is steady, the flow over the top and bottom surfaces of the airfoil both meet a stagnation point at the trailing edge. So, for the 2-D flow over a body with a sharp trailing edge, vorticity is shed (convected) into the flow only if the flow is unsteady.

The amount of circulation added to the wake in a time step, Δt, follows from Eq.

2.19 and the Giesing/Maskell model and is shown in Eq. 2.21.

$$\begin{aligned} \Delta\Gamma_w &= \tfrac{\gamma_U^2}{2}\Delta t \quad \tfrac{d\Gamma}{dt} < 0 \\ \Delta\Gamma_w &= -\tfrac{\gamma_L^2}{2}\Delta t \quad \tfrac{d\Gamma}{dt} > 0 \end{aligned} \tag{2.21}$$

The wake is constructed using a collection of discrete vortices where one discrete vortex is released from the trailing edge during each time step. The circulation around the wake is simply the summation of the strength of all of the discrete vortices that comprise the wake, where the strength of each discrete vortex is $\Delta\Gamma_w(t_k)$ (Eq. 2.22).

$$\Gamma_w = \sum_{k=1}^{M} \Gamma_k \tag{2.22}$$

The velocity induced by the wake can be calculated using the Biot-Savart law. This velocity is shown in Eq. 2.23 where σ signifies the radius of the vortex blob [36].

$$\mathbf{V}_w(\mathbf{r}, t) = -\frac{1}{2\pi}\mathbf{e}_z \times \sum_{k=1}^{M} \Gamma_k \frac{\mathbf{r} - \mathbf{r}_k}{|\mathbf{r} - \mathbf{r}_k|^2 + \sigma^2} \tag{2.23}$$

The vortex blob method is employed here to combat instabilities in the solution which can be created by the free convection of singular functions. The method will be described in Section 2.2.3.

The flow solution is obtained as a linear superposition of the continuous vortex sheet (modeling the boundary layer), discrete vortices (modeling the wake) , and the uniform free stream flow (all of which are solutions to Laplace's equation) in such a way as to satisfy the no-penetration boundary condition of the Neumann type (Eq. 2.24).

$$(\mathbf{V}_B + \mathbf{V}_w + \mathbf{V}_\infty) \cdot \mathbf{n} = 0 \tag{2.24}$$

The boundary condition is met at successive time steps with a discrete vortex shed into the flow at the end of each one. Each discrete vortex of the wake is convected at the local velocity which is induced by the vortex sheet representing the bound vorticity in the boundary layer and the other discrete vortices of the wake.

The pressures over the surface are calculated using the unsteady Bernoulli equation (Eq. 2.25).

$$\frac{\partial\phi}{\partial t} + \frac{1}{2}V^2 + \frac{p}{\rho} = \quad \text{Constant} \tag{2.25}$$

The aerodynamic forces and moments are determined by integrating the pressures around the airfoil. The specifics of the discretization of the airfoil and the problem setup and solution can be seen in Appendix B.

2.2.3 Vortex Blob Method

As previously stated, the vortex panel method sheds a wake which is modeled by discrete vortices. Since the vortex sheet is not a solid surface, it cannot support a force. Keeping the sheet force-free is accomplished by convecting each discrete vortex with the local velocity. The local velocity at each free vortex is the summation of the velocity induced by the free stream, continuous vortex sheet, and other free vortices. Since the vortices are mathematically singular, close proximity between vortices will result in very large velocities and they will propel each other far from the field of interest during a time step. Equation 2.9 shows that as $\mathbf{r}$ approaches $\mathbf{r_o}$ the induced velocity approaches infinity. Leonard (Ref. [33]) discusses the convection of discrete vortices and points out that this instability in the solution is inevitable if enough time steps are taken. This problem can be lessened with the use of vortex "blobs," which are vortices with finite cores. The induced velocities in the finite cores are described by distribution functions. The Biot-Savart law can be augmented with a function, $g(d)$, as is shown in Eq. 2.26.

$$\begin{aligned} \mathbf{V}(\mathbf{r},t) &= -\frac{1}{2\pi}\sum_{k=1}^{M}\frac{(\mathbf{r}-\mathbf{r_k})\times\mathbf{e}_z\Gamma_k g(d)}{|\mathbf{r}-\mathbf{r_k}|^2} \\ d &= \frac{|\mathbf{r}-\mathbf{r_k}|}{\sigma_k} \end{aligned} \tag{2.26}$$

The parameter, σ, is the radius of the vortex blob. Leonard (Ref. [33]) describes a Gaussian distribution function of the form shown in Eq. 2.27.

$$F(d) = \frac{e^{-d^2}}{\pi} \tag{2.27}$$

The function g can then be calculated as

$$\begin{aligned} g(d) &= 2\pi\int_0^d F(d')d'dd' \\ &= 1-e^{-d^2} \end{aligned} \tag{2.28}$$

This distribution function eliminates the mathematical singularity at $\mathbf{r} = \mathbf{r_k}$ and allows for a more stable solution.

A plot of the induced velocity for the vortex blob with a Gaussian distribution can be seen in Fig. 2.4. The vortex panel method used in this research has a wake vortex induced velocity shown in Eq. 2.23 which results from the distribution in Eq. 2.29.

$$g(d) = \frac{d^2}{1 + d^2} \tag{2.29}$$

It is obvious from Eq. 2.23 that a non-zero vortex blob radius would eliminate the singularity at $\mathbf{r} = \mathbf{r_k}$. A plot of the induced velocity for the vortex blob with the distribution of Eq. 2.29 can be seen in Fig. 2.5. The radius of the vortex blobs should be chosen according to the nominal separation of vortices in the shed wake. If we say that the nominal separation is some multiple of the free stream velocity and the time step, σ can be obtained by trial and error being the lowest possible value to yield a stable solution. For this work, σ is given in Eq. 2.30 where the constant, σ', is adjusted from case to case.

$$\sigma = \sigma' V_\infty \Delta t \tag{2.30}$$

2.2.4 Extension for Bluff Body Aerodynamics

For the 2-D flow over a bluff body, the flow has two separation points as opposed to the single separation point at a sharp trailing edge. It will, therefore, have two attachment points (the stagnation point and an attachment point in the wake). This can be seen in Fig. 2.1. The model for the bluff body, therefore, has to deal with two shedding rates, since vorticity is convected away at the two separation points. To do this, we must look at the flow near a separation point as sketched in Fig. 2.6. Reference [37] uses the unsteady Bernoulli equation (Eq. 2.25) to determine the vorticity shedding rate by treating the vortex sheet as a flow discontinuity in terms of the pressure, velocity, pressure head, and velocity potential.

Since we are not dealing with a multienergy flow, the pressure head is a constant throughout the flowfield. The bluff body analogue to the Kutta condition is that the pressure on both sides of the shed vortex sheet near the separation point is equal.

This will give Eq. 2.31 where the Δ refers to the discontinuity across the separation streamline and the $\bar{V}$ refers to the velocity of the separation streamline (average of the velocity on either side of the separation streamline).

$$\bar{V}\Delta V = -\frac{\partial \Delta\phi}{\partial t} \tag{2.31}$$

This equation is a parallel to Eq. 2.17 for the sharp trailing edge case.

If one ignores entrainment in the separation bubble, the circulation around the solid body can be related to the potential jump across the two vortex sheets which comprise the wake.

$$\Gamma = \Delta\phi_2 - \Delta\phi_1 \tag{2.32}$$

The subscript "1" refers to the lower separation point and the subscript "2" refers to the upper separation point according to Fig. 2.6. Equation 2.32 along with Eq. 2.31 describes the rate of change of the circulation as a function of the velocity on either side of the two wake vortex sheets (see Eq. 2.33).

$$-\frac{d\Gamma}{dt} = \left.\frac{\gamma_U^2 - \gamma_L^2}{2}\right|_2 - \left.\frac{\gamma_U^2 - \gamma_L^2}{2}\right|_1 \tag{2.33}$$

The subscript "U" refers to just upstream of the separation point and the subscript "L" refers to just downstream of the separation point. These subscripts are held over from those used in the sharp trailing edge Giesing/Maskell model. Their use here is consistent with the sign of the shed vortex strength. So, according to vorticity conservation, Eq. 2.18, the vortex shedding rate for the entire wake (upper and lower sheets) is

$$\frac{d\Gamma_w}{dt} = \left.\frac{\gamma_U^2 - \gamma_L^2}{2}\right|_2 - \left.\frac{\gamma_U^2 - \gamma_L^2}{2}\right|_1 \tag{2.34}$$

This is simply the sum of the shedding rates at the two separation points.

It can be argued that in order to have a bluff body separation bubble the shedding rates at each separation point cannot be zero (as was the case for the steady flow over a body with a sharp trailing edge). So, for the 2-D flow over a bluff body, vorticity is always shed into the flow. The flow is never actually steady, therefore it must be solved in a time dependent fashion. The flow will reach a quasi-steady state in which the circulation around the solid body is steady in the mean. The actual value will

continue to oscillate slightly about the mean due to an instability in the separation location and the periodic nature of vortex shedding. At this quasi-steady state, Eq. 2.35 will hold in the mean.

$$\left.\frac{\bar{\gamma}_U^2 - \bar{\gamma}_L^2}{2}\right|_2 = \left.\frac{\bar{\gamma}_U^2 - \bar{\gamma}_L^2}{2}\right|_1 \tag{2.35}$$

Since there is no loss of pressure head due to viscosity, the attachment point in the wake region will be a stagnation point with pressure coefficient of unity. The base pressure in the separation region must be adjusted to calculate base drag. Observation of actual 2-D flows shows that the base pressure is relatively constant throughout the separation bubble and is approximately that just outside of the separation streamline at the point of separation [43]. Thus the base pressure is taken here to be the mean of the pressures just upstream of the separation streamlines at the two separation points. It turns out that the pressures at these two points are nearly identical to one another.

2.2.5 Extension for Ground Effect Aerodynamics

The vortex panel method is extended here for the flow over a body in ground effect by using the method of images. An in-depth discussion of this method can be found in Ref. [48]. The method of images models a solid ground plane at $z = 0$ by placing the mirror image of the solid body at the negative value of the height. Due to symmetry across the $z = 0$ line, the no-penetration condition is automatically satisfied there. A schematic of the problem can be seen in Fig. 2.7. The subscript "1" refers to the image and the subscript "2" refers to the solid body. The method of images involves the analysis of flow over multiple bodies even if the original problem is for flow over a single solid body. For example, the flow over a single airfoil in ground effect is accomplished by analyzing the flow over two airfoils situated symmetrically about the intended ground plane (as is shown in Fig. 2.7). Since this flow involves two separation points (one at each trailing edge) and it is symmetric about $z = 0$, it automatically conserves vorticity in the entire region. It is very important to understand that vorticity conservation must be satisfied in each half region separately,

since the region of interest is just $z > 0$. Within the subregion, $z > 0$, vorticity conservation and shedding rates are determined identically to the out-of-ground effect counterpart.

There is no attempt made to satisfy a no-slip boundary condition on the ground plane. In the real flow problem, the ground plane would be moving at the free stream velocity as seen from a body-fixed coordinate system. This inability to match that boundary condition, along with the inviscid assumption causes a disparity in the predictions of this model with reality for the extreme ground effect case. For this case the flow between the vehicle and the ground plane is dominated by the diffusion of vorticity created at the two boundaries in close proximity to one another. The assumption of a thin viscous region (which we model with an infinity thin vortex sheet) breaks down since the viscous region will span the entire gap height between the vehicle and the ground plane when the flow becomes fully developed.

2.2.6 Flow Separation Model

Since the main flow solver is an inviscid one (no diffusion), important viscous effects need to be predicted by other means. Flow separation is the departure of the vorticity from the thin viscous region about the solid boundary into the flowfield. This occurs when the retarding effects of viscosity overcome the inertial forces of the fluid near the solid boundary. The location of separation along with the vorticity shedding rates at those points determines the circulation around the solid body and, therefore, the forces and moments. It is very important for the success of the optimization design to be able to consistently predict separation locations, at least relatively, from design to design.

The main separation region at the rear of the MAGLEV vehicle is definitely a turbulent separation due to the high cruise Reynolds number. The separation criterion used as part of this aerodynamic model is one developed by Stratford in 1959 [49]. This criterion is described by Eq. 2.36.

$$C_p \left(x \frac{dC_p}{dx} \right)^{\frac{1}{2}} \left(10^{-6} Re \right)^{-\frac{1}{10}} = \quad \text{Constant} \tag{2.36}$$

Stratford uses 0.39 for the constant if the curvature of the pressure distribution is positive and 0.35 if it is negative. It is obvious from this equation that the relation is only valid in regions of positive (adverse) pressure gradient. This equation is used in marching fashion from the point of minimum pressure to the point where the equation is satisfied (separation location). The Stratford criterion depends only upon values at the current location being evaluated making it simple to implement. The variable, x, is the distance along the surface measured from the point of minimum pressure. The pressure coefficient is measured relative to the pressure at the minimum pressure point. The Reynolds number is based on the surface velocity at the point of minimum pressure and a distance to a fictitious stagnation point. This distance is based on the momentum thickness of an equivalent turbulent flow over a flat plate. The value of the left hand side of Eq. 2.36 increases monotonically from its value of zero at the minimum pressure point to the value required for flow separation. It is clear from Eq. 2.36 that higher Reynolds numbers and lower adverse pressure gradients forestall the separation point.

Reference [50] discusses and compares several different separation criteria for incompressible, 2-D flow. The comparisons are based on performance in the prediction of separation location and pressure coefficient for a collection of experiments including both exterior and interior flows. The Stratford criterion is shown to consistently predict early separation. It was outperformed only by the modified Townsend criterion and the Boeing in-house boundary layer calculations. The superior performance came at the price of increased complexity. The modified Townsend criterion requires pressure coefficients upstream of the separation point and the skin friction coefficient at the point of minimum pressure. It also predicts a separation pressure coefficient rather than the actual separation location. The Boeing method requires an entire boundary layer calculation to be performed every time the separation location is to be updated. This would result in increased run times. The Stratford criterion was chosen for use here due to its easy implementation and consistent predictions. Figure 2.8 is a reproduction of a figure from Ref. [50]. It shows the predictions of the Stratford criterion compared with the experimental values of pressure coefficient at the separation point. The predictions are offset from the exact pressures although

the consistency can be seen in the banded nature of the predictions.

The location of separation is a function of several variables, one of which is the gradient of the pressure coefficient along the surface. Since the predicted velocity over the body surface is piecewise linear, the gradient of the pressure jumps discontinuously at the nodes between panels. This becomes a problem when the separation point moves from one panel to the next. The value of the Stratford criterion (the left hand side of Eq. 2.36) is therefore discontinuous at the nodes. In order to provide a continuously differentiable pressure distribution for the Stratford criterion, we replace the pressure distribution with piecewise cubic splines. A spline routine from Burden and Faires [51] is used to construct the clamped cubic splines using the pressure values at the nodes. This provides an analytic pressure distribution which is twice continuously differentiable over the whole surface. The Stratford criterion is satisfied using a bisection method which guarantees convergence to the separation location. A Newton or Secant method was not employed, since these methods run the risk of converging to the wrong root or diverging. The cubic splines are only used for the location of separation points. The calculated pressure coefficients are used for the integration of force and moment coefficients.

2.2.7 Solution to The Vortex Panel Method

The solution to the vortex panel method involves satisfying the no-penetration boundary condition over several time steps. At each time step, there are N unknowns representing the singularity strengths for the vortex sheet and $N + 1$ equations consisting of the no-penetration condition at the N collocation points and the statement of vorticity conservation. These equations can be seen for the discretized geometry in Appendix B. They are organized in the standard form of $Ax = b$.

The solution proceeds in the following fashion. After the geometry is read in, the panel lengths, collocation point locations, and time independent influence coefficients (the A matrix) are calculated. The time increment is calculated in order to have the free point vortices of the wake at a comparable distance to the nominal surface panel length. The number of time steps is chosen to allow a sufficient amount of time to

achieve a steady state. The vortex blob radius is calculated according to Eq. 2.30 which depends upon the calculated value of Δt.

Following the impulsive start, all calculations are made at every time step. The time dependent portion of the solution begins with the shedding of vortices from the previous time step according to Eq. 2.21 or Eq. 2.34. They are shed from the sharp trailing edge or the separation points for bluff body calculations. For the first time step, the vortices are shed from the second and n^{th} node and are of zero strength. The time dependent influence coefficients are calculated (the b vector). These consist of the wake influence coefficients, since a new vortex is shed after each time step and the position of all of the wake vortices changes during each time step. The current calculations do not involve any dynamic movement of the solid bodies, so the influence coefficients associated with the vortex sheet remain as part of the time independent matrix.

The system of linear equations is solved via a least squares optimization which minimizes the sum of the squares of the elements in the residual vector. This is done, since the system of equation is overdetermined by one equation. The DGELS subroutine from the LAPACK mathematics library is used for this calculation.

Once the no-penetration condition is satisfied for that time step, the locations of the shed vortices are updated according to the induced velocities and the separation location is updated according to the Stratford condition (for bluff bodies)(Eq. 2.36). At this point, we begin a new time step and shed vortices again. This set of calculations is repeated for the predetermined number of time steps. For the steady solution, the linear system of equations is solved once with the steady trailing edge condition as the auxiliary condition ($n + 1^{th}$ equation).

For simplicity sake, two different codes are used to calculate the flow for a sharp trailing edge body and a bluff body. These codes are named *pnlsharp* and *pnlbluff*. *Pnlbluff* can be seen in Appendix E. For the sharp trailing edge calculations, the pressure, force, and moment coefficients are calculated at the final time step when the flow is at steady state. The lift coefficient and drag coefficient are nondimensionalized by the chord, and the pitching moment coefficient is nondimensionalized by the chord

squared (Eq. 2.37).

$$\begin{aligned} C_L &= \frac{L}{qc} \\ C_D &= \frac{D}{qc} \\ C_m &= \frac{m}{qc^2} \end{aligned} \tag{2.37}$$

Since the bluff body flow never truly becomes steady, the coefficients are averaged over several time steps after the circulation becomes steady in the mean. The lift coefficient and drag coefficient are nondimensionalized by the maximum thickness (d) and the pitching moment coefficient is nondimensionalized by the thickness and chord (Eq. 2.38).

$$\begin{aligned} C_L &= \frac{L}{qd} \\ C_D &= \frac{D}{qd} \\ C_m &= \frac{m}{qdc} \end{aligned} \tag{2.38}$$

2.2.8 Skin Friction Model for Out-of-Ground Effect Case

The skin friction drag calculation is performed using the PMARC_12 boundary layer analysis which includes the Thwaites/Curle integral method for the laminar boundary layer and the Nash/Hicks integral method for the turbulent boundary layer calculations. A detailed description of the boundary layer analysis can be found in the PMARC_12 operating manual [52]. Empirical relations are used to determine laminar separation with turbulent reattachment and natural transition. Turbulent separation occurs when the friction velocity goes to zero. The implementation of this portion of PMARC_12 involves the proper connection of the 2-D vortex panel method flow solver with the PMARC_12 boundary layer calculation subroutines as a post processor. The viscous flow analysis is performed only once for each geometry following the completion of the time stepping inviscid flow solution.

2.2.9 Skin Friction Model for Ground Effect Case

For the ground effect case, the viscous flow in the gap between the vehicle and the guideway is modeled using a turbulent Couette/Poiseuille flow calculation in a 2-D channel. The flow in the non-parallel sections of the train underbody is ignored for simplicity. The flow is assumed to be fully developed over the whole length, and the single skin friction coefficient obtained from this calculation is applied over every panel on the vehicle underbody. The turbulent Couette/Poiseuille flow can be determined by solving Eq. 2.39. This equation can be solved by numerical integration. A detailed outline of the solution procedure can be seen in Appendix C along with a schematic diagram of the flow.

$$\begin{aligned} \frac{dp}{dx} &= \frac{d}{dy}\left[(\mu+\mu_T)\frac{du}{dy}\right] \\ u_0 &= 0.0 \\ u_h &= u_\infty \end{aligned} \tag{2.39}$$

The eddy viscosity is modeled separately in the inner and outer regions. Since it was found that the Law of the Wall also applies to pipe flows, the Reichart turbulence model is used for the inner region (Eq. 2.40).

$$\mu_T = k\rho\nu\left[\left(\frac{yu_*}{\nu}\right) - y_a^+ \tanh\left(\frac{yu_*}{\nu y_a^+}\right)\right] \tag{2.40}$$

For the outer region, the eddy viscosity is calculated using a model for internal flows suggested by Reynolds [53].

$$\mu_T = 0.192k\rho u_* h \tag{2.41}$$

These turbulence models require the calculation of the friction velocity, u_*, which depends upon the wall shear stress. The integration of Eq. 2.39 is therefore embedded within a root finding scheme for the wall shear stress. The pressure gradient is a constant and is determined by the vortex method solution of the inviscid flowfield. The subroutine which performs this calculation can be seen in Appendix E.

The results of this viscous flow analysis are compared with experimental values obtained by El Telbany [54]. These experiments were for fully developed turbulent

flow between parallel walls with one wall moving. This was accomplished using a moving belt in a wind tunnel. Measurements were made for many cases of varying wall separation, wall velocity, and mass flow. Plots for three different mass flows can be seen in Fig. 2.9. This plot shows two solutions for Couette type flows which are flows in which the ratio of wall shear stress is positive and a solution for Poiseuille type flows which are flows in which the ratio of wall shear stress is negative. There is excellent agreement between the calculated velocity profiles and the experimental velocity profiles. The mass flow was determined by numerically integrating the velocity data points.

2.2.10 Verification of the 2-D Model

This subsection was written with two purposes in mind. The first is to show the differences between the doublet panel method and the vortex panel method, especially when dealing with ground effects flows. Calculations were performed on a Clark Y airfoil for this purpose. The second purpose is to examine several flows using the vortex panel method to verify it for use in the optimization loop. Bluff body flows were calculated for a circular cylinder and a 3.5:1 elliptic cylinder. Calculations were then made for the side view of the Northrop Grumman MAG950 and MAG1002 designs.

The Clark Y airfoil was chosen for the purpose of comparing the doublet panel method and the vortex panel method due to its flat underside. This will allow us to see the main difference between these two methods. The Clark Y is situated at an angle of attack of approximately 2^o such that the flat underside is perfectly horizontal. The airfoil at angle of attack and surface grid can be seen in Fig. 2.10. Since this is a sharp trailing edge flow, the flowfield can be solved in either a steady or unsteady fashion. The unsteady calculation is an impulsively-started problem. A wake is shed over successive time steps until the flow reaches steady state.

A plot of vortex panel method pressure coefficient for the Clark Y out-of-ground effect can be seen in Fig. 2.11 for a steady calculation, as well as for an unsteady calculation with 400 time steps and one unsteady calculation with 800 time steps.

This plot shows that as the unsteady solution is allowed to progress in time the solution approaches that of the steady flow. The 2-D flow over a sharp trailing edge body requires many time steps to reach steady state, since the starting vortex must move a sufficient distance from the airfoil (which is infinite in span). A rule of thumb is that the wake should be allowed to develop to approximately 30 chords in length. Since we are only concerned here with bodies in translation all of the remaining calculations for sharp trailing edge flows are performed in a steady fashion.

Figure 2.12 shows a comparison of the pressure coefficient over the Clark Y airfoil out-of-ground effect calculated by the doublet panel method and the vortex panel method. This plot shows general agreement in the predicted pressure coefficient with some slight difference on the lower surface and at the trailing edge. These small differences can be attributed to the difference between discrete and continuous surface singularities as well as the different (yet consistent) implementation of the trailing edge conditions.

Figure 2.13 shows a comparison of the pressure coefficient over the Clark Y airfoil in ground effect calculated by the doublet panel method and the vortex panel method. The airfoil is situated at an altitude of $1/10^{th}$ chord. There is a large difference in the pressure coefficient calculated by these two methods. An interesting and enlightening result is the difference in the pressure coefficient predicted for the lower surface. This lower surface is in close proximity to the ground plane, and the flow between these two surfaces is essentially a 2-D flow in a narrow gap. The doublet panel method predicts a uniform pressure along this gap which is the expected result of a linear method. On the other hand, the vortex panel method predicts a pressure drop in the gap in qualitative agreement with real flows. This result is usually attributed only to high-order aerodynamics methods and is predicted here due to the better kinematic match between the vortex panel method and a real flow.

Figure 2.14 is a plot of the Clark Y lift coefficient as a function of the height-to-chord ratio. Since the airfoil has a flat bottom, there is only a slight loss of lift prior to lift reversal ($\Delta C_L = -0.0040$). Lift reversal is evident as the height-to-chord ratio approaches zero. Figure 2.14 also shows points for the doublet panel method predictions for out-of-ground effect and $0.1c$ in ground effect flows. As was the case

for the pressure coefficient profiles, the out-of-ground effect predictions are similar for these two methods, while the ground effect predictions show a large difference. The doublet panel method predicts only a slight increase in lift due to the close ground proximity. The effect of height-to-chord ratio on pitching moment about the leading edge can be seen in Fig. 2.15. Pitching moment also reverses from a slight increase to a large negative change as height-to-chord ratio approaches zero. The remainder of the calculations in this work employ the vortex panel method due to its superior performance for ground effect predictions.

The vortex panel method for 2-D bluff body flow was verified on several infinite cylinders, the first of which is the circular cylinder. The initial calculations were performed with the vortex panel method and no flow separation model. Figure 2.16 shows the surface pressure coefficient over the circular cylinder for both the out-of-ground effect and ground effect cases. The out-of-ground effect case shows excellent agreement with the analytic solution for potential flow over a circular cylinder (Eq. 2.42).

$$C_p = 1 - 4\sin^2\theta \tag{2.42}$$

The angle θ in this equation is the polar coordinate. Negative lift is predicted for the ground effect flow due to accelerated potential flow under the cylinder. This negative lift becomes greater as the height-to-diameter ratio decreases. Lift reversal cannot be predicted at this level, since the mechanism for this phenomena is in the location and strength of vortex shedding. Figure 2.17 shows the velocity profile along the vertical centerline of the circular cylinder for the out-of-ground effect case. Along this line, the only component of the velocity is in the horizontal direction. The velocity profile matches the analytic solution, which can be seen in Eq. 2.43.

$$\frac{u}{U_\infty} = \cos\theta\left(1 - \frac{R^2}{r^2}\right) + \sin\theta\left(1 + \frac{R^2}{r^2}\right) \tag{2.43}$$

R is the radius of the circular cylinder. Figure 2.18 shows the velocity profile along the lower vertical centerline of the circular cylinder for the ground effect case. This plot shows the nature of the image method velocity profile which is neither a true road condition nor a wind tunnel condition. The wind tunnel condition is characterized by

a ground plane velocity of zero while the road condition is characterized by a ground plane velocity equal to the free stream velocity.

Calculations were next performed on the circular cylinder using the vortex panel method with the bluff body separation model. These calculations were performed at a Reynolds number of 8.6 million. For the bluff body calculations, Reynolds number is used to determine the skin friction drag and the separation location, while for sharp trailing edge bodies, Reynolds number only enters the problem in the skin friction drag calculation. The vortex panel method itself is still an infinite Reynolds number calculation. The flow developed for 0.5 seconds which was sufficient to reach steady state. A vortex blob diameter of $3.5V_\infty\Delta t$ is required to obtain a stable solution. Figure 2.19 shows the pressure coefficient for the out of ground effect case as compared to experimentally obtained values [55]. The pressure coefficients shown here are the mean values over the last eighty time steps, since the solution is always unsteady. This plot shows that as Reynolds number increases the pressure coefficient plots are approaching that for the infinite Reynolds number limit vortex method prediction. The base pressure decreases with increased Reynolds number, while the surface pressures prior to separation increase. This difference prior to separation can be accounted for by the displacement thickness of the boundary layers for the finite Reynolds number cases.

Figure 2.20 shows the calculated shed vortex sheets which roll up into the Von Karman vortex street. Separation occurs at approximately 105^o where 0^o is the most upstream point. A time history of the lift and drag coefficients for the out-of-ground effect calculation can be seen in Fig. 2.21. Lift and drag coefficient are based on cylinder diameter. The calculation takes around 50 time steps to settle out from the impulsive start after which the flow exhibits oscillating behavior. We obtained a Strouhal number of 0.359 and a mean drag coefficient of 0.8371 based on cylinder diameter. Both of these numbers compare favorably with published experimental values shown in Delany [56] and Roshko [57]. The drag coefficient is slightly high due to the lower base pressure of the infinite Reynolds number limiting case. The Strouhal number is also higher than the Roshko data at Reynolds numbers ranging from 4 to 8 million (0.26 to 0.28). Delany measured Strouhal numbers ranging between 0.3 and

0.4 at slightly lower Reynolds numbers (1 to 2 million).

Ground effect calculations were performed on the circular cylinder for comparison with experimental data both published (Bearman and Zdravkovich [58]) and obtained in house. Bearman and Zdravkovich performed wind tunnel experiments on a circular cylinder over a fixed ground plane. They tested at a Reynolds number of 48000 based on cylinder diameter and used a trip strip to obtain turbulent flow over the ground plane. This Reynolds number is clearly subcritical for flow over a circular cylinder. Subcritical flow involves laminar separation while supercritical flow involves turbulent separation. Experiments were also performed at Virginia Tech in the open jet wind tunnel which has a 0.99 meter diameter test section exit. The experiments were performed for two of Bearman's ground clearances at a higher Reynolds number (300000) although it was still too low to provide supercritical flow. This tunnel can provide supercritical flow at a Reynolds number of 250000 for out-of-ground effect flows due to the tunnels high free stream turbulence (approximately 4%). Figures 2.22 through 2.25 show the pressure coefficients over the circular cylinder for the different experiments and the vortex panel method calculations. These figures show the results at height-to-diameter ratios of 0.1, 0.4, 1.0, and 2.0 respectively. The Virginia Tech experiments (indicated by the author's last name) were performed for the two lowest ground clearances. These experimental results match those of Bearman. The vortex panel method which only predicts supercritical flow naturally differs from the experimental results. The delayed separation which is characteristic of supercritical flow results in the greater acceleration of the flow as it remains attached until after the maximum thickness of the cylinder.

Calculations were also performed on a 3.5:1 elliptic cylinder in order to compare the vortex panel method results to the RANS calculations and experiments of Ranzenbach and Barlow [59]. These were performed at a Reynolds number of 1.5 million based on chord. Force and moment coefficients are also based on the chord (length of the major axis). The RANS calculations were performed for both wind tunnel conditions ($u(y = 0) = 0$) and road conditions ($u(y = 0) = V_\infty$) while the vortex method uses the method of images. The experiments were performed for wind tunnel conditions only. Figure 2.26 shows the elliptic cylinder and its surface grid for

the vortex panel method. The vortex panel method was solved over three seconds which was sufficient to reach steady state flow. A vortex blob diameter of $5V_\infty \Delta t$ was required to obtain a stable solution. For the out-of-ground effect case, the vortex panel method predicted a drag coefficient of 0.0465 compared to the RANS prediction of 0.0394. Figure 2.27 shows the lift coefficient as a function of the height which is nondimensionalized using the length of the minor axis of the ellipse. Figure 2.28 shows the drag coefficient as a function of the height ratio. As the height is decreased, both the predicted lift coefficient and the drag coefficient increase. They also have higher values than the experimental values or the RANS calculations. The general trends of the coefficients as a function of the nondimensional height are captured by the vortex panel method as well as reasonable numerical values.

Some insight into these results can be gained by looking at the separation and stagnation point locations. Figure 2.29 shows the separation locations and stagnation point locations for the elliptic cylinder out-of-ground effect. The vortex panel method using Stratford's criterion predicted separation aft of the RANS predictions. The vortex panel method predicted a higher out-of-ground effect drag coefficient due to a lower base pressure coefficient prediction. Figures 2.30 and 2.31 show the same information for the ground effect case at nondimensional altitudes of 0.473 and 0.175 respectively. The vortex panel method predicts greater augmentation of the separation locations and stagnation point locations resulting in greater lift reversal as the ground clearance is decreased.

Lastly, calculations were performed to verify the vortex panel method against Northrop Grumman RANS calculations [28] for the flow over a 2-D MAGLEV vehicle in ground effect. The RANS calculations were performed to match wind tunnel conditions for experiments performed by Tyll, Liu, and co-workers [8] [60] at Virginia Tech. These were for a $1/10^{th}$ scale model at a Reynolds number of 3.75 million per meter. The scaled vehicle studied here is $2.4m$ in length and cruises at an altitude of $0.01m$. The vortex blob diameter is set at $1.75V_\infty \Delta t$ for the ground effect case to obtain stable solutions. Figure 2.32 shows the paneling for the Grumman MAG950. Figure 2.33 shows the vortex sheets calculated for the Grumman MAG950 design for both in and out-of-ground effect. The out-of-ground effect (OGE) calculation shows

the development of the Von Karman vortex street. The starting vortex is evident at the downstream end of the sheet. This flow structure is disrupted by the presense of the ground plane for the in ground effect (IGE) case.

Figure 2.34 shows a plot of pressure coefficient versus the nondimensional vehicle length for the Northrop Grumman MAG950. This plot shows excellent agreement between the RANS calculation and the vortex method calculation. The vortex panel method predicts a reasonable pressure drop of the gap flow as well as a reasonable base pressure (slightly high). The difference in the pressure coefficient at the aft end of the vehicle is due to the buildup of a boundary layer for the RANS case. The increasing boundary layer thickness provides for a more moderate adverse pressure gradient over the top surface. The thick viscous region on the lower surface accounts for the difference in pressure coefficient on that surface at the aft end of the vehicle. The vortex panel method solution shows an expansion as the flow leaves the parallel section of the underbody just prior to the section of attempted pressure recovery. Figure 2.35 shows a plot of pressure coefficient versus the nondimensional vehicle length for the Northrop Grumman MAG1002. It too shows an excellent match of the vortex panel method solution to the high-order, RANS calculations. The pressure drop in the gap is predicted well along with an excellent match for the base pressure.

The integrated force and moment coefficients calculated by the vortex panel method are shown for the five 2-D, Northrop Grumman designs in Table 2.1. These coefficients are based upon the vehicle height, and the pitching moment coefficient is taken about the leading edge of the vehicle. These values show similar qualitative results to the RANS calculations performed by Northrop Grumman. The highest drag coefficients are experienced by the MAG950 and MAG1007 designs. The major difference in the predictions is for that of the MAG1459 which we predict to have an extremely low drag coefficient as compared to the other designs. The prediction of such a low drag is due to a high leading edge suction which will be explained in the results sections. The optimum drag coefficient designs have a similar shape to the MAG1459. The drag breakdown for these vehicles shows that all of these side view shapes yield between 70% and 75% of the total drag due to base drag. Since a majority of the skin friction drag is due to the viscous flow in the gap between

the track and vehicle, attempts to lower the drag coefficient will deal mostly with a reduction in base drag. So, potential drag coefficient improvement via changes in the vehicle shape is around 75%.

Tables 2.2 and 2.3 show the lift and drag coefficient comparisons between in and out-of-ground effect flow for the MAG950. These comparisons are done here for the wind tunnel scale case. Lift reversal is evident as the lift coefficient increases by approximately 180% of its out-of-ground effect value for the altitude of 0.01 meters ($\frac{h}{d} = 0.029$). The drag coefficient for the IGE case is higher than the OGE case due to increases in both skin friction drag and base drag. The table shows that the base drag makes up approximately 64% of the drag increase. The out-of-ground effect values closely match those predicted by the RANS calculations [28]. They predicted a lift coefficient of around 1.0 and a drag coefficient of around 0.16. Similar to the Northrop Grumman study, the vortex panel method predicted an approximate doubling of the drag coefficient when the vehicle is brought in ground effect.

The verification for flow over the MAGLEV vehicles was performed at wind tunnel scale, although, all of the design optimizations are performed at full scale conditions. A comparison of wind tunnel to full scale condition calculations can be seen in Fig. 2.36 and 2.37. Figure 2.36 shows the pressure coefficient over the Northrop Grumman MAG950 out-of-ground effect as calculated by the vortex method. The two cases are for the full-scale Reynolds number of 30.0 million and the wind tunnel case with Reynolds number of 1.3 million. The pressure coefficient predictions show nearly identical profiles except for the aft end of the vehicles. The difference between these two profiles is caused by the later separation for the full scale case due to the higher Reynolds number. In addition to this, force and moment coefficients differ, since no attempt was made to fix the location of the boundary layer transition. For the MAG950, out-of-ground effect, the lift coefficient for the wind tunnel scaled case is 1.2024 and that for the full scale vehicle is 1.4130. The drag coefficient for the wind tunnel case is 0.168 and that for the full scale case is 0.147. These can be seen in Table 2.4.

Figure 2.37 shows the pressure coefficient over the Northrop Grumman MAG950 in ground effect as calculated by the vortex panel method. The two Reynolds number

cases are shown. The profiles for the ground effect case show similar results to that of the out-of-ground effect case. The pressure coefficient profiles are nearly identical over most of the vehicle surface. The full-scale case experiences a later separation than the wind tunnel scale case, since the Reynolds number is higher. It, therefore, expands more prior to the attempted pressure recovery and recovers to a higher pressure coefficient than the wind tunnel scale case. The drag coefficient for the full scale case is lower than that for the wind tunnel scale case (0.203 and 0.253 for the MAG950 full scale and wind tunnel scale respectively). The lift coefficient is higher for the full scale (3.461) than for the wind tunnel scale (3.362) for the MAG950. These numbers can be seen in Table 2.5.

The test cases for the 2-D aerodynamics model shows that the 2-D, ground effect flow around bluff bodies can be consistently modeled using the vortex panel method. Lift reversal is captured with the use of the Stratford criteria for determining the separation locations and the proper modeling of the mechanics of viscous flow. Differences between the vortex panel method predictions and the accepted true values are accounted for by the vortex panel method assumptions, in particular the infinite Reynolds number limit and the implementation of the ground effect using the method of images. The results are qualitatively consistent and quantitatively realistic. The 2-D vortex panel method makes an excellent analysis tool for integration in an MDO design methodology due to its performance and quick calculation times (approximately 6.5 CPU minutes for a 104 panel MAGLEV side view design on a Silicon Graphics Power Challenge with an R8000 processor chip).

2.3 3-D Model

This section considers the two different models which are 3-D extensions to the 2-D doublet panel and vortex panel methods. The 3-D doublet panel method used here is PMARC_12 (Panel Method Ames Research Center) [52]. The 3-D extension to the vortex panel method was developed by Mracek and Mook [40] [61]. The doublet panel method is equipped with an image method ground plane simulation. It was extended for flow around a bluff body. The vortex panel method has an unsteady wake

model which can be used for a closed tube wake. The code available to us, which was written by Mracek, is formulated specifically for thin lifting surfaces. An extension for thick lifting bodies is unavailable. This code is extended for ground effect flow via the image method. Since there are no 3-D turbulent separation criteria, we only consider geometries with known separation locations. Each model is discussed in its own subsection below. The work presented here does not include the integration of these 3-D aerodynamics models into the MDO framework. The intention here is to evaluate their capabilities with respect to such an integration.

2.3.1 3-D Doublet Panel Method

The 3-D doublet panel method implementation used here is PMARC_12. This code involves the solution to Laplace's equation based on Green's Identity. A discussion of Green's Identity and its application to the solution to Laplace's equation in 3-D can be seen in Appendix D. A more detailed discussion can be seen in the PMARC_12 manual [52]. This method employs a 3-D source distribution and a 3-D doublet distribution. The source strength is set to cancel out the normal component of the free stream flow. This results from the mathematical statement of no penetration and the implicit formulation (Dirichlet) of that boundary condition. The 3-D distributed doublet singularity is mathematically identical to a ring vortex on the panel perimeter. So, like its 2-D counterpart, PMARC_12 deals with discrete vorticity which is kinematically different from a real fluid flow over a solid surface.

The auxiliary condition for a trailing edge used in PMARC_12 is the steady state implementation of the Kutta condition (Eq. 2.7). This condition is used in PMARC_12 for both steady and unsteady flow. This wake model is incorrect and has been changed here to that which is shown in Eq. 2.8. This wake model is for an unsteady flow and will converge to steady state conditions if the solution is permitted to sufficiently develop in time. It can also be used for the flow over a bluff body with separation (closed tube wake) according to the assumptions discussed in Section 2.2.4 for 2-D flow. Ground effect is simulated using the method of images.

2.3.2 Verification of 3-D Doublet Panel Method

The 3-D doublet panel method, PMARC_12, was verified first for the flow over sharp trailing edge bodies and bluff bodies. We also looked at the prediction capabilities of ground effect flow. The verification was also performed to look at the corrected separation line condition which employs the unsteady implementation of the Kutta condition.

To verify the prediction capability for the flow over a sharp trailing edge body, we used an aspect ratio 1.0 rectangular wing with a ClarkY airfoil section. The wing is situated at an angle of attack, so that the flat underside is aligned with the horizontal. Flow calculations are performed using both the steady trailing edge condition (which comes with PMARC) and the unsteady trailing edge condition (which was written into the code by the author). A time history of the lift coefficient for the impulsively started wing can be seen in Fig. 2.38. The top plot is for out-of-ground effect flow and the bottom plot is for ground effect flow. The solutions via the two different trailing edge conditions appear to arrive at approximately the same steady state lift coefficient although the unsteady trailing edge formulation predicts a longer transient. The out-of-ground effect lift coefficient is approximately 0.16 while the ground effect lift coefficient is approximately 0.18 (based on planform area). The wing and the shed vortex sheet can be seen in Fig. 2.39 for the out-of-ground effect case and in Fig. 2.40 for the ground effect case. The wake for the ground effect case spreads out laterally due to the induced velocity of the image wake. This is in agreement with the observed behavior of wing tip vortices near the ground. If one's interests are only in the steady state coefficient values, then the original PMARC wake model can suffice. However, the unsteady model can provide time accurate values for the flow over a sharp trailing edge body and is essential for the flow over a bluff body.

Bluff body flow was verified using a sphere, since there is an abundance of data to compare against and the separation location is widely known. Since the flow over a bluff body is never truly steady, the unsteady wake model was used. The use of the steady trailing edge conditions for the case of a bluff body with a closed tube wake would force a closed stagnation line which is not physically possible. A solution time history for the impulsive start of flow over a sphere can be seen in Fig. 2.41. Flow is

set to separate at approximately 104°, according to the accepted value for turbulent flow over a sphere. The drag coefficient becomes steady after approximately 11 time steps. Figure 2.42 shows the pressure coefficient predicted by PMARC as compared to experimentally determined values at a Reynolds number of over 4×10^5 [62]. There is excellent agreement between the doublet panel method and the experimentally determined values. Figure 2.42 also shows a portion of the shed closed tube vortex sheet behind the sphere.

2.3.3 3-D Vortex Panel Method

The 3-D vortex panel method is a 3-D version of the 2-D vortex panel method and was developed by Mracek and Mook [40] [61]. It is an alternative to the vortex lattice method which has discrete panels with concentrated vorticity (equivalent to the doublet panel method). In this model, the solid surface of a body is modeled using a continuous vortex sheet which represents the thin viscous region much the same as was done for the 2-D vortex panel method. The sheet strength is set up to vary linearly along the sides of the elements by using hat functions. These elements (panels) are triangular so that all of the vertices lie on the surface of the body. Such panels provide smoothly varying values of pressure and velocity. The layout of the elements can be seen in Fig. 2.43.

The calculation of the flow over lifting bodies is handled by shedding a wake which develops over time. The kutta condition is implemented in a similar fashion as was done for the 2-D vortex panel method. This implementation employs Euler's (or Bernoulli's) equation, and the Kutta condition is imposed in the most general sense which is for unsteady conditions. This condition will reach a steady state if the wake is permitted to shed for a sufficient number of time steps. Based on the same assumptions as were made for the 2-D case, one can also use this condition for bluff body flow (closed tube wake). If we ignore entrainment, we can treat a separation bubble by simply stating that the pressure on either side of the shed wake near the separation point is identical. Using this trailing edge condition (described in detail for the 2-D case) it is apparent that the vorticity from the infinitely thin viscous

region is shed into the wake. The wake is still modeled using discrete vorticity (ring vortices) identical to those is the doublet panel method. A vortex edge core lies along the trailing edge or the separation line (for the bluff body case) in order to attach this discrete vorticity wake to the continuous vortex sheet. This is required in order to have nonzero vorticity at such a separation line. The strength is chosen so that the gradient of the circulation around the core in the direction parallel to the line of separation is equal to the negative of the sheet strength at that point. The piecewise linear sheet strength will, therefore, result in a quadratic circulation distribution. The strength of the adjoining vortex ring is the mean value of the circulation along that segment of the edge core (Fig. 2.43). Spatial conservation of vorticity in the wake is maintained by using an adaptive mesh to split rings into smaller ones when they stretch out too much.

This method is a linear one which involves the solution to Laplace's equation via the linear superposition of analytic solutions to the equation. These analytic solutions are the vortex sheet which models the thin viscous region near the solid surface, ring vortices which are used to model the convected wake, and the edge cores used to join them. The strengths of all of the elements are determined in order to satisfy the no-penetration boundary condition on the surface. This is shown here as a system of linear equations

$$\begin{aligned} \mathbf{V}\cdot\mathbf{n} &= 0 \\ \left[\begin{array}{cc} A+C & D \end{array}\right] \left\{\begin{array}{c} \mathbf{\Omega} \\ G \end{array}\right\} &= \{U-W\} \end{aligned} \tag{2.44}$$

where $\mathbf{\Omega}$ is the vorticity and G is the strength of the discrete wake elements, U is the free stream velocity, and W is the velocity induced by the wake elements shed at previous time steps.

In order for the vortex sheet to resemble a viscous fluid region near a solid surface, the vorticity field must be solenoidal. This is due to the vorticity being the curl of the velocity vector field. The divergence of the curl of any vector field must be zero. For the 2-D vortex panel method this was satisfied automatically, since the vorticity and velocity vectors are always perpendicular to one another. For 3-D flow, this is

not the case, so the divergenceless condition must be satisfied explicitly.

$$\begin{aligned} \nabla \cdot \gamma &= 0 \\ \begin{bmatrix} B & 0 \end{bmatrix} \begin{Bmatrix} \mathbf{\Omega} \\ G \end{Bmatrix} &= \{0\} \end{aligned} \tag{2.45}$$

The compatibility condition at the separation lines is shown below.

$$\begin{aligned} \frac{d\Gamma}{dx} &= -\gamma \\ \begin{bmatrix} E & F \\ J & 0 \end{bmatrix} \begin{Bmatrix} \mathbf{\Omega} \\ G \end{Bmatrix} &= \{0\} \end{aligned} \tag{2.46}$$

As was already mentioned, the Kutta condition is implemented using Bernoulli's equation and setting the pressures across the separation line (or trailing edge) equal to one another.

$$\begin{aligned} \Delta C_p &= 0 \\ \begin{bmatrix} K & L \end{bmatrix} \begin{Bmatrix} \mathbf{\Omega} \\ G \end{Bmatrix} &= \{P\} \end{aligned} \tag{2.47}$$

Instead of working through the algebra to obtain a square system of equations, the problem is solved using a least squares optimization to minimize the sum of the squares of the residual. The divergenceless condition, compatibility condition, and Kutta condition are treated as weighted constraints. This complete system of equations can be seen in Eq. 2.48.

$$\begin{bmatrix} A+B & D \\ w_1 B & 0 \\ w_2 E & w_2 F \\ w_3 J & 0 \\ w_4 K & w_4 L \end{bmatrix} \begin{Bmatrix} \mathbf{\Omega} \\ G \end{Bmatrix} = \begin{Bmatrix} U - W \\ 0 \\ 0 \\ w_4 P \end{Bmatrix}. \tag{2.48}$$

Just as for the 2-D vortex panel method, the 3-D version solves directly for the surface velocity if we impose the no-slip condition at the solid surface. The strength of the vortex sheet (vorticity) is equal in magnitude to the boundary layer edge velocity

but is rotated 90° about an axis normal to the surface at that point. The specifics associated with this method and the matrix elements are covered in the previously cited work by Mracek and Mook. This method provides a better kinematic match to a real, high Reynolds number, viscous flow than the doublet panel method.

Ground effect is implemented using the method of images. It is only necessary to augment Eq. 2.44 with the influence coefficients for the image of the body, edge core, and wake. The divergenceless condition only needs to be satisfied in the real region. That is also the case for the compatibility condition and the kutta condition.

The code written by Mracek, *threed.f*, is set up for two specific types of flows; non-lifting flows over thick bodies, and lifting flows over thin bodies. An attempt was made to extend Mracek's code for lifting flow over thick bodies although the reformulation was never successful. Calculations were made for lifting flow over thin bodies for both the out of ground effect and in ground effect cases. An extension of this design methodology for full 3-D designs should consider the development of such a model.

2.3.4 Verification of 3-D Vortex Panel Method

The 3-D vortex panel method was used to calculate the flow over a rectangular wing with aspect ratio 1.0 and a Clark Y airfoil section in an attempt to draw a comparison to the 3-D doublet panel method, as was done for the 2-D case. This computation is for a thin body so a mean camber line for the Clark Y is used. The lift coefficient for the out-of-ground effect case is 0.125, based on planform area. The wing and the shed wake can be seen in Fig. 2.44. The lift coefficient for the ground effect case in 0.084. Lift reversal is not predicted. The wing and the shed wake for the ground effect case can be seen in Fig. 2.45. One cannot draw a comparison between the discrete vorticity, doublet panel method, and the continuous vorticity, vortex panel method for 3-D ground effect flow while using this thin body formulation. A general discussion of the vortex panel method for thick lifting bodies can be found in Ref. [61].

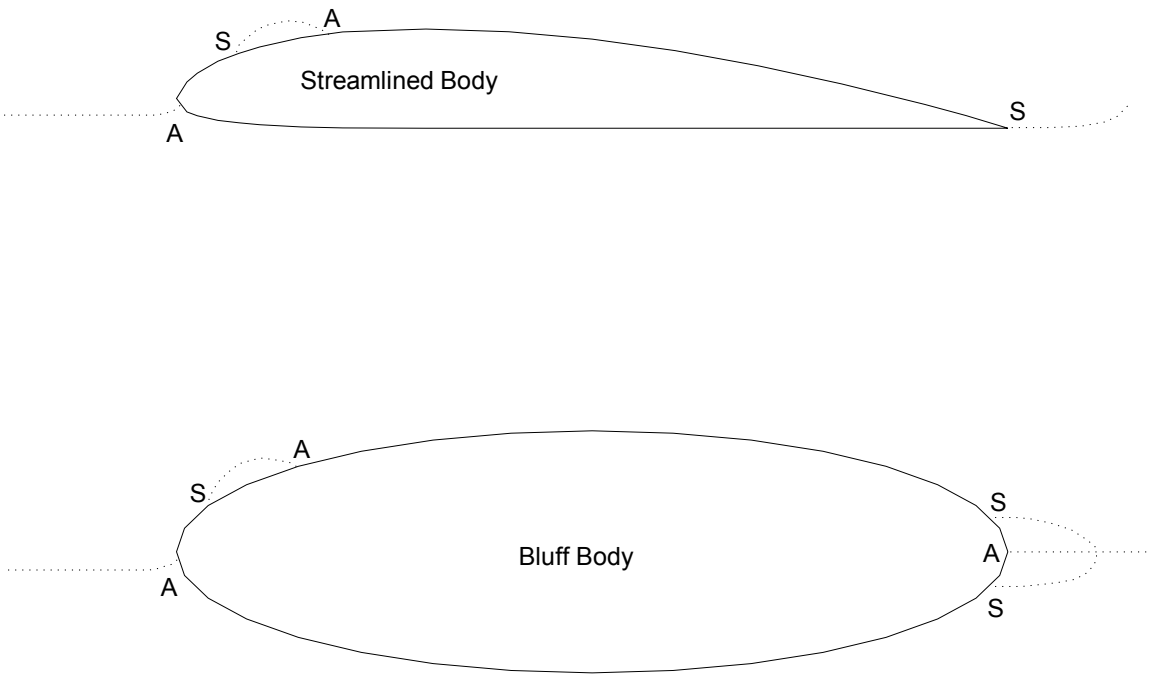

Figure 2.1: Attachment (A) and Separation (S) for Different Flow Situations (after Ref. [46])

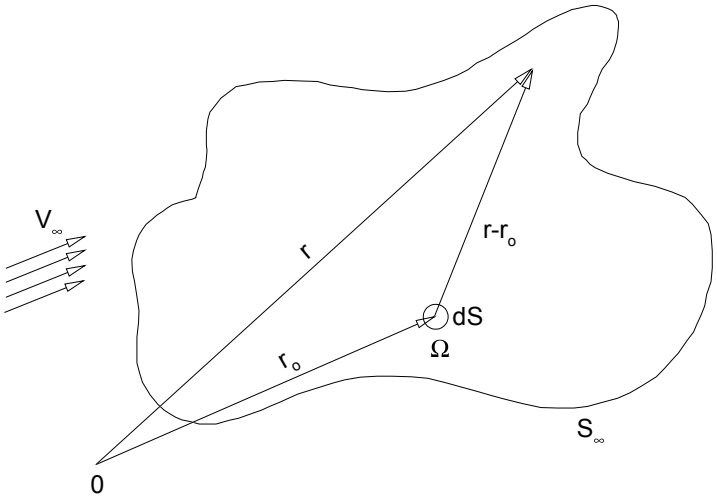

Figure 2.2: Schematic of Biot-Savart Law

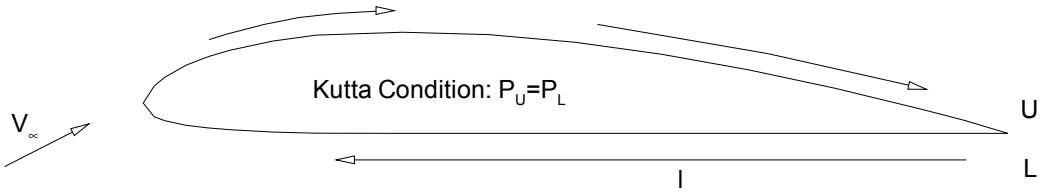

Figure 2.3: Path of Integration of Euler's Equation Around Airfoil

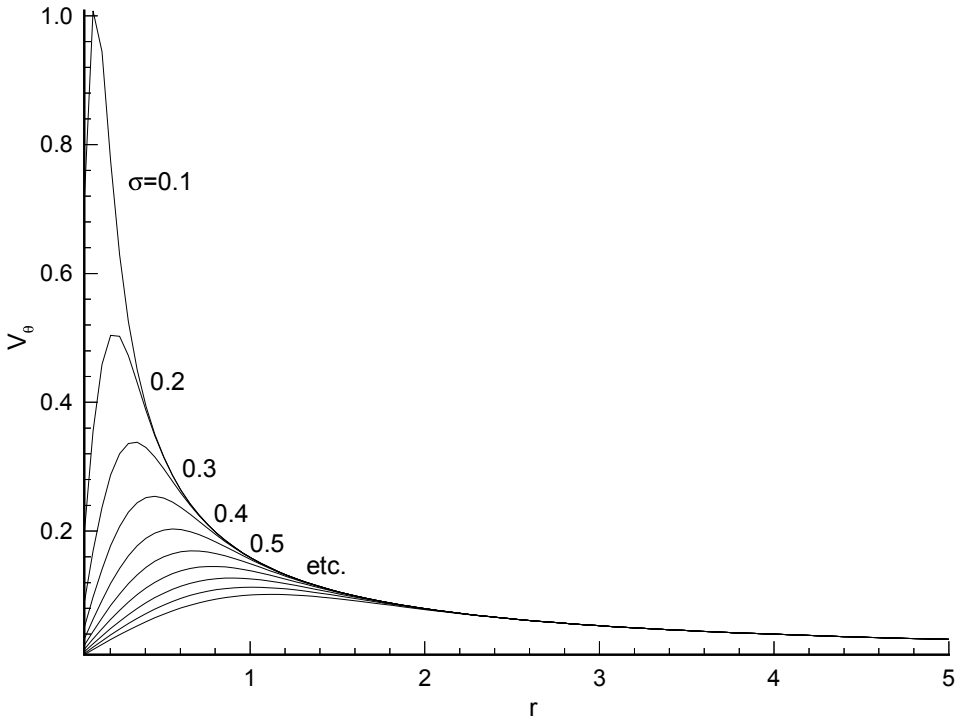

Figure 2.4: Gaussian Core Distribution for Vortex Blob Method

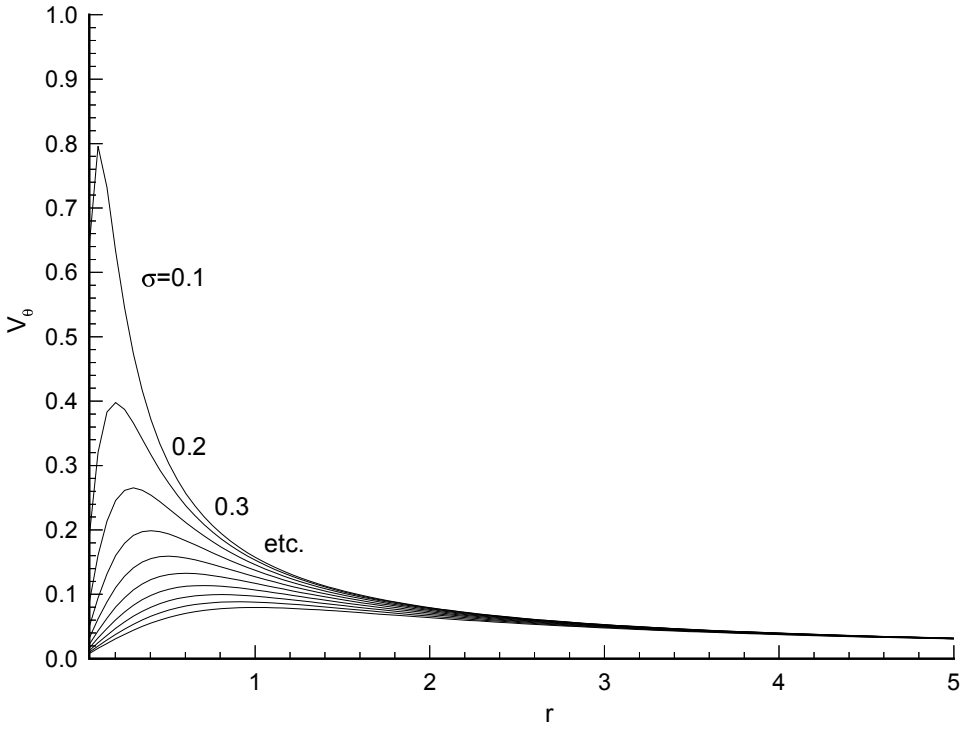

Figure 2.5: Vortex Blob Method Distribution Function

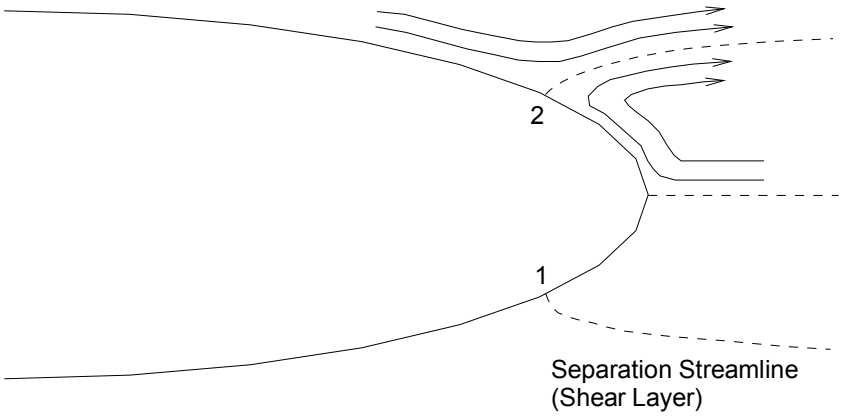

Figure 2.6: Two Dimensional Flow Separation

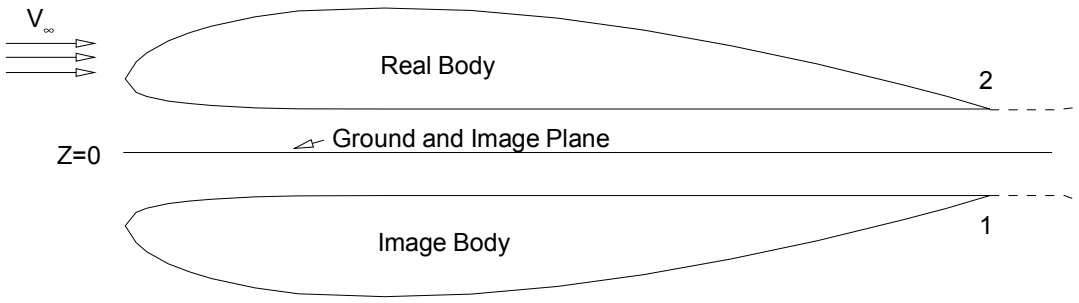

Figure 2.7: Schematic of Method of Images

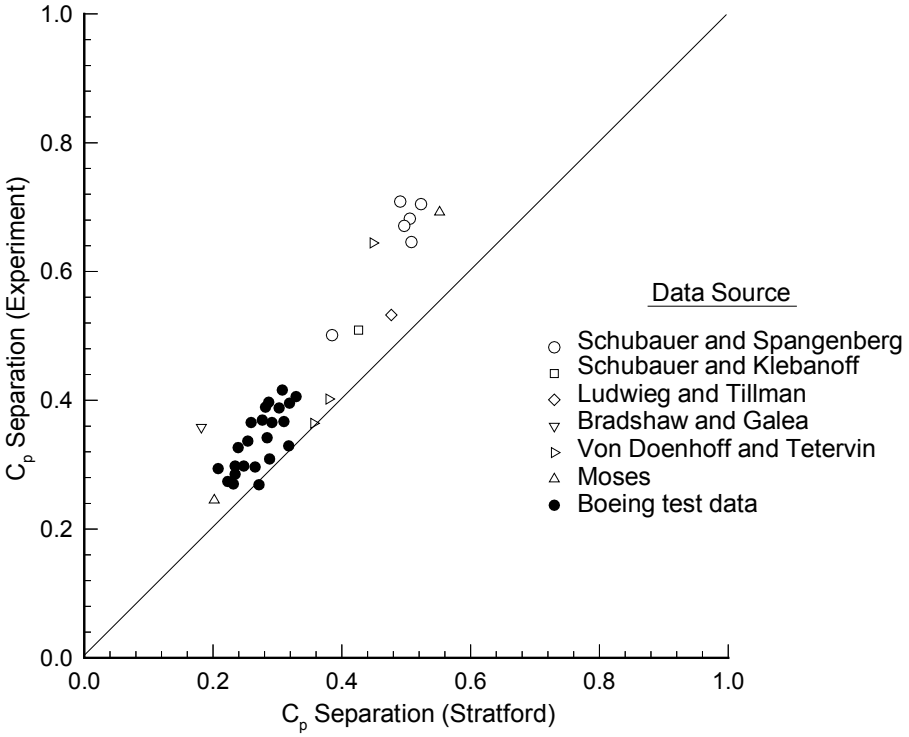

Figure 2.8: Evaluation of Stratford's Separation Criterion with Experimental Data [50]

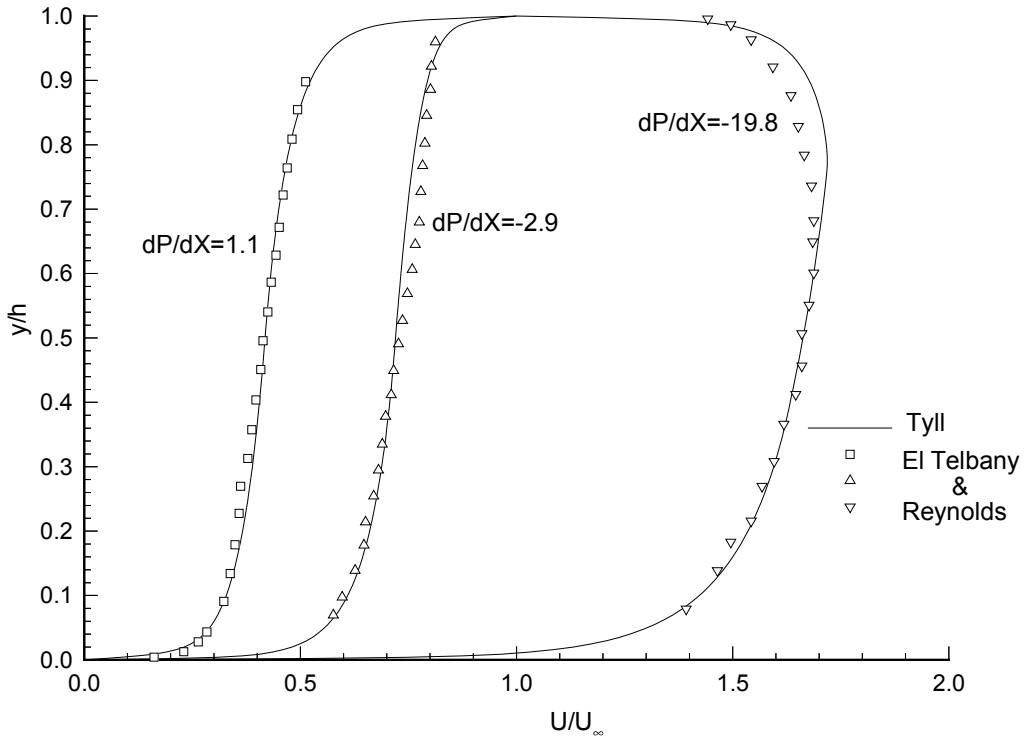

Figure 2.9: Comparison on Analysis and Experiment for Couette/Poiseuille Flow Velocity Profiles [54]

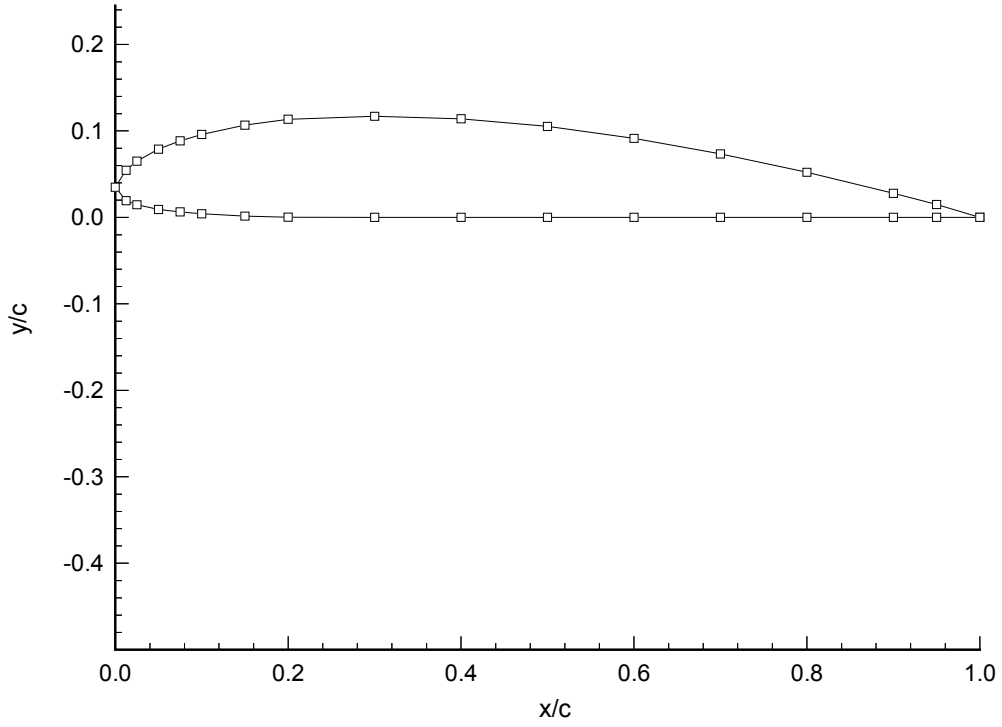

Figure 2.10: Surface Grid of Clark Y Airfoil

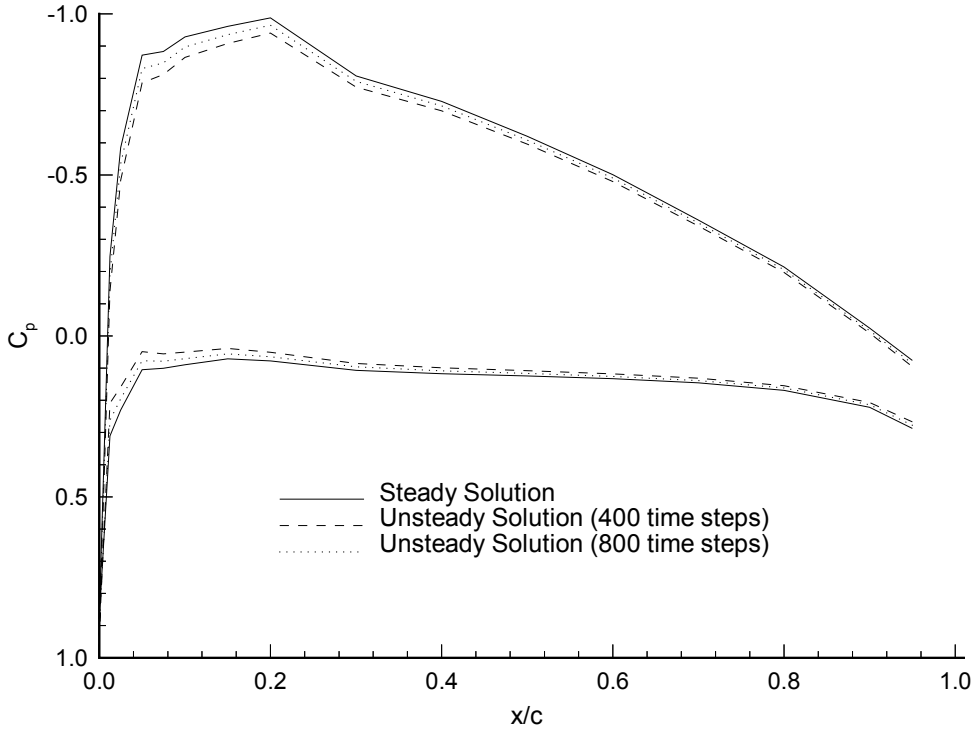

Figure 2.11: Predicted Clark Y Airfoil Pressure Coefficients Using Steady and Unsteady Vortex Panel Methods (Out of Ground Effect)

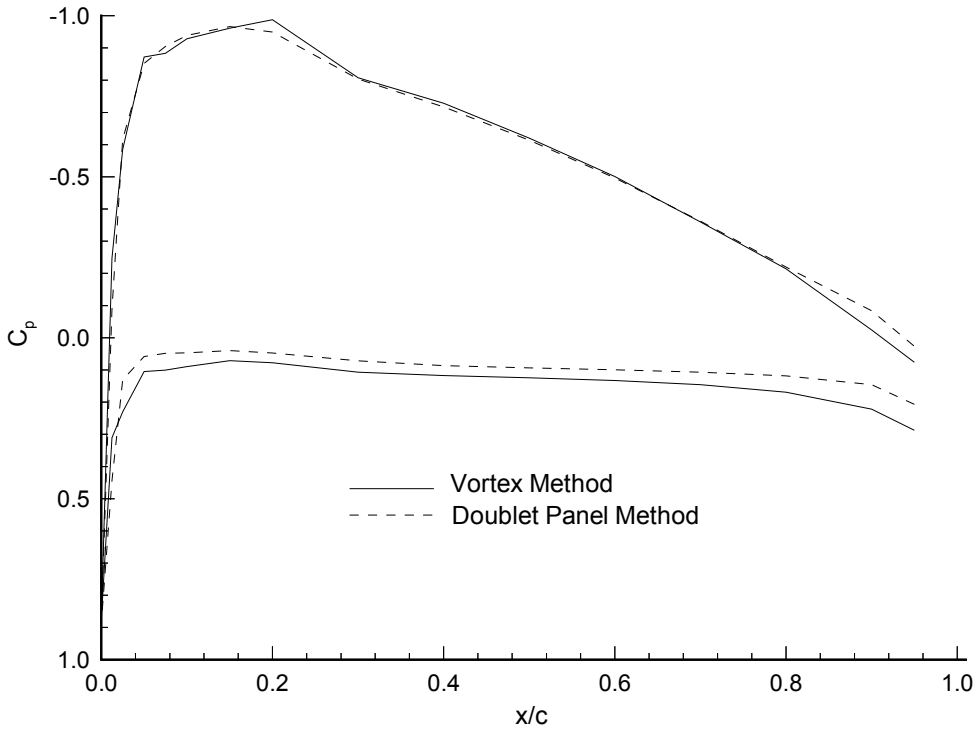

Figure 2.12: Comparison of Doublet Panel Method and Vortex Panel Method Pressure Coefficient Predictions on Clark Y Airfoil Out of Ground Effect

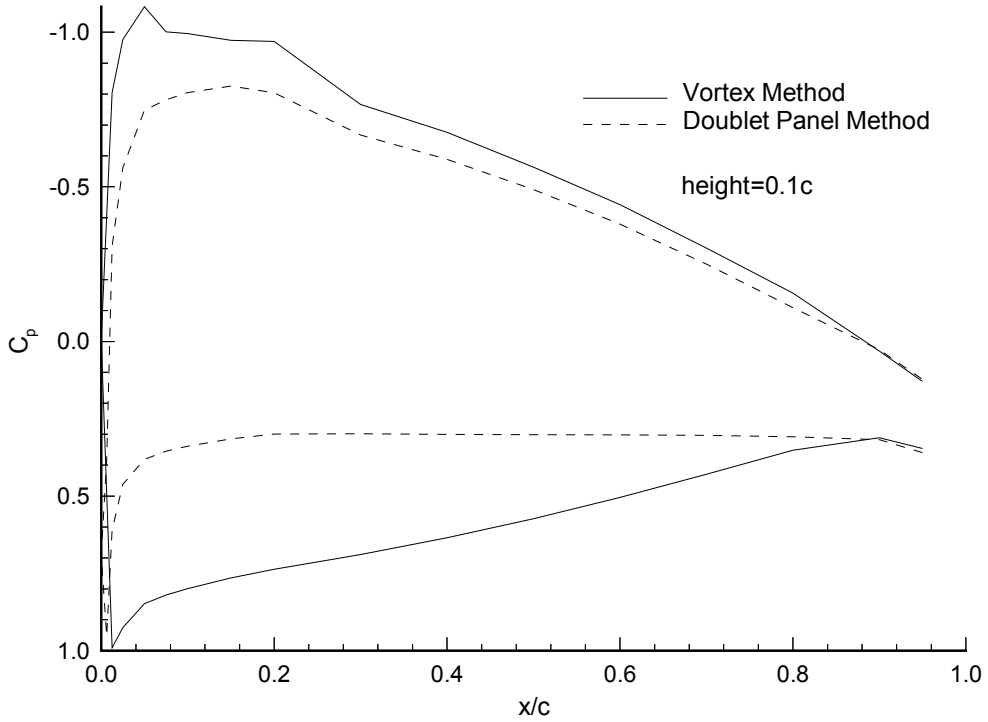

Figure 2.13: Comparison of Doublet Panel Method and Vortex Panel Method Pressure Coefficient Predictions on Clark Y Airfoil In Ground Effect

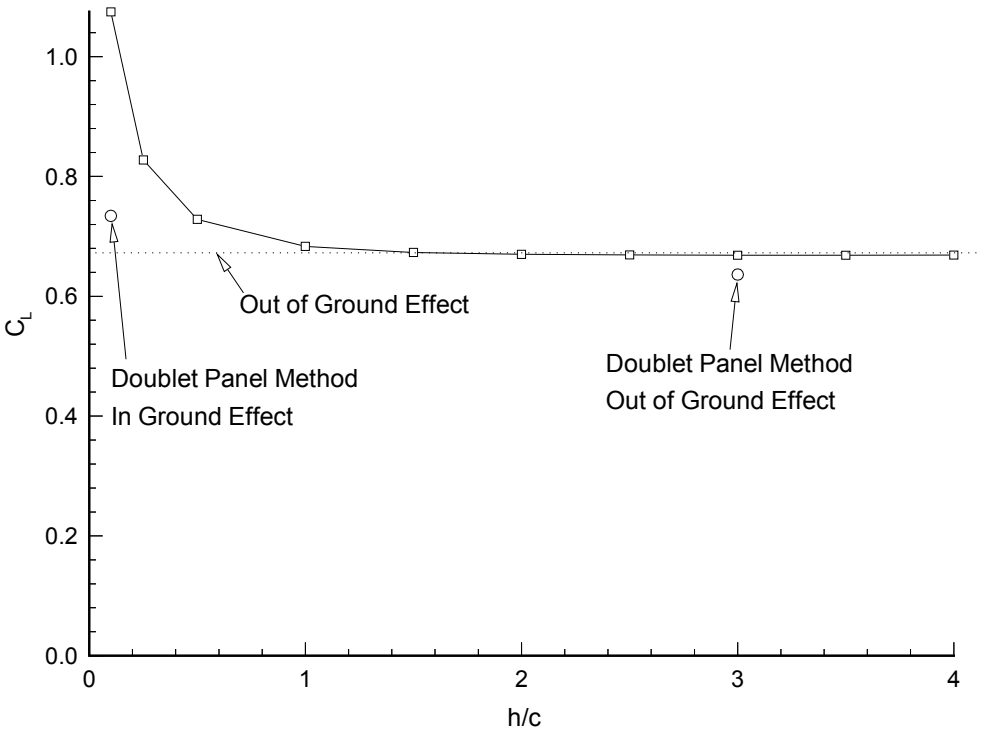

Figure 2.14: Predicted Lift Coefficient vs Height for Clark Y Airfoil Using the Vortex Panel Method

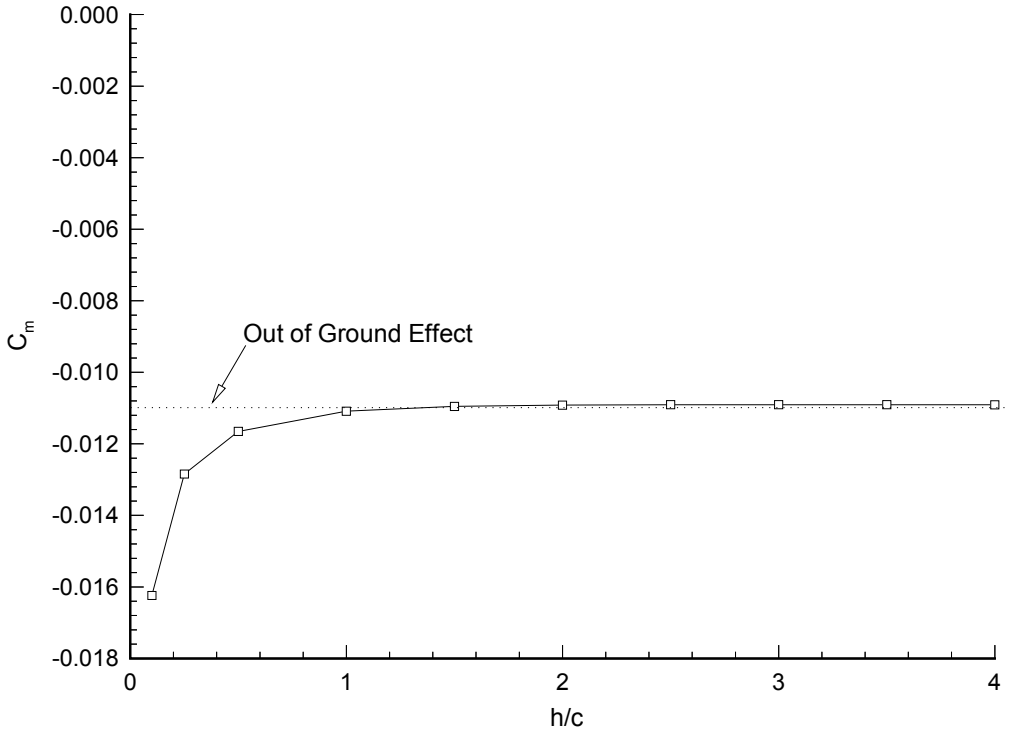

Figure 2.15: Predicted Pitching Moment Coefficient vs Height for Clark Y Airfoil Using the Vortex Panel Method

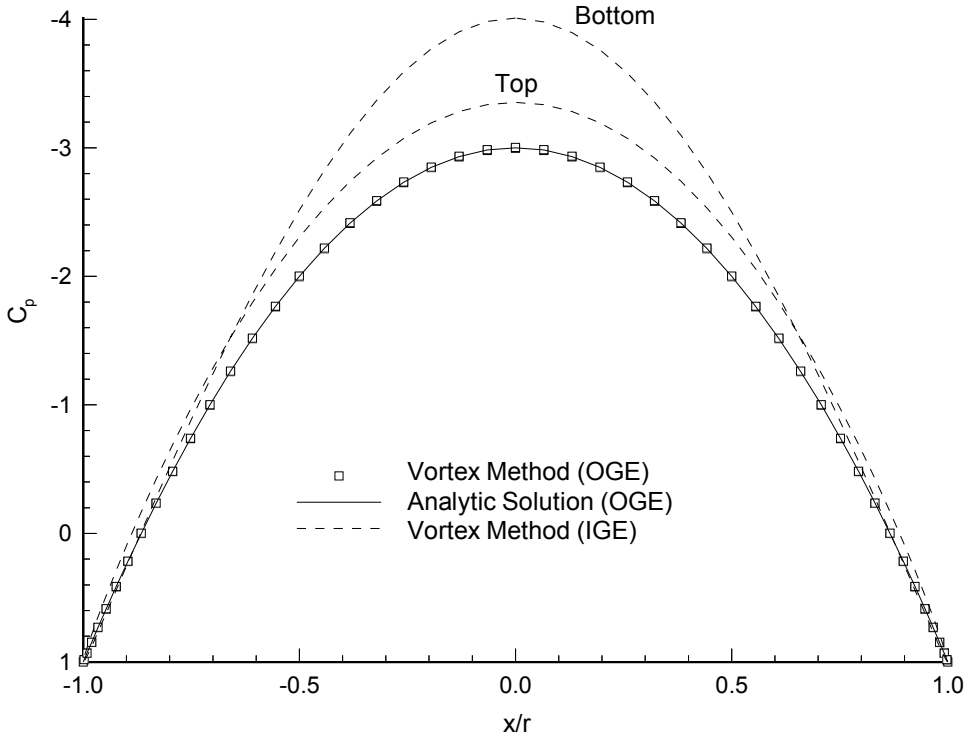

Figure 2.16: Pressure Coefficient Over Circular Cylinder w/o Separation

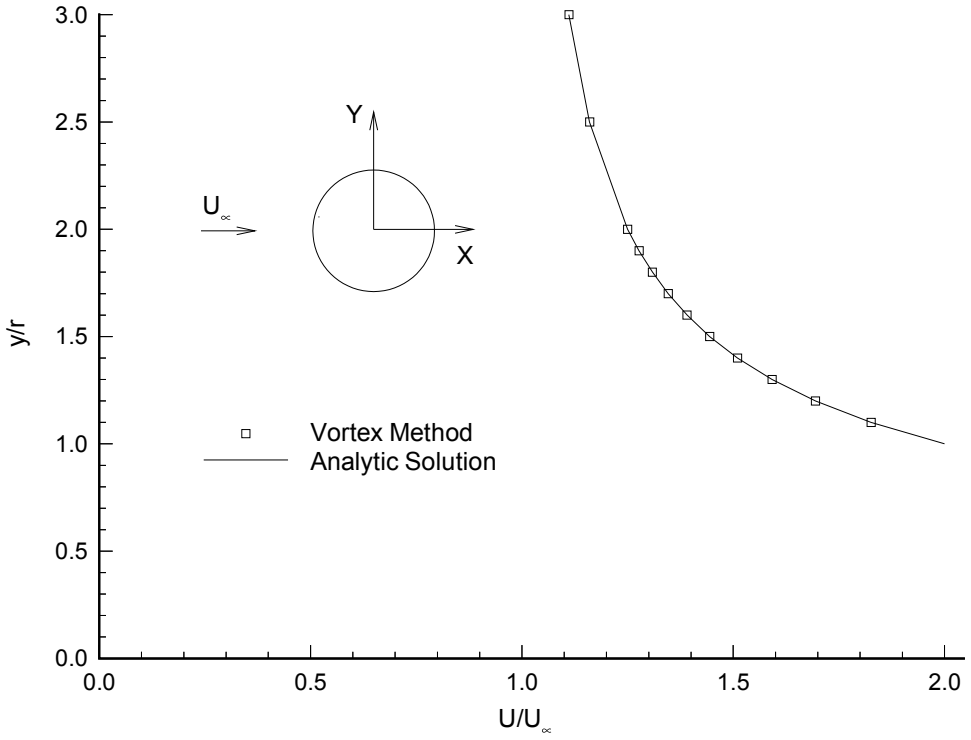

Figure 2.17: Velocity Profile Over Circular Cylinder w/o Separation Top Vertical Centerline, Out of Ground Effect

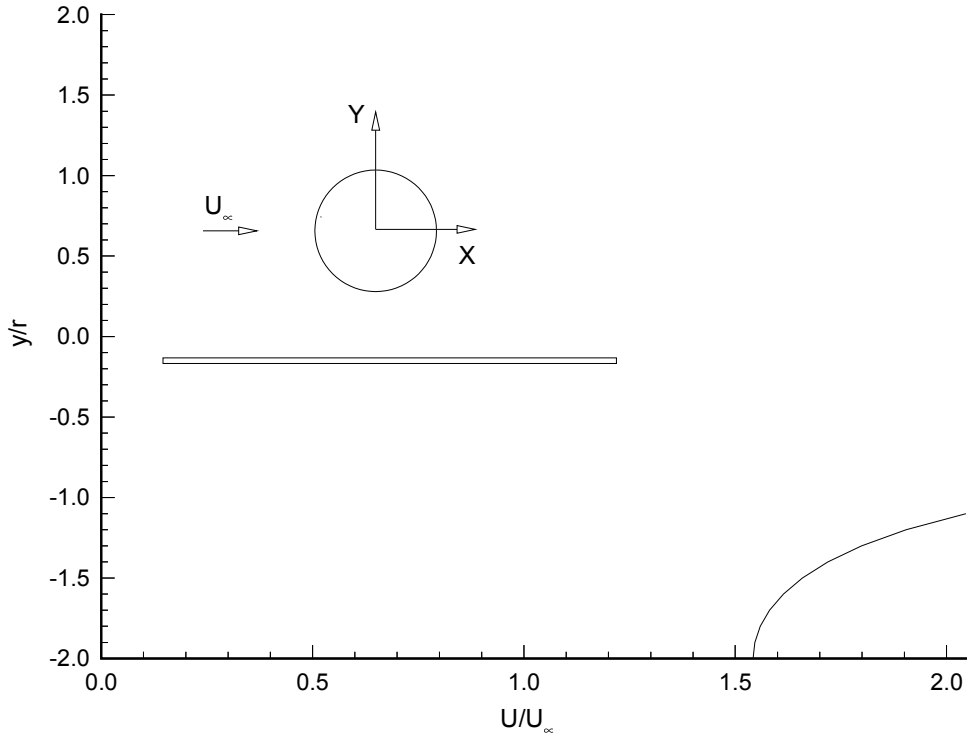

Figure 2.18: Velocity Profile Over Circular Cylinder w/o Separation Bottom Vertical Centerline, In Ground Effect

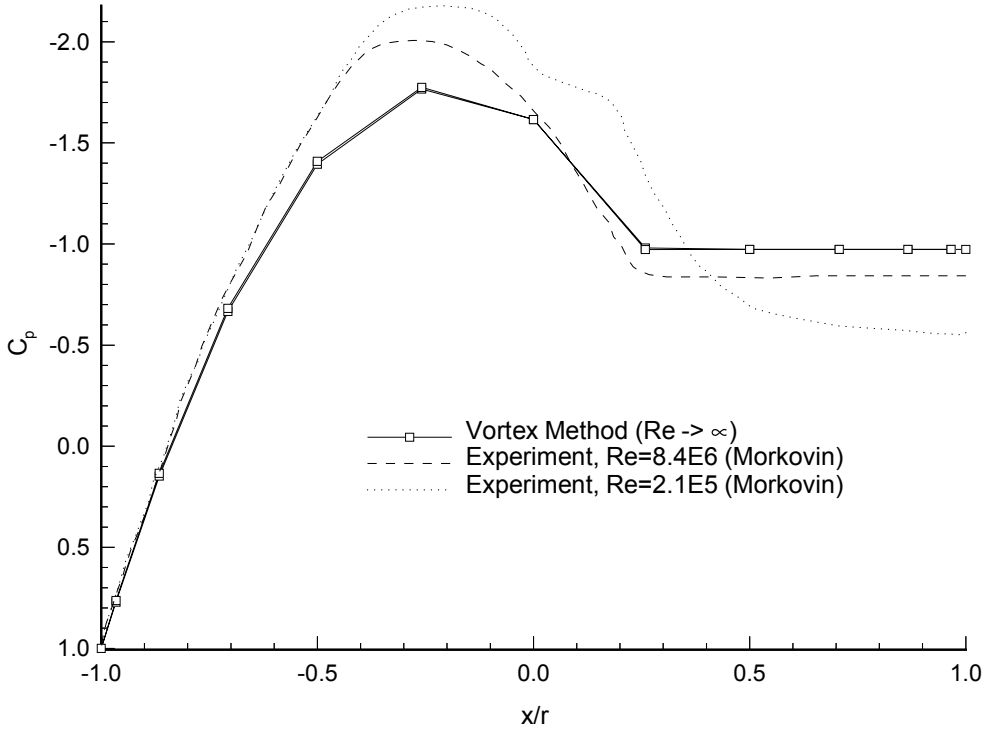

Figure 2.19: Pressure Coefficient Over Circular Cylinder Out of Ground Effect

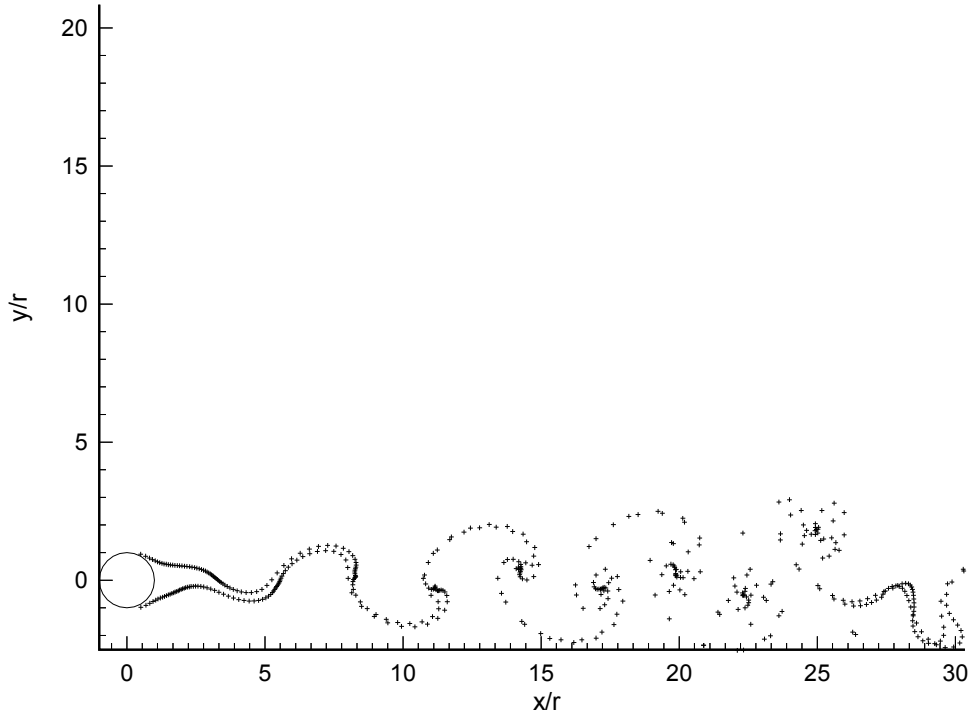

Figure 2.20: Separated Flow Over Circular Cylinder by the Vortex Panel Method

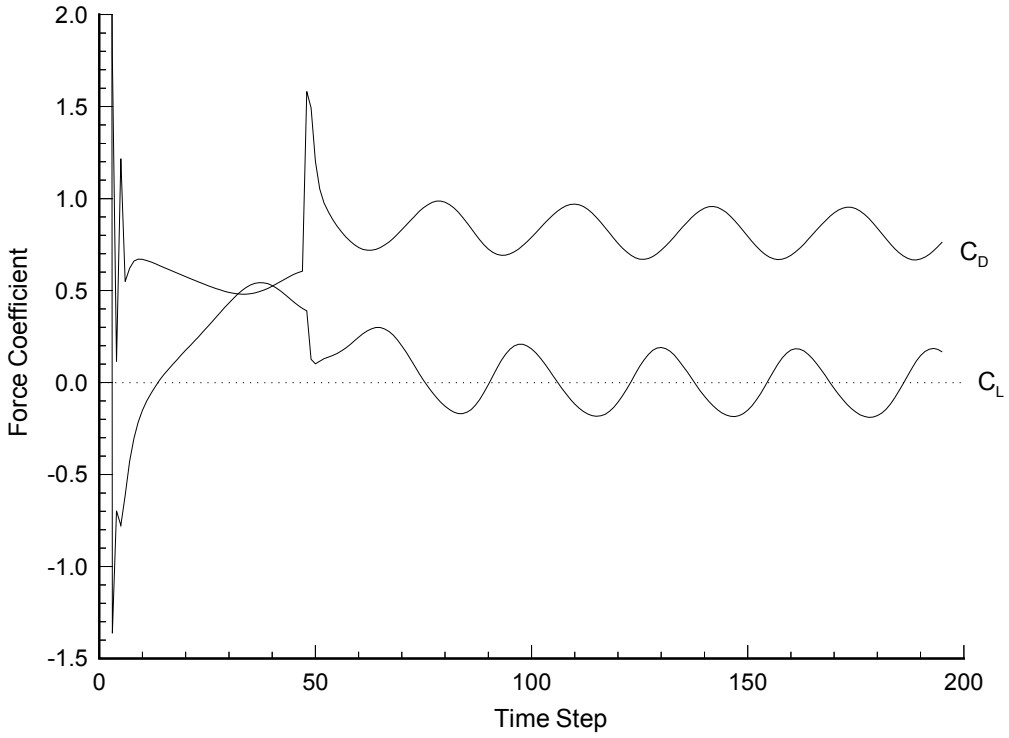

Figure 2.21: Time History of Lift and Drag Coefficient for Circular Cylinder Out of Ground Effect predicted by the Vortex Panel Method

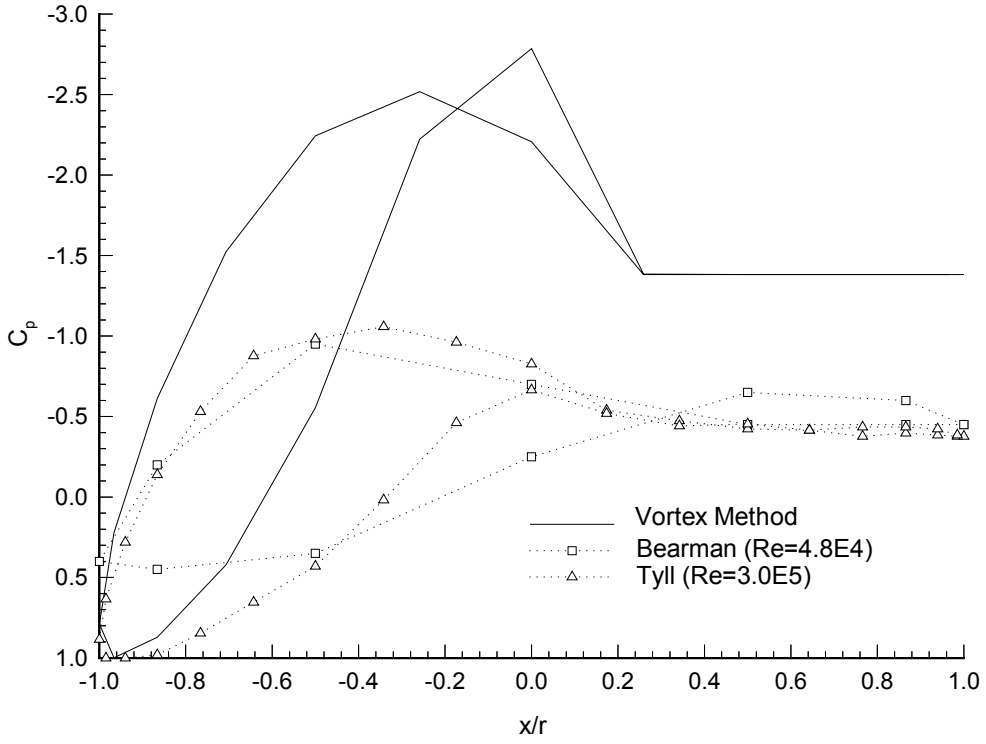

Figure 2.22: Pressure Coefficient Over Circular Cylinder In Ground Effect (h/d=0.1)

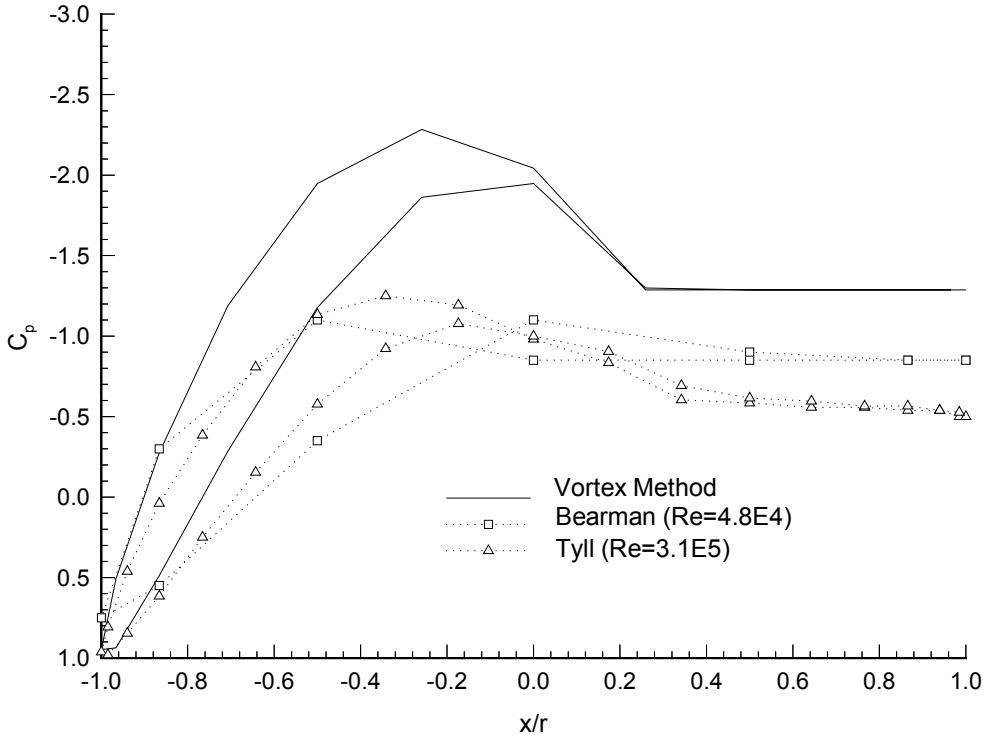

Figure 2.23: Pressure Coefficient Over Circular Cylinder In Ground Effect (h/d=0.4)

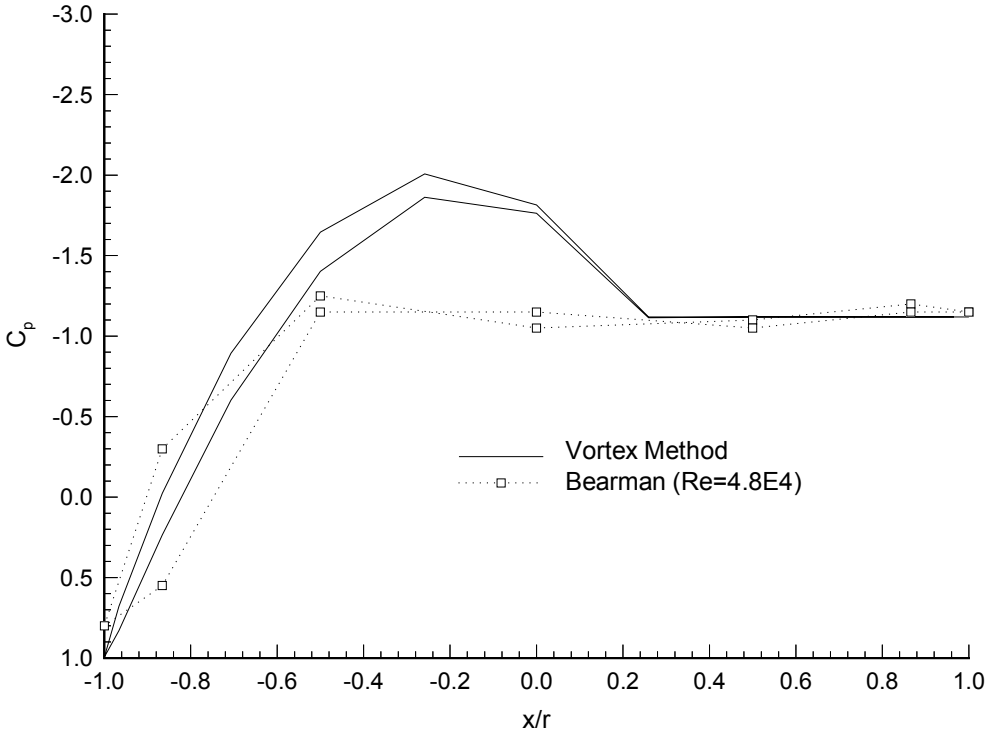

Figure 2.24: Pressure Coefficient Over Circular Cylinder In Ground Effect (h/d=1.0)

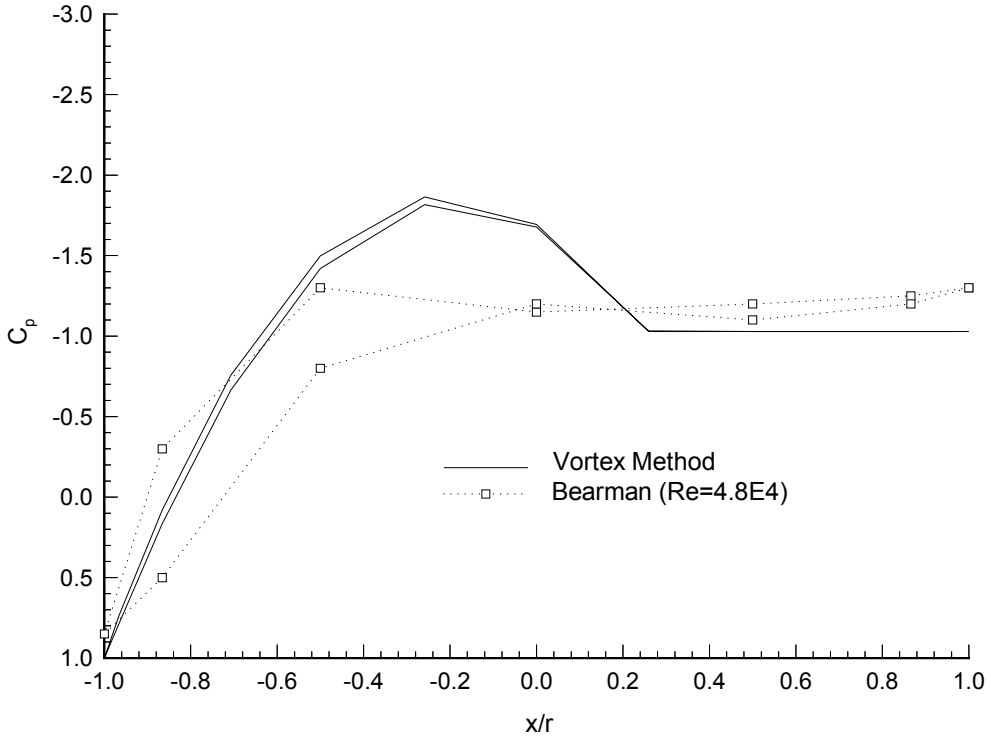

Figure 2.25: Pressure Coefficient Over Circular Cylinder In Ground Effect (h/d=2.0)

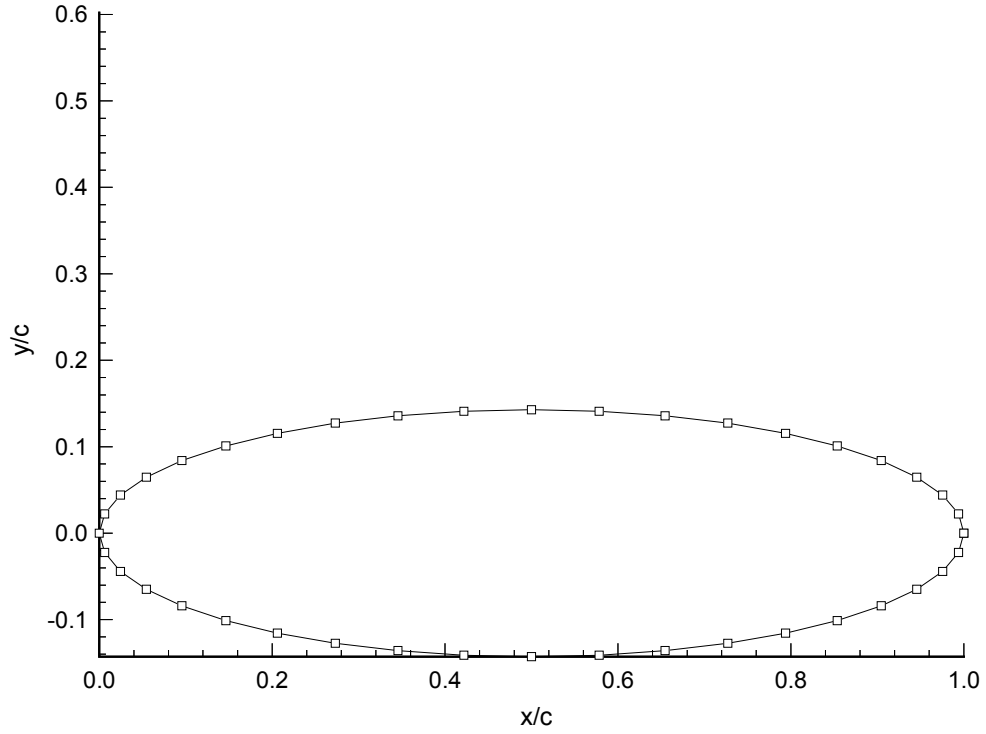

Figure 2.26: Surface Grid of Elliptic Cylinder

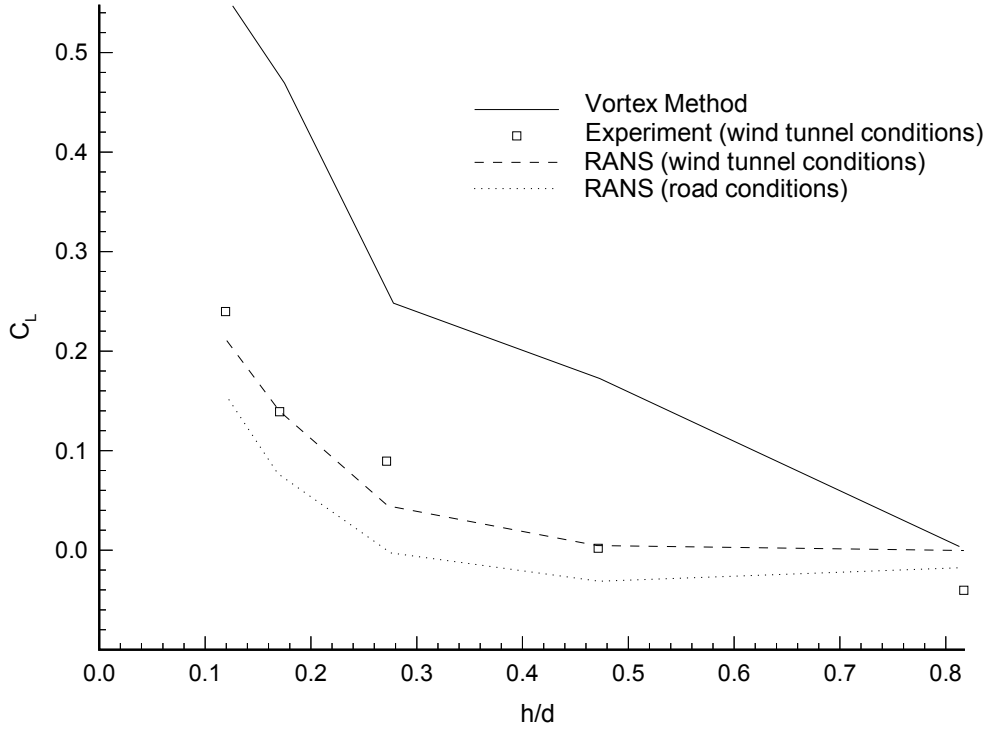

Figure 2.27: Lift Coefficient of a 3.5:1 Elliptic Cylinder vs Height to Width Ratio

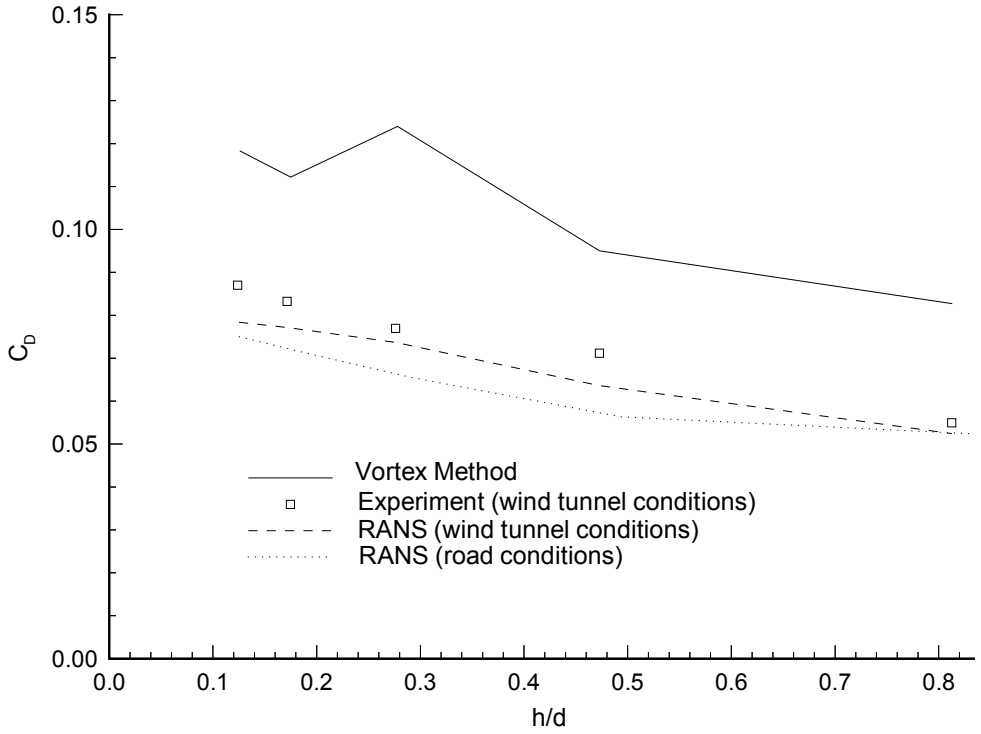

Figure 2.28: Drag Coefficient of a 3.5:1 Elliptic Cylinder vs Height to Width Ratio

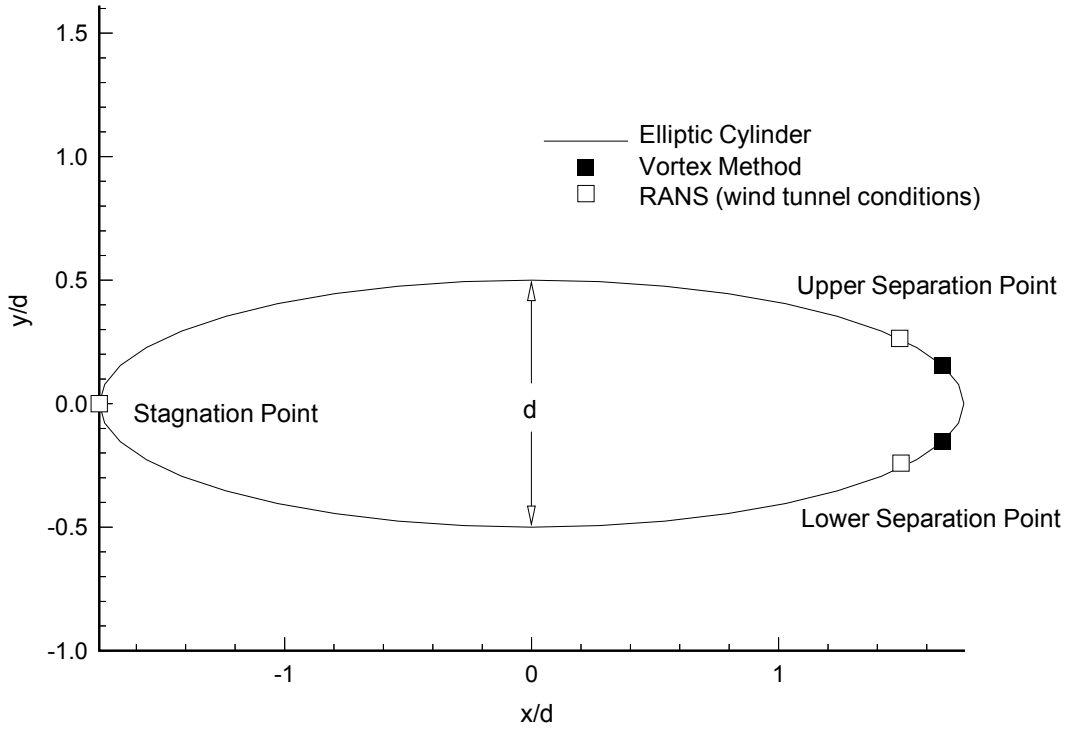

Figure 2.29: Separation and Stagnation Point Locations for Elliptic Cylinder Out of Ground Effect

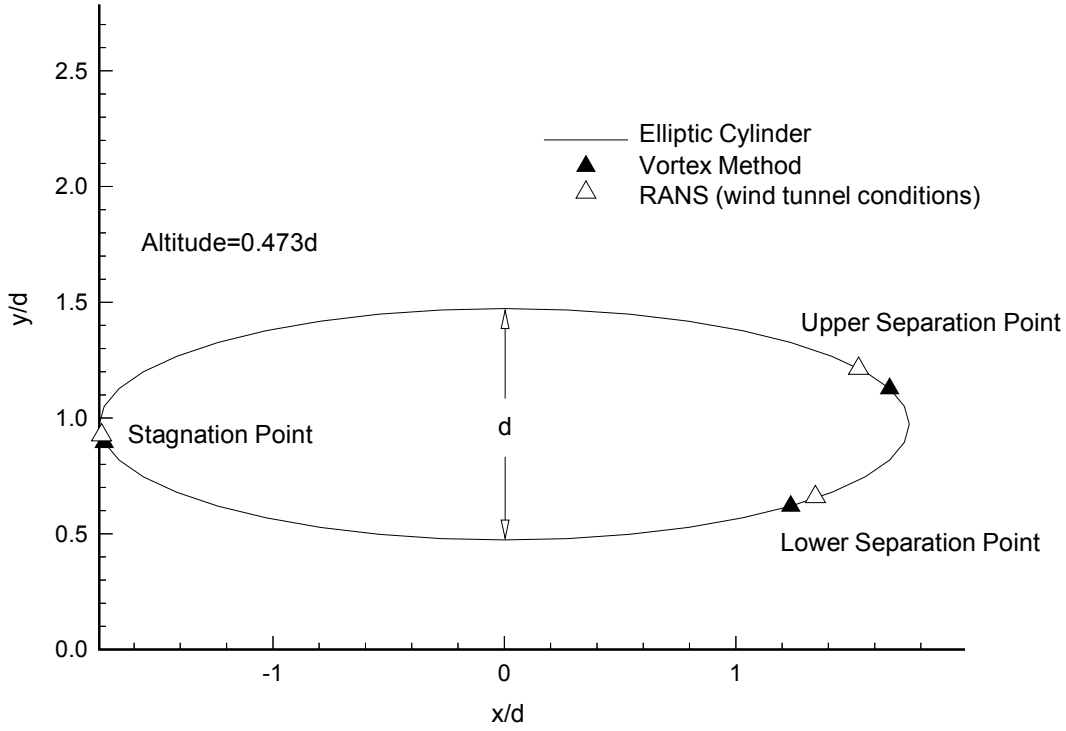

Figure 2.30: Separation and Stagnation Point Locations for Elliptic Cylinder at height-to-diameter ratio of 0.473

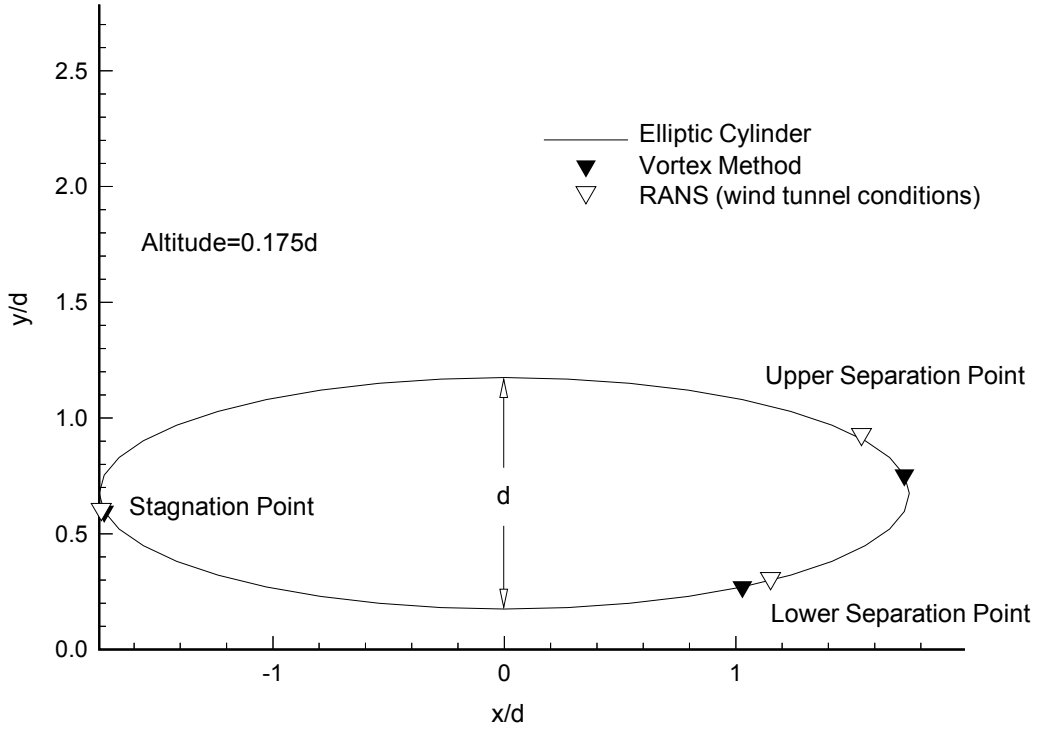

Figure 2.31: Separation and Stagnation Point Locations for Elliptic Cylinder at height-to-diameter ratio of 0.175

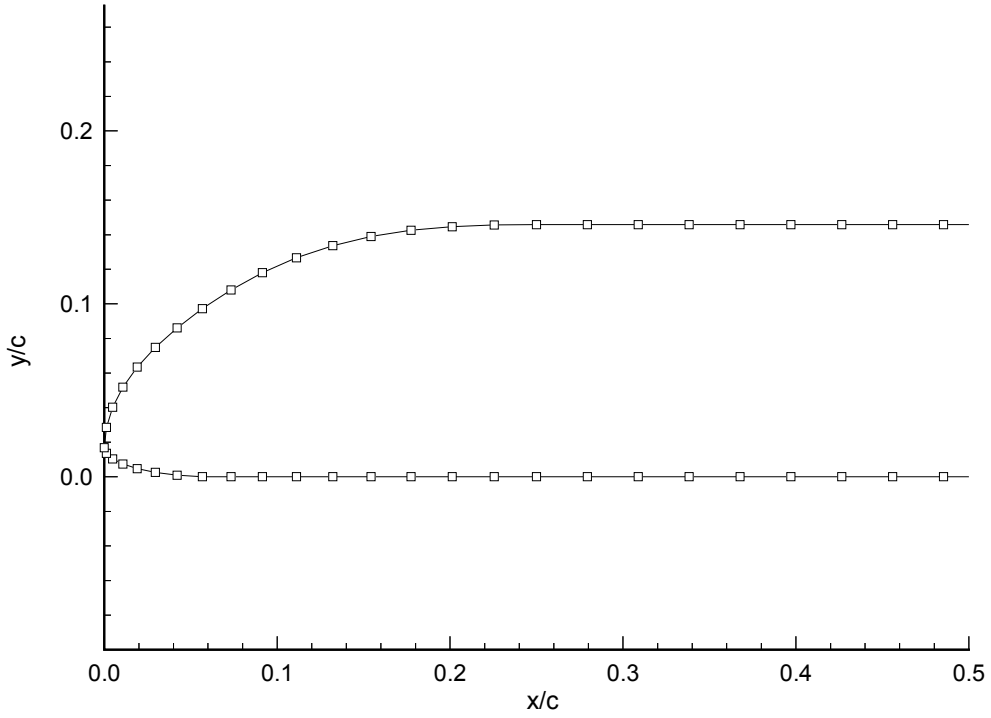

Figure 2.32: Surface Grid for Grumman MAG950

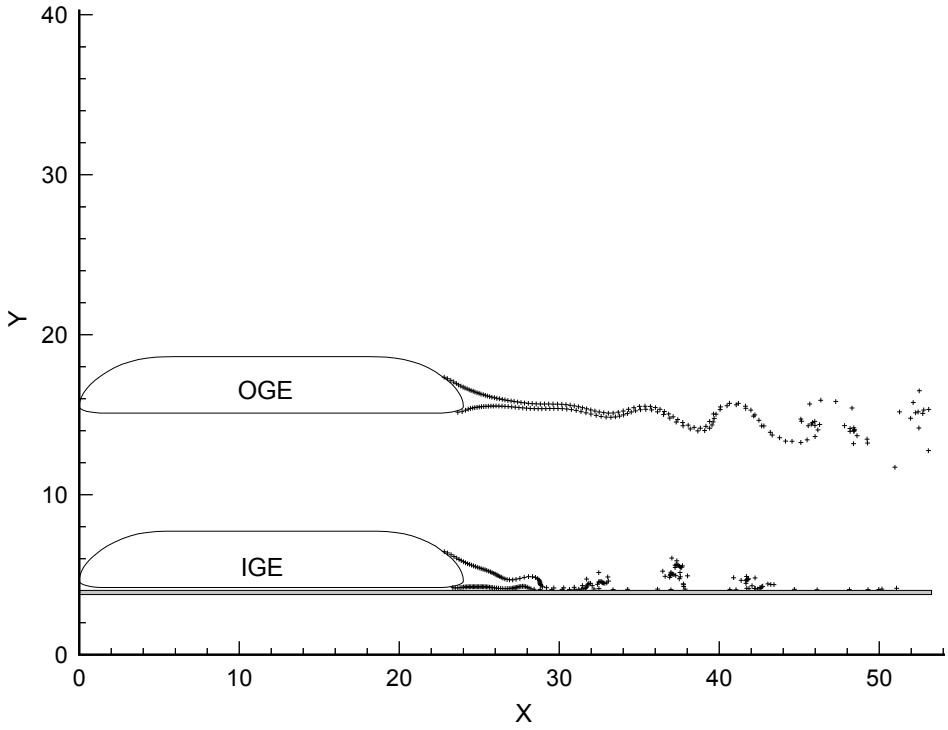

Figure 2.33: Vortex Panel Method Solution for MAG950

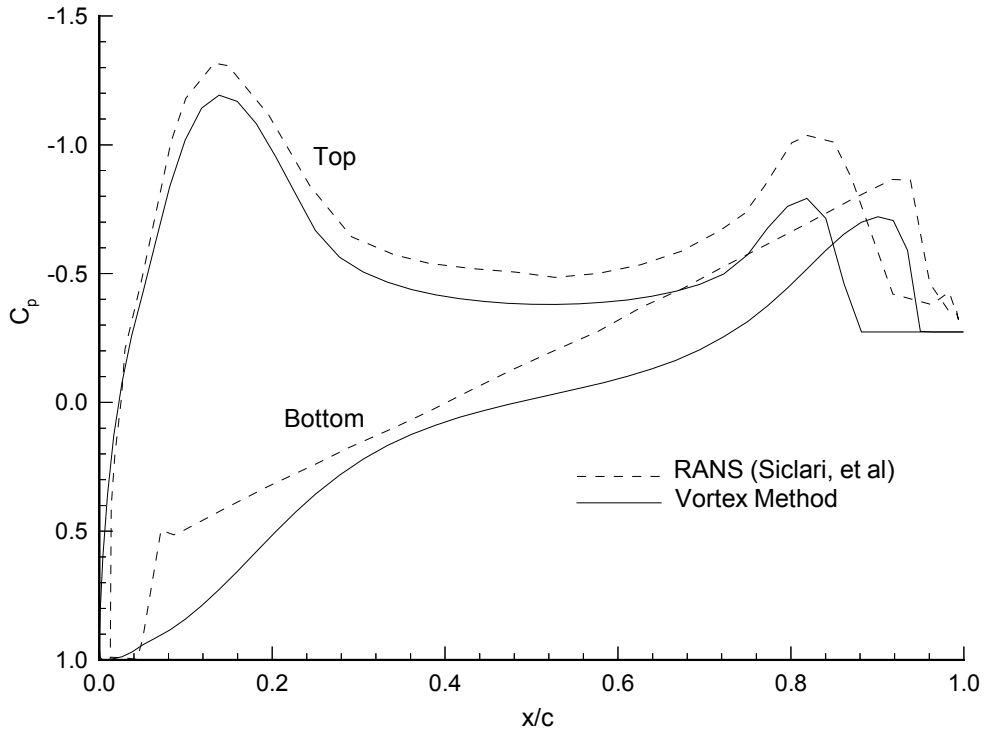

Figure 2.34: Pressure Coefficient over the MAG950 2-D Side View In Ground Effect ($\frac{h}{d} = 0.029$)

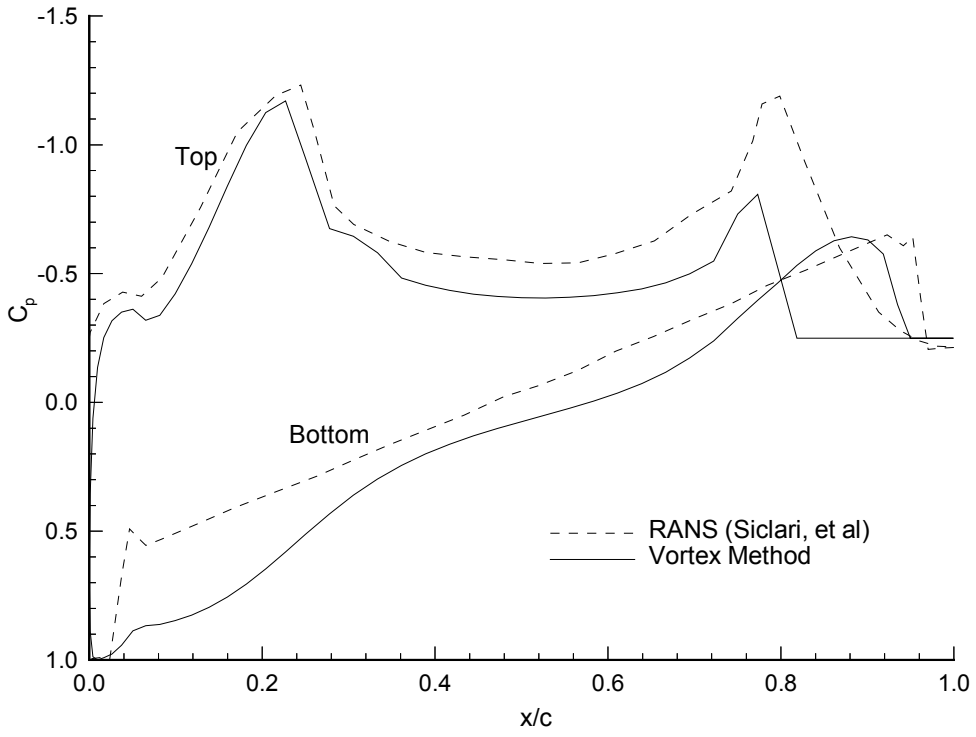

Figure 2.35: Pressure Coefficient over the MAG1002 2-D Side View In Ground Effect ($\frac{h}{d} = 0.029$)

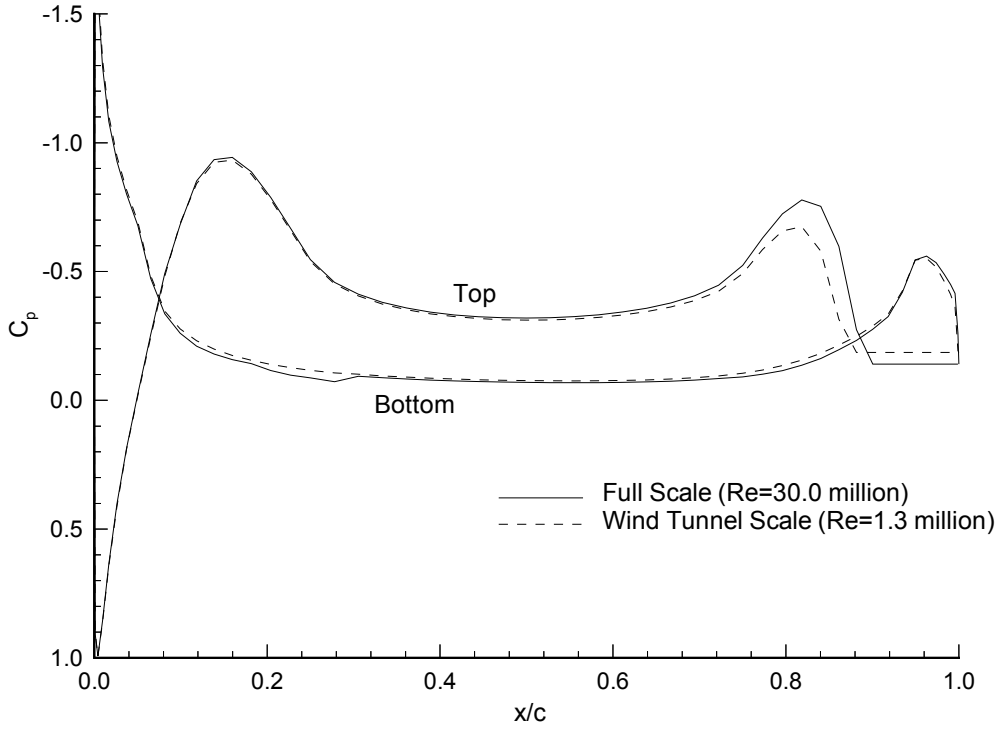

Figure 2.36: Pressure Coefficient for the Full Scale and Wind Tunnel Scale Cases of MAG950 Out of Ground Effect (Vortex Panel Method)

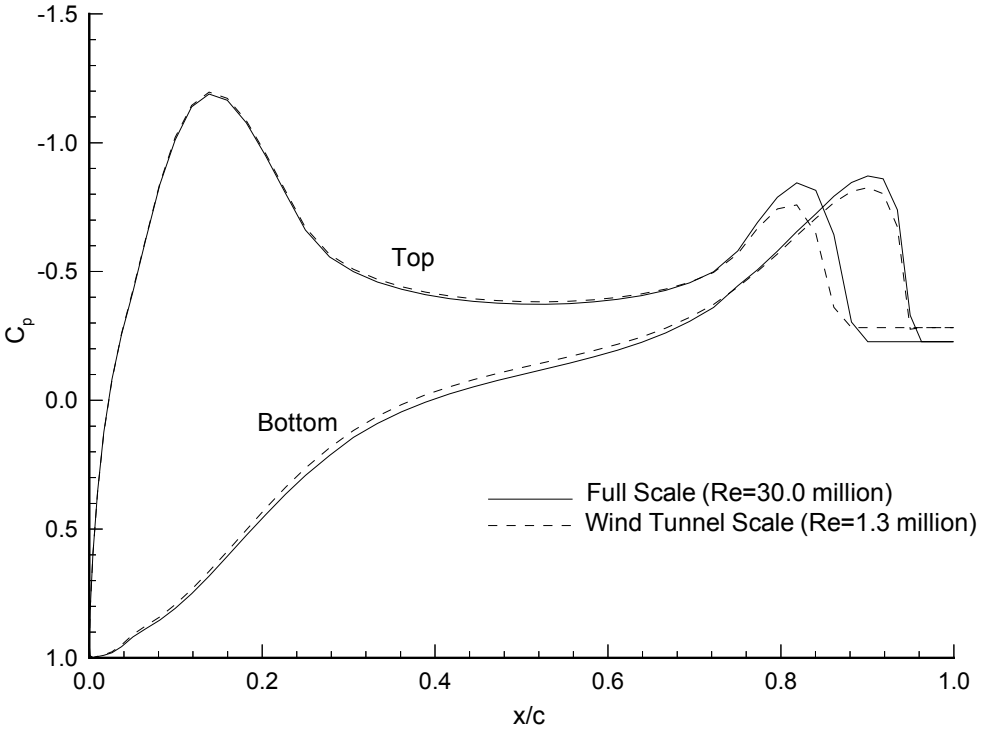

Figure 2.37: Pressure Coefficient for the Full Scale and Wind Tunnel Scale Cases of MAG950 In Ground Effect (Vortex Panel Method)

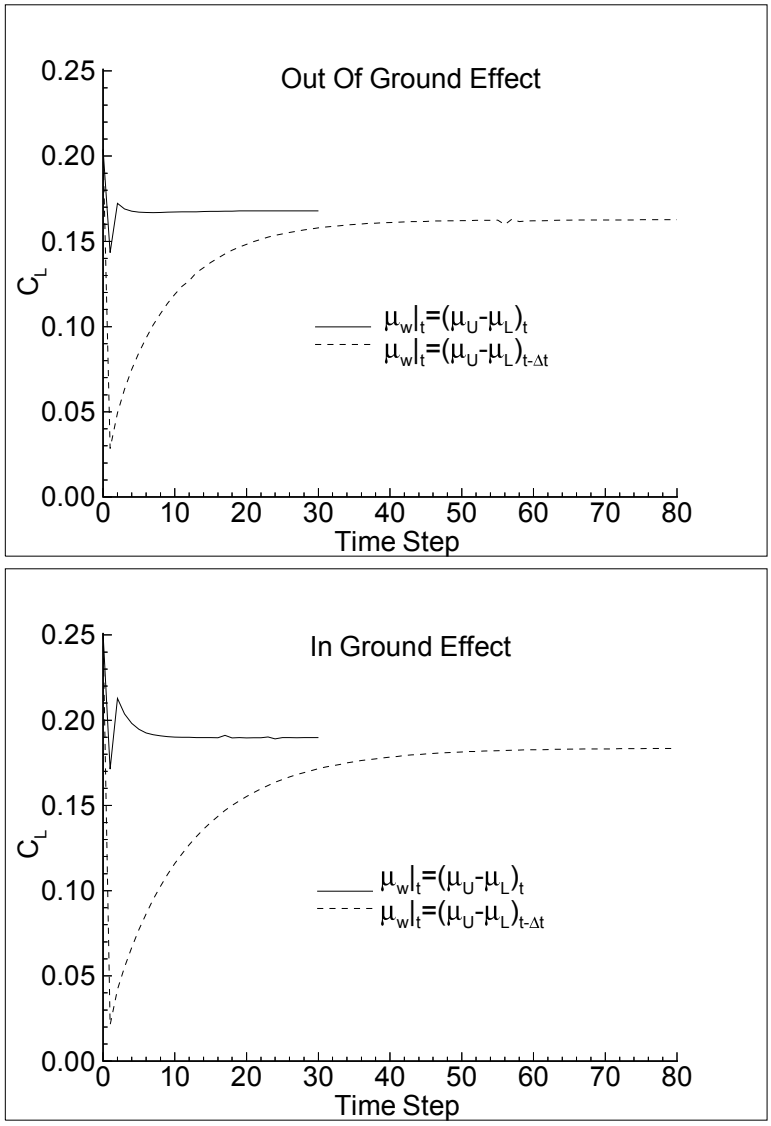

Figure 2.38: Solution Time History for Flow Over a Finite Thickness ClarkY Airfoil (AR=1.0) Out of Ground Effect (Top) and In Ground Effect (Bottom); Doublet Panel Method

Figure 2.39: Flow Over A ClarkY Airfoil (AR=1.0) Out of Ground Effect; Doublet Panel Method

Figure 2.40: Flow Over A ClarkY Airfoil (AR=1.0) In Ground Effect; Doublet Panel Method

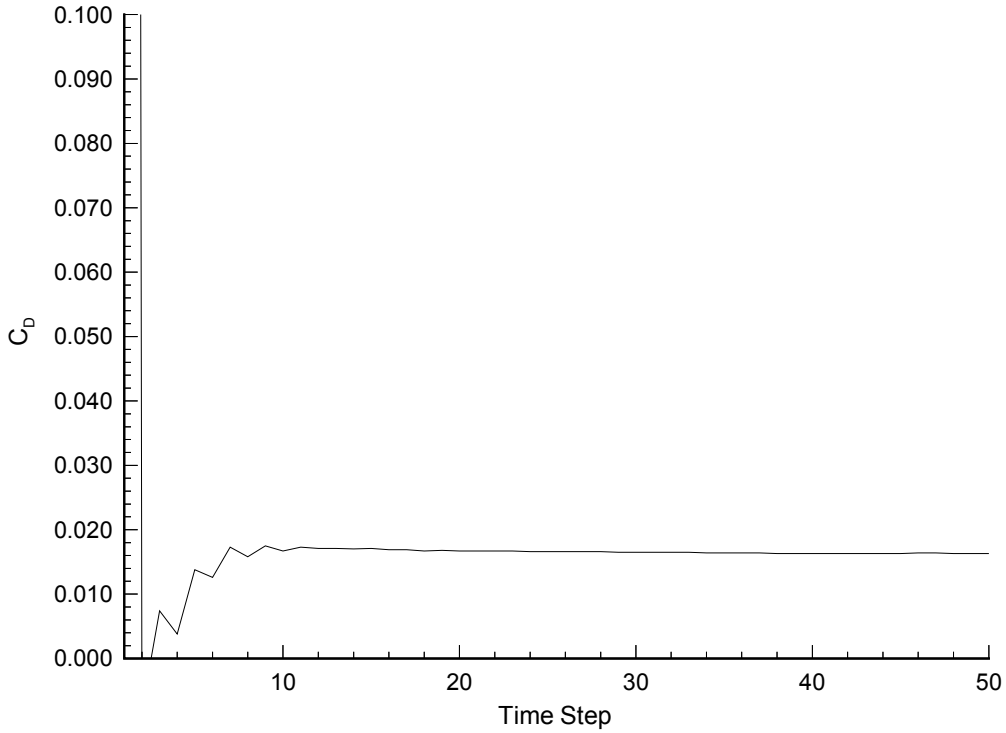

Figure 2.41: Solution Time History for Flow Over a Sphere With Turbulent Separation as Predicted by the Doublet Panel Method

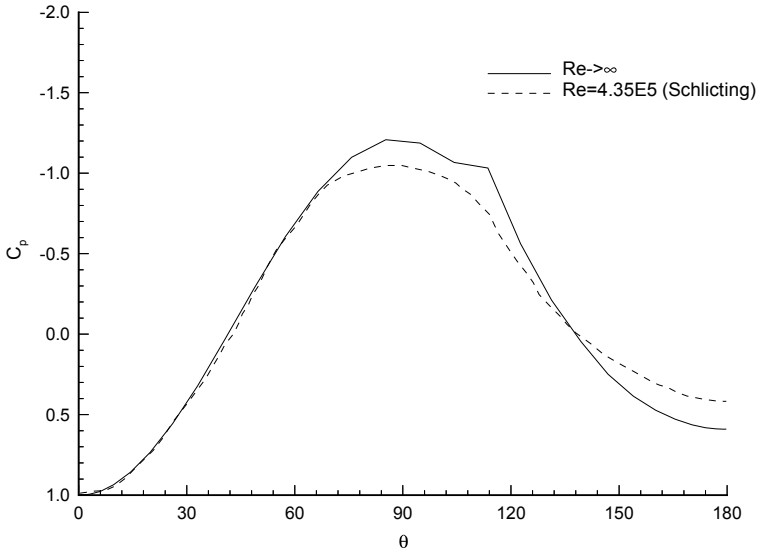

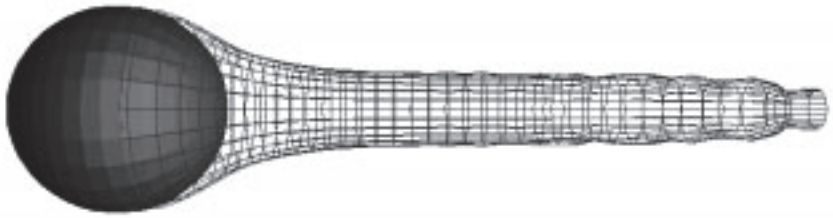

Figure 2.42: Pressure Coefficient for Flow Over a Sphere With Turbulent Separation as Predicted by the Doublet Panel Method (Separation at 104°) [62]

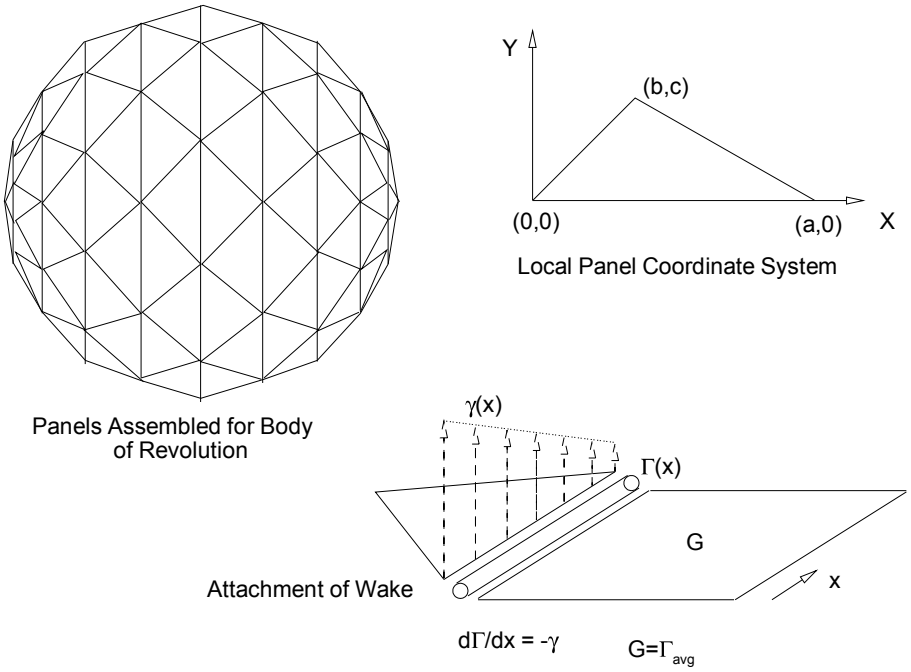

Figure 2.43: 3-D Vortex Panel Method, Panels and Panel Assembly

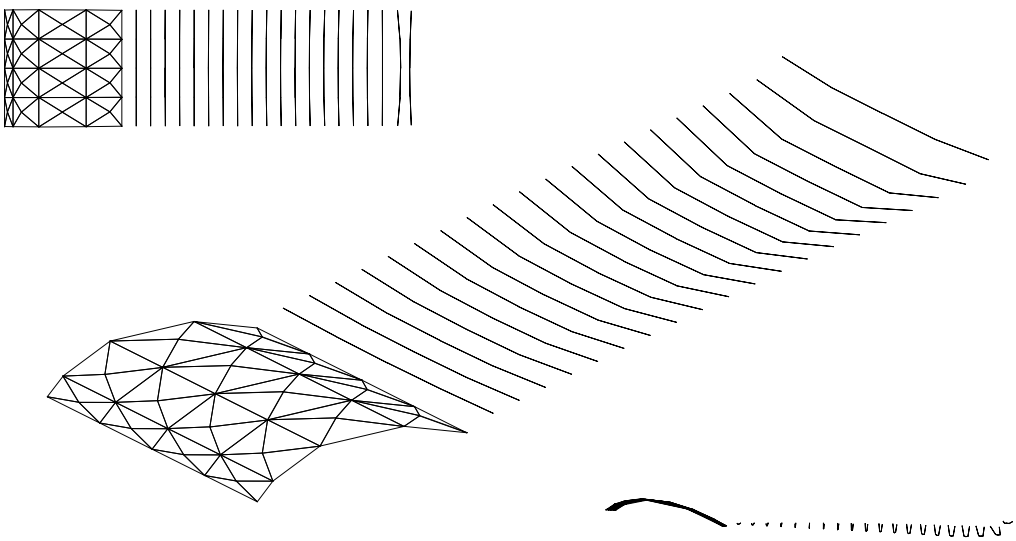

Figure 2.44: Mean Camber Line of ClarkY, Aspect Ratio of 1.0, Out of Ground Effect (Vortex Panel Method)

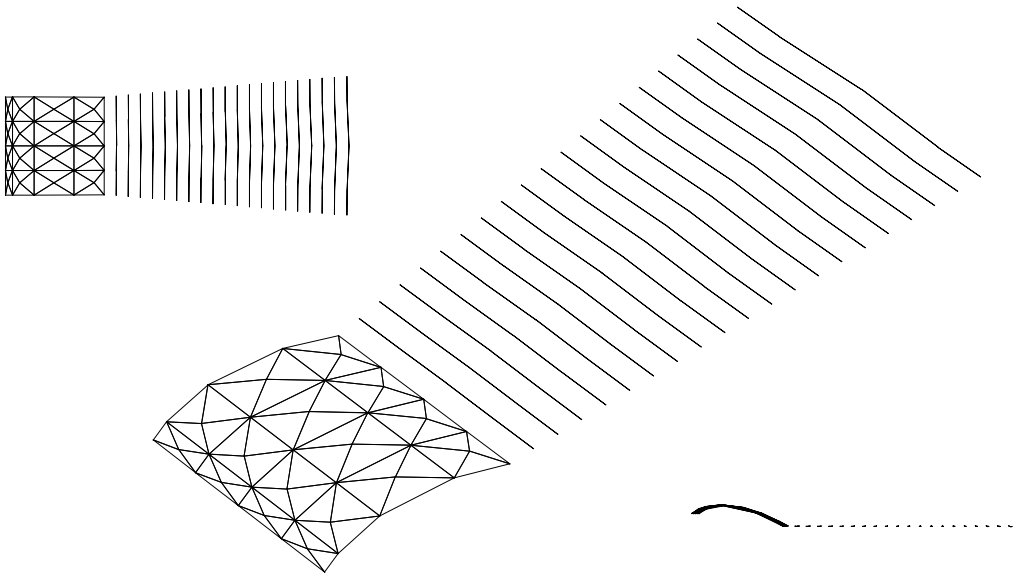

Figure 2.45: Mean Camber Line of ClarkY, Aspect Ratio of 1.0, In Ground Effect (Vortex Panel Method)

Model	C_L	C_D	C_m
MAG950	3.362	0.253	-0.059
MAG1002	3.926	0.217	-0.086
MAG1007	2.683	0.247	-0.027
MAG1742	2.885	0.213	-0.037
MAG1459	3.914	0.053	-0.083

Table 2.1: Force and Moment Coefficients for Northrop Grumman MAGLEV Designs Calculated Using the Vortex Panel Method

Model	OGE	IGE
Base	1.204	3.361
Total	1.202	3.362

Table 2.2: Comparison of In and Out of Ground Effect Lift Coefficients for the Wind Tunnel Scale MAG950 Using the Vortex Panel Method

Model	OGE	IGE
Base	0.131	0.185
Total	0.168	0.253

Table 2.3: Comparison of In and Out of Ground Effect Drag Coefficients for the Wind Tunnel Scale MAG950 Using the Vortex Panel Method

	Wind Tunnel Scale	Full Scale
C_L	1.202	1.413
C_D	0.168	0.147

Table 2.4: A Comparison of Wind Tunnel Scale and Full Scale Force Coefficient Predictions for the MAG950, Out of Ground Effect Using the Vortex Panel Method

	Wind Tunnel Scale	Full Scale
C_L	3.362	3.461
C_D	0.253	0.203

Table 2.5: A Comparison of Wind Tunnel Scale and Full Scale Force Coefficient Predictions for the MAG950, In Ground Effect Using the Vortex Panel Method

Chapter 3

Structural Weight Model

The main function of the structures module is to calculate the structural weight as a function of the vehicle geometry for a nominal fifty person vehicle. It is assumed here that the structure of the MAGLEV vehicle is similar to that of a subsonic aircraft fuselage. Shaw [23] describes the aluminum cabin to have a sheet and stringer structure with internal frames and longerons. This enables use of the empirical equations for aircraft structural weight which are widely available. The structural weight and the design gross weight are found by simultaneously solving the following two equations,

$$W_{fuselage} = 0.3280(W_{dg}N_Z)^{0.5}L^{0.25}S_f^{0.302}(\frac{L}{D})^{0.10} \tag{3.1}$$

$$W_{dg} = W_{fuselage} + W_{magnet} + W_{payload} + W_{misc} \tag{3.2}$$

where the miscellaneous weight includes furnishings, instruments, controls, etc. This weight equation is for a transport aircraft fuselage and was taken from an aircraft design text by Raymer [63].

The design gross weight equation is altered to include MAGLEV specific items. The magnet weight is taken to be $114.4lbs$ (52 kg) for each of the 24 superconducting magnets (Ref. [22]). The payload weight is taken to be $205lbs$ (93.2 kg) for each of the 50 passengers and two crew members. This weight includes luggage. The

miscellaneous equipment includes the seats and all of the ancillary equipment. Each seat has a mass of 14.55 kg. The ancillary equipment is treated as a fixed weight and is determined to be 47800 lbf. This number was calculated using weight estimations by Allen [26] which states 72000 lbf (320 kn) design gross weight. By subtracting the payload, seats, motor, and estimated structural weight (9000 lbf [23]), one can calculate the remaining fixed weight. These equations can be altered to account for the use of composite materials using a mass modifier. This modifier is currently set at 1.0 for aluminum but can be adjusted to 0.8 for composite material.

The use of this empirical weight equation is correct from a structural standpoint, although, the structural sizing for railed vehicles is handled differently from that of aircraft. Aircraft are structurally sized to handle a specific maneuver by considering the maximum load factor it will have to withstand. Railed vehicles are structurally sized for a longitudinal buffer shock. Shaw [23] specifies a maximum 2g vertical acceleration which is used as the load factor (N_Z) in the weight equation. This is very low compared to maximum load factors for aircraft. For example, a utility category Cessna 152, general aviation aircraft has a maximum load factor of 4.4g. Since aerodynamic loads are very low and the levitation forces are fairly uniform over the length of the vehicle, the MAGLEV structure will be very light. The 3 meter per second bumper impact, specified in the system technical requirements [5], cannot be handled in this preliminary design setting. In addition to the shock load, there are other specifications dealing with impact with guideway obstructions, thrown objects, bird strikes, and bullet strikes.

Weight calculations are very important in the design of aerospace vehicles since the mission profile usually involves carrying a payload over a distance. The weight growth factor is defined in order to determine if the payload can be carried. The definition can be seen in Eq. 3.3.

$$\text{Weight Growth Factor} = \frac{1}{1 - \dfrac{\text{Empty Weight}}{\text{Gross Takeoff Weight}}} \tag{3.3}$$

It can be deduced from this equation that lower growth factors are favorable, since lower vehicle empty weight increases the possible payload weight. As the weight growth factor increases, the payload weight becomes a smaller fraction of the whole.

Zero payload weight corresponds to a weight growth factor of infinity. The empty weight for a MAGLEV vehicle includes the structure, levitation and guidance system, propulsion system, ancillary equipment, and cabin furnishings. Herbst [64] estimates a growth factor for MAGLEV vehicles of 2.0. This compares to 2.4, which is a common growth factor for transport aircraft. Growth factors for aircraft can be as high as 4.0, while growth factors for launch vehicles can be as high as 20.0. Based on weight estimations presented by Allen [26], the growth factor for the Grumman MAGLEV system is slightly less than 4.0.

The gross takeoff weight can be as much as the available lift which is the combined aerodynamic and magnetic lift. This type of analysis can be used to figure out the maximum potential speed for these vehicles given the current technology. For increased speed requirements, the Linear Synchronous Motor (LSM) propulsion system must be larger and, therefore, heavier. The propulsion system weight increases resulting in a decrease in payload weight. This trade-off can be continued until there is zero payload. This system will give the maximum possible vehicle speed. Likewise, speed can be compromised in order to achieve greater payload capacity.

Chapter 4

Acquisition Cost Model

The acquisition cost model calculates the investment cost involved in acquiring a MAGLEV vehicle. This should not be confused with the vehicle price which is the cost plus some mark-up value. This cost model does not deal with the other costs associated with this transportation system such as the cost of the guideway, electrical distribution, stations, maintenance, and facilities. A work breakdown structure for the entire transportation system was prepared by Parsons Brinckerhoff and can be seen in a paper by Deutsch [3]. It includes estimates of all of the capital costs of the transportation system. The design of the vehicles is of primary importance to the rail companies offering MAGLEV service. The overall system costs will be seen by these companies as user fees. The vehicle design does impact the cost of the system as a whole although these relationships are out of the scope of this work. For example, lower vehicle weight can impact the cost of the guideway structure. Bohlke [25] discusses guideway costs and shows some studies looking at the effect of span between guideway supports on the cost.

The acquisition cost of the MAGLEV vehicle is the total cost involved in creating the vehicles. This includes the cost of producing the vehicle structure, the furnishings, HVAC, levitation and guidance systems, propulsion, control systems, communications, breaking system, and on board power supply (APU). Information is not available on the costs of most of these components. Since they are present on any vehicle design, this model concerns itself with only the structural costs. The cost of

the structure is a function of the vehicle shape and complexity, materials used, manufacturing processes chosen, and company procedures dealing with the use of different production facilities.

The different types of cost models are discussed in a paper by Rais-Rohani [32]. The two main categories of models are the Parametric Cost Models (PCM) and the Manufacturing Process Cost Model (MPCM). Parametric cost models are cost equations based on design variables as arguments. Weight engineering models fall into this category. These models are easy to use, although they are not very accurate. They ignore product and process complexity and depend upon a database of past cases. Cost accrued from cost drivers not present in the database cases will not be predicted by the model. These models are good to use in the conceptual design phase, since accuracy requirements are lower and not much is know about the vehicle in question.

Manufacturing process cost models include more detail about the materials and manufacturing processes used. They also address labor, time, and assembly. These models have higher accuracy than the PCM models, although they require much more information to build. This information may not be available at the conceptual or preliminary stages of a design process. Costs are accumulated on a process level giving these models the higher accuracy and sensitivity. Gutowski [65] refers to these types of models as primitive task models, since the whole manufacturing process is broken down to a collection of elementary activities which incur costs that add up to the whole. These activity based models require information from manufacturing process planning records, bills of material, and accounting records. This information is difficult to obtain for a company outsider since it is the source of a company's competitive advantage. Detailed knowledge of a company's cost is usually proprietary information, since it enables them to be competitive via aggressive pricing.

The optimization design undertaken in this work is a conceptual design so there is little detailed information available which would be necessary for the use of an MPCM. This information would include stringer and longeron spacing and surface skin panel size and shape. In addition to this, there have been no production level MAGLEV vehicles from which to construct a database for a PCM. As an interim model, this

work employs RAND corporation's DACPA IV model for transport aircraft [66]. This model is a parametric cost model which describes the cost of an aircraft as a function of the vehicle size, structural materials, gross vehicle weight, and cruising speed. As was done for the structural weight model, we assume that the MAGLEV vehicle structure is similar to that of a transport aircraft. In addition to that, we assume that similar manufacturing processes will be used to build the MAGLEV vehicle as are used for transport aircraft. The database used to construct the DACPA IV model is constructed from aircraft with specifications shown below.

$$\begin{aligned} \text{Empty Weight} &: 9753 - 320085(lbf) \\ \text{Maximum Speed} &: 389 - 1250(kn) \\ \text{No. of Flight Test Vehicles} &: 10 - 33 \end{aligned}$$

The MAGLEV application is out of range for the maximum speed and the number of flight test vehicles (low for both categories).

The total acquisition cost predicted by the DACPA IV model includes the engineering cost, tooling cost, manufacturing cost, quality control cost, development cost, test cost, and materials cost. The engineering cost is a function of the empty weight, velocity, quantity of vehicles, and an engineering labor rate. The tooling cost is a function of the empty weight, velocity, quantity of vehicles, and a tooling labor rate. The manufacturing cost is a function of the empty weight, velocity, quantity of vehicles, and a manufacturing labor rate. The quality control cost is a function of the empty weight, velocity, quantity of vehicles, and a quality control labor rate. The development cost is a function of only the empty weight and velocity. The test cost is a function of the empty weight, velocity, and number of test vehicles, while the material cost is a function of empty weight, velocity and total number of vehicles. The actual aircraft cost model includes the engine and avionics cost. This part of the model was not used here. Replacement costs for MAGLEV specific items were not included, since this information is unavailable. All of the cost predictions are in 1986 dollars and are not adjusted. The model is run for a 100 vehicle fleet and 2 test vehicles. The labor rates are shown below.

$$\text{Engineering Labor Rate} = \$59.10/hr$$

$$\begin{aligned} \text{Tooling Labor Rate} &= \$60.70/hr \\ \text{Quality Control Labor Rate} &= \$55.40/hr \\ \text{Manufacturing labor Rate} &= \$50.10/hr \end{aligned}$$

Vehicle cost modifiers can be applied to account for materials. The cost modifier is 1.0 for an aluminum structure and 1.1 for composite structures. The acquisition cost model resides in the same subroutine that calculates the life cycle cost. This can be seen in Appendix E. As was previously mentioned, parametric models have low sensitivity and cannot predict outside of the realm of the vehicles used for the database. This analysis will, therefore, neglect costs incurred by some of the detailed MAGLEV design geometries. Acquisition cost will vary little from design to design.

Chapter 5

Direct Operating Cost Model

The direct operating cost model calculates the direct operating costs as a function of the mission profile, vehicle gross weight, energy costs, and aerodynamic coefficients. Excluded are the costs associated with operating personnel, support infrastructure, charges on the guideway installation cost , maintenance, and terminal operations, since these costs are fixed with respect to changes in the vehicle shape design. Costs associated with longitudinal trim and guidance are also excluded. All of the assumed parameters involved in this model were taken from feasibility studies on MAGLEV vehicles [3] [6].

The operating cost model calculates the force required to levitate and propel the vehicle for the duration of its mission. The vehicle weight is provided by the structures model, and the aerodynamic coefficients are provided by the aerodynamics model. The required magnetic lift is the aerodynamic lift subtracted from the vehicle weight. The force to be put out by the magnets is this term divided by the $\cos 35^o$ since the magnets are angled to provide both lift and lateral guidance. The levitation power required is calculated as the product of the system current and voltage. The current is given as a function of levitation force in the final report of the government MAGLEV system assessment team [6]. The voltage is a constant. The power required to overcome the aerodynamic drag is the product of the drag force and the vehicle speed. This value is divided by the system efficiency which is nearly 1.0 for the linear synchronous motor and 0.82 for the converter station. Magnetic drag is not accounted

for here, since it is small compared to aerodynamic drag at cruise speed [6]. Magnetic drag becomes predominate at lower speeds. The total power required is the combined power for propulsion, levitation, and auxiliary power. The auxiliary power is that for the superconducting magnets, cooling system, HVAC, and lighting. The total power is multiplied by the trip time to give the energy requirements for the trip. The energy costs are calculated using the consumption charges and demand charges used in the feasibility studies [3] [17] [27].

The vehicle mission profile is that of an 800 kilometer trip at $134\frac{m}{s}$ ($300mph$). There are no intermediate stops, and it is assumed that the vehicle travels at its cruise speed over the entire trip distance (no acceleration or deceleration). The system is operational 16 hours per day, 365 days per year. Fifty person vehicles are used with an average passenger load of 2000 per hour. The auxiliary power required is 85 kw and is constant over the entire speed range. The assumed electric charges are $\$0.05/kwh$. The assumed electric demand charges are $\$7.50/kw$ and are accrued monthly.

The inclusion of energy costs in the multidisciplinary conceptual and preliminary designs is important for several reasons. Analyzing technical performance may lead the designer to designs with lower energy consumption, although no consideration is given to the efficiency of the energy source. Herbst [64] cites an example pertaining to the comparison of MAGLEV vehicles to aircraft. A MAGLEV vehicle might require less energy to complete a similar mission as an aircraft although its energy source (Rankine cycle power plant) operates at a lower efficiency than the energy source for the aircraft (Brayton cycle engine). The use of operating cost as a figure of merit for these vehicle designs accounts for this efficiency and serves as a uniform measure for operating performance. As for the fixed operating costs which this model ignores, Deutsch [3] estimates the personnel and material costs to be $49 million per year and $48 million per year respectively. Deutsch also estimates the energy costs (variable) to be $172 million per year. This number is very close to the yearly energy costs calculated by this operating cost model for typical designs. The subroutine for the direct operating cost model can be found in Appendix E.

Chapter 6

Life Cycle Cost Model

The definition of life cycle costs is all of the cost incurred from the conceptual design phase, production and deployment of the system, through to the retirement and disposal of the system. The consideration of the "cradle to grave" costs in the design process is crucial to the determination of long term profitability of the MAGLEV transportation system. The life cycle cost can be viewed as the equivalent value of the system cash flow over the lifespan at some zero time. For the comparison of alternatives with similar lives, one can use either a present worth method or a capitalized cost method. The present worth method is the calculation of a net present worth of the system and is used for the comparison of alternatives with finite lives. The work presented here uses this type of calculation. For systems with infinite horizons, capitalized cost methods are used in which the life cycle cost is the amount of money needed at a zero time to perpetually support the system using only the earned interest. The MAGLEV vehicles are analyzed here for a finite life, although a capitalized cost approach may be warranted if system life extensions are expected.

As was mentioned, this model is a present worth method in which the life cycle cost is presented as a net present value of the system cash flow over the lifespan of the system via a discounted cash flow analysis. This model does not include fixed costs, since we are looking here at making design decisions for vehicle shape based on its effect on the overall system performance. These fixed costs include the development cost, disposal costs, fixed direct operating costs, indirect operating costs, etc. Such

costs, along with stations and guideway costs, must be included when analyzing the transportation system as a whole for comparison with other modes of transportation.

The variable costs associated with changes in the vehicle shape design are the investment cost (acquisition) and the discounted operating cost. The investment cost is provided by the acquisition cost model, and the yearly operating cost is provided by the direct operating cost model. Several assumptions are made concerning the system economics. The lifespan is set at 15 years. Over this time, the average inflation rate is 3% per annum, the interest rate (return on investment) is 6% per annum, the tax rate is 50%, and the growth in traffic is 4% per annum. These values were taken from Ref. [17] which is part of the Grumman system concept definition. This model also has a revenue stream which is not employed for the studies performed as part of this work. Estimates for the fixed costs can be obtained from the work breakdown structure for the Grumman system. This can be seen in Ref. [3] prepared by Parsons Brinkerhoff. Their estimate for total capital cost amounts to $12302 per meter of track (the work breakdown structure was prepared for a 1000 km track system). Of this total, $7934 per meter is associated with the guideway, $1836 with the electrical, communications, and control for the system, and $882 with buildings and equipment (including stations). Their estimate for the vehicle cost is $1650 per meter, although these costs are variable with respect to the design variables of this multidisciplinary design.

The use of life cycle cost as a figure of merit is necessary to compare the designs based on performance and cost components. Life cycle cost is a universal figure of merit including all of the lower level objectives and indicators. It balances the initial capital investment with the annual costs associated with operating the system.

Chapter 7

MDO Problem Statement

To demonstrate the effectiveness of this design tool, we will perform a sample problem with five design variables. For the purpose of comparison, a portion of the Northrop Grumman MAGLEV design process [28] was redone here using this MDO methodology. Northrop Grumman was one of four companies contracted by the National MAGLEV Initiative (NMI) to develop vehicle designs. For the aerodynamic design they developed a design methodology geared towards minimizing aerodynamic drag using RANS as an analysis tool. They began with over 2000 2-D side view geometries and a separate set of 2-D plan view geometries. The side view geometry definition can be seen in the Fig. 7.1 in terms of the design variables [28]. The design variables are XN, XF, θ, N, and F. L is fixed at 6.0 meters and H is fixed at 3.5 meters. A 12.0 meter long parallel section separates the vehicle nose from its identical tail. This identical nose and tail provide for dual direction capability.

According to the Grumman selection process, fourteen of the 2-D side view geometries were chosen by the designers to represent the whole design space. 2-D RANS calculations were performed for the out of ground effect case, and five side view geometries were chosen based on minimum drag. RANS calculations were then performed on these five geometries for the IGE case. From these five side view geometries, 3-D geometries were constructed using the 2-D plan view designs chosen from a separate selection process. The design process continued using 3-D RANS calculations and the five final designs were chosen for experimental evaluation in the Virginia Tech

moving track wind tunnel facility [8] [67].

The five design variable problem dealt with in this work repeats the 2-D, side view design using the MDO design methodology, minimizing drag coefficient. The optimum design is compared to the five 2-D side view designs developed using the Northrop Grumman methodology. These five designs are shown in Fig. 7.2. Optimizations are also performed for additional figures of merit such as acquisition cost, operating cost, life cycle cost, empty weight, and lift to drag ratio. The mission profile for this example is that of an intercity haul of 800 kilometers non stop. The acceleration and braking are ignored for this example problem although it can be incorporated in future studies set at the maximum allowable normal mode value of 0.16g [5]. The analyses are performed for a single, 50 person car although the mission may call for a larger capacity.

The mathematical problem statement for a general optimization problem is, minimize the objective function, which is a function of n design variables, subject to m constraints (Eq. 7.1).

$$\begin{aligned} &\min \quad f(\mathbf{x}) \quad \mathbf{x} \in R^n \\ &\text{subject to} \quad \mathbf{l} \leq \mathbf{c}(\mathbf{x}) \leq \mathbf{u} \quad \mathbf{c} \in R^m \end{aligned} \tag{7.1}$$

Optimization methods fall into two major categories which are calculus-based methods and search methods. Calculus-based methods use gradient information to navigate through the design space to find local optimum points. This area of optimization technology is fairly mature compared to the search methods. These methods involve mathematical criteria to indicate convergence to an optimal point (Kuhn Tucker conditions). These methods have strong theoretical background and converge fairly quickly. Their weakness is that they require gradient information and, therefore, a differentiable design space. In addition to this, they do not search for global optima. There are iterative methods which attempt to find global optima, using calculus-based methods, although, there is no method to prove that the solution is a global optimum point [68].

Search methods available include genetic algorithms, simulated annealing, and

neural networks. These methods search for global optima and do not have smoothness requirements on the design space. Although, these methods cannot guarantee the convergence to a global optimum point, they are slow (require many analyses), and can only handle constraints using an augmented penalty function. The work presented here involves a calculus-based method called Sequential Quadratic Programming (SQP). This method was chosen since it is theoretically well founded, converges quickly, and involves a rigorous mathematical requirement for optimality.

Sequential Quadratic Programming is an optimization method for constrained optimizations with nonlinear constraints; it can handle linear constraints and unconstrained problems although methods specifically designed for those problems might be more efficient. In this method, at each iteration step, the optimizer attempts to minimize a quadratic model of the Lagrangian subject to a linear model of the constraints (quadratic subproblem). This problem can be stated as:

$$\begin{aligned} \min \quad & \mathbf{g}^T\mathbf{p} + \frac{1}{2}\mathbf{p}^T H\mathbf{p} \\ \text{subject to} \quad & \mathbf{l} \leq \mathbf{c}(\mathbf{x}) + A\mathbf{p} \leq \mathbf{u} \end{aligned} \tag{7.2}$$

The minimizing function is the linear and quadratic term of the Taylor Series expansion for the Lagrangian. The vector, $\mathbf{g}$, is the gradient of the objective function. The vector, $\mathbf{p}$, is the search direction, and the matrix, H, is an approximation to the Hessian of the Lagrangian. The matrix, A, is the Jacobian of the constraints. At each iteration, the optimality criteria are imposed in order to solve for a new search direction. This optimality criteria states that the gradient of the Lagrangian equals zero and that the constraints are satisfied (Eq. 7.3).

$$\begin{bmatrix} H_k & -A_k^T \\ A_k & 0 \end{bmatrix} \begin{Bmatrix} \mathbf{p}_k \\ \eta_k \end{Bmatrix} = \begin{Bmatrix} -\mathbf{g}_k \\ -\mathbf{c}_k \end{Bmatrix} \tag{7.3}$$

η is a vector of the Lagrange multipliers of the linearly constrained quadratic subproblem. A detailed discussion of SQP methods and of optimization theory in general can be seen in Ref. [69]. A detailed discussion about the specific SQP algorithm used here can be found in the DOT users manual [70].

The 5 design variable problem uses the five geometry variables outlined in Fig. 7.1. The problem also involves two constraints. The first constraint requires XF to

be greater than or equal to XN. The second constraint requires the drag coefficient to be positive. This constraint is necessary to avoid areas in the design space where the aerodynamic model fails. For low-order methods, "kinks" in the surface can result in singularities and, therefore, very large negative pressure coefficients which could result in a thrust. These solutions are mathematically viable but physically unrealistic. This problem can also be lessened by choosing proper bounds on the design variables.

A 7 design variable problem is adopted as an alternative way to perform the optimizations. The reasons for this higher dimensional problem and the benefits of this change in the problem statement will be discussed in the Results section. The problem formulation requires 7 constraints and a separate scaling scheme.

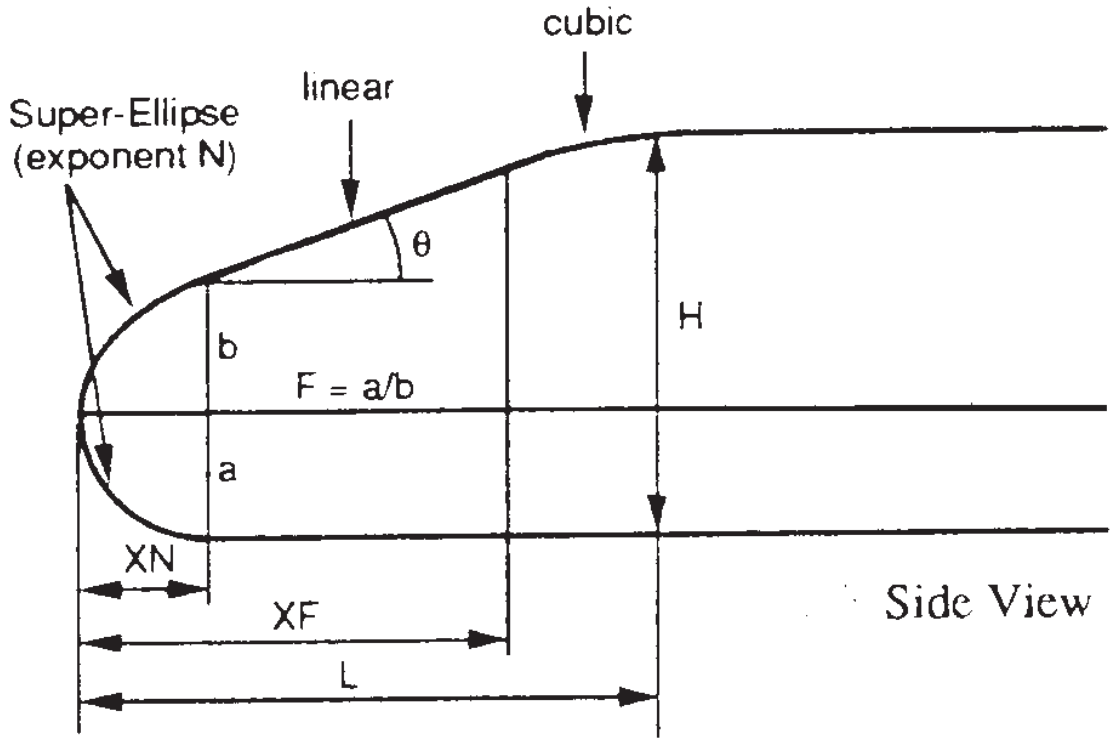

Figure 7.1: Geometry Definition [28]

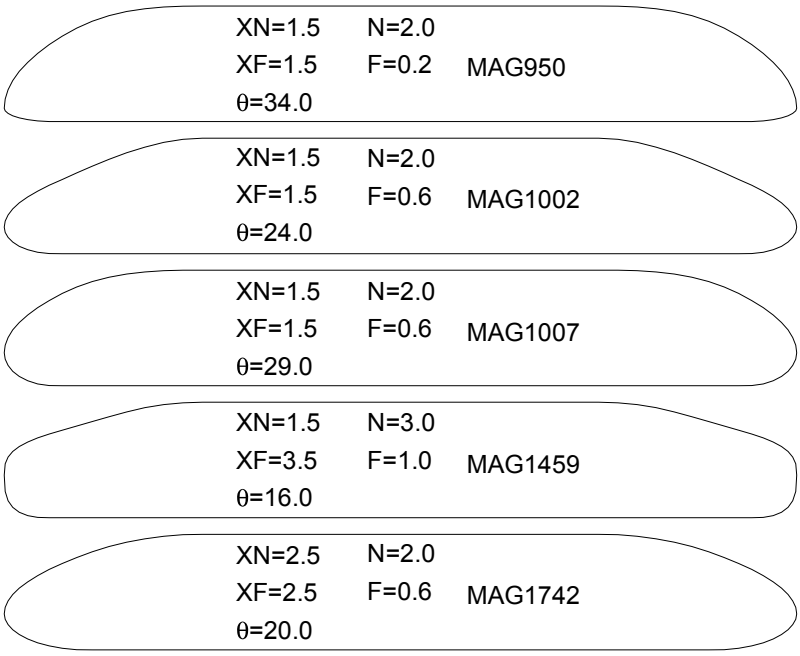

Figure 7.2: Northrop Grumman 2-D Side View Designs

Chapter 8

Results

This section deals with the results from the optimization design studies performed using the design methodology for the 2-D, side view, MAGLEV vehicles in ground effect. We first discuss the 5 design variable problem which turns out to be flawed due to a non-smooth design space. A higher dimensional problem with 7 design variables is then developed to combat the deficiency in the original formulation. Optimizations are then performed, using the 7 design variable problem for several objective functions. The designs and their attributes are discussed and compared to those from Northrop Grumman which were used as baseline designs for this study.

The 5 design variable problem uses the 5 geometry variables outlined in Fig. 7.1 and two constraints. The first constraint requires XF to be greater than XN, and the second constraint requires the drag coefficient to be positive, as discussed in Chapter 7. An optimization was performed using the Northrop Grumman MAG1007 as a baseline design. The SQP optimizer never hones in on an optimum point during the computation time allotted. This is due to the non-smooth design space which causes the SQP algorithm to take steps through the design space based on bad gradient information. Non-smooth design space is typical of real engineering problems and is a major obstacle in engineering design optimization. The bumps in the design space stem from the analyses of flow over bluff bodies. Small, continuous changes in the geometry definition variables can produce discontinuous values for the aerodynamic coefficients. This is mainly a result of movement of the separation points.

Figure 8.1 is a plot of the optimization with the MAG1007 baseline and drag coefficient as the objective function. The abscissa shows the design space index which steps one for every SQP iteration. This index does not indicate the search direction in the 5 dimensional space, nor does it indicate the length of each step. The total length traveled from the baseline to iteration number 15 is 3.41. The direct distance between the two points is 2.2. The optimization path is shown as a solid line with boxes indicating the discrete steps taken by the optimizer.

To illustrate the problem with the 5 design variable formulation, we can take a closer look at iteration number 12. The distance along the search direction from iteration 12 to iteration 13 is 0.0452. The step along this search direction results in a higher objective function. The actual design space along this step in the 5 dimensional search direction is shown with a dashed line. The section shown here is constructed using 20 evenly spaced steps along the search direction for a length twice that of the optimization step. The non-smooth nature of the design space is apparent. Using the gradient information obtained by finite differencing at iteration 12, along with the approximation for the Hessian of the Lagrangian, a quadratic model of the Lagrangian is formed. The quadratic model of the Lagrangian is shown in Fig. 8.1 as the dashed/dotted line. Based on the gradient information at iteration 12 as well as the build up of gradient information from passed iterations in the approximation to the Hessian, the optimizer thinks it is stepping in a direction which lowers the Lagrangian. There are no active constraints during this optimization, so a lowered Lagrangian should correspond to a lower objective function. Due to the violation of the smoothness requirement the quadratic subproblems are not representative of the actual design space in the region of the iteration.

In order to combat this deficiency with this formulation of the problem, it was instead reposed as a 7 design variable optimization. The two additional design variables are the locations of the top and bottom surface separation points. The aerodynamic forces are functions of the vehicle shape and the flow conditions (the 5 design variables and the Reynolds number). More exactly, the geometry and the free stream flow conditions determines the separation locations, and therefore the circulation, which determines the forces on the vehicle which are the integrated pressure and skin

friction over the surface.

According to this new formulation, these two separation locations are independent variables and not functions of the 5 original design variables as they once were. As independent variables they will most probably not match their correct value according to their functional dependence on the other variables and flow parameters. So, we are solving for flows in which the separation locations do not match the pressure field in hopes that this projected design space is smoother than that in 5 dimensions. Two equality constraints are then imposed which require each separation location to match the pressure field; the Stratford Criterion is imposed as a constraint [71]. Each equality constraint is enforced using two inequality constraints so this formulation adds four new constraints to the SQP problem. Optimization theory requires that the solution be feasible at the optimum point but allows for infeasible iteration steps along the way. The idea of projecting the design space in such a manner as to smooth out the design space was developed during personal conversations with Dr. Eugene Cliff. This formulation utilizes a seventh constraint which requires the flow to remain attached until reaching the aft end of the vehicle thereby avoiding designs which cannot be handled by the boundary layer calculation.

One problem associated with the implementation of this idea is that the objective function is a much stronger function of the separation locations than of the 5 geometry variables. If left as is, this formulation of the problem will result in optimizations requiring many SQP iterations. The separation locations which are strong variables will be changed much more than the geometry variables which are weak variables. Affine scaling is used to prevent this. This scaling is aimed at producing equal changes in the objective function for equal changes in each of the scaled design variables. Equation 8.1 shows the functional form of the scaling.

$$\mathbf{x} = \mathbf{NOM} + \mathrm{SCALE} \times \mathbf{Z} \tag{8.1}$$

The unscaled design variables, $\mathbf{x}$, are sent to the analyses while the scaled design variables, $\mathbf{Z}$, are sent to the optimizer. The ranges of the scaled design variables go from approximately 0.0 to 1.0 for the range of interest in the corresponding unscaled variables. The matrix, SCALE, is a diagonal matrix with the diagonal elements

corresponding to the value of the derivative of $\mathbf{x}$ with respect to $\mathbf{Z}$ that makes the coefficient of the linear term of the Taylor Series expansion of the objective function with respect to the scaled variables a constant (Eq. 8.2).

$$\begin{aligned} \text{OBJ} &= f(\mathbf{x}) \\ \text{OBJ} - \text{OBJ}_o &= \sum_{i=1}^{n} \frac{\partial f}{\partial Z_i} \Delta Z_i + \ldots \\ &= \sum_{i=1}^{n} \frac{\partial f}{\partial x_i} \frac{\partial x_i}{\partial Z_i} \Delta Z_i + \ldots \\ &= \sum_{i=1}^{n} \frac{\partial f}{\partial x_i} \text{SCALE}_i \Delta Z_i + \ldots \\ \frac{\partial f}{\partial x_i} \text{SCALE}_i &= \text{Constant for all i} \end{aligned} \tag{8.2}$$

Figure 8.2 shows the optimization path through the design space using this 7 design variable formulation. It is an equivalent plot to that shown in Fig. 8.1 for the 5 dimensional case. Again, we are looking at iteration number 12. The dark boxes indicate that the iteration step is at an infeasible point in the design space. The scaled length of the step in the search direction between iteration steps 12 and 13 is 0.5110. The objective function along this search direction in 7 dimensional space is shown as the dashed line for twice the length of the iteration step. The design space is much smoother than its 5 dimensional counterpart and will, therefore, be more conducive for finite differencing derivatives. The quadratic model of the Lagrangian along the search direction is shown in the dashed/dotted line. The quadratic model of the Lagrangian increases as does the objective function. Both iteration 12 and 13 are infeasible points, so there is at least one active constraint included in the Lagrangian. The quadratic model is developed using better gradient information and does a better job following the design space. The optimization is successfully completed after 18 iterations. The total length traveled through the design space from the baseline to the optimum point is 7.82, and the straight line distance between the two points in the 7 dimensional space is 0.50. The 7 design variable formulation has provided a projected design space which is navigable by calculus-based optimizers.

Another benefit of the 7 design variable formulation is that the CPU time required per analysis is reduced to approximately 1.5 minutes, down from 6.5 minutes on a

Silicon Graphics Power Challenge with an R8000 processor chip. By prescribing the separation locations and not letting them develop over time, the transient from the impulsive start is approximately 50 time steps shorter. Since the CPU time is approximately proportional to the square of the number of time steps, any reduction in the number of time steps taken will greatly shorten the computational time.

The 7 design variable formulation does have a drawback. The non-smooth design space was replaced with a smooth one and highly convex equality constraints. The two inequality constraints, forming the top separation point equality constraint, are prohibitive in finding a global optimum point. Figure 8.3 shows a set of analyses between two optimum drag coefficient points. The first point was arrived at from a MAG950 baseline design while the second point was arrived at from a MAG1007 baseline. The search direction is a straight line from one point to the other in 7 dimensional space. The dotted line shows the equality constraint tolerance. Any constraint value within ± 0.03 is considered to be satisfied. The values of the constraints for the top and bottom separation points are shown in the dashed line. The top separation point constraint is highly convex and is violated for most of the space between these two optima along the straight path between the two points. The highly convex equality constraints result in a design space with many isolated, local optima i.e. a 7 dimensional "egg crate." Different starting points in the design space will lead to different optimum points. The two optimum points based on drag coefficient have objective functions with nearly the same magnitude (Fig. 8.3). In order to use this method as a design tool, one must optimize several times from different positions in the design space and make an engineering decision as to which design to accept. This is essential for the optimization problem here due to the nature of the design space and is good practice for any problem, since there is no mathematical proof for the convergence to a global optimum point. Improvements to this method might involve the development of another formulation which can provide the differentiable objective function without the inclusion of convex equality constraints.

Optimizations are performed for the objective functions of drag coefficient, lift to drag ratio, empty weight, vehicle cost, operating cost, and life cycle cost. All of these optimizations employ the 7 design variable problem formulation. The aerodynamic

analyses are performed for full-scale vehicles.

8.1 Optimum Drag Coefficient Designs

The optimizations for drag coefficient as the objective function were run from two different baselines - MAG950 and MAG1007. Figure 8.4 shows the baseline, MAG950, and the optimized drag coefficient design derived from it. The drag coefficient was reduced from 0.2025 to 0.0489. This 75.9% reduction is due to a 95.4% reduction in the base drag and a 1.43% reduction in the skin friction drag. The pressure coefficient plots for the the baseline and optimum points for this design are shown in Fig. 8.5.

Figure 8.6 shows the baseline, MAG1007, and the optimized drag coefficient design derived from it. This design is referred to as the OPTCD2 design and the MAG950 baseline design is referred to as the OPTCD1 design based solely on the order that the calculations were performed. This optimization results in an optimum point different from that of the OPTCD1 design. The drag coefficient is reduced from 0.1984 to 0.0424. This 78.6% reduction in the drag coefficient is due to a 99.2% reduction in the base drag and a 4.4% reduction in the skin friction drag. The pressure coefficient plots for the the baseline and optimum points for this design are shown in Fig. 8.7. The "blips" in the pressure coefficient profiles for the optimum designs are due to the panel spacing and quantity which are not adjusted during the optimization. Figure 8.8 shows the OPTCD2 pressure coefficient as calculated during the optimization and after the surface grid is refined. Improvements to this methodology might include automatic grid refinements during the optimization process.

Figure 8.9 shows a comparison of both optimum drag coefficient designs. The optimizations from the two different baseline designs resulted in two local optima with roughly the same objective function value. Both optimum designs are more blunt than their baselines and yet they achieve minimum drag coefficients. These designs exploit the ground effect phenomena to greatly reduce the base drag. As part of the lift reversal phenomena, the upstream stagnation point is pulled down to a lower position. A blunt nose quickly expands the flow producing a leading edge suction which offsets the base drag caused by flow separation. Figures 8.10 and

8.11 show the two minimum drag coefficient designs along with top surface pressure profiles for in and out of ground effect flow. The respective stagnation point locations are indicated. It is apparent that for ground effect flow these designs provide a large amount of expansion around the leading edge of the vehicle. The leading edge suction here may be slightly augmented due to the aerodynamics model. We can recall the calculations performed for the flow over an elliptic cylinder in ground effect (Fig. 2.31) where the vortex method predicts a larger shift in the attachment and separation point locations than is predicted using a Navier-Stokes CFD code.

For a point of comparison a design optimization was performed to minimize the drag coefficient while assuming an out of ground effect aerodynamic condition. This was performed to show the difference in the aerodynamics problem and the need to design specifically for ground effect flow. The optimization was performed from the MAG950 baseline. Figure 8.12 shows the baseline and the optimum design. This design shows a side view which is very close to being symmetric top to bottom. The asymmetric geometry definition prevents this from occurring. The drag coefficient for the out of ground effect flow was reduced from 0.1472 to 0.0510. The pressure coefficient plot in Fig. 8.13 shows the optimum drag coefficient design with higher base pressure than that of the baseline. In contrast to this design, the ground effect designs have a drooped nose and a blunt top surface used for the quick expansion of the top surface flow. The ground effect drag coefficient for this design is 0.1529, so the use of out of ground effect analyses for the design of ground effect vehicles is not advised.

Figure 8.14 shows a comparison of the two minimum drag coefficient designs to the five 2-D, side view designs from Northrop Grumman. All of these designs were evaluated based on drag coefficient as a figure of merit. The optimum designs are both blunt and resemble the Northrop Grumman MAG1459. As calculated here by the vortex panel method, the MAG1459 is the lowest drag coefficient design proposed by Northrop Grumman. As was calculated using a Navier-Stokes CFD code [28], the MAG1459 had the second lowest drag coefficient.

These optimizations resulted in changes to the other figures of merit which we are dealing with via separate optimizations. Both optimum drag coefficient designs

resulted in vehicles with slightly higher weight and, therefore, higher vehicle cost due to the weight engineering model. Due to the lower drag coefficients, both designs resulted in much lower operating costs and, therefore, lower life cycle cost. These designs will be compared to the designs based on the other figures of merit in a quantitative fashion in Section 8.6.

8.2 Maximum Lift to Drag Ratio Designs

Next, optimizations were performed to maximize the lift to drag ratio, because this ratio traditionally plays a major role in determining the efficiency and performance of aerospace vehicles. A high lift to drag ratio design can possibly lead to lower direct operating cost since less energy would be required to provide magnetic levitation and propulsion. Since optimizations are usually formulated in terms of a minimization problem this one was set up to minimize the ratio of drag to lift. For these calculations, four baselines are used; the MAG950, MAG1007, and the two minimum drag coefficient designs - OPTCD1 and OPTCD2. The optimization for the baseline MAG1007 resulted in an infeasible solution, so it is not shown here. The results of the other three optimizations are shown in Fig. 8.15. The solid lines represent the baseline designs and the dashed lines represent the optimum designs. The design from the MAG950 baseline results in a 63.9% increase in the lift to drag ratio from its baseline value of 17.09 to the optimum value of 28.01. The design from the OPTCD1 drag coefficient optimum baseline results in an assumed convergence due to a null search direction on the first iteration. The OPTCD1 drag coefficient optimum is also a local optimum point for the lift to drag ratio at a value of 68.03. The greatest value for lift to drag ratio was achieved with the OPTCD2 optimized drag coefficient point as a baseline. The lift to drag ratio was increased marginally from 83.33 to 84.75. This final design provides the greatest objective function found among the sampled local optima. It will be used in Section 8.6 as the design for maximum lift to drag ratio even though we have no mathematical proof that this design point is the global optimum point. A bar chart of the normalized lift to drag ratio can be seen in Fig. 8.16.

8.3 Optimum Operating Cost Designs

Optimizations for minimizing the operating cost were then performed for four baseline designs; the MAG950, MAG1007, and the two minimum drag coefficient designs - OPTCD1 and OPTCD2. The objective function is scaled due to the large magnitude of its values.

$$\text{OBJ} = \frac{|\text{Operating Cost}|}{1.0E^8} \tag{8.3}$$

The absolute value of the operating cost is taken, since its value is usually taken to be negative.

The four baseline designs and their resulting optima can be seen in Fig. 8.17. The solid lines represent the baseline designs and the dashed lines represent the optimum designs. The design based on the MAG950 baseline is similar to the corresponding design for lift to drag ratio in Fig. 8.15, and it actually has a higher lift to drag ratio (44.05). This is what provides the lower operating cost, since less energy is expended to lift and propel the vehicle. The maximum lift to drag ratio design does not exactly correspond to the minimum operating cost design, since the propulsion and levitation systems operate at different efficiencies and energy consumptions. In addition to this, the maximum lift to drag ratio design can have higher drag. The design from the MAG1007 baseline resulted in a 33.6% reduction in the operating costs. The design from the OPTCD1 optimized drag coefficient baseline results in an assumed convergence due to a null search direction on the first iteration. The lowest value for the operating cost resulted from the OPTCD2 optimized drag coefficient design baseline. The optimization takes one step to an infeasible design with a slightly higher objective function. The design is shown in Fig. 8.17 even though it is not feasible.

Figure 8.18 shows the normalized operating cost for the four optimizations discussed here. The MAG950 operating cost is used to normalize all of the values. It can be seen that all of the optimum points have similar values for the objective function. Due to the highly convex equality constraints in the design space, we are forced to make decisions concerning the best designs based on the completion of several calculations to find local optima. The lowest operating cost among these calculations is for the OPTCD2 optimized drag coefficient baseline design. This design will therefore

be used as the minimum operating cost design for the comparisons in Section 8.6.

8.4 Optimum Acquisition Cost Designs

Optimizations were performed to minimize the acquisition cost from the four baseline designs; the MAG950, MAG1007, and two optimized drag coefficient designs - OPTCD1 and OPTCD2. A scaled objective function is used due to the large magnitude of the acquisition cost.

$$\text{OBJ} = \frac{\text{Acquisition Cost}}{1.0E^7} \tag{8.4}$$

This acquisition cost is the cost of a single vehicle. The total investment cost is calculated as part of the life cycle cost calculation. The vehicle cost is directly proportional to the vehicle weight, so the minimum cost vehicle is also the minimum weight vehicle. These were presented previously as two separate figures of merit but are discussed here together due to the models used. According to the weight model, the minimum weight vehicle will have the minimum surface area, or length for a 2-D design. The design from the baseline MAG1007 in Fig. 8.19 provides the minimum acquisition cost, since it has the minimum surface length. The top and bottom surfaces of the nose are practically straight lines which gives the least surface length. This design provides a 0.08% reduction in the acquisition cost due to the 0.10% reduction in empty weight. The total range of vehicle weights is very small, and so, due to the weight engineering model, the vehicle cost is very insensitive to the design variables. This problem is discussed further in Chapter 4.

The minimum acquisition cost design provides minor improvements at the price of penalties in operating cost and life cycle cost. These penalties result from the poor aerodynamics of this minimum acquisition cost design ($C_D = 0.2305$). The operating cost increases by 4.3% and the life cycle cost increases by 0.8% (both increases are from nonoptimal values). Figure 8.19 also shows designs from the MAG950 and optimized drag coefficient design baselines. The MAG950 and optimized drag coefficient OPTCD1 baseline designs result in assumed convergence due to a null search direction on the first SQP iteration. The optimized drag coefficient OPTCD2 baseline

design moves slightly to reduce the vehicle cost by less than 0.005%. A bar chart of the normalized acquisition cost, referred to the MAG950 acquisition cost, for the four optimizations performed can be seen in Fig. 8.20. The ordinate ranges from 0.98 to 1.00, so the reader can detect the small differences in acquisition cost among the designs.

8.5 Optimum Life Cycle Cost Designs

Finally, life cycle cost optimizations were performed with a scaled objective function due to the large magnitudes of the life cycle cost.

$$\text{OBJ} = \frac{|\text{Life Cycle Cost}|}{1.0E^9} \tag{8.5}$$

The optimizations were performed from four baseline designs; the MAG950, MAG1007, and the two optimized drag coefficient designs - OPTCD1 and OPTCD2. The baselines and their respective optima can be seen in Fig. 8.21. The solid line represents the baseline and the dashed line represents the optimum design. Both of the optimized drag coefficient baseline designs resulted in null search directions and are, therefore, also local minimum life cycle designs. The optimization from the MAG950 baseline resulted in a 6.9% reduction in the life cycle cost and the optimization from the MAG1007 baseline resulted in a 7.1% reduction in the life cycle cost. All of the local optima have similar values of the objective function. This can be seen in Fig. 8.22 which shows the normalized life cycle cost for the four optimizations performed. The normalization was performed using the life cycle cost for the MAG950. The relatively small reduction in the life cycle cost (less than 10%) is due to the insensitive acquisition cost model. Improvements to this model will allow us to tap into a large component of the life cycle cost. The minimum life cycle cost design is that from the optimized drag coefficient design, OPTCD2.

8.6 Comparison of Designs for Various Figures of Merit

In the previous sections of this chapter, a single design was chosen from each to represent the optimum design for that figure of merit. In this section, these designs are compared to gain insight into the design problem and the workings of the MDO design methodology. Each of these optimum designs is not necessarily a global optimum point, since there is no way to prove convergence to such a point. In addition to this, the highly convex equality constraints precludes searching for a global optimum point.

The bar charts in Fig. 8.23 and 8.24 show a comparison of the designs based on different figures of merit. The designs are shown on the abscissa and are identified by the objective function optimized for each one. The optimum designs for the drag coefficient, operating cost, and life cycle cost are the same design. The maximum lift to drag ratio design is one arrived at from optimizing the minimum drag coefficient design to minimize the ratio of drag to lift. The minimum acquisition cost design is one arrived at by optimizing from the MAG1007 baseline. The MAG950 and MAG1007 baseline designs are also shown.

The drag coefficient for each of the optimized designs is shown at the top of Fig. 8.23. The optimum acquisition cost design has the highest drag coefficient, followed by the two baseline designs. The optimum drag coefficient, direct operating cost, and life cycle cost designs are the same design, and they, therefore, have the same attributes. These designs have nearly the same drag coefficient as the optimum lift to drag ratio design which has a marginally higher drag coefficient.

Also shown in Fig. 8.23 is a plot of the lift to drag ratio for the different designs. The lowest values of the lift to drag ratio are obtained by the baseline designs and the optimum acquisition cost design. The optimum lift to drag ratio design has a marginally greater ratio than the design with optimum drag coefficient, direct operating cost, and life cycle cost.

A plot of normalized direct operating cost can be seen at the top of Fig 8.24. The values are normalized using the MAG950, so it has a normalized cost of unity.

The baseline designs and the optimum acquisition cost design have the highest direct operating cost due their poor aerodynamic performance. The remaining designs have similar values for the direct operating cost. The optimized lift to drag ratio design actually has a slightly lower operating cost than the optimum operating cost design. Results such as this are entirely possible due to the convex equality constraints in the design space.

Figure 8.24 also shows plots for the acquisition cost and the life cycle cost, at the middle and the bottom. Both of these plots are normalized using the MAG950 values. The plot of normalized acquisition cost shows the ordinate from 0.980 to slightly higher than unity. This is done so that the reader can detect the slight differences in vehicle cost among the designs. The optimum acquisition cost design has a marginally lower acquisition cost. The optimum life cycle cost design shows a slightly less than 10.0% reduction in the life cycle cost. The optimum lift to drag ratio design has a slightly lower life cycle cost than the optimum life cycle cost design. This is due to the lower operating cost experienced by this design. The difference in the life cycle cost between these designs in indistinguishable on this plot and is almost certainly within the uncertainty on these cost models. Greater variation in designs and sensitivity to the design variables can be achieved with the use of a more advanced acquisition cost model. Table 8.1 shows the geometry variables for all of the optimum designs.

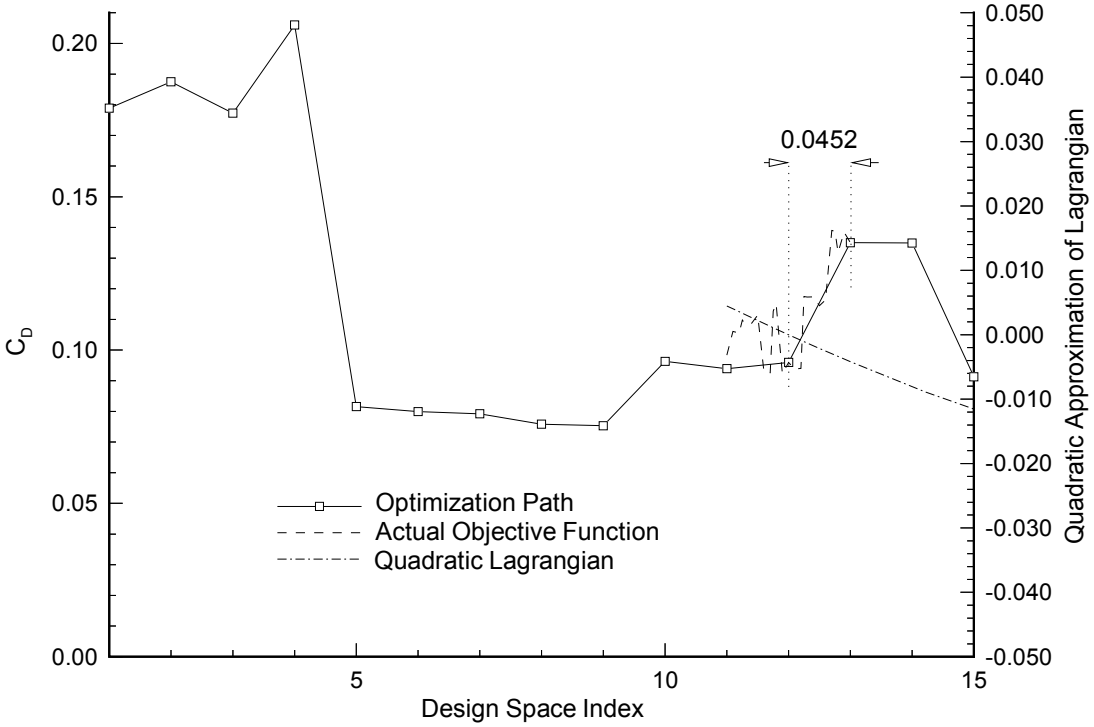

Figure 8.1: 5 Design Variable Optimization for Drag Coefficient

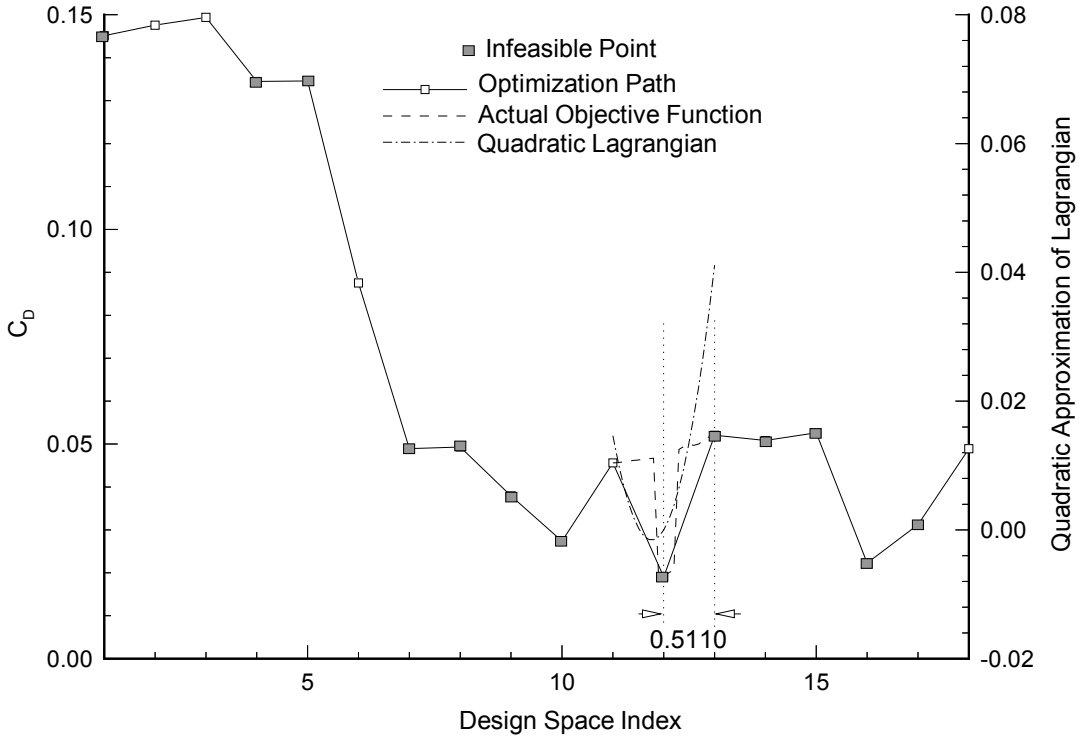

Figure 8.2: 7 Design Variable Optimization for Drag Coefficient

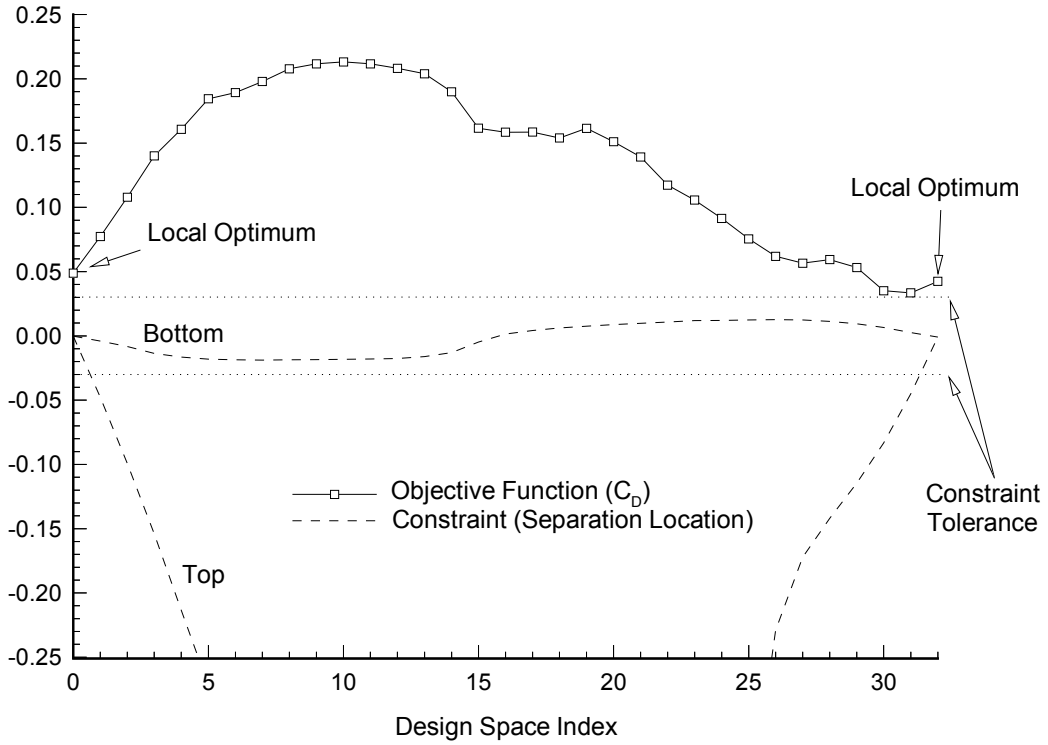

Figure 8.3: Design Space Between Local Drag Coefficient Optima; MAG950 at the Left End and MAG1007 at the Right End

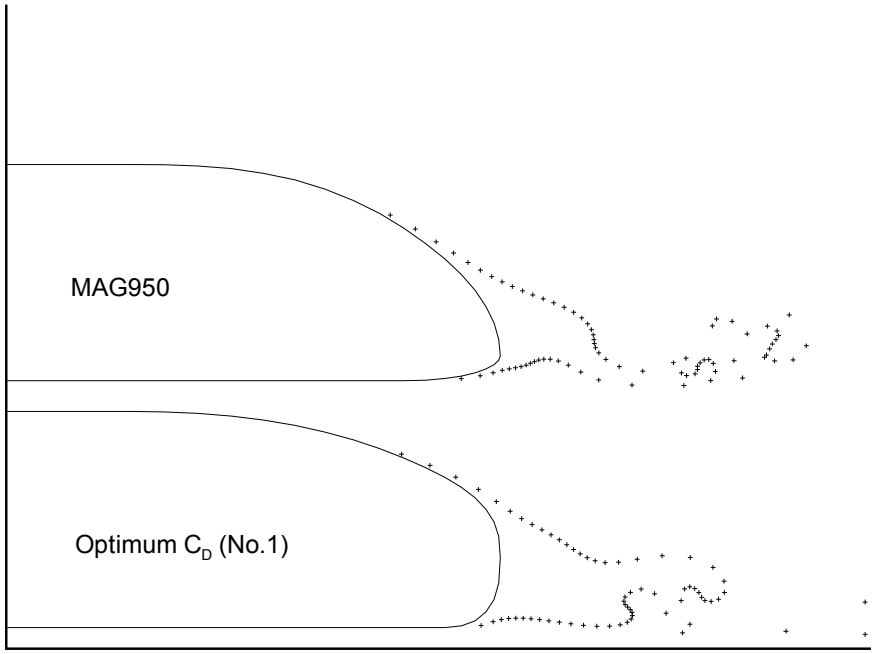

Figure 8.4: Optimum Drag Coefficient Design Using MAG950 Baseline

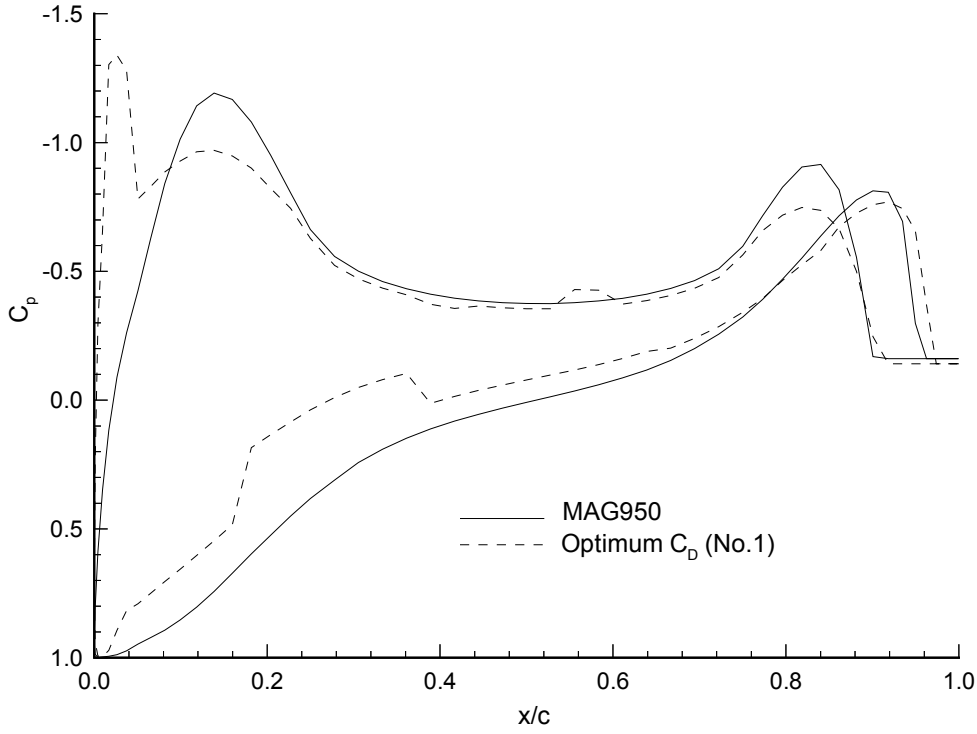

Figure 8.5: Pressure Coefficients for Optimum Drag Coefficient Design Compared to MAG950 Baseline

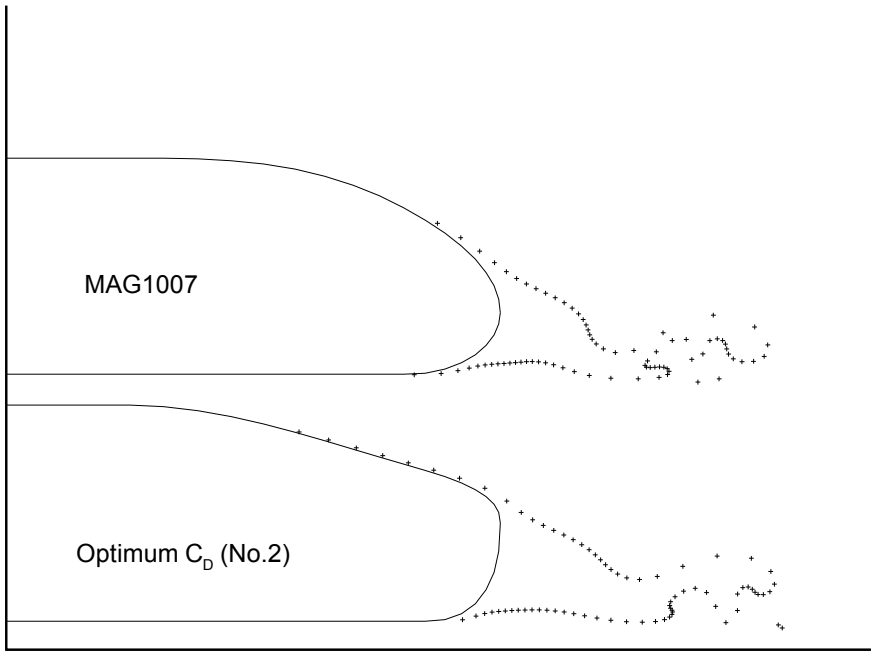

Figure 8.6: Optimum Drag Coefficient Design Using MAG1007 Baseline

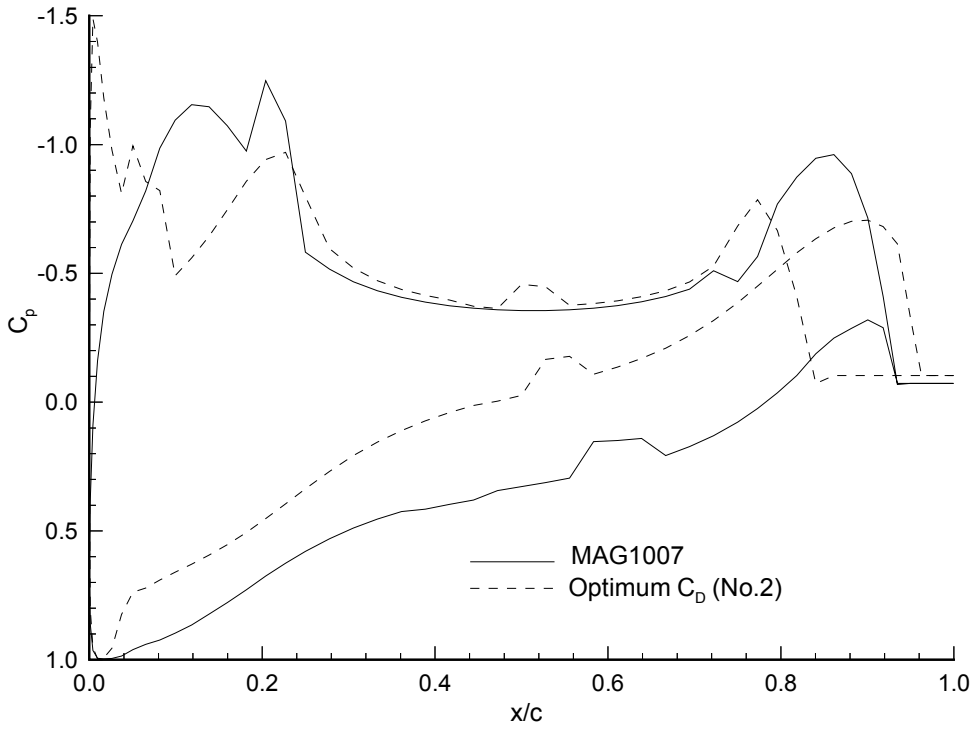

Figure 8.7: Pressure Coefficients for Optimum Drag Coefficient Design Compared to MAG1007 Baseline

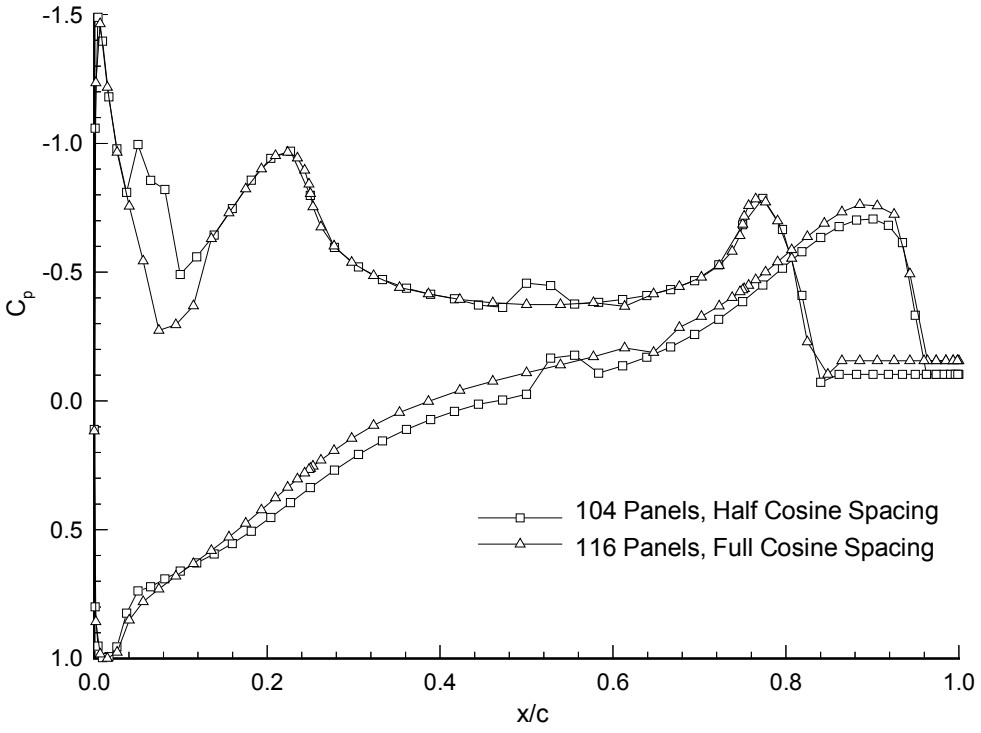

Figure 8.8: OPTCD2 Pressure Coefficient Predictions With and Without Panel Spacing Adjustments

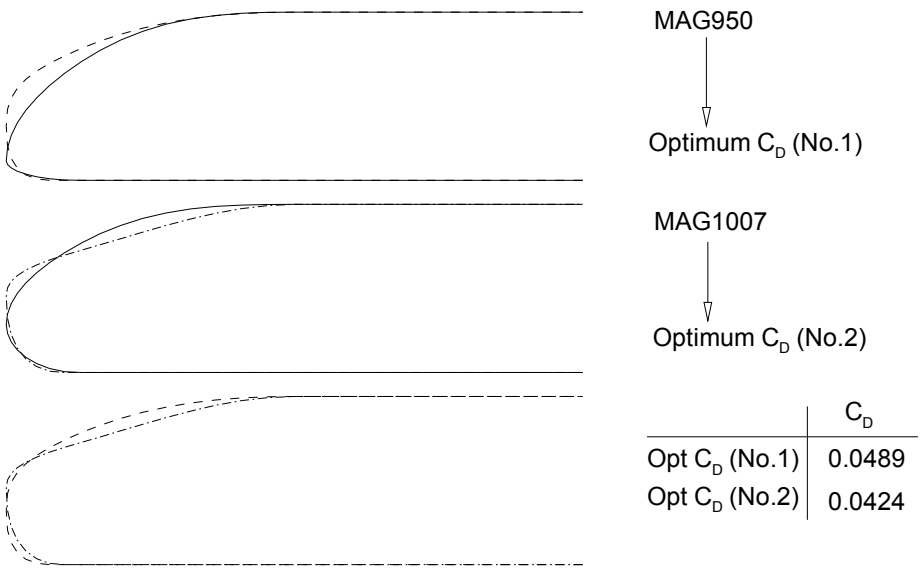

Figure 8.9: Comparison of Two Optimum Drag Coefficient Designs

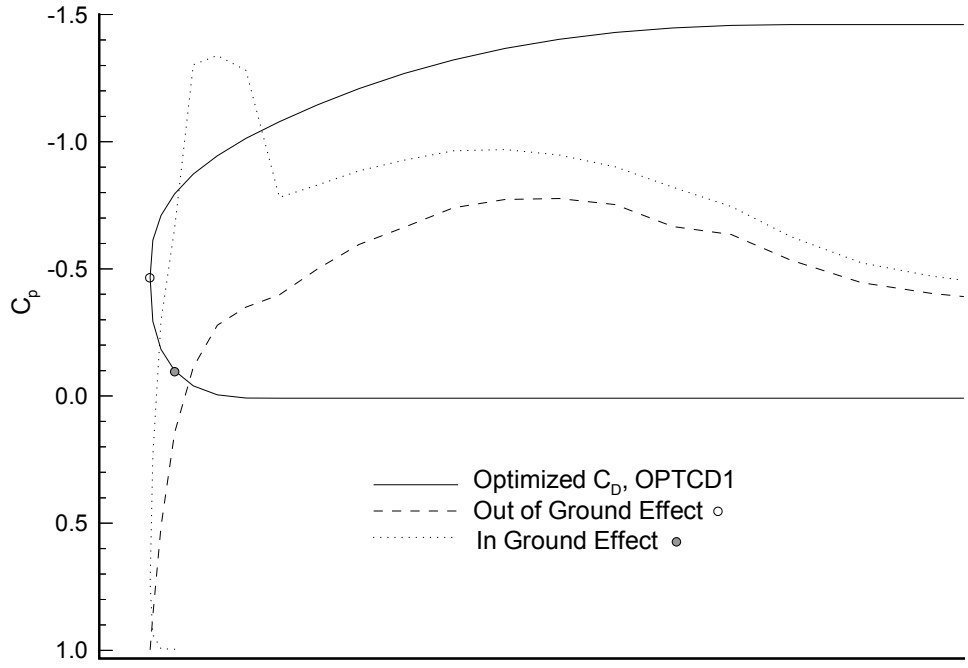

Figure 8.10: Leading Edge Suction Due to Ground Effect on Optimized Drag Coefficient Design, OPTCD1

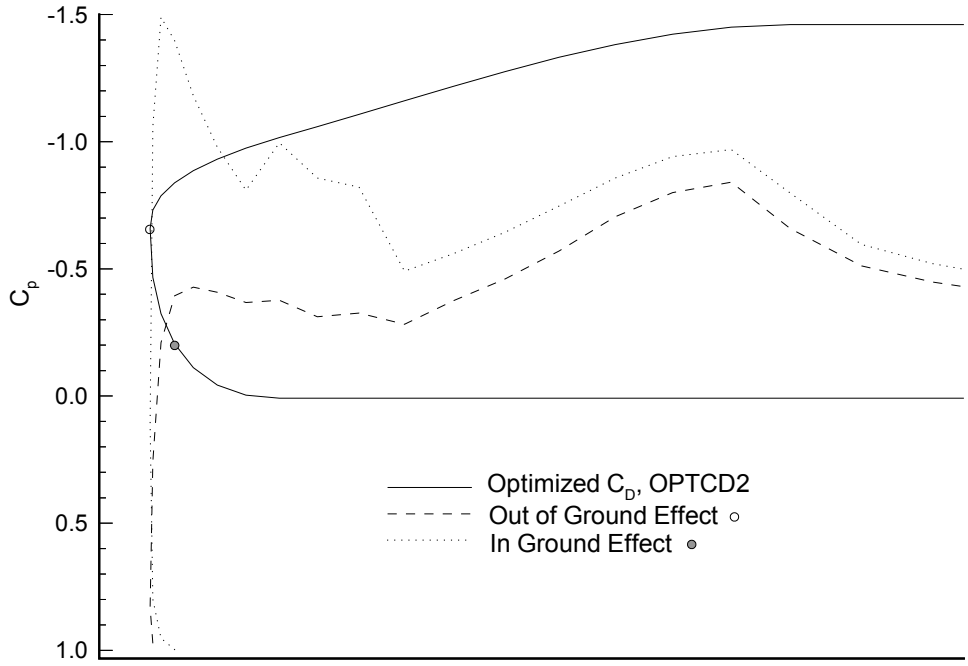

Figure 8.11: Leading Edge Suction Due to Ground Effect on Optimized Drag Coefficient Design, OPTCD2

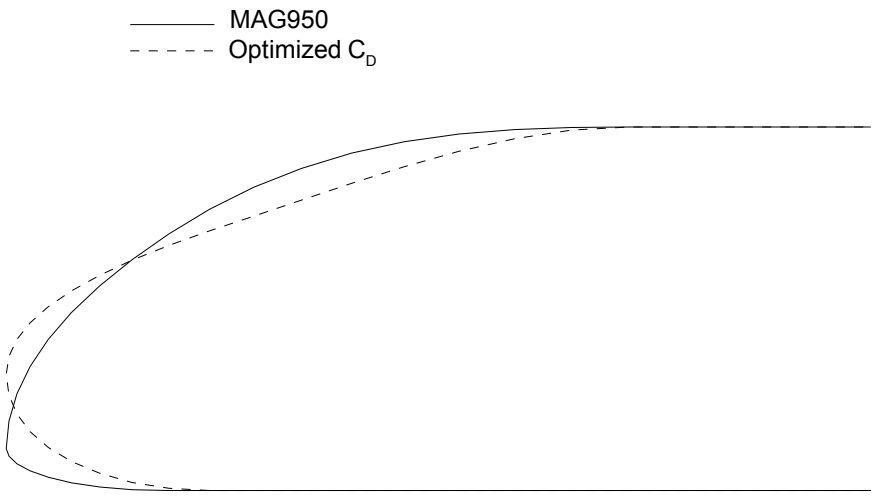

Figure 8.12: Optimum Drag Coefficient Design Using MAG950 Baseline for Out of Ground Effect Condition

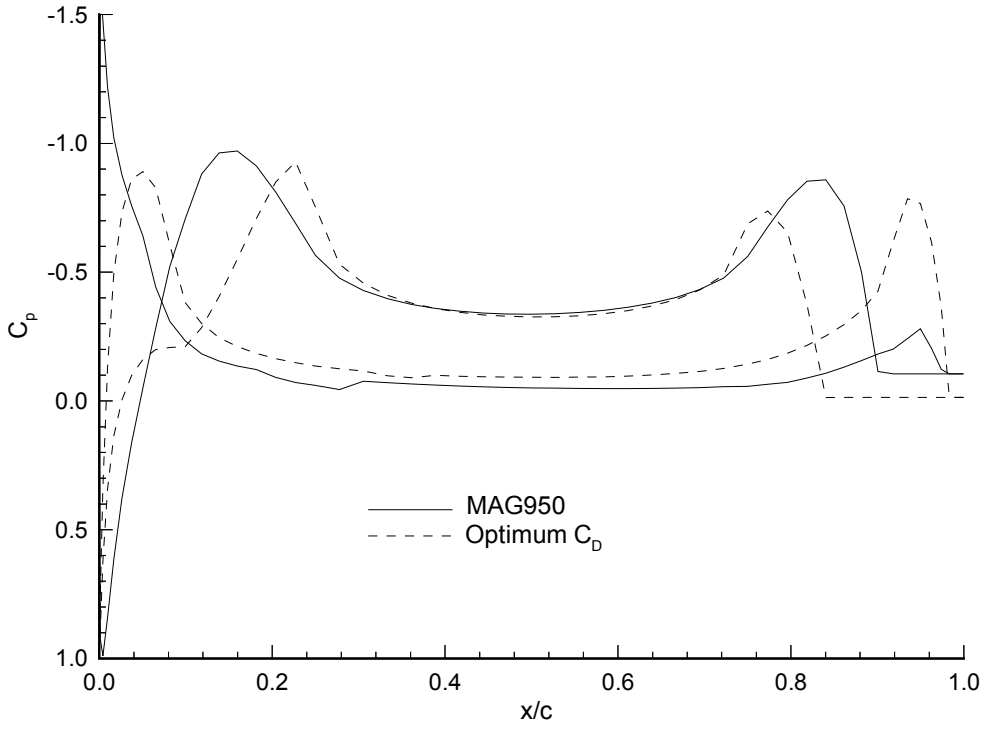

Figure 8.13: Pressure Coefficients for Optimum Drag Coefficient Design Operating Out of Ground Effect Compared to MAG950 Baseline

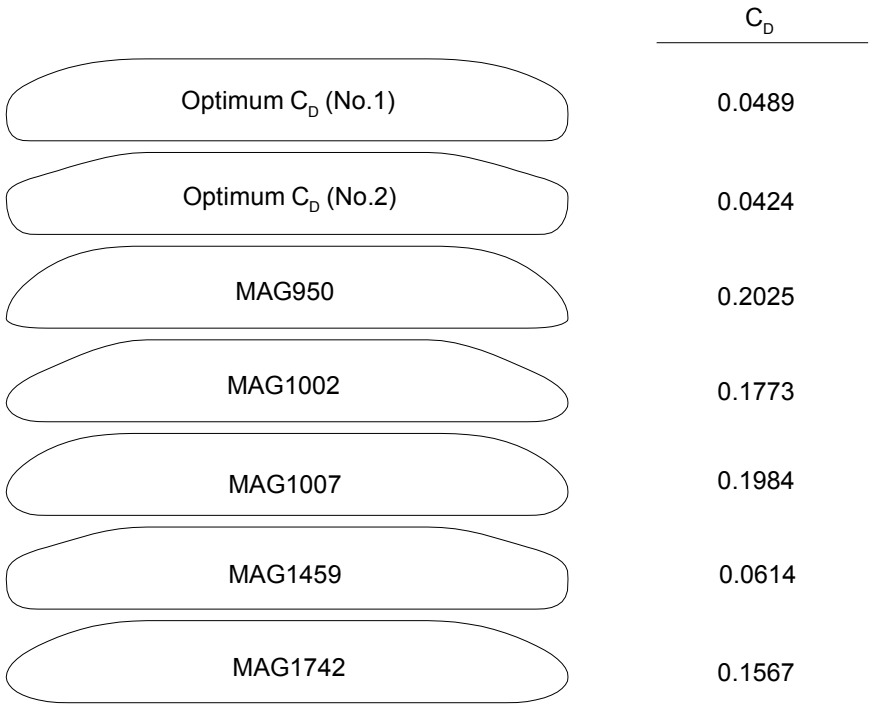

Figure 8.14: Optimized Drag Coefficient Designs vs. Northrop Grumman Designs

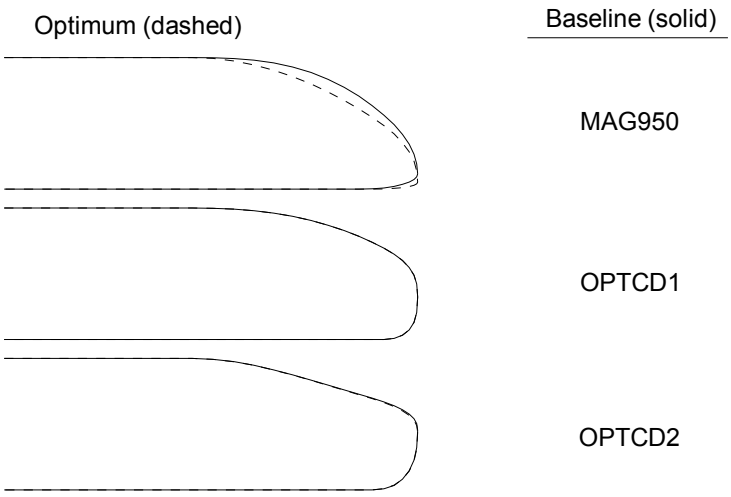

Figure 8.15: Maximum Lift to Drag Ratio Designs

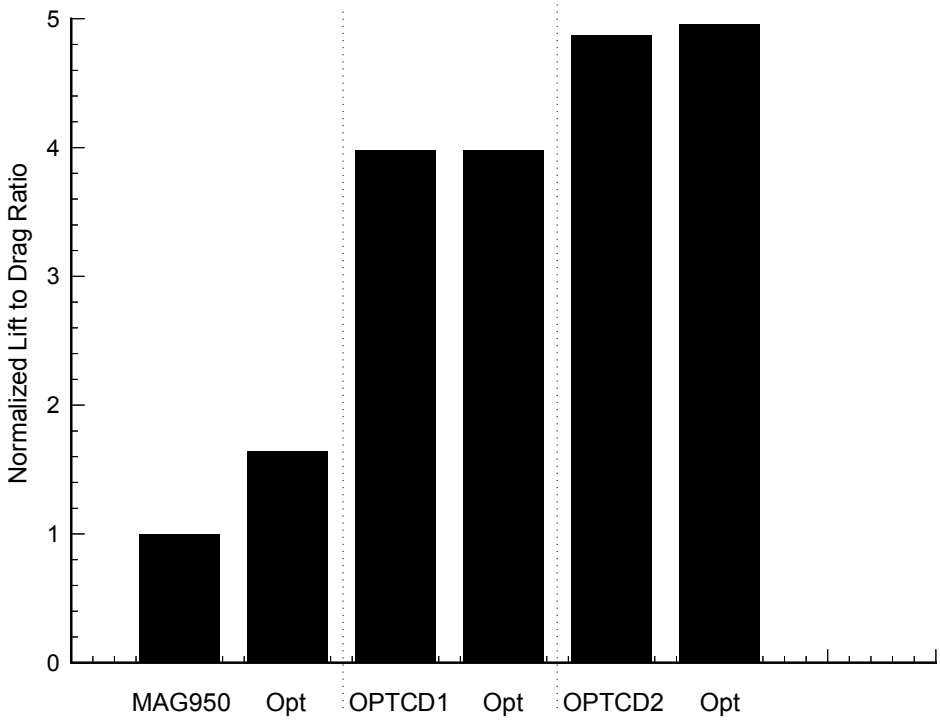

Figure 8.16: Comparison of Lift to Drag Ratio Designs

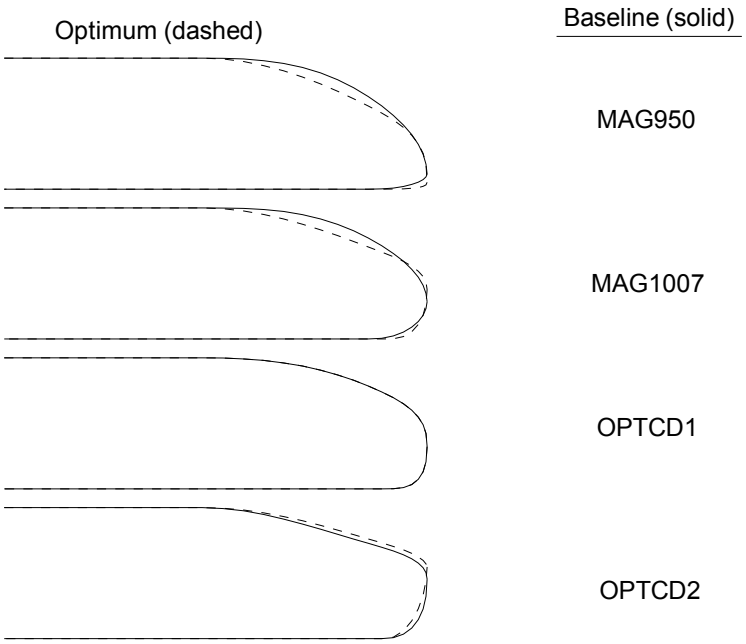

Figure 8.17: Minimum Operating Cost Designs

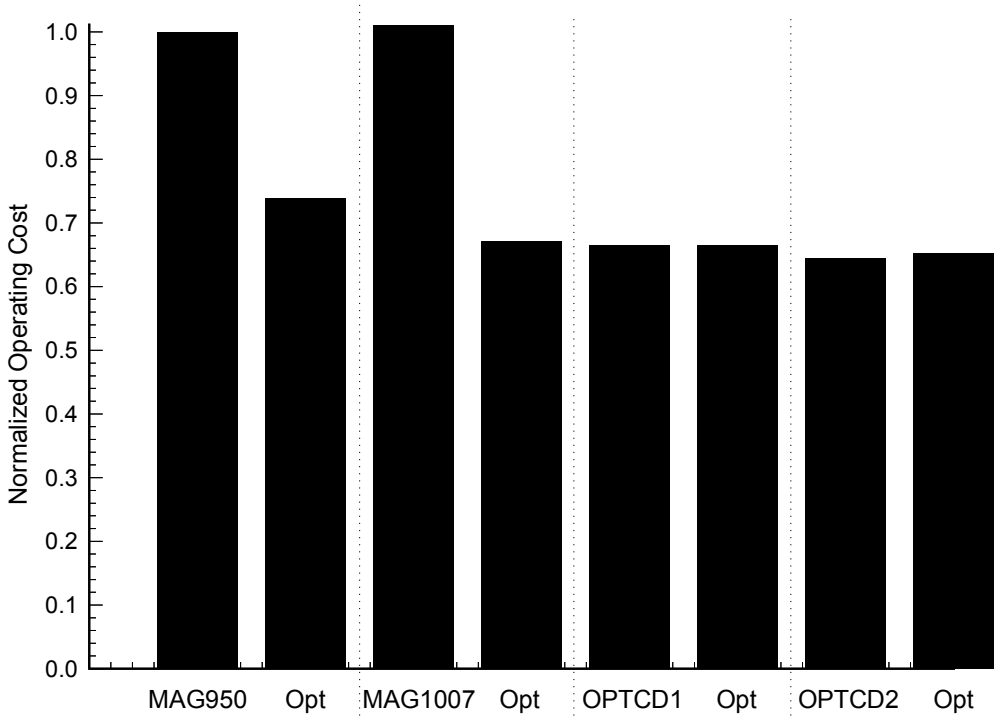

Figure 8.18: Comparison of Operating Cost Designs

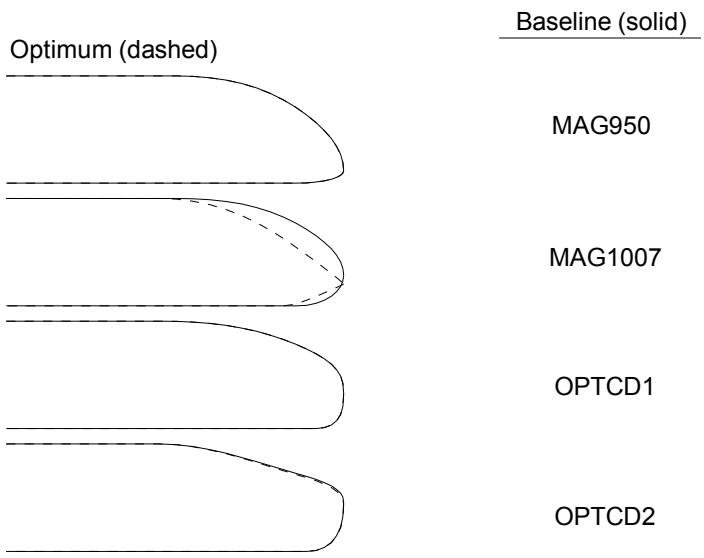

Figure 8.19: Minimum Acquisition Cost Designs

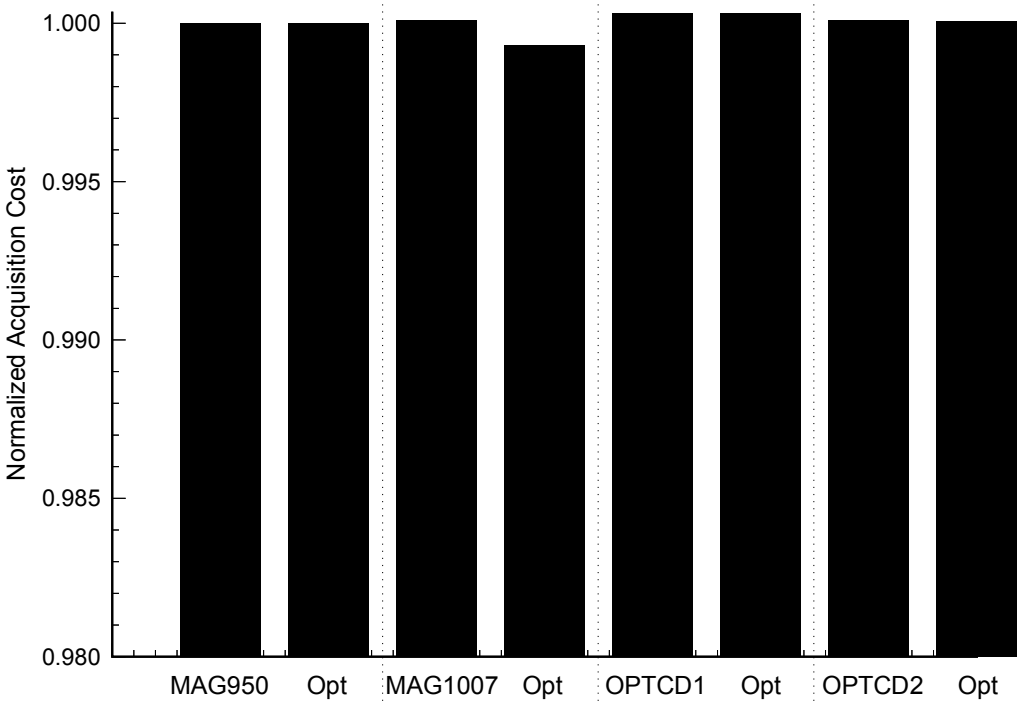

Figure 8.20: Comparison of Acquisition Cost Designs

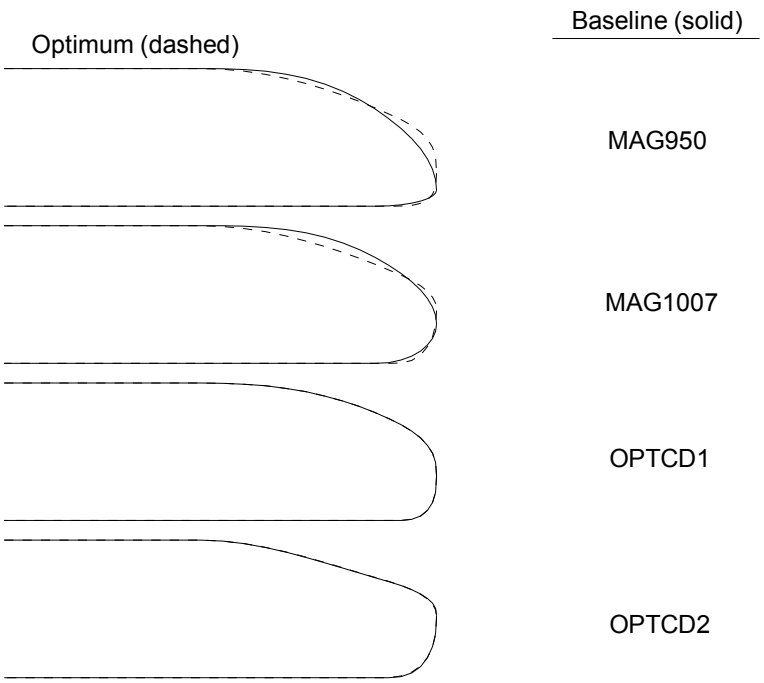

Figure 8.21: Minimum Life Cycle Cost Designs

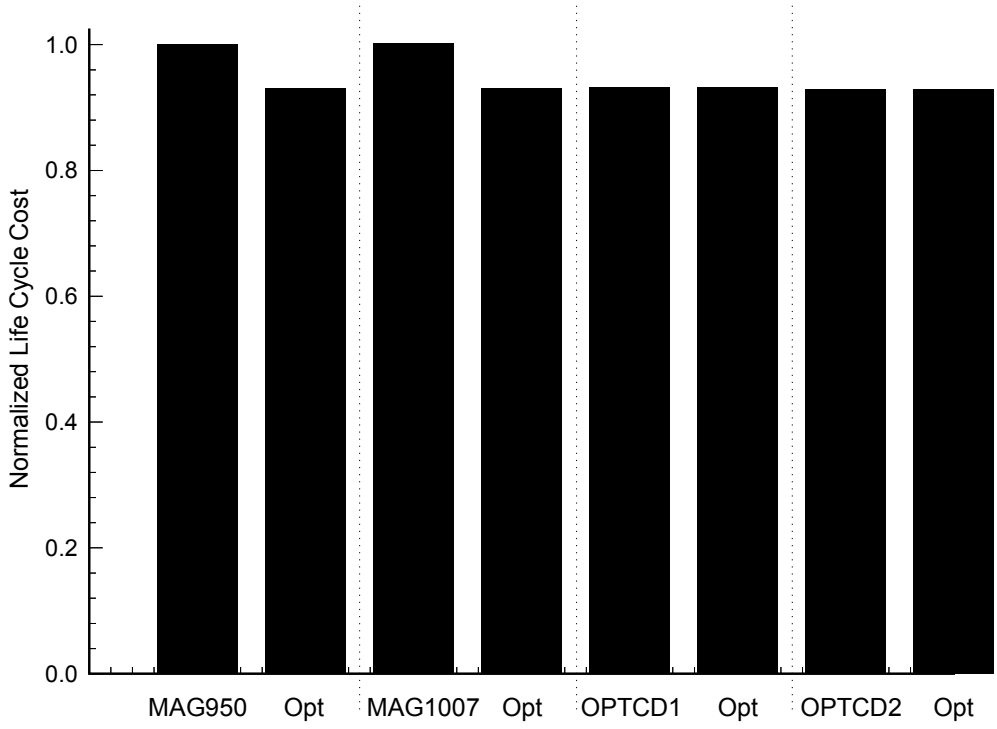

Figure 8.22: Comparison of Life Cycle Cost Designs

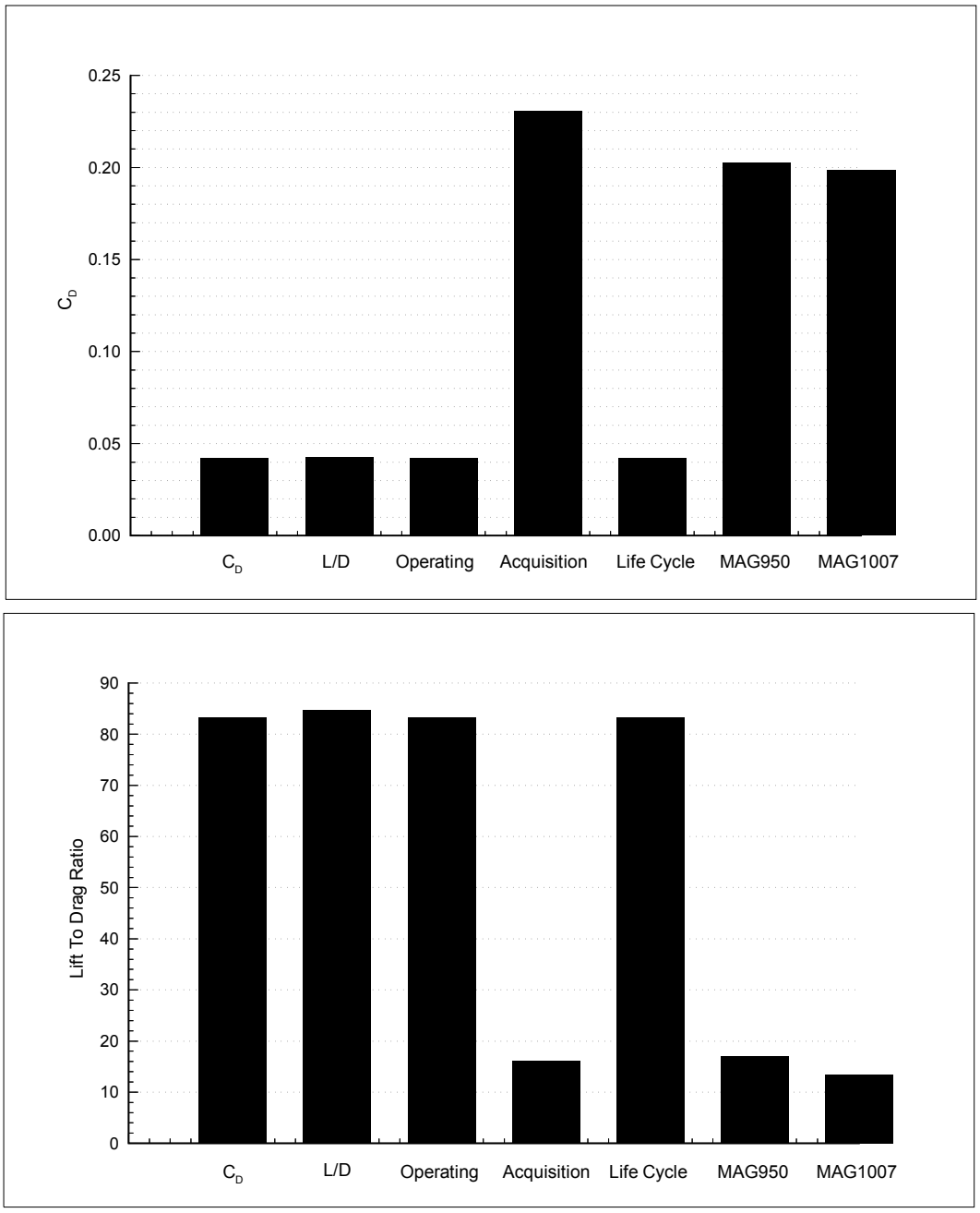

Figure 8.23: A Comparison of Drag Coefficient and Lift to Drag Ratio among Optimum Designs for Different Figures of Merit

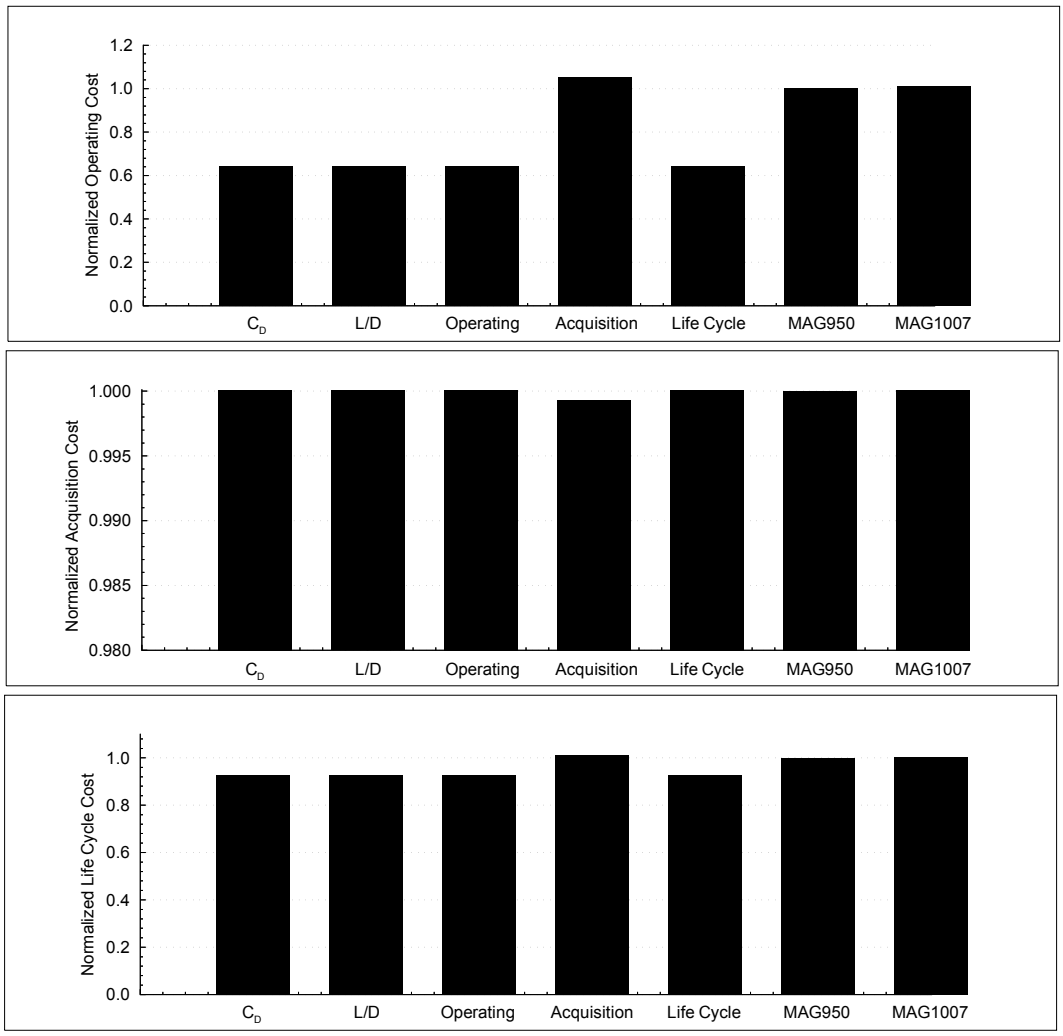

Figure 8.24: A Comparison of Operating Cost, Acquisition Cost, and Life Cycle Cost Among Optimum Designs for Different Figures of Merit

	C_D	L/D	DOC	Acq Cost	LCC	MAG950	MAG1007
XN	1.22	1.29	1.22	1.74	1.22	1.50	1.50
XF	1.61	1.63	1.61	1.78	1.61	1.50	1.50
θ	16.13	16.40	16.13	35.13	16.13	34.00	29.00
N	2.42	2.44	2.42	1.08	2.42	2.00	2.00
F	1.86	1.66	1.86	0.54	1.86	0.20	0.60

Table 8.1: Geometry Variables of Optimum Designs

shows significant and sensible differences between designing for minimum life cycle cost and other figures of merit. The minimum life cycle cost design is identical to that of the minimum direct operating cost and minimum drag designs. This showed the need for a more sensitive acquisition cost model which is not based on weight engineering. With one in place the minimum life cycle cost would be a balance between a low operating cost and low investment cost according to the economic factors chosen. The development and inclusion of such a model is necessary if continued work is to be done in this area. Other recommendations for future work can be seen below.

9.1 Recommendations for Future Work

The work presented in this dissertation is only the beginning of work that is needed in this area. The MDO methodology is developed in a modular fashion to better facilitate the update of the individual models. Future work should include the improvement of all of the analyses. Higher fidelity cost models are required, especially for the acquisition cost. The further development of low-order aerodynamic analyses should be continued for 3-D flow over bodies with boat tails. The lack of a 3-D flow separation model restricts such methods to flows over bodies with know separation locations, such as the boat tail bodies. The 3-D vortex panel method code should be extended for lifting flows on thick bodies. This should be pursued in order to eventually perform full 3-D configuration optimizations. Once this capability is achieved, higher dimensional optimization problems can be attempted. Future work should also be done to develop a problem formulation with smoother design space without adding highly convex equality constraints.

Bibliography

[1] "Current State of the Art On Multidisciplinary Design Optimization (MDO)." White paper, AIAA, September 1991.

[2] "The CoE Final Summary MAGLEV Report." Final report, US Army Corps of Engineers, 1995.

[3] Deutsch, L. "Maglev Cost and performance Parameters." In *Maglev 93 Conference*. Argonne National Laboratory, 1993.

[4] Tyll, J., Eaglesham, M., Schetz, J., Deisenroth, M., and Mook, D. "An MDO Design Methodology For The Concurrent Aerodynamic/Cost Design of MAGLEV Vehicles." *AIAA Paper No. 96-4036*, 1996.

[5] Whitten, B. T. "MAGLEV System Technical Requirements." Technical report, Ensco, Inc., Springfield, VA, July 1993.

[6] Lever, J. "Technical Assessment of MAGLEV System Concepts." Final report, US Army Cold Regions Research and Engineering Laboratory, Hanover, NH, March 1993.

[7] Stix, G. "Air Trains." *Scientific America*, 1992.

[8] Tyll, J., Liu, D., Schetz, J., and Marchman III, J. "Experimental Studies of MAGLEV Aerodynamics." *AIAA Journal*, 34, no. 12:2465, December 1996.

[9] Pulliam, W., Marshakov, A., Tyll, J., Schetz, J., and Marchman III, J. "Aerodynamics of the AMT MAGLEV Train Design." *AIAA Paper No. 96-2476*, 1996.

[10] *RTRI Home Page, http://www.rtri.or.jp/index.html*. 1997.

[11] Normile, D. "Maglev Floats Forward." *Popular Science*, p. 43, June 1997.

[12] Kaiden, T., Hosaka, S., and Mazda, T. "A Validation of Numerical Simulation With Field Testing of JR MAGLEV Vehicle."

[13] Shimbo, Y. and Hosaka, S. "Steady and Unsteady Pressure Measurement on High Speed Train."

[14] Miyakawa, J. and Hosaka, S. "Aerodynamic Design Of Frontal Shape For JR MAGLEV Train."

[15] Peters, J. "Aerodynamics of Very High Speed Trains and MAGLEV Vehicles: State of the Art and Future Potential." *Int. Journal of Vehicle Design, Special Publication SP3*, pp. 308–341, 1983.

[16] Merklinghaus, W. and Mnich, P. "The MAGLEV Transrapid System On The Way To Application -Test Results-." *IEEE*, pp. 211–218, 1987.

[17] Proise, M., Deutsch, L., Gran, R., Herbermann, R., Kalsi, S., and Shaw, P. "System Concept Definition of the Grumman Superconducting Electromagnetic Suspension (EMS) Maglev Design." In *Maglev 93 Conference*. Argonne National Laboratory, 1993.

[18] Gran, R. "Benefits of Magnetically Levitated High Speed Transportation for the United States." In *SAE Future Transportation Conference*, 1990.

[19] Gran, R. J. "The Benefits of MAGLEV Technology." *AIAA Paper No. 93-2949*, 1993.

[20] Kalsi, S., Herbermann, R., Falkowski, C., Hennessy, M., and Bourdillon, A. "Magnet Design Optimization for grumman Maglev Concept." In *Maglev 93 Conference*. Argonne National Laboratory, 1993.

[21] Kalsi, S. "On- Vehicle Power Generation at all Speeds for Electromagnetic Maglev Concept." In *Maglev 93 Conference*. Argonne National Laboratory, 1993.

[22] Herbermann, R. "Self Nulling Hybrid Maglev Suspension System." In *Maglev 93 Conference*. Argonne National Laboratory, 1993.

[23] Shaw, P. "Overview of Maglev Vehicle Structural Design Philosophy, Material Selection and manufacturing Approach." In *Maglev 93 Conference*. Argonne National Laboratory, 1993.

[24] Ende, R., Siclari, M., and Carpenter, G. "Aerodynamic Analysis of Grumman Maglev Vehicle." In *Maglev 93 Conference*. Argonne National Laboratory, 1993.

[25] Bohlke, B. and Burg, D. "Parametric Design and Cost Analysis for EMS Maglev Guideway." In *Maglev 93 Conference*. Argonne National Laboratory, 1993.

[26] Allen, J. and Ghali, M. "Innovative Spine Girder Guideway Design for Superconducting EMS Maglev System." In *Maglev 93 Conference*. Argonne National Laboratory, 1993.

[27] Gran, R. and Proise, M. "Five Degree of Freedom Analysis of the Grumman Superconducting Electromagnetic Maglev Vehicle Control/Guideway Interaction." In *Maglev 93 Conference*. Argonne National Laboratory, 1993.

[28] Siclari, M., Ende, R., and Carpenter, G. "The Application of Navier-Stokes Computations To The Design Of High-Speed, Low-Drag Magnetically Levitated (MAGLEV) Vehicle Shapes." *AIAA Paper No. 95-1908-CP*, 1995.

[29] "Aerodynamic Forces on Maglev Vehicles." Dot/fra/nmi-92/21, National MAGLEV Initiative, 1992.

[30] Johnson, V. S. "Minimizing Life Cycle Cost for Subsonic Commercial Aircraft." *Journal of Aircraft*, 27:139–145, 1990.

[31] Jensen, S., Rettie, I., and Barber, E. A. "Role of Figures of Merit in Design Optimization and Technology Assessment." *Journal of Aircraft*, 18:76–81, 1979.

[32] Rais–Rohani, M. and Dean, E. "Toward Manufacturing and Cost Considerations in Multidisciplinary Aircraft Design." *AIAA Paper No. 96-1620*, 1996.

[33] Leonard, A. "Vortex Methods for Flow Simulation." *Journal of Computational Physics*, 37:289–335, 1980.

[34] Katz, J. "A Discrete Vortex Method for the Non-Steady Separated Flow Over an Airfoil." *Journal of Fluid Mechanics*, 102:315–328, 1981.

[35] Mendenhall, M. R., Perkins Jr., S. C., and Lesieutre, D. J. "Vortex Cloud Model for Body Vortex Shedding and Tracking." In *Tactical Missle Aerodynamics: Prediction Methodology*, pp. 225–285. American Institute of Aeronautics and Astronautics, 1992.

[36] Mook, D. T. and Dong, B. "Perspective: Numerical Simulations of Wakes and Blade-Vortex Interaction." *Journal of Fluids Engineering*, 116:5–21, 1994.

[37] Giesing, J. P. "Vorticity and Kutta Condition for Unsteady Multienery Flows." *Journal of Applied Mechanics*, 1969.

[38] Basu, B. and Hancock, G. "The Unsteady Motion of a Two -Dimensional Aerofoil in Incompressible Inviscid Flow." *Journal of Fluid Mechanics*, 87:159–178, 1978.

[39] Coulliette, C. and Plotkin, A. "Airfoil Ground Effect Revisited." *AIAA Paper No. 95-1832-CP*, 1995.

[40] Mracek, C. P. and Mook, D. T. "Numerical Simulation of Three-Dimensional Lifting Flows by a Vortex Panel Method." *AIAA Paper No. 88-4336-CP*, 1988.

[41] "Final Report on the National MAGLEV Initiative." Dot/fra/nmi-93/03, US Department of Transportation, http://www.bts.gov/NTL/DOCS/TNM.html, 1993.

[42] *TRO7 Home Page, http://www.mvp.del.* 1997.

[43] Bearman, P. "REVIEW – Bluff Body Flows Applicable to Vehicle Aerodynamics." *Journal of Fluids Engineering*, 102:265–274, 1980.

[44] Klopfer, G. H. and Mehta, U. B. "Aerodynamic Computations for a High-Speed, Magnetic-Flight System." *AIAA Paper No. 95-0749*, 1995.

[45] Wu, J. "A Theory For Aerodynamic Forces and Moments." Technical report, Georgia Institute of Technology, June 1978.

[46] Rosenhead, L., editor. *Laminar Boundary Layers*, chapter II. Introduction. Boundary Layer Theory. Oxford University Press, 1963.

[47] Karamcheti, K. *Principles of Ideal-Fluid Aerodynamics*. Robert E. Krieger Publishing Company, 1966.

[48] Katz, J. and Plotkin, A. *Low-Speed Aerodynamics From Wing Theory to Panel Methods*. McGraw–Hill, Inc., 1991.

[49] Stratford, B. "The Prediction of Separation of the Turbulent Boundary Layer." *Journal of Fluid Mechanics*, 5:1–16, 1959.

[50] Hahn, M., Rubbert, P. E., and Mahal, A. S. "Evaluation of Separation Criteria and Their Application to Separated Flow Analysis." Technical Report AFFDL-TR-72-145, The Boeing Commercial Airplane Company, January 1973.

[51] Burden, R. L. and Faires, J. D. *Numerical Analysis*. PWS Publishing Company, 1993.

[52] Ashby, D. L., Dudley, M. R., Iguchi, S. K., Browne, L., and Katz, J. *Potential Flow Theory and Operation Guide for the Panel Code PMARC_12*. NASA Ames Research Center, Moffett Field, California, December 1992.

[53] Schetz, J. *Boundary Layer Analysis*. Prentice-Hall, 1993.

[54] El Telbany, M. and Reynolds, A. "Velocity Distributions in Plane Turbulent Channel Flows." *Journal of Fluid Mechanics*, 100:1–29, 1980.

[55] Morkovin, M. "Flow Around Circular Cylinder – A Kaleidoscope of Challenging Fluid Phenomena." *ASME Symposium on Fully Separated Flows*, pp. 102–118, 1964.

[56] Delany, N. and Sorensen, N. "Low-Speed Drag of Cylinders of Various Shapes." *NACA TN 3038*, 1953.

[57] Roshko, A. "Experiments on the Flow Past a Circular Cylinder at Very High Reynolds Number." *Journal of Fluid Mechanics*, 10:345, 1961.

[58] Bearman, P. and Zdravkovich, M. "Flow Around a Circular Cylinder Near a Plane Boundary." *Journal of Fluid Mechanics*, 89:33–47, 1978.

[59] Ranzenbach, R. and Barlow, J. B. "Two Dimensional Elliptic Bluff Body In Ground Effect - Wind Tunnel and Road Conditions." *AIAA Paper No. 96-2473-CP*, 1996.

[60] Tyll, J., Liu, D., Schetz, J., and Marchman III, J. "Experimental Studies of MAGLEV Aerodynamics." *AIAA Paper No. 95-1917*, 1995.

[61] Mracek, C. P. *A Vortex Method for Potential Flows with Applications to Dynamics and Controls*. Ph.D. thesis, Virginia Polytechnic Institute and State University, Blacksburg, VA, August 1988.

[62] Schlichting, H. *Boundary - Layer Theory*. McGraw-Hill, 1979.

[63] Raymer, D. P. *Aircraft Design: A Conceptual Approach*. American Institute of Aeronautics and Astronautics, 1992.

[64] Herbst, W. "Weight And Performance Characteristics of Magnetically Suspended High-Speed Trains As Compared To Aircraft." *SAWE Paper No. 1059*, 1975.

[65] Gutowski, T. and et al. "Developement of a Theoretical Cost Model for Advanced Composite Fabrication." *Composites Manufacturing*, 5, no. 4:231, 1994.

[66] Hess, R. and Romanoff, H. "Aircraft Airframe Cost Estimating Relationships: All Mission Types." A RAND NOTE N-2283/2-AF, RAND, December 1987.

[67] Liu, D. J., Marshakov, A., Marchman, J., and Schetz, J. "Aerodynamic Evaluation of Two Maglev Vehicle Designs." *SAE Paper No. 960905*, 1996.

[68] Frank, P., Booker, A., Caudell, T., and M.J., H. "A Comparison of Optimization and Search Methods for Multidisciplinary Design." *AIAA Paper No. 92-4827*, 1992.

[69] Gill, P. E., Murray, W., and Wright, M. H. *Practical Optimization*. Academic Press, 1981.

[70] Vanderplaats, Miura & Associates, Inc., Goleta, CA. *DOT Users Manual*, 1993.

[71] *Personal Conversation with Dr. Eugene Cliff*. 1997.

[72] Wu, J. C. and Sankar, N. L. "Aerodynamic Force And Moment In Steady And Time-Dependent Viscous Flows." *AIAA Paper No. 80-0011*, 1980.

[73] Aris, R. *Vectors, Tensors, and the Basic Equations of Fluid Mechanics*. Dover Publications, Inc., 1962.

Appendix A

Vorticity Conservation Conditions

This appendix contains a derivation of the vorticity conservation conditions for incompressible flow with uniform density and kinematic viscosity. This derivation is based on the outline by Wu in Ref. [45] and [72] and is derived here for the reader's convenience. Begin with the continuity equation for an incompressible flow, the Navier-Stokes equation, and the definition of vorticity which are shown below in a respective order.

$$\nabla \cdot \mathbf{V} = 0 \tag{A.1}$$

$$\frac{\partial \mathbf{V}}{\partial t} + (\mathbf{V} \cdot \nabla)\mathbf{V} = -\frac{1}{\rho}\nabla P + \nu \nabla^2 \mathbf{V} \tag{A.2}$$

$$\nabla \times \mathbf{V} = \boldsymbol{\Omega} \tag{A.3}$$

This derivation involves several vector identities which are shown in Eq. A.4, A.5, A.6, A.7, and A.8 [73].

$$\nabla^2 \mathbf{V} = \nabla(\nabla \cdot \mathbf{V}) - \nabla \times (\nabla \times \mathbf{V}) \tag{A.4}$$

$$\nabla \times (\nabla P) = 0 \tag{A.5}$$

$$\nabla \times (\mathbf{V} \times \boldsymbol{\Omega}) = \mathbf{V}(\nabla \cdot \boldsymbol{\Omega}) - \boldsymbol{\Omega}(\nabla \cdot \mathbf{V}) + (\boldsymbol{\Omega} \cdot \nabla)\mathbf{V} - (\mathbf{V} \cdot \nabla)\boldsymbol{\Omega} \tag{A.6}$$

$$\begin{aligned}(\mathbf{V}\cdot\nabla)\mathbf{V} &= \frac{1}{2}\nabla(\mathbf{V}\cdot\mathbf{V}) - \mathbf{V}\times(\nabla\times\mathbf{V}) \\ &= \frac{1}{2}\nabla(\mathbf{V}\cdot\mathbf{V}) - \mathbf{V}\times\boldsymbol{\Omega} \end{aligned} \tag{A.7}$$

$$\nabla\cdot(\nabla\times\mathbf{V}) = 0 \tag{A.8}$$

Equation A.4 is a vector identity for the Laplacian of a vector and is written here for the velocity vector. Equation A.5 states that the curl of the gradient of a scalar is always zero. This identity is written here for the scalar, pressure, although it is valid for any scalar and will be used for other scalars in this derivation. Equation A.6 is a vector identity involving any two vectors and is written here in the form it will be used involving the velocity and vorticity vectors. Equation A.7 is a vector identity for a single vector and is shown here for velocity along with the definition for vorticity. Equation A.8 is a vector identity which states that the divergence of the curl of a vector is always zero. Written here for the velocity vector, we see that vorticity is a solenoidal vector field.

Since all of the vorticity conservation conditions stem from the vorticity transport equation, the derivation of the latter will be the first step. If we apply the vector identity of Eq. A.4 along with the definition of vorticity in Eq. A.3 and the continuity equation in Eq. A.1 to replace the diffusion term in the Navier-Stokes equation (Eq. A.2), the result is Eq. A.9.

$$\frac{\partial\mathbf{V}}{\partial t} + (\mathbf{V}\cdot\nabla)\mathbf{V} = -\frac{1}{\rho}\nabla P - \nu\nabla\times\boldsymbol{\Omega} \tag{A.9}$$

The next step towards obtaining the vorticity transport equation is to take the curl of this equation. This can be done by taking the curl of each term individually as is shown in Eq. A.10.

$$\nabla\times\frac{\partial\mathbf{V}}{\partial t} + \nabla\times[(\mathbf{V}\cdot\nabla)\mathbf{V}] = \nabla\times\left[-\frac{1}{\rho}\nabla P\right] - \nabla\times[\nu\nabla\times\boldsymbol{\Omega}] \tag{A.10}$$

For the first term on the left hand side of Eq. A.10, the curl can be brought inside the partial derivative with respect to time and along with the definition of vorticity

can be written as the partial derivative of vorticity with respect to time. The first term on the right hand side can be set to zero due to the vector identity of Eq. A.5. Using the vector identity of Eq. A.4 for the vorticity vector in the second term on the right hand side we can rewrite Eq. A.10 as is shown in Eq. A.11.

$$\frac{\partial \mathbf{\Omega}}{\partial t} + \nabla \times [(\mathbf{V} \cdot \nabla)\mathbf{V}] = \nu \nabla^2 \mathbf{\Omega} \tag{A.11}$$

Using the vector identity of Eq. A.7, the second term on the left hand side of Eq. A.11 can be replaced

$$\nabla \times [(\mathbf{V} \cdot \nabla)\mathbf{V}] = -\nabla \times (\mathbf{V} \times \mathbf{\Omega}) \tag{A.12}$$

resulting in

$$\frac{\partial \mathbf{\Omega}}{\partial t} = \nabla \times (\mathbf{V} \times \mathbf{\Omega}) + \nu \nabla^2 \mathbf{\Omega} \tag{A.13}$$

Using the vector identities of Eq. A.6 and A.8 along with the continuity equation, the first term on the right hand side of Eq. A.13 can be rewritten and Eq. A.14, the vorticity transport equation for a 3-D, incompressible, uniform density, uniform viscosity flow is obtained.

$$\begin{aligned} \frac{\partial \mathbf{\Omega}}{\partial t} + (\mathbf{V} \cdot \nabla)\mathbf{\Omega} &= (\mathbf{\Omega} \cdot \nabla)\mathbf{V} + \nu \nabla^2 \mathbf{\Omega} \\ \frac{D\mathbf{\Omega}}{Dt} &= (\mathbf{\Omega} \cdot \nabla)\mathbf{V} + \nu \nabla^2 \mathbf{\Omega} \end{aligned} \tag{A.14}$$

This equation closesly resembles the form of the Navier-Stokes equation with the exception of one additional term which has no counterpart. The first term on the right hand side of Eq. A.14 describes the change in vorticity due to the stretching of a vortex line. It should also be noted here that the description of a flow by vorticity conservation is done without having to deal with a pressure term. This is seen as a major advantage over the corresponding momentum conservation. This equation can be written in a slightly different manner by applying the vector identity of Eq. A.4 written for vorticity along with the vector identity of Eq. A.8 on the last term on the right hand side of the vorticity transport equation. This is shown in Eq. A.15, which is the starting point for the derivation of the vorticity conservation conditions for several physical situations.

$$\frac{D\boldsymbol{\Omega}}{Dt} = (\boldsymbol{\Omega} \cdot \nabla)\mathbf{V} - \nu\nabla \times (\nabla \times \boldsymbol{\Omega}) \tag{A.15}$$

Before the derivation is continued separately for 2-D and 3-D flow it is useful to define the physical regions and boundaries of the flowfields in question. For 3-D flow, a region refers to a volume and a surface refers to that which forms the boundary to the region. Two-dimensional flow is an infinitely long extrusion along a single coordinate direction, so for these flows, a region refers to the in-plane area and the surface refers to the closed curve that forms the boundary to that region. The entire limitless region occupied by both solids and fluids is referred to as R_∞. This region is only bounded externally by a surface at infinity, S_∞. Solid regions are referred to as R_j where the subscript j is the index number of the solid object. These regions are externally bounded by surfaces, S_j, with corresponding indices j. The fluid region, R_f is externally bounded by S_∞ and internally bounded by S_S, where S_S signifies all of the solid surfaces collectively. Normal vectors point to the exterior of their associated region. A schematic diagram of the different regions and surfaces can be seen in Fig. A.1.

For 2-D flow, the vorticity and velocity are always orthogonal to one another with the velocity vector in the plane of the flow and the vorticity vector in the direction normal to the plane of flow. Therefore, the vorticity is also orthogonal to the gradient of velocity, and Eq. A.15 reduces to Eq. A.16.

$$\frac{D\boldsymbol{\Omega}}{Dt} = -\nu\nabla \times (\nabla \times \boldsymbol{\Omega}) \tag{A.16}$$

It should also be noted here that the vorticity vector does not have a component normal to a solid fluid boundary. Equation A.17 is a relation between surface and volume integrals and is written here for any arbitrary vector, $\mathbf{q}$.

$$\iiint_R \nabla \times \mathbf{q} dR = -\oiint_S \mathbf{q} \times \mathbf{n} dS \tag{A.17}$$

If we integrate Eq. A.16 over the fluid region, R_f, and apply Eq. A.17 to the right hand side we obtain Eq. A.18.

$$\frac{d}{dt}\iint_{R_f(t)} \boldsymbol{\Omega} dR = \nu \oint_{S_S(t)} (\nabla \times \boldsymbol{\Omega}) \times \mathbf{n} dS \tag{A.18}$$

The surface integral is written here solely over the solid surface, since there can be no diffusion at the infinity boundary. The left hand side results from applying Reynolds transport theorem along with the continuity equation to the integral of the total derivative of vorticity. The right hand side of Eq. A.18 can now be replaced with the use of the Navier-Stokes equation. If we take the cross product of each term in Eq. A.9 with the solid surface normal vector and integrate over the solid surface, we obtain Eq. A.19, where the normal vector points to the exterior of the fluid region, R_f.

$$\oint_{S_S} \frac{D\mathbf{V}}{Dt} \times \mathbf{n} dS = -\frac{1}{\rho} \oint_{S_S} \nabla P \times \mathbf{n} dS - \nu \oint_{S_S} (\nabla \times \mathbf{\Omega}) \times \mathbf{n} dS \tag{A.19}$$

The first term on the right hand side is always zero. This can easily be seen by transforming the term to a volume integral using Eq. A.17. The integrand, $\nabla \times \nabla P$, is always zero as stated by the vector identity in Eq. A.5. Replacing the right hand side of Eq. A.18 with the left hand side of Eq. A.19 results in Eq. A.20.

$$\frac{d}{dt} \iint_{R_f(t)} \mathbf{\Omega} dR = - \oint_{S_S} \frac{D\mathbf{V}}{Dt} \times \mathbf{n} dS \tag{A.20}$$

We now make use of the no-slip boundary condition on the solid surface which simply states that at the boundary S_S the total derivative of velocity with respect to time is identical for both the fluid and solid. Therefore, a version of Eq. A.20 can be written for the entire region, R_∞. This can be seen in Eq. A.21 where the right hand side comes from applying Eq. A.17 to the right hand side of Eq. A.20 with the unit normal vector pointing to the exterior of the solid region instead of to the exterior of the fluid region.

$$\begin{aligned}
\frac{d}{dt} \iint_{R_f(t)} \mathbf{\Omega} dR &= -\sum_j \iint_{R_j} \nabla \times \frac{D\mathbf{V}}{Dt} dR \\
\frac{d}{dt} \iint_{R_f(t)} \mathbf{\Omega} dR &= -\sum_j \iint_{R_j} \frac{D\mathbf{\Omega}}{Dt} dR \\
\frac{d}{dt} \iint_{R_f(t)} \mathbf{\Omega} dR &= -\sum_j \frac{d}{dt} \iint_{R_j} \mathbf{\Omega} dR
\end{aligned} \tag{A.21}$$

This results in Eq. A.22.

$$\frac{d}{dt} \iint_{R_f} \mathbf{\Omega} dR + \sum_j \frac{d}{dt} \iint_{R_j} \mathbf{\Omega} dR = 0$$

$$\begin{aligned} R_f + \sum_j R_j &= R_\infty \\ \frac{d}{dt} \iint_{R_\infty} \mathbf{\Omega} dR &= 0 \end{aligned} \tag{A.22}$$

So, for 2-D, incompressible, uniform density, uniform viscosity flow, the total vorticity for the combined region (fluid and solid) is constant with time. The vorticity of the solid region is simply twice its angular velocity.

For 2-D, inviscid flow it can easily be seen from the 2-D vorticity transport equation (Eq. A.16) that the diffusion term on the right hand side is equal to zero. The resulting equation is the 2-D version of Kelvin's Theorem, shown here in Eq. A.23.

$$\frac{D\mathbf{\Omega}}{Dt} = 0 \tag{A.23}$$

It states that the vorticity of a fluid element remains constant with time. This work is stated here for an incompressible fluid although it can be shown that this holds for the more general case of a barotropic fluid regardless of compressibility [47]. For consistency, the vorticity conservation condition for the inviscid case, which is presented as a stipulation on the substantial derivative of vorticity, can be rewritten in an integral form. This differential equation holds for the fluid region, so if we integrate Eq. A.23 over the region R_f and apply Reynolds transport theorem we obtain the following equation.

$$\frac{d}{dt} \iiint_{R_f} \mathbf{\Omega} dR = 0 \tag{A.24}$$

This equation closely resembles the vorticity conservation condition for 2-D viscous flow in Eq. A.22 except the integral excludes the solid regions. This is a result of the absence of a no-slip condition, so vorticity in the fluid region has no relation to the vorticity in the solid region which is equal to two times the angular velocity of a solid body rotation. If the solid bodies have zero angular velocity, Eq. A.22 is identical to the corresponding inviscid condition in Eq. A.24.

For 3-D flow the approach to deriving the vorticity conservation expression differs greatly from the approach involving the integration of Eq. A.15 over the regions. This is due to the fact that in order to maintain complete generality of the flow situation

the $(\mathbf{\Omega}\cdot\nabla)\mathbf{V}$ term cannot be eliminated. The vorticity vector has a component normal to the solid fluid boundaries and due to the no-slip condition this normal component is continuous across that boundary. The derivation makes use of two vector identities shown in Eq. A.25 and A.26 where ψ and ϕ are scalars or vectors as indicated by bold face type.

$$\nabla \cdot (\psi\boldsymbol{\phi}) = \psi\nabla \cdot \boldsymbol{\phi} + \boldsymbol{\phi} \cdot \nabla\psi \tag{A.25}$$

$$\nabla(\boldsymbol{\psi} \cdot \boldsymbol{\phi}) = (\nabla\boldsymbol{\phi})\boldsymbol{\psi} + (\nabla\boldsymbol{\psi})\boldsymbol{\phi} \tag{A.26}$$

These vector identities can be used to derive Eq. A.28 with the manipulations shown in Eq. A.27. This analysis also notes that vorticity is solenoidal and that we are assuming that $\mathbf{a}$ is a constant vector. The gradient of the position vector, $\mathbf{r}$, is the identity matrix.

$$\begin{aligned}\nabla \cdot [(\mathbf{a} \cdot \mathbf{r})\mathbf{\Omega}] &= (\mathbf{a} \cdot \mathbf{r})(\nabla \cdot \mathbf{\Omega}) + \mathbf{\Omega} \cdot \nabla(\mathbf{a} \cdot \mathbf{r}) \\ \nabla(\mathbf{a} \cdot \mathbf{r}) &= (\nabla\mathbf{a})\mathbf{r} + (\nabla\mathbf{r})\mathbf{a}\end{aligned} \tag{A.27}$$

$$\nabla \cdot [(\mathbf{a} \cdot \mathbf{r})\mathbf{\Omega}] = \mathbf{a} \cdot \mathbf{\Omega} \tag{A.28}$$

The derivation will also use the Divergence Theorem which is shown for an arbitrary vector, $\mathbf{q}$, in Eq. A.29.

$$\iiint_R \nabla \cdot \mathbf{q} dR = \oiint_S \mathbf{q} \cdot \mathbf{n} dS \tag{A.29}$$

If the integrand in the volume integral of the Divergence Theorem is replaced with the left hand side of Eq. A.28 and the constant vector, $\mathbf{a}$, is cancelled out on both sides of the equation, the resulting equation is Eq. A.30.

$$\iiint_{R_f} \mathbf{\Omega} dR = \oiint_{S_S} \mathbf{r}(\mathbf{\Omega} \cdot \mathbf{n}) dS \tag{A.30}$$

This equation is written for the fluid region, R_f. A similar equation can be written for the solid region as in Eq. A.31 taking note that the normal vector for this equation is pointing opposite to that for the equations written for the fluid region.

$$\iiint_{R_S} \mathbf{\Omega} dR = \oiint_{S_S} \mathbf{r}(\mathbf{\Omega} \cdot \mathbf{n}) dS \tag{A.31}$$

Due to the no-slip condition, the right hand side of Eq. A.31 is the negative of the right hand side of Eq. A.30, and we can write

$$\iiint_{R_f} \mathbf{\Omega} dR = -\iiint_{R_S} \mathbf{\Omega} dR \tag{A.32}$$

Therefore, for the 3-D, incompressible, uniform density,uniform viscosity flow, the vorticity conservation statement is that the integral of the vorticity over the combined fluid and solid regions is always zero.

$$\begin{aligned} \iiint_{R_\infty} \mathbf{\Omega} dR &= 0 \\ R_\infty &= R_f + R_S \end{aligned} \tag{A.33}$$

For 3-D, inviscid flow, it can easily be seen from the 3-D vorticity transport equation (Eq. A.15) that the diffusion term on the right hand side is equal to zero leaving

$$\frac{D\mathbf{\Omega}}{Dt} = (\mathbf{\Omega} \cdot \nabla)\mathbf{V} \tag{A.34}$$

This is the 3-D version of Kelvin's theorem which is identical to the 2-D equation in Eq. A.23 if the flow starts from rest, i.e. no initial vorticity. Similar to our treatment of the 2-D Kelvins theorem, we can integrate Eq. A.34 over the region R_f and apply Reynolds transport theorem to obtain

$$\iiint_{R_f} \mathbf{\Omega} dR = \oiint_{S_S} \mathbf{r}(\mathbf{\Omega} \cdot \mathbf{n}) dS \tag{A.35}$$

According to the Helmholtz Vorticity Theorems, a vortex filament in an inviscid flow cannot end at a solid boundary, so the right hand side of Eq. A.35 is zero resulting in Eq. A.36.

$$\iiint_{R_f} \mathbf{\Omega} dR = 0 \tag{A.36}$$

In review, the four vorticity conservation equations derived here can be found in Eq. A.22, A.33, A.23, and A.34 and are presented here again for easy reference.

$$\begin{aligned} 3-D \quad & \begin{cases} Viscous: \iiint_{R_\infty} \mathbf{\Omega} dR = 0 \\ Inviscid: \iiint_{R_f} \mathbf{\Omega} dR = 0 \end{cases} \\ 2-D \quad & \begin{cases} Viscous: \frac{d}{dt} \iint_{R_\infty} \mathbf{\Omega} dR = 0 \\ Inviscid: \frac{d}{dt} \iint_{R_f} \mathbf{\Omega} dR = 0 \end{cases} \end{aligned} \tag{A.37}$$

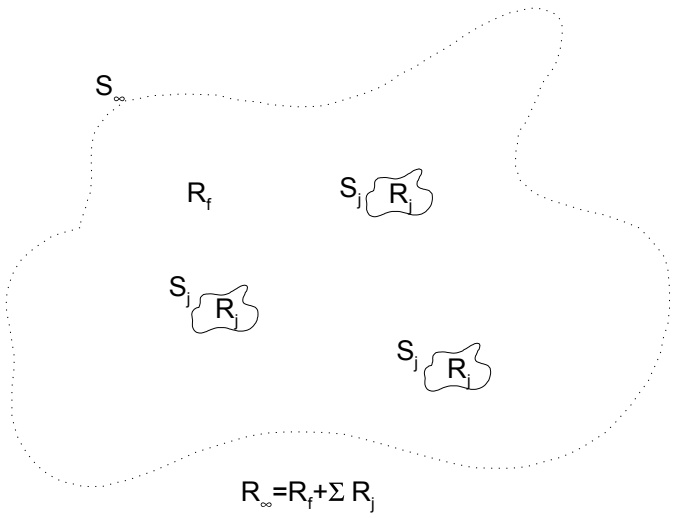

Figure A.1: Regions and Boundaries in Flowfield

Appendix B

2-D Vortex Panel Method Solution

The flow solution is obtained as a linear superposition of the continuous vortex sheet, point vortices, and uniform free stream flow, all of which are solutions to Laplaces equation, in such a way as to satisfy the no-penetration boundary condition of the Neumann type. The continuous vortex sheet is comprised of N panels with piecewise linear vortex sheet strength connected at $N+1$ nodes. The boundary condition is imposed at a single collocation point located at the midpoint of each panel. The boundary condition is shown in Eq. B.1

$$(\mathbf{V}_B + \mathbf{V}_w + \mathbf{V}_\infty) \cdot \mathbf{n} = 0 \tag{B.1}$$

$\mathbf{V}_B$ is the velocity induced by the boundary layer, $\mathbf{V}_w$, is the velocity induced by the shed wake, and $\mathbf{V}_\infty$ is the velocity induced by the free stream flow. The vorticity conservation condition is simultaneously imposed.

$$\frac{1}{2}\sum_{i=1}^{N}(\gamma_i + \gamma_{i+1})\Delta l_i + \Gamma_t + \sum_{k=1}^{M}\Gamma_k = \quad \text{Constant} \tag{B.2}$$

Throughout this work, i is the index for the surface panel inducing a velocity, k is the index for the wake point vortices inducing a velocity, and j is the index for the panel at which the no-penetration boundary condition is being imposed. The velocity induced by the vortex sheet, $\mathbf{V}_B$, is composed of the N linear sections of the sheet plus a point vortex at the trailing edge as indicated in Eq. B.3. This point vortex

replaces the vortex sheet at the trailing edge and easily allows for the toggling between conditions for the Giesing/Maskell trailing edge model.

$$\mathbf{V}_B(\mathbf{r},t) = \sum_{i=1}^{N} \mathbf{V}_{b_i}(\mathbf{r},t) - \frac{1}{2\pi}\mathbf{e}_z \times \frac{\Gamma_t(t)(\mathbf{r}-\mathbf{r}_t)}{|\mathbf{r}-\mathbf{r}_t|^2} \tag{B.3}$$

Equation B.4 describes the velocity induced by the shed wake as the summation of the velocities induced by the M individual point vortices that comprise the wake.

$$\mathbf{V}_w(\mathbf{r},t) = -\frac{1}{2\pi}\mathbf{e}_z \times \sum_{k=1}^{M} \Gamma_k \frac{\mathbf{r}-\mathbf{r}_k}{|\mathbf{r}-\mathbf{r}_k|^2 + \sigma^2} \tag{B.4}$$

The uniform free stream is taken as magnitude unity and is shown in Eq. B.5 where α is the angle of attack.

$$\mathbf{V}_\infty = \cos\alpha \mathbf{E}_x + \sin\alpha \mathbf{E}_y \tag{B.5}$$

As was previously mentioned, the body is discretized into N panels. The solution takes place in two reference frames; a global reference frame and a panel local reference frame. The discretized body, along with the two reference frames are shown in Fig. B.1 for a 2-D airfoil case. Upper case letters refer to values in the global coordinate system, while lower case letters refer to values in the panel local coordinate system. The boundary condition is imposed in the global coordinate system. Equation B.6 shows the length of panel i

$$\Delta l_i = \sqrt{(X_{i+1}-X_i)^2 + (Y_{i+1}-Y_i)^2} \tag{B.6}$$

and Eq. B.7 shows the direction cosines for the coordinate transformation between global and panel local coordinate systems.

$$\begin{aligned} d_1 &= \frac{(X_{i+1}-X_i)}{\Delta l_i} \\ d_2 &= \frac{(Y_{i+1}-Y_i)}{\Delta l_i} \end{aligned} \tag{B.7}$$

The transformation from global to panel local coordinate system can be seen in Eq. B.8.

$$\begin{aligned} x &= d_1(X_j - X_i) + d_2(Y_j - Y_i) \\ y &= -d_2(X_j - X_i) + d_1(Y_j - Y_i) \end{aligned} \tag{B.8}$$

Equations B.9 through B.12 show the ingredients for the calculation of the contribution of the linearly varying vortex sheet on panel i to the velocity (Eq. B.13).

$$\Delta\theta = \tan^{-1}\left(\frac{x}{y}\right) - \tan^{-1}\left(\frac{x-\Delta l_i}{y}\right) \tag{B.9}$$

$$R = \frac{(x-\Delta l_i)^2 + y^2}{x^2+y^2} \tag{B.10}$$

$$\begin{aligned} v_{1xi} &= \frac{1}{2\pi\Delta l_i}[(\Delta l_i - x)\Delta\theta - \frac{1}{2}y\ln R] \\ v_{1yi} &= \frac{1}{2\pi\Delta l_i}[y\Delta\theta - \Delta l_i + \frac{1}{2}(\Delta l_i - x)\ln R] \\ v_{2xi} &= \frac{1}{2\pi\Delta l - i}[x\Delta\theta + \frac{1}{2}y\ln R] \\ v_{2yi} &= \frac{1}{2\pi\Delta l_i}[\Delta l_i - y\Delta\theta + \frac{1}{2}x\ln R] \end{aligned} \tag{B.11}$$

$$\begin{aligned} V_{1Xi} &= d_1 v_{1xi} - d_2 v_{1yi} \\ V_{1Yi} &= d2 v_{1xi} + d_1 v_{1yi} \\ V_{2Xi} &= d_1 v_{2xi} - d_2 v_{2yi} \\ V_{2Yi} &= d_2 v_{2xi} + d_1 v_{2yi} \end{aligned} \tag{B.12}$$

$$\mathbf{V}_{b_i}(X,Y,t) = \gamma_i[V_{1Xi}\mathbf{E}_X + V_{1Yi}\mathbf{E}_Y] + \gamma_{i+1}[V_{2Xi}\mathbf{E}_X + V_{2Yi}\mathbf{E}_Y] \tag{B.13}$$

The velocity induced by the infinitely thin boundary layer from Eq. B.3 can be seen in terms of the global coordinates in Eq. B.14.

$$\mathbf{V}_B = \sum_{i=1}^{N}\mathbf{V}_{b_i} + \frac{1}{2\pi}\Gamma_t(t)\frac{(Y-Y_t)\mathbf{E}_X - (X-X_t)\mathbf{E}_Y}{(X-X_t)^2+(Y-Y_t)^2} \tag{B.14}$$

Likewise, the velocity induced by the wake and free stream can be seen in Eq. B.15 and B.16 respectively in terms of the global coordinates.

$$\mathbf{V}_w(X,Y,t) = \frac{1}{2\pi}\sum_{k=1}^{M}\Gamma_k\frac{(Y-Y_k)\mathbf{E}_X - (X-X_k)bfE_Y}{(X-X_k)^2+(Y-Y_k)^2+\sigma^2} \tag{B.15}$$

$$\mathbf{V}_\infty(X,Y,t) = \cos\alpha\mathbf{E}_X + \sin\alpha\mathbf{E}_Y \tag{B.16}$$

At each time step, the Giesing/Maskell trailing edge model is used to determine the value of Γ_k which is the $\Delta\Gamma_w$ for that time step using Eq. B.17.

$$\begin{aligned} \Gamma_t > 0 \quad & \begin{cases} \Gamma_t = \frac{\gamma_U \Delta l_U}{2} \\ \Delta\Gamma_w = \frac{2\Gamma_t^2}{\Delta l_U^2}\Delta t \end{cases} \\ \Gamma_t < 0 \quad & \begin{cases} \Gamma_t = \frac{\gamma_L \Delta l_L}{2} \\ \Delta\Gamma_w = -\frac{2\Gamma_t^2}{\Delta l_L^2}\Delta t \end{cases} \end{aligned} \tag{B.17}$$

Equation B.18 shows the boundary condition with the unit normal written out explicitly in terms of the global coordinates.

$$\begin{aligned} (\mathbf{V}_B + \mathbf{V}_w + \mathbf{V}_\infty) \cdot \mathbf{n} &= 0 \\ (\mathbf{V}_B + \mathbf{V}_w + \mathbf{V}_\infty) \cdot \left[-\frac{(Y_{j+1} - Y_j)}{\Delta l_j}\mathbf{E}_X + \frac{(X_{j+1} - X_j)}{\Delta l_j}\mathbf{E}_Y \right] &= 0 \end{aligned} \tag{B.18}$$

The dot product of each velocity contributor with the unit outward normal of a panel j on which the boundary condition is being imposed can be seen in Eq. B.19, B.20, and B.21 for the vortex sheet, wake, and free stream respectively.

$$\begin{aligned} \mathbf{V}_B \cdot \mathbf{n} = & \\ & \sum_{i=1}^{N} -(\gamma_i V_{1Xi} + \gamma_{i+1} V_{2Xi}) \left(\frac{Y_{j+1} - Y_j}{\Delta l_j} \right) + (\gamma_i V_{1Yi} + \gamma_{i+1} V_{2Yi}) \left(\frac{X_{j+1} - X_j}{\Delta l_j} \right) \\ & -\frac{1}{2\pi}\Gamma_t(t) \frac{(Y_j - Y_t)}{(X_j - X_t)^2 + (Y_j - Y_t)^2} \frac{(Y_{j+1} - Y_j)}{\Delta l_j} \\ & -\frac{1}{2\pi}\Gamma_t(t) \frac{(X_j - X_t)}{(X_j - X_t)^2 + (Y_j - Y_t)^2} \frac{(X_{j+1} - X_j)}{\Delta l_j} \end{aligned} \tag{B.19}$$

$$\begin{aligned} \mathbf{V}_w \cdot \mathbf{n} = & \\ & \frac{1}{2\pi} \sum_{k=1}^{M} \Gamma_k \left[-\frac{(Y_j - Y_k)}{(X_j - X_k)^2 + (Y_j - Y_k)^2 + \sigma^2} \left(\frac{Y_{j+1} - Y_j}{\Delta l_j} \right) \right. \\ & \left. -\frac{(X_j - X_k)}{(X_j - X_k)^2 + (Y_j - Y_k)^2 + \sigma^2} \left(\frac{X_{j+1} - X_j}{\Delta l_j} \right) \right] \end{aligned} \tag{B.20}$$

$$\mathbf{V}_\infty \cdot \mathbf{n} = -\cos\alpha \left(\frac{Y_{j+1} - Y_j}{\Delta l_j} \right) + \sin\alpha \left(\frac{X_{j+1} - X_j}{\Delta l_j} \right) \tag{B.21}$$

The boundary condition, Eq. B.1 can be separated into the part that needs to be solved for and the part that is known from previous time steps (right hand side) as shown in Eq. B.22.

$$\mathbf{V}_B \cdot \mathbf{n} = -(\mathbf{V}_w + \mathbf{V}_\infty) \cdot \mathbf{n} \tag{B.22}$$

At each time step, another point vortex is shed and added to the wake. Each point vortex is also convected at the local velocity, so that the new point vortex location is equal to the old location plus the product of the velocity and the time step. So at each time step, the right hand side (RHS) is updated and the unknown strengths of the vortex sheet at the panel nodes along with the trailing edge point vortex are calculated by solving the linear system of equations (Eq. B.23), where $a_{j,i}$ is given in Eq. B.24.

$$\begin{bmatrix} & & \\ & a_{j,i} & \\ & & \end{bmatrix} \begin{bmatrix} \gamma_2 \\ \vdots \\ \gamma_n \\ \Gamma_t \end{bmatrix} = \begin{bmatrix} \\ RHS \\ \\ \end{bmatrix} \tag{B.23}$$

$$\begin{aligned} a_{j,i} = &-V_{2X_{i-1}} \left(\frac{Y_{j+1} - Y_j}{\Delta l_j} \right) + V_{2Y_{i-1}} \left(\frac{X_{j+1} - X_j}{\Delta l_j} \right) \\ &-V_{1X_i} \left(\frac{Y_{j+1} - Y_j}{\Delta l_j} \right) + V_{1Y_i} \left(\frac{X_{j+1} - X_j}{\Delta l_j} \right) \end{aligned} \tag{B.24}$$

Since the trailing edge flow is described using the point vortex of strength Γ_t the vortex sheet strength is set to zero at the trailing edge ($\gamma_1 = \gamma_{n+1} = 0$), therefore they are excluded from the system of equations. It can be seen that the coefficient for the γ at the node involves a V_2 from the panel behind the node $(i-1)$ and a V_1 from the panel ahead of the node (i). Figure B.2 shows two adjacent panels and their shared node along with the linear hat function for the velocity distribution over the two panels associated with the sheet strength at the node. It should be noted that the V functions are not the linear hat functions themselves but the influence coefficients of the linear sheet strength distribution on panel j. The matrix entries for the vorticity conservation equation are shown in Eq. B.25.

$$a(N+1, i) = \frac{1}{2}\Delta l_{i-1} + \frac{1}{2}\Delta l_i \tag{B.25}$$

Caution must be taken in the calculation of the diagonal elements of the a matrix, $a_{i,i}$, since the values of y are zero. When calculating $\Delta\theta$ it must be explicitly specified from which side of the panel zero is being approached. To avoid this problem, the values for this special case are explicitly provided in Eq. B.26 instead of being calculated using Eq. B.11.

$$\begin{array}{c} x = \frac{\Delta l}{2} \\ y \to 0^+ \end{array} \left\{ \begin{array}{c} \Delta\theta = -\pi \\ R = 1 \end{array} \right. \qquad \begin{array}{l} v_{1xi} = -\frac{1}{4} \\ v_{1yi} = -\frac{1}{2\pi} \\ v_{2xi} = -\frac{1}{4} \\ v_{2yi} = \frac{1}{2\pi} \end{array} \tag{B.26}$$

The same approach is taken for the solution of the bluff body problem. For this case, there are two separation points and, therefore, two wakes. The bluff body extension to the model does not employ point vortices on the surface of the solid region, such as the one placed at the trailing edge of the streamlined body so the vector of unknowns consists only of the vortex sheet strengths at the N distinct nodes (Eq. B.27).

$$\begin{bmatrix} & & \\ & a_{j,i} & \\ & & \end{bmatrix} \begin{bmatrix} \gamma_1 \\ \vdots \\ \gamma_n \end{bmatrix} = \begin{bmatrix} \\ RHS \\ \\ \end{bmatrix} \tag{B.27}$$

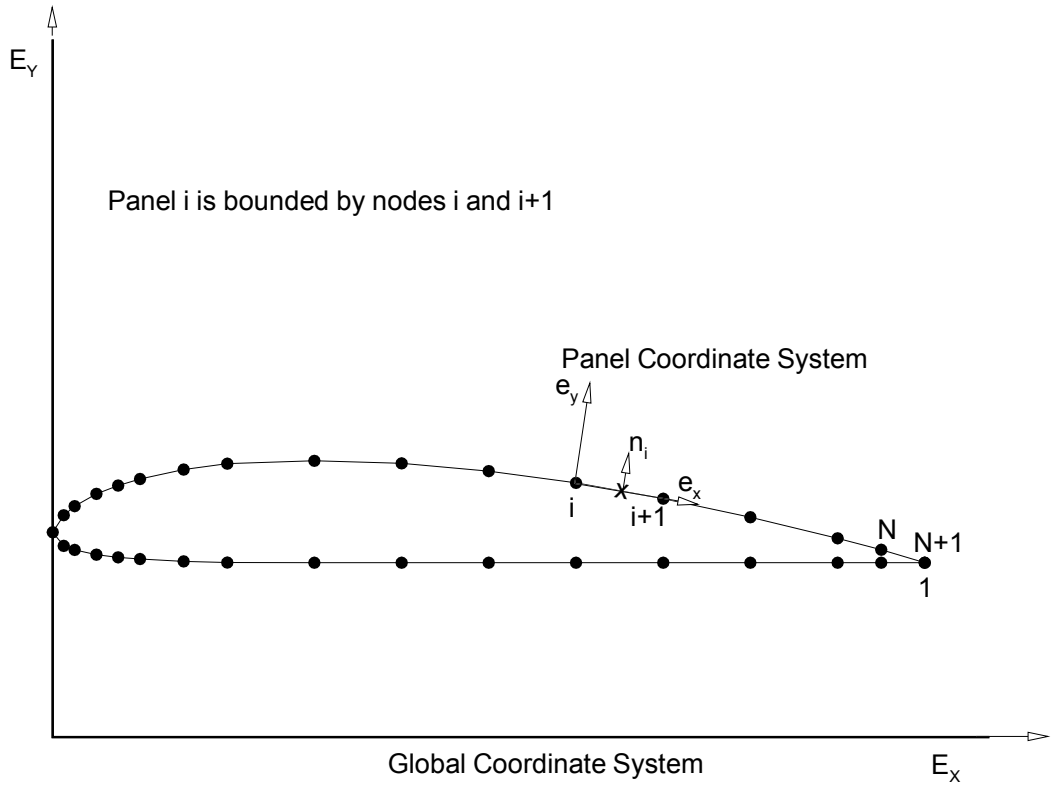

Figure B.1: Discretized Geometry and Coordinate Systems

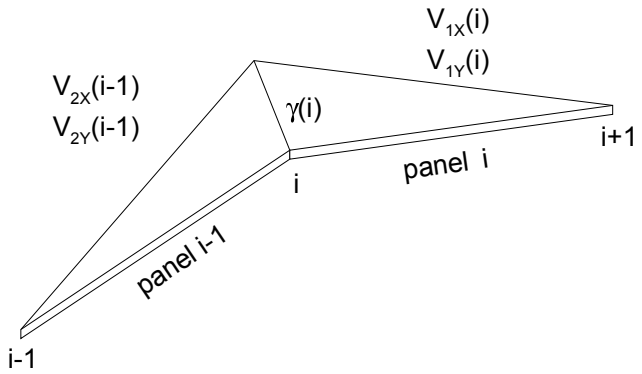

Figure B.2: Adjacent Panels and Hat Functions

Appendix C

2-D Turbulent Gap Flow Calculation

The fully-developed, turbulent flow in a thin 2-D gap with one wall moving can be analyzed by solving Eq. C.1, which is the momentum equation for such a flow.

$$\begin{aligned} \frac{dp}{dx} &= \frac{d}{dy}\left[(\mu+\mu_T)\frac{du}{dy}\right] \\ u_0 &= 0.0 \\ u_h &= u_\infty \end{aligned} \tag{C.1}$$

This simply states that the pressure gradient in the longitudinal direction of the pipe is equal to the shear stress gradient in the lateral direction of the pipe. The boundary condition at the two pipe walls forces a zero velocity at the lower wall and a possibly none zero velocity at the upper wall. A schematic diagram of the flow can be seen in Fig. C.1. Equation C.2 results from integrating both sides of Eq. C.1 with respect to y.

$$\frac{dp}{dx}y = (\mu+\mu_T)\frac{du}{dy} - \mu\left.\frac{du}{dy}\right|_0 \tag{C.2}$$

Integrating a second time with respect to y yields

$$u - u_0 = \int_0^y \frac{\frac{dp}{dx}y'}{\mu+\mu_T}dy' + \left.\frac{du}{dy}\right|_0 \int_0^y \frac{\mu}{\mu+\mu_T}dy' \tag{C.3}$$

The boundary condition at $y = 0$, $u(0) = 0$, allows us to eliminate u_0 and the boundary condition at $y = h$, $u(h) = u_\infty$, allows us to solve for the velocity gradient at the $y = 0$ wall.

$$\left.\frac{du}{dy}\right|_0 = \frac{u_\infty - \int_0^h \frac{\frac{dp}{dx}y'}{\mu+\mu_T}dy'}{\int_0^h \frac{\mu}{\mu+\mu_T}dy'} \tag{C.4}$$

If Eq. C.4 is inserted into Eq. C.3 we obtain the solution for longitudinal velocity at any height, y.

$$u(y) = \int_0^y \frac{\frac{dp}{dx}y'}{\mu+\mu_T}dy' + \frac{u_\infty - \int_0^h \frac{\frac{dp}{dx}y'}{\mu+\mu_T}dy'}{\int_0^h \frac{\mu}{\mu+\mu_T}dy'} \int_0^y \frac{\mu}{\mu+\mu_T}dy' \tag{C.5}$$

The eddy viscosity is modeled separately in the inner and outer regions. These models are the Reichart turbulence model and a pipe flow outer region model from Reynolds shown in Eq. C.6 in a respective order.

$$\begin{aligned} \mu_T &= k\rho\nu\left[\left(\frac{yu_*}{\nu}\right) - y_a^+ \tanh\left(\frac{yu_*}{\nu y_a^+}\right)\right] \\ \mu_T &= 0.192k\rho u_* h \end{aligned} \tag{C.6}$$

The friction velocity, u_*, is dependent on the final solution so the integration, Eq. C.5, must be solved iteratively within a root finding scheme to update values of the wall shear stress.

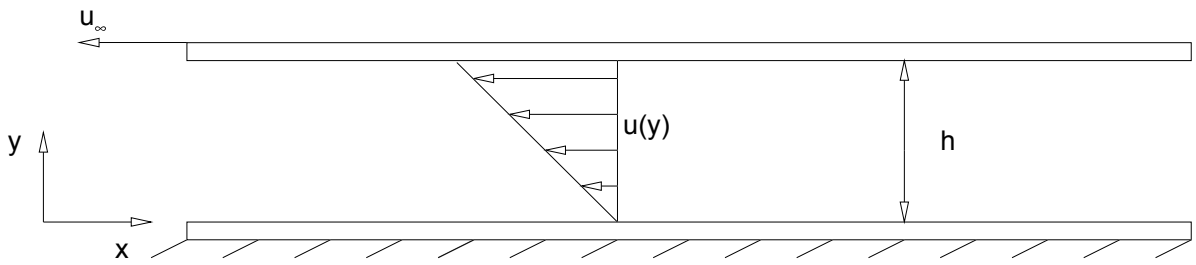

Figure C.1: 2-D Pipe Flow with a Moving Wall and Pressure Gradient

Appendix D

Green's Identity Formulation

For this outline of the Green's Identity formulation of a linear aerodynamic analysis, i.e. a panel method, one is looking at the exterior flow in a region with only one interior boundary. The extension for multiple interior boundaries is trivial. The flow is divided into two regions, R_f, the region of interest, and R_i. The exterior boundary of R_f is S_∞ and the interior boundary is S which is composed of S_B, the surface of solid body, and S_w, the surface of a shed wake. The normal vector of the boundaries point to the outside of the region being considered. These regions can be seen pictorially in Fig. D.1. Laplace's equation must hold in both the interior region, R_i and the exterior region, R_f,

$$\begin{aligned} \nabla^2\Phi &= 0 \\ \nabla^2\Phi_i &= 0 \end{aligned} \tag{D.1}$$

where Φ is the total velocity potential which is equal to a free stream potential plus a perturbation potential, ϕ.

$$\Phi = \phi_\infty + \phi \tag{D.2}$$

Green's Theorem is used to find the velocity potential at a point, P. Green's Theorem is the Divergence Theorem written for a vector composed of two scalar functions of position, $\Phi_1\nabla\Phi_2 - \Phi_2\nabla\Phi_1$.

$$\iint_S (\Phi_1\nabla\Phi_2 - \Phi_2\nabla\Phi_1)\cdot\mathbf{n}dS = \iiint_R (\Phi_1\nabla^2\Phi_2 - \Phi_2\nabla^2\Phi_1)dR \tag{D.3}$$

If the scalars of Green's Theorem are solutions to Laplace's equation, the right hand side of Eq. D.3 equals zero. These harmonic functions are placed on the interior boundary, and the no-penetration condition (Dirichlet) is imposed on the boundaries. The formulation is slightly different for 2-D and 3-D flows, so the discussion is continued in separate sections for the two cases. Detailed discussions can be found in Refs. [47], [48], and [52].

D.1 2-D Flows

For the 2-D formulation, set $\Phi_1 = \ln r$ and $\Phi_2 = \Phi$ where r is the scalar distance from some point, P. Φ_1 and Φ_2 are both solutions to Laplace's equation, so the right hand side of Green's Theorem is zero. If Eq. D.3 is evaluated at point P and P is in the region R_f, then the resulting expression can be seen in Eq. D.4.

$$\Phi(P) = -\frac{1}{2\pi}\int_S [\ln r \nabla\Phi - \Phi\nabla \ln r] \cdot \mathbf{n} ds \tag{D.4}$$

Care must be taken to exclude the point P from the region of integration, since $\ln r$ approaches infinity as r approaches zero. This is accomplished by enclosing P in a circular boundary of radius ϵ and taking the limit as ϵ approaches zero. If Eq. D.3 is evaluated at point P and P is in the region R_i, then the resulting expression can be seen in Eq. D.5.

$$0 = -\frac{1}{2\pi}\int_S [\ln r \nabla\Phi_i - \Phi_i\nabla \ln r] \cdot \mathbf{n} ds \tag{D.5}$$

Add Eq. D.5 to Eq. D.4 noting that for each of these expressions the normal vector points in the opposite direction to get

$$\Phi(P) = -\frac{1}{2\pi}\int_S [(\nabla\Phi - \nabla\Phi_i)\ln r - (\Phi - \Phi_i)\nabla \ln r] \cdot \mathbf{n} ds \tag{D.6}$$

The functional form of the integrand in Eq. D.6 is that of a 2-D source and 2-D doublet with strengths σ and μ respectively. These strengths are described in Eq. D.7.

$$\begin{aligned} -\sigma &= \frac{\partial\Phi}{\partial n} - \frac{\partial\Phi_i}{\partial n} \\ -\mu &= \Phi - \Phi_i \end{aligned} \tag{D.7}$$

For a modeled exterior flow, the interior boundary, S can be composed of the boundary of a solid surface, S_B and the boundary of a wake, S_w. If we ignore entrainment into the wake, then there are no source terms on the wake boundary. At the exterior boundary, S_∞, all of the perturbation potentials approach zero and the potential is equal to ϕ_∞. With all of this in mind, Eq. D.6 can be rewritten as Eq. D.8.

$$\Phi(P) = \frac{1}{2\pi}\int_{S_B}[\sigma \ln r - \mu\frac{\partial}{\partial n}(\ln r)]ds - \frac{1}{2\pi}\int_{S_w}\mu_w\frac{\partial}{\partial n}(\ln r)]ds + \phi_\infty(P) \tag{D.8}$$

The no-penetration boundary condition is imposed implicitly using the Dirichlet type boundary condition. This condition states that setting the total potential in the region R_i, Φ_i, equal to a constant is equivalent to imposing no flow through the boundary. The condition can also be imposed by setting Φ_i equal to ϕ_∞ even though the potential of the free stream is not a constant. Therefore, Eq. D.8 reduces to Eq. D.9.

$$\frac{1}{2\pi}\int_{S_B}[\sigma \ln r - \mu\frac{\partial}{\partial n}(\ln r)]ds - \frac{1}{2\pi}\int_{S_w}\mu_w\frac{\partial}{\partial n}(\ln r)]ds = 0 \tag{D.9}$$

The boundary condition is automatically satisfied at the infinity boundary. This is a property of the analytic solutions to Laplaces equation (harmonic functions).

If the interior boundary is discretized into panels, Eq. D.9 can be written as shown in Eq. D.10, where N_B is the number of panels comprising the surface S_B and N_w is the number of panels comprising the wake S_w.

$$\Sigma_{k=1}^{N_B}(\mu_k C_{jk}) + \Sigma_{k=1}^{N_B}(\sigma_k B_{jk}) + \Sigma_{k=1}^{N_w}(\mu_{w_k} C_{jk}) = 0|_{j=1,N_B} \tag{D.10}$$

The coefficients B and C are shown in Eq. D.11.

$$\begin{aligned} B_{jk} &= \frac{1}{2\pi}\int_k \ln r ds \\ C_{jk} &= -\frac{1}{2\pi}\int_k \frac{\partial}{\partial n}(\ln r)ds \end{aligned} \tag{D.11}$$

The strength of the wake doublets, μ_w, is determined by an auxiliary condition. The source strengths are determined using the Dirichlet boundary condition. Equation D.7 defines the source strength as the dot product of the gradient of the potential jump across a panel with the normal vector of that panel. Since the definition of no-penetration requires $\frac{\partial \Phi}{\partial n} = 0$ and the potential of the interior region is equal to the

free stream potential, the source strength is equal to the normal component of the free stream velocity (Eq. D.12).

$$\begin{aligned} -\sigma_k &= \left(\frac{\partial \Phi}{\partial n} - \frac{\partial \Phi_i}{\partial n}\right)_k \\ &= -\frac{\partial \phi_\infty}{\partial n} \\ &= -\mathbf{V}_\infty \cdot \mathbf{n} \end{aligned} \tag{D.12}$$

This leaves the surface doublet strengths as the N_B unknowns to match the N_B equations.

The coefficients, B and C are the influence coefficients for a distributed source and distributed doublet. These can easily be evaluated in the panel reference frame which is described in Fig. D.2. The influence coefficient B is evaluated in Eq. D.13.

$$\begin{aligned} \int_{x_1}^{x_2} \ln r dx &= \frac{1}{2}\left[(x-x_1)\ln(r_1^2) - (x-x_2)\ln(r_2^2) - 2(x_2-x_1) + 2z(\theta_2-\theta_1)\right] \\ r_1^2 &= (x-x_1)^2 + z^2 \\ r_2^2 &= (x-x_2)^2 + z^2 \\ \theta_1 &= \tan^{-1}\frac{z}{x-x_1} \\ \theta_2 &= \tan^{-1}\frac{z}{x-x_2} \end{aligned} \tag{D.13}$$

The influence coefficient C is evaluated in Eq. D.14.

$$\begin{aligned} \int_{x_1}^{x_2} \frac{\partial}{\partial n}(\ln r) dx &= -\frac{\partial}{\partial z}\int_{x_1}^{x_2} (\ln r) dx \\ &= -\left[\theta_2 - \theta_1\right] \end{aligned} \tag{D.14}$$

The negative sign is due to the normal vector pointing in the negative direction. The influence coefficient of the distributed doublet in Eq. D.14 is mathematically identical to that of discrete vortices at the panel nodes. The strength of the discrete vortex at x_1 is equal to μ and that at x_2 is equal to $-\mu$.

D.2 3-D Flows

For the 3-D formulation, set $\Phi_1 = \frac{1}{r}$ and $\Phi_2 = \Phi$. If P is in the region R_f, Green's Theorem yields Eq. D.15. A sphere of radius ϵ surrounds point P in order to exclude

it from the region of integration. The limit as ϵ approaches zero is taken just as was done for the 2-D case.

$$\Phi(P) = \frac{1}{4\pi} \iint_S [\frac{1}{r}\nabla\Phi - \Phi\nabla\frac{1}{r}] \cdot \mathbf{n} ds \tag{D.15}$$

If P is in R_i, then Green's Theorem yields

$$0 = \frac{1}{4\pi} \iint_S [\frac{1}{r}\nabla\Phi_i - \Phi_i\nabla\frac{1}{r}] \cdot \mathbf{n} ds \tag{D.16}$$

Equation D.17 is a result of the summation of Eq. D.15 and D.16.

$$\Phi(P) = \frac{1}{4\pi} \iint_S [\frac{1}{r}\nabla(\Phi - \Phi_i) - (\Phi - \Phi_i)\nabla\frac{1}{r}] \cdot \mathbf{n} ds \tag{D.17}$$

Since the functional forms of the integrand are that of a 3-D source distribution and a 3-D doublet distribution, the strengths of these distributions are the coefficients (Eq. D.7). Equation D.18 shows Eq. D.7 substituted into Eq. D.17.

$$\Phi(P) = -\frac{1}{4\pi} \iint_{S_B} [\sigma\frac{1}{r} - \mu\nabla\frac{1}{r}] \cdot \mathbf{n} ds + \frac{1}{4\pi} \iint_{S_w} [\mu_w\nabla\frac{1}{r}] \cdot \mathbf{n} ds + \phi_\infty(P) \tag{D.18}$$

The no-penetration boundary condition is imposed in the same implicit fashion as was done in 2-D in a Dirichlet formulation. The 3-D equivalent to Eq. D.9 is shown in Eq. D.19.

$$-\frac{1}{4\pi} \iint_{S_B} [\sigma\frac{1}{r} - \mu\frac{\partial}{\partial n}(\frac{1}{r})] ds + \frac{1}{4\pi} \iint_{S_w} [\mu_w\frac{\partial}{\partial n}(\frac{1}{r})] ds = 0 \tag{D.19}$$

If the interior boundary is discretized, then Eq. D.19 can be written in discretized form as in Eq. D.10 with the matrix components shown in Eq. D.20 and D.21.

$$B_{jk} = -\frac{1}{4\pi} \iint_k \frac{1}{r} ds \tag{D.20}$$

$$C_{jk} = \frac{1}{4\pi} \iint_k \frac{\partial}{\partial n}(\frac{1}{r}) ds \tag{D.21}$$

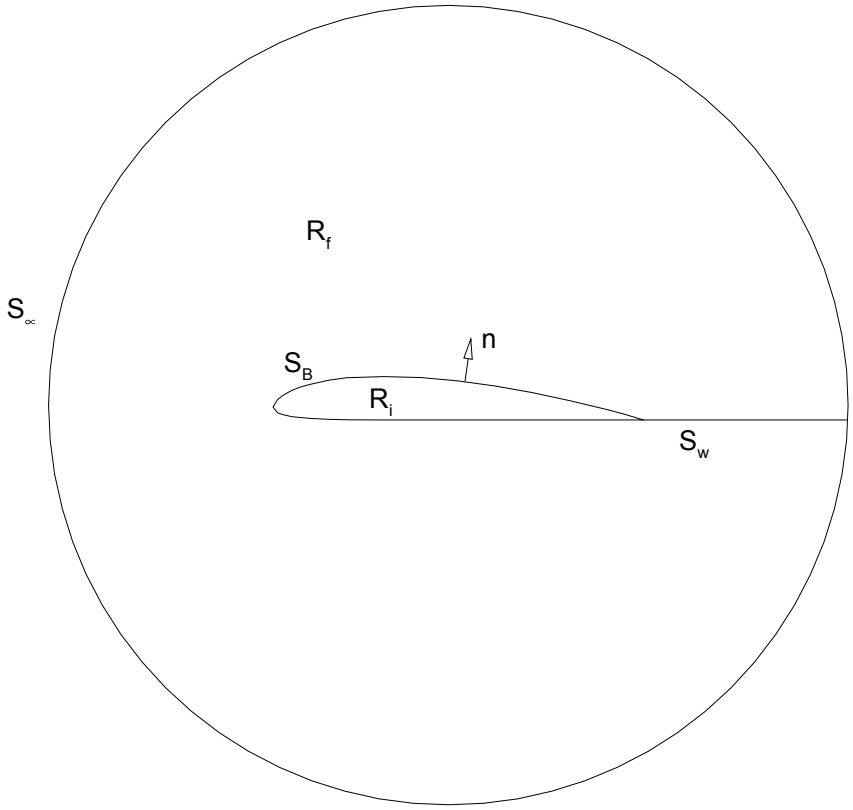

Figure D.1: Regions for Green's Identity Formulation of Panel method

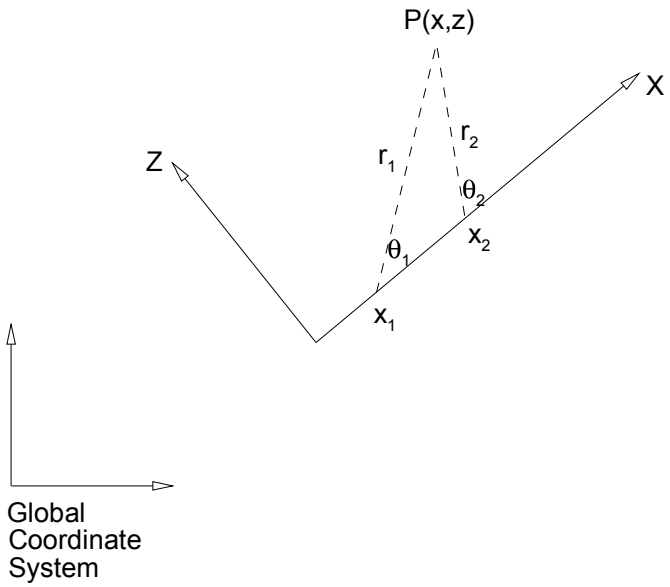

Figure D.2: Description of Panel Reference Frame

Appendix E

Computer Codes

The program, *main*, connects the optimizer to all of the analyses and allows the user to adjust all variables pertaining to the optimization. The user can adjust the design variables, variable bounds, constraints, and DOT software options. Call statements for the analysis codes allow for quick and easy replacement of the individual analyses.

E.1 main.f

```
************************************************************
* Program: mainc.f
* Author : Jason Tyll
* Date   : 4/1/97
* purpose: Calls DOT and analysis codes.
*          Set up for 7 Design Variable Problem.
************************************************************


      IMPLICIT DOUBLE PRECISION (A-H,O-Z)
      parameter(ndv=7,nrwk=1000,nriwk=300)
      dimension iprm(20), iwk(nriwk)

      dimension x(ndv), xl(ndv), xu(ndv), rprm(20), wk(nrwk)
      dimension xmap(ndv)
      dimension g(7)


      info=0
      method=3
      iprint=7
      ncon=7
```

```
*     Design variables and variable limits
      x(1)=0.042857
      x(2)=-0.05
      x(3)=0.03683
      x(4)=1.00105
      x(5)=0.10619
      x(6)=-8.3216
      x(7)=-4.8250
      xl(1)=0.286
      xl(2)=0.1667
      xl(3)=0.0377
      xl(4)=-0.0588
      xl(5)=-0.00840
      xl(6)=0.1416
      xl(7)=-0.0637
      xu(1)=1.
      xu(2)=1.
      xu(3)=1.
      xu(4)=1.
      xu(5)=1.
      xu(6)=1.
      xu(7)=1.
      minmax=-1
      do i=1,20
        rprm(i)=0.0
        iprm(i)=0
      end do
      rprm(7)=0.05
      iprm(2)=-1


*     Transform the design variables to nonscaled values
*     (Affine Scaling)
      xmap(1)=3.5*x(1)
      xmap(2)=0.5+3.0*x(2)
      xmap(3)=14.7+35.3*x(3)
      xmap(4)=1.111+1.887*x(4)
      xmap(5)=0.166+7.854*x(5)
      xmap(6)=21.67+2.3298*x(6)
      xmap(7)=20.24+3.768*x(7)

*     Call the analyses
      call geomc(xmap)
      call xinyout(xmap,ysep1,ysep2)
      call pnlbluffc3(cd,cl,xmap(6),xmap(7),ysep1,ysep2,con1,con2,
     1                cdbase,ITRBSEP,npanel,info)
      call mvehicc(vehicmss,wempty)
      call opcost(cd,cl,vehicmss,flevit,encost)
      call lifecost(wempty,encost,clc,coperate,cvehic,cinvest)
      write(*,*) wempty,encost,clc,coperate,cvehic
        write(*,*) i,cd,cl,cm
        write(*,*) i, con1, con2
```

```
*     Call the optimizer (DOT SQP Method)
10    call DOT(info,method,iprint,ndv,ncon,x,xl,xu,obj,minmax,
     1         g,rprm,iprm,wk,nrwk,iwk,nriwk)
*     If the optimization is complete, perform optimization at optimum
*      point and exit the program.
      if (info.eq.0) then
*       transform the design variables to unscaled values
*       (this mapping is repeated for the optimization loop which
*        begins at line 10)
        xmap(1)=3.5*x(1)
        xmap(2)=0.5+3.0*x(2)
        xmap(3)=14.7+35.3*x(3)
        xmap(4)=1.111+1.887*x(4)
        xmap(5)=0.166+7.854*x(5)
        xmap(6)=21.67+2.3298*x(6)
        xmap(7)=20.24+3.768*x(7)
        call geomc(xmap)
        call xinyout(xmap,ysep1,ysep2)
        call pnlbluffc3(cd,cl,xmap(6),xmap(7),ysep1,ysep2,con1,con2,
     1                  cdbase,ITRBSEP,npanel,info)
        call mvehicc(vehicmss,wempty)
        call opcost(cd,cl,vehicmss,flevit,encost)
        call lifecost(wempty,encost,clc,coperate,cvehic,cinvest)
        obj=abs(cd/cl)
        write(*,*) wempty,encost,clc,coperate,cvehic
        goto 20
      end if
*     Calculate the objective function and the constraints.
      if (info.eq.1) then
*       transform the design variables to unscaled values
*       (this mapping is repeated for the optimization loop which
*        begins at line 10)
        xmap(1)=3.5*x(1)
        xmap(2)=0.5+3.0*x(2)
        xmap(3)=14.7+35.3*x(3)
        xmap(4)=1.111+1.887*x(4)
        xmap(5)=0.166+7.854*x(5)
        xmap(6)=21.67+2.3298*x(6)
        xmap(7)=20.24+3.768*x(7)
        call geomc(xmap)
        call xinyout(xmap,ysep1,ysep2)
        call pnlbluffc3(cd,cl,xmap(6),xmap(7),ysep1,ysep2,con1,con2,
     1                  cdbase,ITRBSEP,npanel,info)
        call mvehicc(vehicmss,wempty)
        call opcost(cd,cl,vehicmss,flevit,encost)
        call lifecost(wempty,encost,clc,coperate,cvehic,cinvest)
        obj=abs(cd/cl)
```

```
        g(1)=(xmap(1)-xmap(2))/xmap(2)
        g(2)=-cdbase
        g(3)=con1
        g(4)=-con1
        g(5)=con2
        g(6)=-con2
        g(7)=dble(npanel/4-ITRBSEP)/dble(npanel)
        write(*,*) wempty,encost,clc,coperate,cvehic
        goto 10
      end if

20    continue
      stop
      end
```

The subroutine, *geomc* generates the side view geometry for the 2-D Northrop Grumman geometry definition. This definition involves 5 design variables and is identical from front to back.

E.2 geomc.f

```
      subroutine geomc(var)
*****************************************************************
* Program: magc.f
* Author:  Jason Tyll
* Date:    2/15/96
* Purpose: Generates side view geometry using
*          Grumman definition (AIAA 95-1908-CP)
*          Set up for 7 Design Variables.
*****************************************************************

      integer imax, jmax, kmax
      double precision l, h
      parameter(imax=17,jmax=20,kmax=20,l=.6,h=.35)
      double precision xn, xf, f, th, n
      double precision x(imax+1), yu(imax+1)
      double precision yl(imax+1),var(7)
      double precision pi,d
      double precision p, q, r, s
      integer i

      open(unit=9,file='mag.dat',status='unknown')

       th=var(3)
       n=var(4)
       f=var(5)
       xn=var(1)
       xf=var(2)

      pi=4.*atan(1.)
      th=th*pi/180.

      do i=1,imax+1
        x(i)=l-l*cos(.5*pi*(real(i)-1.)/(real(imax)))
      end do

      do i=1,imax+1
        if (x(i).le.xn) then
        yu(i)=n*tan(th)/(xn**((1.-n)/n))*x(i)**(1./n)
        yl(i)=-f*n*tan(th)*xn*(1.-(abs(x(i)-xn)/xn)**n)**(1./n)
        end if
        if (x(i).gt.xn .and. x(i).le.xf) then
        yu(i)=n*tan(th)*xn+tan(th)*(x(i)-xn)
        yl(i)=-f*n*tan(th)*xn
```

```
         end if
         if (x(i).gt.xf) then
         p=(-2.*(h-f*n*tan(th)*xn)+2.*(n*tan(th)*xn+tan(th)*
     1      (xf-xn))+tan(th)*(l-xf))/(l-xf)**3.
         q=(3.*(h-f*n*tan(th)*xn)-3.*(n*tan(th)*xn+tan(th)*
     1      (xf-xn))-2.*tan(th)*(l-xf))/(l-xf)**2.
         r=tan(th)
         s=n*tan(th)*xn+tan(th)*(xf-xn)
         yu(i)=p*(x(i)-xf)**3.+q*(x(i)-xf)**2.+r*(x(i)-xf)+s
         yl(i)=-f*n*tan(th)*xn
         end if
       end do

*      Output the geometry.
       do i=1,imax+1
         write(9,*) 4.*l-x(i), yl(i)+f*n*tan(th)*xn
       end do
       do i=1,imax
         write(9,*) 3.*l-real(i)/real(imax+1)*2.*l, 0.
       end do
       do i=imax+1,1,-1
         write(9,*) x(i), yl(i)+f*n*tan(th)*xn
       end do
       do i=2,imax+1
         write(9,*) x(i), yu(i)+f*n*tan(th)*xn
       end do
       do i=1,imax
         write(9,*) l+real(i)/real(imax+1)*2.*l, yu(imax+1)
     1             +f*n*tan(th)*xn
       end do
       do i=imax+1,1,-1
         write(9,*) 4.*l-x(i), yu(i)+f*n*tan(th)*xn
       end do


       close(9)
       return
       end
```

The aerodynamic analysis using the unsteady vortex panel method for separated flow over bluff bodies in ground effect is performed in subroutine, *pnlbluff*. The user can make adjustments to variables involved in the aerodynamic analysis in the "parameter" statements and immediately following the variable declarations.

E.3 pnlbluff.f

```
      subroutine pnlbluffc3(cd,cl,xsep1,xsep2,ysep1,ysep2,
     1                      con1,con2,cdbase,ITRBSEP,n,infodot)
************************************************************
* Program: pnlbluffc3.f
* Author:  Jason Tyll
* Date:    4/1/97 (updated to c3 on 4/17/97)
* Purpose: unsteady vortex panel method
*          (method was developed from Mook, JFE, 1994)
*          For separated flow over bluff bodies.
*          7 Design variable formulation.
*          Use cubic splines to model piecewise linear pressure
*            distribution for the Stratford Criterion.
************************************************************

*     declarations
      integer i, j, n, tstep, timemax, tt, t,  nmax, info, lwork
      integer i1,i2
      integer sep1, sep2, nmin,nminest, infodot,ITRBSEP
      integer step, tmmax
      integer nstag, icon
      double precision nu, rho, strat
      double precision ratio, time, L, deltt, h
      parameter(nmax=200, ratio=1.,time=0.43,tmmax=600,L=24.,h=3.5)
      parameter(nu=1.56E-5, rho=1.177)
      parameter(strat=0.39)
      double precision pi, alpha, al, gnd, alt
      double precision xmom, zmom, sigma(tmmax)
      double precision xx(nmax+1), yy(nmax+1)
      double precision xxw1(tmmax),yyw1(tmmax)
      double precision xxw2(tmmax),yyw2(tmmax)
      double precision xxwtmp1(tmmax),yywtmp1(tmmax)
      double precision xxwtmp2(tmmax),yywtmp2(tmmax)
      double precision deltl(nmax), co(nmax,2)
      double precision d1, d2, x, y, deltth, R
      double precision v1x(nmax), v1y(nmax), v2x(nmax), v2y(nmax)
      double precision vv1x(nmax), vv1y(nmax), vv2x(nmax), vv2y(nmax)
      double precision a(nmax+1,nmax), b(nmax,1)
      double precision g(nmax),gw1(tmmax),gw2(tmmax),glast(nmax)
```

```
      double precision u, v
      double precision work(2*nmax+1)
      double precision delx, dely, cl, cd, cm, cp(nmax),cf(2000)
      double precision cdbase, vel(nmax)
      double precision error
      double precision uinf
      double precision s(nmax+1),dcpds(nmax),c(nmax)
      double precision cpmin,reo, xxmin, cfgap, dpdx
      double precision ssep1,ssep2,gsep1,gsep2
      double precision xsep1,xsep2,ysep1,ysep2
      double precision glast_sep1, glast_sep2
      double precision atmp(nmax+1,nmax)
      double precision clavg, cdavg, cmavg, cpavg(nmax)
      double precision clmin,clmax,cdmin,cdmax,cmmin,cmmax
      double precision split, combine
      double precision phib0(nmax,nmax),phib1(nmax,nmax)
      double precision phifs(nmax),phi(nmax),philast(nmax)
      double precision phivu(nmax,tmmax),phivl(nmax,tmmax)
      double precision con1, con2
      double precision fpo,fpn,root1,root2,smin,p0,p1,cpmintry
      double precision aa(nmax),bb(nmax),cc(nmax),dd(nmax)
      real time1, time2, tarray(2)

      open(unit=8,file='cpsd.dat',status='unknown')
      open(unit=9,file='mag.dat',status='old')
      open(unit=69,file='thist.dat',status='unknown')


      pi=4.*atan(1.)


*     user input
*     The number of panels (must be divisible by 4)
      n=104
*     The angle of attack in degrees (must be zero for ground effect)
      alpha=0.
      al=alpha*pi/180.
*     Set gnd to 0. for OGE or 1. for IGE
      gnd=1.
*     altitude in units of cord
      alt=0.1
*     separation panel #1
*      sep1=2
*     separation panel #2
*      sep2=n
*     Free Stream Velocity
      uinf=134.


*     calculate time increment and number of time steps
      deltt=2.*L/n/uinf/ratio
      timemax=idnint(time/deltt)
```

```
*     Initialize Arrays
      do i=1,nmax
        deltl(i)=0.
        co(i,2)=0.
        v1x(i)=0.
        v1y(i)=0.
        v2x(i)=0.
        v2y(i)=0.
        vv1x(i)=0.
        vv1y(i)=0.
        vv2x(i)=0.
        vv2y(i)=0.
        b(i,1)=0.
        g(i)=0.
        glast(i)=0.
        cp(i)=0.
        cpavg(i)=0.
        cf(i)=0.
        vel(i)=0.
        dcpds(i)=0.
        c(i)=0.
      end do
      do i=1,timemax
        xxw1(i)=0.
        xxw2(i)=0.
        yyw1(i)=0.
        yyw2(i)=0.
        gw1(i)=0.
        gw2(i)=0.
        xxwtmp1(i)=0.
        xxwtmp2(i)=0.
        yywtmp1(i)=0.
        yywtmp2(i)=0.
        sigma(i)=0.
      end do
      do i=1,nmax+1
        xx(i)=0.
        yy(i)=0.
        s(i)=0.
      end do
      do i=1,nmax+1
        do j=2,nmax
          a(i,j)=0.
          atmp(i,j)=0.
        end do
      end do
      do i=1,2*nmax+1
        work(i)=0.
      end do
      do i=1,nmax
        do j=1,nmax
          phib0(i,j)=0.
          phib1(i,j)=0.
```

```
        end do
        phifs(i)=0.
        phi(i)=0.
        philast(i)=0.
        do j=1,timemax
          phivu(i,j)=0.
          phivl(i,j)=0.
        end do
      end do
*******

*     point about which pitching moment is calculated
      xmom=0.
      zmom=0.405+alt

*     zero out the average force & moment coeff
      clavg=0.
      cdavg=0.
      cmavg=0.
      do i=1,n
        cpavg(i)=0.
      end do

*     read in the panel end points
*     note: global position variables (xx,yy), local variables (x,y)
      do j=1,n+1
        read(9,*) xx(j),yy(j)
      end do

      do j=1,n+1
        yy(j)=yy(j)+alt
      end do

*     set initial separation points
      ysep1=ysep1+alt
      ysep2=ysep2+alt
      sep1=2
      do j=2,n/2
        if (abs(xsep1-xx(j)).lt.abs(xsep1-xx(sep1))) then
          sep1=j
        end if
      end do
      sep2=n
      do j=n/2,n+1
        if (abs(xsep2-xx(j)).lt.abs(xsep2-xx(sep2))) then
          sep2=j
        end if
      end do
      gsep1=0.
      gsep2=0.

*     calculate panel lengths
      do j=1,n
        deltl(j)=sqrt((xx(j+1)-xx(j))**2.+(yy(j+1)-yy(j))**2.)
```

```
      end do

*     establish surface points (colocation points)
      do j=1,n
        co(j,1)=(xx(j)+xx(j+1))/2.
        co(j,2)=(yy(j)+yy(j+1))/2.
      end do

****Start Clock****
      call etime(tarray)
      time1=tarray(1)

*     establish influence coefficients
      do j=1,n

      phifs(j)=uinf*(xx(j)*cos(al)+yy(j)*sin(al))

        do i=1,n


          d1=(xx(i+1)-xx(i))/deltl(i)
          d2=(yy(i+1)-yy(i))/deltl(i)

          x=d1*(co(j,1)-xx(i))+d2*(co(j,2)-yy(i))
          y=-d2*(co(j,1)-xx(i))+d1*(co(j,2)-yy(i))+1.E-12
          deltth=atan(x/y)-atan((x-deltl(i))/y)
          R=((x-deltl(i))**2.+y**2.)/(x**2.+y**2.)

          v1x(i)=1./(2.*pi*deltl(i))*
     1           ((deltl(i)-x)*deltth-0.5*y*log(R))
          v1y(i)=1./(2.*pi*deltl(i))*
     1           (y*deltth-deltl(i)+0.5*(deltl(i)-x)*log(R))
          v2x(i)=1./(2.*pi*deltl(i))*(x*deltth+0.5*y*log(R))
          v2y(i)=1./(2.*pi*deltl(i))*
     1           (deltl(i)-y*deltth+0.5*x*log(R))

          vv1x(i)=d1*v1x(i)-d2*v1y(i)
          vv1y(i)=d2*v1x(i)+d1*v1y(i)
          vv2x(i)=d1*v2x(i)-d2*v2y(i)
          vv2y(i)=d2*v2x(i)+d1*v2y(i)

          phib0(j,i)=-1./(2.*pi)*(x*atan(y/x)-(x-deltl(i))*
     1               atan(y/(x-deltl(i)))-0.5*y*log(R))
          phib1(j,i)=-1./(2.*pi)*(-x*y*0.5*log(R)-0.5*y*deltl(i)
     1               +(x**2.-y**2.)*0.5*atan(y/x)-
     1               (x**2.-deltl(i)**2.-y**2.)*0.5*atan(y/
     1               (x-deltl(i))))
        end do

        do i=2,n
          a(j,i)=-(vv2x(i-1)+vv1x(i))*(yy(j+1)-yy(j))/deltl(j)
     1           +(vv2y(i-1)+vv1y(i))*(xx(j+1)-xx(j))/deltl(j)
```

```
         end do

         a(j,1)=-(vv2x(n)+vv1x(1))*(yy(j+1)-yy(j))/deltl(j)
     1           +(vv2y(n)+vv1y(1))*(xx(j+1)-xx(j))/deltl(j)

         if (gnd.eq.1.) then
         do i=1,n


           d1=(xx(i+1)-xx(i))/deltl(i)
           d2=(yy(i+1)-yy(i))/deltl(i)

           x=d1*(co(j,1)-xx(i))+d2*(co(j,2)+yy(i))
           y=-d2*(co(j,1)-xx(i))+d1*(co(j,2)+yy(i))
           deltth=atan(x/y)-atan((x-deltl(i))/y)
           R=((x-deltl(i))**2.+y**2.)/(x**2.+y**2.)

           v1x(i)=1./(2.*pi*deltl(i))*
     1           ((deltl(i)-x)*deltth-0.5*y*log(R))
           v1y(i)=1./(2.*pi*deltl(i))*
     1           (y*deltth-deltl(i)+0.5*(deltl(i)-x)*log(R))
           v2x(i)=1./(2.*pi*deltl(i))*(x*deltth+0.5*y*log(R))
           v2y(i)=1./(2.*pi*deltl(i))*
     1           (deltl(i)-y*deltth+0.5*x*log(R))

           vv1x(i)=d1*v1x(i)-d2*v1y(i)
           vv1y(i)=d2*v1x(i)+d1*v1y(i)
           vv2x(i)=d1*v2x(i)-d2*v2y(i)
           vv2y(i)=d2*v2x(i)+d1*v2y(i)

         end do

         do i=2,n
           a(j,i)=a(j,i)+(vv2x(i-1)+vv1x(i))*(yy(j+1)-yy(j))/deltl(j)
     1           -(vv2y(i-1)+vv1y(i))*(xx(j+1)-xx(j))/deltl(j)
         end do

         a(j,1)=a(j,1)+(vv2x(n)+vv1x(1))*(yy(j+1)-yy(j))/deltl(j)
     1           -(vv2y(n)+vv1y(1))*(xx(j+1)-xx(j))/deltl(j)



         end if

       end do

*      establish constraint equation
       do i=2,n
         a(n+1,i)=0.5*(deltl(i-1)+deltl(i))
       end do

       a(n+1,1)=0.5*(deltl(n)+deltl(1))
```

```
*     begin time steps
      do tstep=2,timemax

*     calculate sigma (votex blob diameter)
      sigma(tstep)=1.75*uinf*deltt

*     update sigma values
      if (tstep.gt.2) then
        do t=2,tstep-1
          sigma(t)=sqrt(sigma(t)**2.+4.*nu*deltt)
        end do
      end if

*     establish strength of shed wake
      gw1(tstep)=-(gsep1**2.)*deltt/2.
      gw2(tstep)=(gsep2**2.)*deltt/2.

*     location of the shed wake
          yyw1(tstep)=ysep1
          yyw2(tstep)=ysep2
          if (tstep.eq.3) then
            xxw1(tstep)=xsep1+0.1*deltl(sep1)
            xxw2(tstep)=xsep2+0.1*deltl(sep2)
          else
            xxw1(tstep)=xsep1+dabs(gsep1)*deltt/5.
            xxw2(tstep)=xsep2+dabs(gsep2)*deltt/5.
          end if


*     Establish  RHS
      do j=1,n
        b(j,1)=uinf*(dcos(al)*(yy(j+1)-yy(j))-dsin(al)
     1         *(xx(j+1)-xx(j)))/deltl(j)
        if (tstep.le.200) then
        do t=2, tstep
          b(j,1)=b(j,1)+1./(2.*pi)/deltl(j)/((co(j,1)-xxw1(t))**2.
     1             +(co(j,2)-yyw1(t))**2.+sigma(t)**2.)*((co(j,2)-
     1             yyw1(t))*(yy(j+1)-yy(j))+(co(j,1)-xxw1(t))*
     1             (xx(j+1)-xx(j)))*gw1(t)
          b(j,1)=b(j,1)+1./(2.*pi)/deltl(j)/((co(j,1)-xxw2(t))**2.
     1             +(co(j,2)-yyw2(t))**2.+sigma(t)**2.)*((co(j,2)-
     1             yyw2(t))*(yy(j+1)-yy(j))+(co(j,1)-xxw2(t))*
     1             (xx(j+1)-xx(j)))*gw2(t)
          b(j,1)=b(j,1)-gnd/(2.*pi)/deltl(j)/((co(j,1)-xxw1(t))**2.
     1             +(co(j,2)+yyw1(t))**2.+sigma(t)**2.)*((co(j,2)+
     1             yyw1(t))*(yy(j+1)-yy(j))+(co(j,1)-xxw1(t))*
     1             (xx(j+1)-xx(j)))*gw1(t)
          b(j,1)=b(j,1)-gnd/(2.*pi)/deltl(j)/((co(j,1)-xxw2(t))**2.
     1             +(co(j,2)+yyw2(t))**2.+sigma(t)**2.)*((co(j,2)+
     1             yyw2(t))*(yy(j+1)-yy(j))+(co(j,1)-xxw2(t))*
     1             (xx(j+1)-xx(j)))*gw2(t)
```

```
         end do
         else
         do t=tstep-199,tstep
           b(j,1)=b(j,1)+1./(2.*pi)/deltl(j)/((co(j,1)-xxw1(t))**2.
     1             +(co(j,2)-yyw1(t))**2.+sigma(t)**2.)*((co(j,2)-
     1             yyw1(t))*(yy(j+1)-yy(j))+(co(j,1)-xxw1(t))*
     1             (xx(j+1)-xx(j)))*gw1(t)
           b(j,1)=b(j,1)+1./(2.*pi)/deltl(j)/((co(j,1)-xxw2(t))**2.
     1             +(co(j,2)-yyw2(t))**2.+sigma(t)**2.)*((co(j,2)-
     1             yyw2(t))*(yy(j+1)-yy(j))+(co(j,1)-xxw2(t))*
     1             (xx(j+1)-xx(j)))*gw2(t)
           b(j,1)=b(j,1)-gnd/(2.*pi)/deltl(j)/((co(j,1)-xxw1(t))**2.
     1             +(co(j,2)+yyw1(t))**2.+sigma(t)**2.)*((co(j,2)+
     1             yyw1(t))*(yy(j+1)-yy(j))+(co(j,1)-xxw1(t))*
     1             (xx(j+1)-xx(j)))*gw1(t)
           b(j,1)=b(j,1)-gnd/(2.*pi)/deltl(j)/((co(j,1)-xxw2(t))**2.
     1             +(co(j,2)+yyw2(t))**2.+sigma(t)**2.)*((co(j,2)+
     1             yyw2(t))*(yy(j+1)-yy(j))+(co(j,1)-xxw2(t))*
     1             (xx(j+1)-xx(j)))*gw2(t)
         end do
         end if

       end do


       b(n+1,1)=0.
       do t=2,tstep
         b(n+1,1)=b(n+1,1)-gw1(t)-gw2(t)
       end do

*      glast will be used to calc the dynamic term in cp equation
       do i=1,n
         glast(i)=g(i)
         philast(i)=phi(i)
       end do

       do j=1,n+1
         do i=1,n
           atmp(j,i)=a(j,i)
         end do
       end do

*      solve system of equations using a linear least squares
*      optimization
       lwork=2*nmax+1
       call DGELS('N',n+1,n,1,atmp,nmax+1,b,nmax+1,work,lwork,info)
       do i=1,n
         g(i)=b(i,1)
         phi(i)=phifs(i)
       end do
       do j=1,n
         do i=1,n-1
           phi(j)=phi(j)+g(i)*phib0(j,i)+g(i+1)*phib1(j,i)
```

```
        end do
       phi(j)=phi(j)+g(n)*phib0(j,n)+g(1)*phib1(j,n)
       end do

*       calculate gsep at prescribed xsep location
        do i=1,n/2-1
          if (xsep1.ge. xx(i+1) .and. xsep1 .le. xx(i)) then
          gsep1=g(i+1)+(xsep1-xx(i+1))/(xx(i)-xx(i+1))*(g(i)-g(i+1))
          end if
        end do
        do i=n/2,n
          if (xsep2.le. xx(i+1) .and. xsep2 .ge. xx(i)) then
          gsep2=g(i)+(xsep2-xx(i))/(xx(i+1)-xx(i))*(g(i+1)-g(i))
          end if
        end do


******update shed vorticy locations for bottom vortex sheet*****
       if (tstep.le.200) then
         i1=2
         i2=tstep
       else
         i1=tstep-199
         i2=tstep
       end if
       do t=i1,i2

       u=0.
       v=0.

*      velocity induced by free stream
       u=uinf*dcos(al)
       v=uinf*dsin(al)

*      velocity induced by airfoil
       do i=1,n
         d1=(xx(i+1)-xx(i))/deltl(i)
         d2=(yy(i+1)-yy(i))/deltl(i)

         x=d1*(xxw1(t)-xx(i))+d2*(yyw1(t)-yy(i))
         y=-d2*(xxw1(t)-xx(i))+d1*(yyw1(t)-yy(i))+1.E-12
         deltth=atan(x/y)-atan((x-deltl(i))/y)
         R=((x-deltl(i))**2.+y**2.)/(x**2.+y**2.)

         v1x(i)=1./(2.*pi*deltl(i))*
      1         ((deltl(i)-x)*deltth-0.5*y*log(R))
         v1y(i)=1./(2.*pi*deltl(i))*
      1         (y*deltth-deltl(i)+0.5*(deltl(i)-x)*log(R))
         v2x(i)=1./(2.*pi*deltl(i))*(x*deltth+0.5*y*log(R))
         v2y(i)=1./(2.*pi*deltl(i))*
      1         (deltl(i)-y*deltth+0.5*x*log(R))

         vv1x(i)=d1*v1x(i)-d2*v1y(i)
         vv1y(i)=d2*v1x(i)+d1*v1y(i)
         vv2x(i)=d1*v2x(i)-d2*v2y(i)
```

```
        vv2y(i)=d2*v2x(i)+d1*v2y(i)

        if (i.eq.n) then
          u=u+g(i)*vv1x(i)+g(1)*vv2x(i)
          v=v+g(i)*vv1y(i)+g(1)*vv2y(i)
        end if
        if (i.ne.n) then
          u=u+g(i)*vv1x(i)+g(i+1)*vv2x(i)
          v=v+g(i)*vv1y(i)+g(i+1)*vv2y(i)
        end if

        phivl(i,t)=-1./(2.*pi)*atan((yy(i)-yyw1(t))/(xx(i)-xxw1(t)))
      end do


      if (gnd.eq.1.) then
        do i=1,n
        d1=(xx(i+1)-xx(i))/deltl(i)
        d2=(yy(i+1)-yy(i))/deltl(i)

        x=d1*(xxw1(t)-xx(i))+d2*(yyw1(t)+yy(i))
        y=-d2*(xxw1(t)-xx(i))+d1*(yyw1(t)+yy(i))
        deltth=atan(x/y)-atan((x-deltl(i))/y)
        R=((x-deltl(i))**2.+y**2.)/(x**2.+y**2.)

        v1x(i)=1./(2.*pi*deltl(i))*
     1         ((deltl(i)-x)*deltth-0.5*y*log(R))
        v1y(i)=1./(2.*pi*deltl(i))*
     1         (y*deltth-deltl(i)+0.5*(deltl(i)-x)*log(R))
        v2x(i)=1./(2.*pi*deltl(i))*(x*deltth+0.5*y*log(R))
        v2y(i)=1./(2.*pi*deltl(i))*
     1         (deltl(i)-y*deltth+0.5*x*log(R))

        vv1x(i)=d1*v1x(i)-d2*v1y(i)
        vv1y(i)=d2*v1x(i)+d1*v1y(i)
        vv2x(i)=d1*v2x(i)-d2*v2y(i)
        vv2y(i)=d2*v2x(i)+d1*v2y(i)

        if (i.eq.n) then
          u=u-g(i)*vv1x(i)-g(1)*vv2x(i)
          v=v-g(i)*vv1y(i)-g(1)*vv2y(i)
        end if
        if (i.ne.n) then
          u=u-g(i)*vv1x(i)-g(i+1)*vv2x(i)
          v=v-g(i)*vv1y(i)-g(i+1)*vv2y(i)
        end if

      end do
      end if

*     velocity induced by wake
      if (tstep.le.200) then
        do tt=2, tstep
        if(tt.ne.t) then
          u=u+gw1(tt)/(2.*pi)*(yyw1(t)-yyw1(tt))/
```

```
1     ((xxw1(t)-xxw1(tt))**2.+(yyw1(t)-yyw1(tt))**2.
1     +sigma(tt)**2.)+gw2(tt)/(2.*pi)*(yyw1(t)-yyw2(tt))/
1     ((xxw1(t)-xxw2(tt))**2.+(yyw1(t)-yyw2(tt))**2.
1     +sigma(tt)**2.)
     u=u-gnd*gw1(tt)/(2.*pi)*(yyw1(t)+yyw1(tt))/
1     ((xxw1(t)-xxw1(tt))**2.+(yyw1(t)+yyw1(tt))**2.
1     +sigma(tt)**2.)-gnd*gw2(tt)/(2.*pi)*(yyw1(t)+yyw2(tt))/
1     ((xxw1(t)-xxw2(tt))**2.+(yyw1(t)+yyw2(tt))**2.
1     +sigma(tt)**2.)
     v=v-gw1(tt)/(2.*pi)*(xxw1(t)-xxw1(tt))/
1     ((xxw1(t)-xxw1(tt))**2.+(yyw1(t)-yyw1(tt))**2.
1     +sigma(tt)**2.)-gw2(tt)/(2.*pi)*(xxw1(t)-xxw2(tt))/
1     ((xxw1(t)-xxw2(tt))**2.+(yyw1(t)-yyw2(tt))**2.
1     +sigma(tt)**2.)
     v=v+gnd*gw1(tt)/(2.*pi)*(xxw1(t)-xxw1(tt))/
1     ((xxw1(t)-xxw1(tt))**2.+(yyw1(t)+yyw1(tt))**2.
1     +sigma(tt)**2.)+gnd*gw2(tt)/(2.*pi)*(xxw1(t)-xxw2(tt))/
1     ((xxw1(t)-xxw2(tt))**2.+(yyw1(t)+yyw2(tt))**2.
1     +sigma(tt)**2.)
   else
     u=u
     v=v
   end if
   end do
 else
   do tt=tstep-199,tstep
   if(tt.ne.t) then
     u=u+gw1(tt)/(2.*pi)*(yyw1(t)-yyw1(tt))/
1     ((xxw1(t)-xxw1(tt))**2.+(yyw1(t)-yyw1(tt))**2.
1     +sigma(tt)**2.)+gw2(tt)/(2.*pi)*(yyw1(t)-yyw2(tt))/
1     ((xxw1(t)-xxw2(tt))**2.+(yyw1(t)-yyw2(tt))**2.
1     +sigma(tt)**2.)
     u=u-gnd*gw1(tt)/(2.*pi)*(yyw1(t)+yyw1(tt))/
1     ((xxw1(t)-xxw1(tt))**2.+(yyw1(t)+yyw1(tt))**2.
1     +sigma(tt)**2.)-gnd*gw2(tt)/(2.*pi)*(yyw1(t)+yyw2(tt))/
1     ((xxw1(t)-xxw2(tt))**2.+(yyw1(t)+yyw2(tt))**2.
1     +sigma(tt)**2.)
     v=v-gw1(tt)/(2.*pi)*(xxw1(t)-xxw1(tt))/
1     ((xxw1(t)-xxw1(tt))**2.+(yyw1(t)-yyw1(tt))**2.
1     +sigma(tt)**2.)-gw2(tt)/(2.*pi)*(xxw1(t)-xxw2(tt))/
1     ((xxw1(t)-xxw2(tt))**2.+(yyw1(t)-yyw2(tt))**2.
1     +sigma(tt)**2.)
     v=v+gnd*gw1(tt)/(2.*pi)*(xxw1(t)-xxw1(tt))/
1     ((xxw1(t)-xxw1(tt))**2.+(yyw1(t)+yyw1(tt))**2.
1     +sigma(tt)**2.)+gnd*gw2(tt)/(2.*pi)*(xxw1(t)-xxw2(tt))/
1     ((xxw1(t)-xxw2(tt))**2.+(yyw1(t)+yyw2(tt))**2.
1     +sigma(tt)**2.)
   else
     u=u
     v=v
   end if
```

```
        end do
      end if

      xxwtmp1(t)=xxw1(t)+u*deltt
      yywtmp1(t)=yyw1(t)+v*deltt

      end do
**************************

******update shed vorticy locations for top  vortex sheet*****
      if (tstep.le.200) then
        i1=2
        i2=tstep
      else
        i1=tstep-199
        i2=tstep
      end if
      do t=i1,i2

      u=0.
      v=0.

*     velocity induced by free stream
      u=uinf*dcos(al)
      v=uinf*dsin(al)

*     velocity induced by airfoil
      do i=1,n
        d1=(xx(i+1)-xx(i))/deltl(i)
        d2=(yy(i+1)-yy(i))/deltl(i)

        x=d1*(xxw2(t)-xx(i))+d2*(yyw2(t)-yy(i))
        y=-d2*(xxw2(t)-xx(i))+d1*(yyw2(t)-yy(i))+1.E-12
        deltth=atan(x/y)-atan((x-deltl(i))/y)
        R=((x-deltl(i))**2.+y**2.)/(x**2.+y**2.)

        v1x(i)=1./(2.*pi*deltl(i))*
     1         ((deltl(i)-x)*deltth-0.5*y*log(R))
        v1y(i)=1./(2.*pi*deltl(i))*
     1         (y*deltth-deltl(i)+0.5*(deltl(i)-x)*log(R))
        v2x(i)=1./(2.*pi*deltl(i))*(x*deltth+0.5*y*log(R))
        v2y(i)=1./(2.*pi*deltl(i))*
     1         (deltl(i)-y*deltth+0.5*x*log(R))

        vv1x(i)=d1*v1x(i)-d2*v1y(i)
        vv1y(i)=d2*v1x(i)+d1*v1y(i)
        vv2x(i)=d1*v2x(i)-d2*v2y(i)
        vv2y(i)=d2*v2x(i)+d1*v2y(i)

        if (i.eq.n) then
          u=u+g(i)*vv1x(i)+g(1)*vv2x(i)
          v=v+g(i)*vv1y(i)+g(1)*vv2y(i)
        end if
        if (i.ne.n) then
          u=u+g(i)*vv1x(i)+g(i+1)*vv2x(i)
```

```
          v=v+g(i)*vv1y(i)+g(i+1)*vv2y(i)
        end if

      phivu(i,t)=-1./(2.*pi)*atan((yy(i)-yyw2(t))/(xx(i)-xxw2(t)))
      end do

      if (gnd.eq.1.) then
        do i=1,n
        d1=(xx(i+1)-xx(i))/deltl(i)
        d2=(yy(i+1)-yy(i))/deltl(i)

        x=d1*(xxw2(t)-xx(i))+d2*(yyw2(t)+yy(i))
        y=-d2*(xxw2(t)-xx(i))+d1*(yyw2(t)+yy(i))
        deltth=atan(x/y)-atan((x-deltl(i))/y)
        R=((x-deltl(i))**2.+y**2.)/(x**2.+y**2.)

        v1x(i)=1./(2.*pi*deltl(i))*
     1         ((deltl(i)-x)*deltth-0.5*y*log(R))
        v1y(i)=1./(2.*pi*deltl(i))*
     1         (y*deltth-deltl(i)+0.5*(deltl(i)-x)*log(R))
        v2x(i)=1./(2.*pi*deltl(i))*(x*deltth+0.5*y*log(R))
        v2y(i)=1./(2.*pi*deltl(i))*
     1         (deltl(i)-y*deltth+0.5*x*log(R))

        vv1x(i)=d1*v1x(i)-d2*v1y(i)
        vv1y(i)=d2*v1x(i)+d1*v1y(i)
        vv2x(i)=d1*v2x(i)-d2*v2y(i)
        vv2y(i)=d2*v2x(i)+d1*v2y(i)

        if (i.eq.n) then
          u=u-g(i)*vv1x(i)-g(1)*vv2x(i)
          v=v-g(i)*vv1y(i)-g(1)*vv2y(i)
        end if
        if (i.ne.n) then
          u=u-g(i)*vv1x(i)-g(i+1)*vv2x(i)
          v=v-g(i)*vv1y(i)-g(i+1)*vv2y(i)
        end if

      end do
      end if

*     velocity induced by wake
      if (tstep.le.200) then
        do tt=2, tstep
        if(tt.ne.t) then
          u=u+gw1(tt)/(2.*pi)*(yyw2(t)-yyw1(tt))/
     1     ((xxw2(t)-xxw1(tt))**2.+(yyw2(t)-yyw1(tt))**2.
     1     +sigma(tt)**2.)+gw2(tt)/(2.*pi)*(yyw2(t)-yyw2(tt))/
     1     ((xxw2(t)-xxw2(tt))**2.+(yyw2(t)-yyw2(tt))**2.
     1     +sigma(tt)**2.)
          u=u-gnd*gw1(tt)/(2.*pi)*(yyw2(t)+yyw1(tt))/
     1     ((xxw2(t)-xxw1(tt))**2.+(yyw2(t)+yyw1(tt))**2.
     1     +sigma(tt)**2.)-gnd*gw2(tt)/(2.*pi)*(yyw2(t)+yyw2(tt))/
```

```
1     ((xxw2(t)-xxw2(tt))**2.+(yyw2(t)+yyw2(tt))**2.
1     +sigma(tt)**2.)
     v=v-gw1(tt)/(2.*pi)*(xxw2(t)-xxw1(tt))/
1     ((xxw2(t)-xxw1(tt))**2.+(yyw2(t)-yyw1(tt))**2.
1     +sigma(tt)**2.)-gw2(tt)/(2.*pi)*(xxw2(t)-xxw2(tt))/
1     ((xxw2(t)-xxw2(tt))**2.+(yyw2(t)-yyw2(tt))**2.
1     +sigma(tt)**2.)
     v=v+gnd*gw1(tt)/(2.*pi)*(xxw2(t)-xxw1(tt))/
1     ((xxw2(t)-xxw1(tt))**2.+(yyw2(t)+yyw1(tt))**2.
1     +sigma(tt)**2.)+gnd*gw2(tt)/(2.*pi)*(xxw2(t)-xxw2(tt))/
1     ((xxw2(t)-xxw2(tt))**2.+(yyw2(t)+yyw2(tt))**2.
1     +sigma(tt)**2.)
   else
     u=u
     v=v
   end if
   end do
 else
   do tt=tstep-199,tstep
   if(tt.ne.t) then
     u=u+gw1(tt)/(2.*pi)*(yyw2(t)-yyw1(tt))/
1     ((xxw2(t)-xxw1(tt))**2.+(yyw2(t)-yyw1(tt))**2.
1     +sigma(tt)**2.)+gw2(tt)/(2.*pi)*(yyw2(t)-yyw2(tt))/
1     ((xxw2(t)-xxw2(tt))**2.+(yyw2(t)-yyw2(tt))**2.
1     +sigma(tt)**2.)
     u=u-gnd*gw1(tt)/(2.*pi)*(yyw2(t)+yyw1(tt))/
1     ((xxw2(t)-xxw1(tt))**2.+(yyw2(t)+yyw1(tt))**2.
1     +sigma(tt)**2.)-gnd*gw2(tt)/(2.*pi)*(yyw2(t)+yyw2(tt))/
1     ((xxw2(t)-xxw2(tt))**2.+(yyw2(t)+yyw2(tt))**2.
1     +sigma(tt)**2.)
     v=v-gw1(tt)/(2.*pi)*(xxw2(t)-xxw1(tt))/
1     ((xxw2(t)-xxw1(tt))**2.+(yyw2(t)-yyw1(tt))**2.
1     +sigma(tt)**2.)-gw2(tt)/(2.*pi)*(xxw2(t)-xxw2(tt))/
1     ((xxw2(t)-xxw2(tt))**2.+(yyw2(t)-yyw2(tt))**2.
1     +sigma(tt)**2.)
     v=v+gnd*gw1(tt)/(2.*pi)*(xxw2(t)-xxw1(tt))/
1     ((xxw2(t)-xxw1(tt))**2.+(yyw2(t)+yyw1(tt))**2.
1     +sigma(tt)**2.)+gnd*gw2(tt)/(2.*pi)*(xxw2(t)-xxw2(tt))/
1     ((xxw2(t)-xxw2(tt))**2.+(yyw2(t)+yyw2(tt))**2.
1     +sigma(tt)**2.)
   else
     u=u
     v=v
   end if
   end do
 end if

 xxwtmp2(t)=xxw2(t)+u*deltt
 yywtmp2(t)=yyw2(t)+v*deltt

 end do
```

```
      do t=1,tstep
        xxw1(t)=xxwtmp1(t)
        yyw1(t)=yywtmp1(t)
        xxw2(t)=xxwtmp2(t)
        yyw2(t)=yywtmp2(t)
      end do

      do j=1,n
      do t=1,tstep
        phi(j)=phi(j)+gw1(t)*phivl(j,t)+gw2(t)*phivu(j,t)
      end do
      end do


*****update separation location using the Stratford Criteria
      s(1)=0.0
      do  i=2,n+1
        s(i)=s(i-1)+SQRT((xx(i)-xx(i-1))**2.+(yy(i)-yy(i-1))**2.)
      end do
      do i=1,n
          cp(i)=1.-g(i)**2./uinf**2.
      end do
      cp(n+1)=cp(1)
      fpo=(cp(2)-cp(1))/(s(2)-s(1))
      fpn=(cp(n+1)-cp(n))/(s(n+1)-s(n))
      call spline(s,cp,fpo,fpn,aa,bb,cc,dd,n)

      cpmin=1.
*     calc estimate for nmin
      do i=3*n/4,n
        if (cp(i).lt.cpmin) then
          cpmin=cp(i)
          nminest=i
          nmin=nminest
        end if
      end do
      cpmin=1.
      do i=nminest-2,n
        if (((2.*cc(i))**2.-4.*3.*dd(i)*bb(i)).ge. 0.) then
          root1=(-2.*cc(i)+((2.*cc(i))**2.-4.*3.*dd(i)*bb(i))**0.5)
     1          /(2.*3.*dd(i))
          root2=(-2.*cc(i)-((2.*cc(i))**2.-4.*3.*dd(i)*bb(i))**0.5)
     1          /(2.*3.*dd(i))
          root1=root1+s(i)
          root2=root2+s(i)
          if (root1.ge.s(i) .and. root1.le.s(i+1)) then
            cpmintry=aa(i)+bb(i)*(root1-s(i))+cc(i)*(root1-s(i))**2.
     1           +dd(i)*(root1-s(i))**3.
            if(cpmintry.lt.cpmin) then
            cpmin=cpmintry
            smin=root1
            nmin=i+1
            goto 35
```

```
            end if
          end if
          if (root2.ge.s(i) .and. root2.le.s(i+1)) then
            cpmintry=aa(i)+bb(i)*(root2-s(i))+cc(i)*(root2-s(i))**2.
     1           +dd(i)*(root2-s(i))**3.
            if(cpmintry.lt.cpmin) then
            cpmin=cpmintry
            smin=root2
            nmin=i+1
            goto 35
            end if
          end if
        end if
       end do
35     continue

       glast_sep1=gsep1
       glast_sep2=gsep2

       p0=s(nmin+1)
       p1=s(n+1)
           call bisection(p0,p1,s,aa,bb,cc,dd,
     1         ssep2,uinf,nu,strat,smin,cpmin,n,icon,1.)
*      calculate constraint
           con2=xsep2-(xx(icon)+(ssep2-s(icon))/(s(icon+1)-s(icon))
     1            *(xx(icon+1)-xx(icon)))



       cpmin=1.
*      calc estimate for nmin
       do i=1,n/4
         if (cp(i).lt.cpmin) then
           cpmin=cp(i)
           nminest=i
           nmin=nminest
         end if
       end do

       cpmin=0.
       do i=1,nminest+2
         if (((2.*cc(i))**2.-4.*3.*dd(i)*bb(i)).ge. 0.) then
           root1=(-2.*cc(i)+((2.*cc(i))**2.-4.*3.*dd(i)*bb(i))**0.5)
     1          /(2.*3.*dd(i))
           root2=(-2.*cc(i)-((2.*cc(i))**2.-4.*3.*dd(i)*bb(i))**0.5)
     1          /(2.*3.*dd(i))
           root1=root1+s(i)
           root2=root2+s(i)
           if (root1.ge.s(i) .and. root1.le.s(i+1)) then
             cpmintry=aa(i)+bb(i)*(root1-s(i))+cc(i)*(root1-s(i))**2.
     1            +dd(i)*(root1-s(i))**3.
             if(cpmintry.lt.cpmin) then
             cpmin=cpmintry
             smin=root1
             nmin=i
             goto 45
```

```
            end if
          end if
          if (root2.ge.s(i) .and. root2.le.s(i+1)) then
            cpmintry=aa(i)+bb(i)*(root2-s(i))+cc(i)*(root2-s(i))**2.
     1           +dd(i)*(root2-s(i))**3.
            if(cpmintry.lt.cpmin) then
            cpmin=cpmintry
            smin=root2
            nmin=i
            goto 45
            end if
          end if
        end if
       end do
45     continue

       p0=s(nmin-1)
       p1=s(1)
           call bisection(p0,p1,s,aa,bb,cc,dd,
     1         ssep1,uinf,nu,strat,smin,cpmin,n,icon,-1.)

*      calculate constraint
       con1=xsep1-(xx(icon)+(s(icon)-ssep1)/(s(icon)-s(icon-1))
     1     *(xx(icon-1)-xx(icon)))


*       write(*,*) 'xsep1=',xsep1,'xsep2=',xsep2
*       write(*,*) 'ysep1=',ysep1,'ysep2=',ysep2
*       write(*,*) 'sep1=',sep1,'sep2=',sep2
*       write(*,*) 'con1=',con1,'con2=',con2
*       write(*,*) 'Constraints in pnlbluffc',con1,con2

*********************************
*      calculate cp,cl,cd,cm at each time step
       cl=0.0
       cd=0.0
       cm=0.0
       if (tstep.gt. timemax-75) then
       do i=1,n
         if (i.eq.1) then
           delx=co(i,1)-co(n,1)
           dely=co(i,2)-co(n,2)
         else
           delx=co(i,1)-co(i-1,1)
           dely=co(i,2)-co(i-1,2)
         end if

*        pressure coeff equation (w/ base pressure model)

         if (i.ge.sep1 .and. i.le.sep2) then
           cp(i)=1.-g(i)**2./uinf**2.
     1        -2./uinf**2.*(phi(i)-philast(i))/deltt
           cpavg(i)=cpavg(i)+cp(i)
         else
           cp(i)=1.-gsep2**2./uinf**2.
     1        -2./uinf**2.*0.5*(phi(sep2)-philast(sep2)+
```

```
     1       phi(sep1)-philast(sep1))/deltt
            cpavg(i)=cpavg(i)+cp(i)
          end if


            if (i.eq.1) then
              cl=cl-(cp(i)+cp(n))/2.*((xx(i)-xx(n))*cos(al)+
     1           (yy(i)-yy(n))*sin(al))/h
              cd=cd+(cp(i)+cp(n))/2.*((yy(i)-yy(n))*cos(al)-
     1           (xx(i)-xx(n))*sin(al))/h
              cm=cm+(cp(i)+cp(n))/2.*((xx(i)-xx(n))*(co(n,1)-xmom)+
     1           (yy(i)-yy(n))*(co(n,2)-zmom))/h
            else
              cl=cl-(cp(i)+cp(i-1))/2.*((xx(i)-xx(i-1))*cos(al)+
     1           (yy(i)-yy(i-1))*sin(al))/h
              cd=cd+(cp(i)+cp(i-1))/2.*((yy(i)-yy(i-1))*cos(al)-
     1           (xx(i)-xx(i-1))*sin(al))/h
              cm=cm+(cp(i)+cp(i-1))/2.*((xx(i)-xx(i-1))*
     1           (co(i-1,1)-xmom)+(yy(i)-yy(i-1))*(co(i-1,2)-zmom))/h
            end if

          end do

          clavg=clavg+cl
          cdavg=cdavg+cd
          cmavg=cmavg+cm


          end if
          write(69,*) tstep,cl,cd

     ***** end time step ****
          end do


          cl=clavg/75.
          cd=cdavg/75.
          cm=cmavg/75.

          cdbase=cd

          write(*,*) 'Cl=',cl,'Cd=',cd,'Cm=',cm

          do i=1,n
            cp(i)=cpavg(i)/75.
          end do

     *    output to file
          if (infodot.eq.0) then
            write(8,*) 'variables="x","y"'
            write(8,*) 'zone f=point'
            do i=1,n


              write(8,*) xx(i),'  ',cp(i)
            end do
```

```
      end if

*      goto 182
****** perform viscous correction calculations****
      do i=1,n+1
        if (cp(i).gt. 1.0) then
          cp(i)=1.0
        end if
      end do
      call visctop(cf,ITRBSEP,nstag,xx,yy,cp,n,L,uinf,nu)
      write(*,*) 'ITRBSEP=',ITRBSEP,'nstag=',nstag
      do j=1,ITRBSEP
        i=nstag-1+j
        if (i.eq.1) then
          delx=co(i,1)-co(n,1)
          dely=co(i,2)-co(n,2)
        else
          delx=co(i,1)-co(i-1,1)
          dely=co(i,2)-co(i-1,2)
        end if
        cl=cl+cf(j)*(dely*cos(al)-delx*sin(al))/h
        cd=cd+cf(j)*(dely*sin(al)+delx*cos(al))/h
        cm=cm+cf(j)*(delx*(co(i,2)-zmom)-dely*(co(i,1)-xmom))/h
      end do

      if (gnd .eq. 0.) then
      call viscbttm(cf,ITRBSEP,nstag,xx,yy,cp,n,L,uinf,nu)
      write(*,*) 'ITRBSEP=',ITRBSEP,'nstag=',nstag
      do j=1,ITRBSEP
        i=nstag+1-j
        if (i.eq.1) then
          delx=co(i,1)-co(n,1)
          dely=co(i,2)-co(n,2)
        else
          delx=co(i,1)-co(i-1,1)
          dely=co(i,2)-co(i-1,2)
        end if
        cl=cl+cf(j)*(-dely*cos(al)+delx*sin(al))/h
        cd=cd+cf(j)*(-dely*sin(al)-delx*cos(al))/h
        cm=cm+cf(j)*(delx*(co(i,2)-zmom)+dely*(co(i,1)-xmom))/h
      end do
      else
      cpmin=cp(nstag)
      do j=nstag,1,-1
        if (cp(j).lt.cpmin) then
          cpmin=cp(j)
          xxmin=xx(j)
        end if
      end do
      dpdx=(cpmin-cp(nstag))/(xxmin-xx(nstag))*0.5*rho*uinf**2.
      call couette(dpdx,-uinf,alt,cfgap)
      do j=nstag,1,-1
```

```
        if (j.eq.1) then
          delx=co(j,1)-co(n,1)
          dely=co(j,2)-co(n,2)
        else
          delx=co(j,1)-co(j-1,1)
          dely=co(j,2)-co(j-1,2)
        end if
        cl=cl+cfgap*(-dely*cos(al)+delx*sin(al))/h
        cd=cd+cfgap*(-dely*sin(al)-delx*cos(al))/h
        cm=cm+cfgap*(delx*(co(j,2)-zmom)+dely*(co(j,1)-xmom))/h
      end do
      end if
182   continue


      if (infodot.eq.0) then
      write(8,*) 'zone'
      do i=1,n+1
          write(8,*) xx(i), yy(i)
      end do

      write(8,*) 'zone'
      do t=2,timemax
          write(8,*) xxw1(t), yyw1(t)
      end do
      write(8,*) 'zone'
      do t=2,timemax
          write(8,*) xxw2(t), yyw2(t)
      end do
      end if

      write(*,*) 'Cl=',cl,'Cd=',cd,'Cm=',cm

      call etime(tarray)
      time2=tarray(1)
      write(*,*) time1, time2, time2-time1

      close(9)
      close(69)

      return
      end



      subroutine spline(s,cp,fpo,fpn,aa,bb,cc,dd,n)
************************************************************
*  Date: 4/17/97
*  Reference: Numerical Analysis by Burden & Faires
*  Purpose:   Calculates Clamped Cubic Spline
************************************************************



      integer i,j,n,nmax
      parameter(nmax=200)
      double precision s(nmax+1),aa(nmax),bb(nmax),cc(nmax),dd(nmax)
```

```
      double precision h(nmax), alp(nmax), l(nmax), mu(nmax)
      double precision z(nmax),cp(nmax)
      double precision fpo,fpn

      do i=1,n+1
        aa(i)=cp(i)
      end do

      do i=1,n
        h(i)=s(i+1)-s(i)
      end do

      alp(1)=3.*(aa(2)-aa(1))/h(1)-3.*fpo
      alp(n+1)=3.*fpn-3.*(aa(n+1)-aa(n))/h(n)

      do i=2,n
        alp(i)=3./h(i)*(aa(i+1)-aa(i))-3./h(i-1)*(aa(i)-aa(i-1))
      end do

      l(1)=2.*h(1)
      mu(1)=0.5
      z(1)=alp(1)/l(1)

      do i=2,n
        l(i)=2.*(s(i+1)-s(i-1))-h(i-1)*mu(i-1)
        mu(i)=h(i)/l(i)
        z(i)=(alp(i)-h(i-1)*z(i-1))/l(i)
      end do

      l(n+1)=h(n)*(2.-mu(n))
      z(n+1)=(alp(n+1)-h(n)*z(n))/l(n+1)
      cc(n+1)=z(n+1)

      do j=n,1,-1
        cc(j)=z(j)-mu(j)*cc(j+1)
        bb(j)=(aa(j+1)-aa(j))/h(j)-h(j)*(cc(j+1)+2.*cc(j))/3.
        dd(j)=(cc(j+1)-cc(j))/(3.*h(j))
      end do


      return
      end


      subroutine bisection(p0,p1,s,aa,bb,cc,dd,p,uinf,nu,strat,
     1                     smin,cpmin,n,icon,pt)
************************************************************************
*  Date: 4/17/97
*  Reference: Numerical Analysis by Burden & Faires
*  Purpose:   Bisection Method for Root Finding
************************************************************************


      integer i,j,n,nmax,maxiter, icon
      double precision tol
      parameter(nmax=200,tol=1.E-7,maxiter=1000)
      double precision aa(nmax),bb(nmax),cc(nmax),dd(nmax)
```

```
 double precision s(nmax+1)
 double precision p0,q0,p1,q1,p,f0,fp0,f1,fp1
 double precision gmin, cpmin, uinf,reo,nu,smin,strat
 double precision  pt


 do j=1,maxiter
 do i=1,n
   if (p0.ge.s(i) .and. p0.le.s(i+1)) then
     f0=aa(i)+bb(i)*(p0-s(i))+cc(i)*(p0-s(i))**2.+dd(i)*
1       (p0-s(i))**3.
     f0=f0-cpmin
     fp0=pt*(bb(i)+2.*cc(i)*(p0-s(i))+3.*dd(i)*(p0-s(i))**2.)
     gmin=((1.-cpmin)*uinf**2.)**(0.5)
     reo=gmin*pt*(p0-s(n/2))/nu
     q0=f0*(pt*(p0-smin)*fp0)**0.5*(1.e-6*reo)**(-0.1)-strat
   end if
 end do



 p=p0+(p1-p0)/2.


 do i=1,n
   if (p.ge.s(i) .and. p.le.s(i+1)) then
     f1=aa(i)+bb(i)*(p-s(i))+cc(i)*(p-s(i))**2.+dd(i)*
1       (p-s(i))**3.
     f1=f1-cpmin
     fp1=pt*(bb(i)+2.*cc(i)*(p-s(i))+3.*dd(i)*(p-s(i))**2.)
     gmin=((1.-cpmin)*uinf**2.)**(0.5)
     reo=gmin*pt*(p1-s(n/2))/nu
     q1=f1*(pt*(p-smin)*fp1)**0.5*(1.e-6*reo)**(-0.1)-strat
     if (pt.eq.1.) then
       icon=i
     else
       icon=i+1
     end if
   end if
 end do


 if (abs(p1-p0)/2..lt.tol) then
   return
 endif
 if (q0*q1.gt.0.) then
   p0=p
 else
   p1=p
 end if

 end do
 write(*,*) 'Method Fails after',maxiter,'iterations'
```

```
return
end
```

The subroutine, *c-p*, performs the turbulent, Couette/Poiseuille flow calculations for the flow in the gap between the vehicle and the ground plane. This calculation is used to obtain the skin friction coefficient for the gap flow and is performed once after steady state conditions are achieved for the unsteady vortex panel method calculation. This calculation uses the Reichart turbulence model.

E.4 c-p.f

```
      subroutine couette(dpdx,uw,h,cf)
*****************************************************************
* Program: c-p.f
* Author:  Jason Tyll
* Date:    12/26/95
* Purpose: Calculates turbulent Couette/Poiseuille flow
*          using Reichart turb model
*****************************************************************

      integer imax,tmax
      parameter(imax=101,tmax=2000)
      double precision ya,k,rho,nu,mu,uw,h,y(imax),u(imax)
      double precision int(imax),tw(tmax+1), tol, diff, twf
      double precision yp(imax), mut1(imax), mut2(imax), deltast
      double precision dpdx,v,w,x,us,uav
      integer i,j,t,iter
      open(unit=1,file='c-p.out',status='unknown')

      pi=4.*atan(1.)
      ya=9.7
      k=0.41
      rho=1.177
      mu=1.84e-5
      nu=mu/rho
      tw(1)=10.
      tol=1.e-3
      twf=0.

*     set up y grid
      do i=1,imax
        y(i)=real(i-1)/real(imax-1)
      end do

*     full cosine spacing of y
      do i=1,imax
        y(i)=h*0.5*(1.-cos(pi*y(i)))
      end do

*     initialize deltastar (will be corrected in iterations)
```

```
      deltast=0.5*h

*     begin iteration to match Tw
      do t=1,tmax
        diff=0.
        us=0.0

*       calculate eddy viscosity for the Reichart turbulence model
        do i=1,(imax+1)/2
          us=sqrt(abs(tw(t)+y(i)*dpdx)/rho)
          mut1(i)=k*rho*nu*((y(i)*us/nu)-ya*tanh(y(i)*us/nu/ya))
          mut2(i)=0.192*k*rho*us*2.*h
        end do
        do i=(imax+1)/2+1,imax
          us=sqrt(abs(tw(t)+y(i)*dpdx)/rho)
          mut1(i)=k*rho*nu*(((h-y(i))*us/nu)-
     1            ya*tanh((h-y(i))*us/nu/ya))
          mut2(i)=0.192*k*rho*us*2.*h
        end do

*       calculate integrand
        do i=1,imax
          yp(i)=sqrt(abs(tw(t))/rho)*y(i)/nu
          if (mut1(i).ge.mut2(i)) then
            int(i)=dpdx*y(i)/(mu+mut2(i))
          else
            int(i)=dpdx*y(i)/(mu+mut1(i))
          end if
        end do

        deltast=0.0

        v=0.0
        w=0.0
        do j=2,imax
            v=v+(int(j)+int(j-1))/2.*(y(j)-y(j-1))
            if (mut1(j).ge.mut2(j)) then
            w=w+mu*(1/(mu+mut2(j))+1/(mu+mut2(j-1)))/2.*(y(j)-y(j-1))
            else
            w=w+mu*(1/(mu+mut1(j))+1/(mu+mut1(j-1)))/2.*(y(j)-y(j-1))
            end if
        end do

        do i=2,imax
          u(i)=0.0
          x=0.0
          do j=2,i
            u(i)=u(i)+(int(j)+int(j-1))/2.*(y(j)-y(j-1))
            if (mut1(j).ge.mut2(j)) then
            x=x+mu*(1/(mu+mut2(j))+1/(mu+mut2(j-1)))/2.*(y(j)-y(j-1))
            else
            x=x+mu*(1/(mu+mut1(j))+1/(mu+mut1(j-1)))/2.*(y(j)-y(j-1))
            end if
          end do
          u(i)=u(i)+uw*x/w-x/w*v
*         correct deltastar
```

```
          deltast=deltast+(2.-(u(i)+u(i-1))/uw)/2.*(y(i)-y(i-1))
        end do

        uav=0.0
        do i=1,imax
          uav=uav+u(i)
        end do
        uav=uav/real(imax)


        diff=abs(tw(t)-mu*(uw-v)/w)
        if (diff.le.tol) then
          twf=tw(t)
          goto 10
        end if

*       wall shear corrected
        tw(t+1)=mu*(uw-v)/w
      end do

      write(1,*) 'No Convergence'
10    continue


*     output
      write(1,*) twf, twf/0.5/rho/(uw*2.)**2., twf/0.5/rho/(uw)**2.
      write(1,*) deltast, uav
      do i=1,imax
        write(1,*) y(i)/h, u(i)/uw
      end do


      cf=mu*abs((u(imax)-u(imax-1))/(y(imax)-y(imax-1)))
     1   /0.5/rho/(uw)**2.

      close(1)
      return
      end
```

The file, *declare*, is a collection of "parameter" statements used for the weight and cost models. The parameters include information about the mission details and the assumed economic factors.

E.5 declare.h

```
************************************************************
* Program: declare.h
* Author : Mark Eaglesham
* Date   :
* purpose: SETUP COMMON INPUT VARIABLES FOR MAGLEV MASS,
*          MANUFACTURING COST,  LIFE CYCLE, &  OPERATING COST
*          PROGRAMS.
*          Use "include" statement in each subroutine.
************************************************************
C  DECLARE.FOR
C     SETUP COMMON INPUT VARIABLES FOR MAGLEV MASS, MANUFACTURING
C     COST & LIFE CYCLE OPERATING COST PROGRAMS


C INITIALIZE PARAMETER NAMES
      double precision MPERMO,MCONT,MSEATS,MANC,MFUSE,LIFTMO,
     x    LIFPOL,MPOLE,
     x    POWPOL,AUPOWR,NPASS,MAVEP,MLUGG,SPEED,TRDIST,ADENS,
     x    FRAREA,CD,CL,MNOSE,MCONTROL,MSEAT
      double precision NUMMOT,MMOT,MPASS,MVEHIC,DRAG,LIFT,TRTIME,
     x    TOTPOW,TENERGY,VCM,VMM,
     x    ENCOST,COSTPP,COSPPM,NTRIPS,INTEREST,PVFACTOR,INFLATN,
     x    ILEVIT,PLEVIT,CLC
      DOUBLE PRECISION X,C1,NZ,NMODULE,L,SF,D,X0,WREST,ROOT,F,DFDX,
     X DF,DX,DXMAX,EPS,MULT
      DOUBLE PRECISION ELECHA,ELEDEM,PLOAD,OPHOURS,YEAR,PRPASS
      DOUBLE PRECISION GROWTH,CGUIDPM,NVEHIC,QUANTITY,MTV,RE,RT
      DOUBLE PRECISION RQ,RM,LMOD,WMOT,WCONTROL,WPASS
      DOUBLE PRECISION WSEATS, WDG,WFUSE,WEMPTY,Q
      DOUBLE PRECISION PDRAG,FVEHIC,FLEVIT,PI,VLEVIT,PAUX,V
      DOUBLE PRECISION PRPASSKM,NTICKETS,REVENUE,TCGUID,CINVEST
      DOUBLE PRECISION TRIPS,COPERATE,CASHFLOW,DEPN,TAXINC,TAXPAID
      DOUBLE PRECISION ATCF,PVATCF
      DOUBLE PRECISION ENGH,ENGC,TOOLH,TOOLC,MFGH,MFGC,QCH,QCC,
     x DEVC,TESTC,MATLC,CVEHIC,CFLEET
      INTEGER IMAX,N
      INTEGER I, LIFE

C INPUT PARAMETER VALUES
      PARAMETER(MPERMO=52., MCONT=47200., MSEAT=14.55, MANC=0.
     X, NMODULE=1., VCM=1.,VMM=1.)
C      Mass/Motor:MPERMO kg/unit: 1470 kg given lit.ref:ref., value
C      Mass of Controls/Module:MCONT kg: assumed from sum of
C                                        other values
C      Mass of Furnishings:MSEAT kg: seat 14.55kg (Raymer)* 100 =
C                                    1455kg
```

```
C      Mass of Ancillary Equipment:MANC kg: assumed included in MCONT
C      Number of Vehicle Modules: NMODULE 1, 2, 3, 4,
C                                 DEPENDING ON CONFIGURATION
C      Vehicle Cost Modifier: VCM=1 aluminum, =1.1 composite
C      Vehicle Mass Modifier: VMM=1 aluminum, =0.8 composite

       PARAMETER(AUPOWR=85.,EFF=0.82)
C      Auxillary power consumption: AUPOWR 85[kW].
C                                   GMSA final report: 49-50
C      Converter Station Output Efficiency: EFF 0.82
C      Efficiency at LSM is approx 1.00


       PARAMETER(MAVEP=93.2, MLUGG=0., SPEED=134., TRDIST=800.)
C      Ave.mass.of passenger: MAVEP 93.2 [kg]
C                             INCL. LUGGAGE. Shaw, Grumman
C      Mass of Luggage: MLUGG 0 [kg] included with MAVEP.
C                       Shaw, Grumman
C      Speed of Vehicle: SPEED 134 [m/s] GMSA final report
C      Trip distance: TRDIST 800 [km] GMSA final report

       PARAMETER(ADENS=1.177, FRAREA=3.5)
C      density of air: ADENS 1.177 [kg/m3] given
C      frontal area:S=FRAREA 3.5*1=3.5 sq.m
C             given lit.ref:3.8m w x 3.6m len(ref Allen &
C             Ghalli, 1993)


       PARAMETER(ELECHA=0.05, ELEDEM=7.50, NTRIPS=19200.,PLOAD=2000.,
      xOPHOURS=16.,YEAR=365.,LIFE=15,PRPASS=0.,GROWTH=0.04,
      xCGUIDPM=19800000.,NVEHIC=100.)
C      Energy Charges: ELECHA=$ 0.05 [$/kW.h]
C                      given lit.ref: ref., value
C      Demand charge: ELEDEM=$ 7.50 [$/mo per kW]
C                     given lit.ref:ref. value
C      Number of trips per month: NTRIPS=2000/50*16*30=19200
C      Passenger load:PLOAD=2000 per hr
C      Operational hours:OPHOURS=16 hrs/day
C      Service level:YEAR=365 days/year
C      Expected lifetime:LIFE=15 years
C      Price per passenger: PRPASS=0 i.e. no revenue (in 1995)
C      Ave.growth in traffic: GROWTH=4% per annum
C      Guideway cost/mile: CGUIDPM=  $19,800,000 per mile (Deutch)
C      Vehicle size: 50 passengers
C      Vehicle availability: 99% of operational time NOT USED
C      No.vehicles reqd.: 100 vehicles:NVEHIC=100

       PARAMETER(INTEREST=1.06,TAX=0.0,INFLATN=0.03)
C      Interest rate: INTEREST=6% per annum
C      Depn:sum of years digits over vehicle life
C      Tax rate: TAX=0.0 or 50%
C      Average inflation: INFLATN=3% per annum

       PARAMETER (QUANTITY=100.,MTV=2.,RE=59.10,RT=60.70,RQ=55.40,
```

```
     x           RM=50.10)
C      Quantity of vehicles to be built:QUANTITY=100
C      Maglev Test Vehicles: MTV=2
C      Labor Cost Rate: Engineering: RE=59.10
C      Labor Cost Rate: Tooling: RT=60.70
C      Labor Cost Rate: Quality Control: RQ=55.40
C      Labor Cost Rate: Manufacturing: RM=50.10

       PARAMETER(NZ=3.00,D=11.6,LMOD=79.2)
C     Nz:ultimate load factor=1.74
C     L:fuselage struct. length=71.61 ft (REMOVED L=71.61,)
C     D:fuselage struct.depth:12.54 ft
```

The subroutine, *mvehicc*, calculates the vehicle mass and the empty weight using the geometry definition as input.

E.6 mvehicc.f

```
      subroutine mvehicc(MVEHIC,WEMPTY)
*****************************************************************
* Program: mvehicc.f
* Author : Mark Eaglesham
* Date   :
* purpose: Calculates empty weight using parametric weight model
*****************************************************************

      INCLUDE "declare.h"

      integer nmax
      parameter(nmax=104)
      double precision xx(nmax+1),yy(nmax+1)

      open(unit=9,file='mag.dat',status='old')

C         Number of Motors: NUMMOT [#]=24 per module ,
C                           GMSA final report.
      NUMMOT=24.*NMODULE
C         Mass of Motors: MMOT [kg]
      MMOT=NUMMOT*MPERMO
C         Mass of Controls: MCONTROL: [kg]
      MCONTROL=MCONT*NMODULE
C         Number of Passengers: NPASS
      NPASS=NMODULE*50.
C         Mass of Passengers: MPASS 9506.4 [kg] calc. product
      MPASS=NPASS*(MAVEP+MLUGG)
C         Mass of Seats
      MSEATS=NPASS*MSEAT

C     CONVERSION OF MASSES TO WEIGHTS: kg TO lbf
      WMOT=2.205*MMOT
      WCONTROL=2.205*MCONTROL
      WPASS=2.205*MPASS
      WSEATS=2.205*MSEATS
      WREST=WMOT+WCONTROL+WPASS+WSEATS

C     GEOMETRIC PARAMETERS OF VEHICLE
      L=NMODULE*LMOD

C     calculate SF (surface area)
      do I=1,nmax+1
        read(9,*) xx(I),yy(I)
      end do
      SF=0.
      do I=2,nmax+1
        SF=SF+sqrt((xx(I)-xx(I-1))**2.+
```

```
     1         (yy(I)-yy(I-1))**2.)*D
C     not unit width for the case of surface area (so we can calc
C     reasonable weight
      end do
      do I=2,nmax+1
        SF=SF+0.5*(xx(I)-xx(I-1))*(yy(I)+yy(I-1))*2.
      end do
C     convert units from m^2 to ft^2
      SF=SF*3.3**2.


C PROGRAM TO SOLVE FOR WDG USING
C      WDG=WREST+WFUSE*NMODULE
C      WFUSE=0.328*(WDG*NZ)**0.5*(L)**0.25*(SF)**0.302*(L/D)**0.1

      C1=0.3280*NZ**0.5*L**0.25*SF**0.302*(L/D)**0.1
      X0=130000.
      EPS=0.1
      IMAX=100
      DXMAX=1.0E8
      MULT=1.
      CALL NEWTON(X0,C1,WREST,EPS,IMAX,DXMAX,MULT,WFUSE,
     X            F,DFDX,N)

      WDG=WFUSE*NMODULE+WREST
      WEMPTY=WDG-WPASS


C      Convert WFUSE to kg
      MFUSE=WFUSE/2.205

C      Mass of Vehicle: MVEHIC=61369.4 [kg] calc.sum
C                       (Lever- for 2 mod vehicle)
      MVEHIC=MMOT+MCONTROL+MPASS+MSEATS+MFUSE*NMODULE
C      Vehicle mass modifier: VMM input as parameter
      MVEHIC=VMM*MVEHIC



      close(9)

      RETURN
      END

C SUBROUTINE TO CALCULATE ROOT OF 2 EQUATIONS USING NEWTON'S METHOD
      SUBROUTINE NEWTON(X,C1,WREST,EPS,IMAX,DXMAX,MULT,
     X ROOT,F,DFDX,N)
C      VARIABLE DECLARATIONS

      INCLUDE "declare.h"

C      ITERATIONS
      DO 1 I=1,IMAX
          DFDX=1.-0.5*C1*(NMODULE*X+WREST)**(-0.5)*NMODULE
          F=X-C1*(NMODULE*X+WREST)**0.5
          DF=DFDX
          IF(DF.EQ.0.)THEN
              WRITE(*,112)I,X,F
              WRITE(*,*) 'ERROR IN NEWTON'
```

```
            RETURN
          ENDIF
          DX=-MULT*F/DF
          IF(ABS(DX).LT.EPS)THEN
              ROOT=X+DX
              N=I
              RETURN
          ELSEIF(ABS(DX).GT.DXMAX)THEN
              WRITE(*,110)I,DX
              WRITE(*,*) 'ERROR IN NEWTON,METHOD DIVERGING'
              RETURN
          ENDIF
          X=X+DX
    1 CONTINUE
      WRITE(*,111)X,F,DX,I
      WRITE(*,*) 'ERROR IN NEWTON,METHOD NOT CONVERGING'

C      MESSAGES
  110 FORMAT('In iteration',I6,'dx=',F15.1,'larger than limit')
  111 FORMAT('Excessive iterations after max steps
     x:f(',F15.1,')=',F15.1/'latest dx=',F15.1,'ITERATIONS=',I6)
  112 FORMAT('In iteration',I6,'df=0: problem with df/dx',2F15.4)

      RETURN
      END
```

The subroutine, *opcost*, calculates the direct operating cost for a single trip using vehicle mass, aerodynamic coefficients, and system performance parameters as input. The power requirements are calculated and the cost is determined using electricity cost and demand charges.

E.7 opcost.f

```
      subroutine opcost(CD,CL,MVEHIC,FLEVIT,ENCOST)
*****************************************************************
* Program: opcost.f
* Author : Mark Eaglesham
* Date   :
* purpose: Calculates the direct operating cost for single trip.
          Calculates power requirements.
*****************************************************************

      INCLUDE "declare.h"


C       Dynamic pressure of freestream air:q= 1/2.rho.V^2
C                                           (RAYMER p.260)
      Q=0.5*ADENS*SPEED**2.
C       Aerodynamic Drag Force  DRAG: D=q.S.Cd [kN](Raymer p.260)
      DRAG=Q*FRAREA*CD/1000.
C       Lift: L=q.S.Cl [kN](Raymer p.260)
      LIFT=Q*FRAREA*CL/1000.
C       Time for trip: TRTIME =7939s =132.3 min = 2.2053hr.
C       given (in hrs)
      TRTIME=TRDIST/SPEED*1000./3600.
C       Power consumption for DRAG: [kW]
      PDRAG=DRAG*SPEED/EFF
C       Force downward [kN] due to vehicle mass plus safety
C       factor of 1.5
      FVEHIC=MVEHIC*9.81/1000.
C       Force required for magnetic levitation [kN]
      FLEVIT=FVEHIC-LIFT
C       Calculate force normal to magnets: FLEVIT/COS(35)
      PI=4.*ATAN(1.)
      FLEVIT=FLEVIT/COS(35.*PI/180.)
C       Read off polynomial curve for current use[kA]
C       [GMSA final report]
      ILEVIT=7.E-9*FLEVIT**3.-2.E-5*FLEVIT**2.+0.0526*FLEVIT+10.045
C Initial method: Levitation power consumpt: POWLIF = 2100.4 [kW]
C                 calc.MAE
C               POWLIF=2100.4
C       Power consumption for Levitation and guidance: P=V*I [kW]
      VLEVIT=42.
      PLEVIT=VLEVIT*ILEVIT
```

```
C       Auxillary power consumption: PAUX [kW]
      PAUX=AUPOWR
C       Total power consumption rate [kW]
      TOTPOW=PDRAG+PLEVIT+PAUX
      write(*,*) 'PDRAG=',PDRAG, 'PLEVIT=',PLEVIT
C ENERGY CONSUMED BY VEHICLE OVER TRIP [kW.h]
      TENERGY=TOTPOW*TRTIME

C ENERGY COST CALCULATION
C      Energy Cost: [$] : calc.sum
      ENCOST=(TENERGY*ELECHA)+(TOTPOW*PLOAD/(NMODULE*50.)/
     1        NTRIPS*ELEDEM)
C      Total cost per passenger per trip: COSTPP 0.0025 [$/passenger]
      NPASS=NMODULE*50.
      COSTPP=ENCOST/NPASS
C      Cost per passenger km ($/passenger km)
      COSPPM=COSTPP/TRDIST


      RETURN
      END
```

The subroutine *lifecost*, calculates the acquisition cost, yearly operating cost, and life cycle cost using a discounted cash flow analysis. The required input to this model is the empty weight, energy cost for a single trip, and economic factors.

E.8 lifecost.f

```
      subroutine lifecost(WEMPTY,ENCOST,CLC,COPERATE,CVEHIC,
     x                    CINVEST)
*****************************************************************
* Program: lifecost.f
* Author : Mark Eaglesham
* Date   :
* purpose: Calculates acquisition cost and yearly operating cost.
*          Performs discounted cash flow analysis to obtain net
*          present value.
*****************************************************************

      INCLUDE 'declare.h'


C      Price per pass. km:
      PRPASSKM=PRPASS/TRDIST
C      Tickets sold:23,360,000 in year zero
      NTICKETS=PLOAD*OPHOURS*YEAR
C      Revenue per year: $ 350,400,000
      REVENUE=NTICKETS*PRPASS
C Cost of Infrastructure
C      Total guideway cost: $9,127,800,000
      TCGUID=CGUIDPM*TRDIST/1.609

C COST OF VEHICLES (DACPA IV COST MODEL: RAYMER P.498)
      V=1.943*SPEED
      ENGH=4.86*WEMPTY**0.777*V**0.894*NVEHIC**0.163
      ENGC=RE*ENGH
      TOOLH=5.99*WEMPTY**0.777*V**0.696*NVEHIC**0.263
      TOOLC=RT*TOOLH
      MFGH=7.37*WEMPTY**0.82*V**0.484*NVEHIC**0.641
      MFGC=RM*MFGH
      QCH=0.133*MFGH
      QCC=RQ*QCH
      DEVC=45.42*WEMPTY**0.630*V**1.3
      TESTC=1243.03*WEMPTY**0.325*V**0.822*MTV**1.21
      MATLC=11.0*WEMPTY**0.921*V**0.621*NVEHIC**0.799
      CFLEET=ENGC+TOOLC+MFGC+QCC+DEVC+TESTC+MATLC
C      Vehicle cost modifier: Material=composite=>VCM=0.8 TO 1.1
      CFLEET=VCM*CFLEET
C      Fleet cost: $ 825,000,000 baseline
      CVEHIC=CFLEET/NVEHIC
C      Investment Cost
      CINVEST=CFLEET
C      Number of trips made per year
      NPASS=NMODULE*50.
```

```
      TRIPS=PLOAD/NPASS*OPHOURS*YEAR
C      Operating Cost
      COPERATE=-ENCOST*TRIPS
C      Initial Cash Flow = - CINVEST
      CLC=-CINVEST
C      Annualized net present value of cash flows for 15 year life
      DO I=1,LIFE
          ATCF=COPERATE
          PVFACTOR=INTEREST**REAL(I)
          PVATCF=ATCF/PVFACTOR
          CLC=CLC+PVATCF
          COPERATE=(1.+GROWTH)*(1.+INFLATN)*COPERATE
      END DO


      RETURN
      END
```